

# Supersymmetry parameter determination at the International Linear Collider

## Dissertation

with the aim of achieving a doctoral degree at the Faculty of  
Mathematics, Informatics and Natural Sciences  
Department of Physics  
of Universität Hamburg

Submitted by

SUVI-LEENA LEHTINEN

2018 in Hamburg

Gutachterinnen der Dissertation:	Dr. Jenny List Prof. Dr. Gudrid Moortgat-Pick
Zusammensetzung der Prüfungskommission:	Dr. Jenny List Prof. Dr. Gudrid Moortgat-Pick Prof. Dr. Sven-Olaf Moch Dr. Christian Sander Prof. Dr. Peter Schleper
Vorsitzender Prüfungskommission:	Prof. Dr. Sven-Olaf Moch
Datum der Disputation:	28.6.2018
Vorsitzender Promotionsausschusses PHYSIK:	Prof. Dr. Michael Potthoff
Leiter des Fachbereichs PHYSIK:	Prof. Dr. Wolfgang Hansen
Dekan der Fakultät MIN:	Prof. Dr. Heinrich Graener

# Abstract

In this thesis, the prospects for determining supersymmetry parameters from observations of supersymmetric particles at the International Linear Collider (ILC) are investigated. Supersymmetry (SUSY) has been proposed in order to solve gaps in the Standard Model of particle physics, among them the hierarchy problem and the unexplained dark matter content in the universe. There are many free parameters in supersymmetry, whose values give rise to the properties of the supersymmetric particles which can be searched for by experiments. While the Large Hadron Collider (LHC) has successfully excluded many possible scenarios, regions of parameter space remain unexplored, especially where the supersymmetric particles decay with little visible energy. For example, models with light higgsinos or scalar tau coannihilation can escape detection at the LHC. These kinds of scenarios could be discovered or excluded by the proposed ILC, which would collide polarised electron and positron beams at the centre-of-mass energy of 500 GeV. The advantages of this machine over the LHC, namely its the clean experimental environment and triggerless detector operation, would allow for the discovery of almost any particle within its kinematic reach.

If supersymmetric discoveries were made at the ILC, it would be possible to measure the properties of the SUSY particles very precisely. These measurements enable determining some of the underlying SUSY parameters via fitting the parameters to the SUSY observations. In this thesis, a 10-parameter or 13-parameter phenomenological Minimal Supersymmetric Standard Model and high-scale 4-6-parameter models (CMSSM, NUHM1 and NUHM2) are fitted to sets of possible observations from the ILC. Two types of scenarios are considered: light higgsinos motivated by naturalness, and scalar tau coannihilation motivated by the dark matter relic density. It is shown that the precision measurements of the SUSY and Higgs sectors allow for determining some of the SUSY parameters. Additionally, strong predictions for unobserved heavy particle masses can be made, leading to guidance on future high-energy particle colliders. Furthermore, it is possible under certain circumstances to check whether the observed particles explain the dark matter relic density. It is shown that the permille or percent-level measurements from the International Large Detector are crucial for making these predictions. Additionally, the determined parameters in the weak scale fits are evolved to the GUT scale to test the gaugino mass unification hypothesis. The results give a strong argument for building an electron-positron collider to close the gaps in the LHC searches or to study any particles that the latter finds.



# Zusammenfassung

In der vorliegenden Arbeit wird untersucht, inwieweit die Beobachtung und Vermessung supersymmetrischer Teilchen am International Linear Collider (ILC) Rückschlüsse auf die Parameter des zugrundeliegenden Modells erlauben. Supersymmetrie (SUSY) ist eine Klasse von Erweiterungen des Standardmodells der Teilchenphysik (SM), die etliche Probleme des SM lösen kann, u.a. das Hierarchieproblem, und eine Erklärung der kosmologisch beobachteten Dunklen Materie liefern kann. SUSY-Modelle enthalten etliche neue Teilchen, die an Collidern entdeckt werden könnten, und deren Eigenschaften von einer Vielzahl von freien Parametern abhängen. Obwohl der Large Hadron Collider (LHC) erfolgreich viele mögliche Szenarien ausgeschlossen hat, bleiben immer noch unerforschte Regionen des Parameterraums — insbesondere in Fällen, in denen der Zerfall der gesuchten Teilchen nur sehr wenig im Detektor sichtbare Energie produziert. Beispielsweise können Modelle mit leichten Higgsinos oder  $\tilde{\tau}$ -coannihilation-Modelle am LHC nur sehr schwer nachgewiesen werden. Solche Szenarien könnten am vorgeschlagenen ILC, der polarisierte Elektronen und Positronen bei Energien von 500 GeV zu Kollision bringen würde, entweder ausgeschlossen oder entdeckt und präzise vermessen werden. Die Vorteile einer solchen Maschine gegenüber dem LHC, nämlich die untergrundarme experimentelle Umgebung und der triggerlose Betrieb der Detektoren ermöglichen die Entdeckung nahezu jeder Art von Teilchen, dessen Produktion kinematisch erlaubt ist.

Wenn am ILC supersymmetrische Teilchen produziert werden, erlauben Präzisionsmessungen ihrer Eigenschaften einige der zugrundeliegenden SUSY-Parameter zu bestimmen, indem verschiedene SUSY-Modelle an die Messdaten angepasst werden. In dieser Arbeit wurden eine 10-Parameter- oder eine 13-Parameter-Version des phänomenologischen minimal-supersymmetrischen Standardmodells sowie verschiedene an der GUT-Skala definierte SUSY-Modelle (CMSSM, NUHM1, NUHM2) an angenommene ILC-Messungen gefittet. Dabei wurden zwei Szenarien betrachtet: ein Modell mit leichten Higgsinos, wie sie in sogenannten „natural SUSY“-Szenarien vorkommen, und ein Modell mit Koannihilation zwischen einem skalaren Tau-Lepton und dem leichtesten SUSY-Teilchen, das die beobachtete Dichte der Dunkle Materie im Universum erklären kann. Es wird gezeigt, dass Präzisionsmessungen an SUSY-Teilchen und am Higgs-Teilchen es erlauben, einige der SUSY-Parameter zu bestimmen. Darüber hinaus können aussagekräftige Vorhersagen über die Massenbereiche schwerer, noch unbeobachteter SUSY-Teilchen gemacht werden, die wichtige Leitlinien für die Planung von Collidern mit noch höheren Energien darstellen. Unter manchen Umständen kann überprüft werden, ob das leichteste SUSY-Teilchen die Reliktdichte der Dunklen Materie erklärt. Es wird gezeigt, dass die Messungen im Promille- bzw. Prozentbereich, wie sie der International Large Detector am ILC vornehmen könnte, entscheidend sind um diese Rückschlüsse ziehen zu können. Außerdem werden die Ergebnisse der an der elektroschwachen Skala durchgeführten Fits zur GUT-Skala evolviert um zu überprüfen, ob einige der SUSY-Parameter an der GUT-Skala sich auf den selben Wert vereinigen. Die Ergebnisse geben eine starke Motivation, einen Elektron-Positron-Collider mit genügend hohen Energie zu bauen, um die Suchen nach neuen Teilchen am LHC zu ergänzen und um Präzisionsmessungen an neuen Teilchen vorzunehmen.



# Contents

<b>1</b>	<b>Introduction</b>	<b>11</b>
<b>2</b>	<b>Supersymmetry</b>	<b>15</b>
2.1	The Standard Model of particle physics . . . . .	15
2.1.1	Particles and interactions . . . . .	15
2.1.2	Standard Model as a gauge theory . . . . .	16
2.2	Problems of the Standard Model . . . . .	21
2.2.1	Dark matter . . . . .	21
2.2.2	Hierarchy problem . . . . .	22
2.2.3	Anomalous magnetic moment of the muon . . . . .	23
2.2.4	Other open problems . . . . .	24
2.3	Supersymmetry basics . . . . .	24
2.3.1	Consequences of $R$ -parity conservation . . . . .	27
2.3.2	Electroweak symmetry breaking in the MSSM . . . . .	28
2.3.3	Masses in the MSSM . . . . .	29
2.3.4	SUSY cross sections, decays and polarisation . . . . .	33
2.4	Renormalisation group flow . . . . .	34
2.5	Constrained models . . . . .	35
2.6	Phenomenological MSSM . . . . .	37
2.7	Dark matter in supersymmetry . . . . .	37
2.7.1	Relic density calculations . . . . .	39
2.7.2	Lightest SUSY particle as dark matter . . . . .	39
2.7.3	Non-collider signatures of dark matter . . . . .	41
2.8	Status of SUSY at LEP and LHC . . . . .	42
2.8.1	Results from LHC . . . . .	42
2.8.2	Future constraints from high-luminosity LHC . . . . .	45
2.8.3	Results from LEP . . . . .	46
<b>3</b>	<b>International Linear Collider</b>	<b>49</b>
3.1	Physics at the ILC . . . . .	49
3.1.1	Advantages of lepton colliders over hadron colliders . . . . .	49
3.1.2	Operating scenarios . . . . .	51
3.1.3	Higgs physics . . . . .	52
3.1.4	Top physics . . . . .	56
3.1.5	Beyond the Standard Model measurements . . . . .	57
3.1.6	Electroweak precision measurements . . . . .	59
3.2	International Linear Collider . . . . .	60
3.2.1	Design goals . . . . .	60
3.2.2	Accelerator overview . . . . .	60
3.2.3	Beam backgrounds . . . . .	61
3.2.4	Polarimeters . . . . .	62
3.2.5	Location and cost . . . . .	63
3.2.6	Political situation . . . . .	64
3.3	International Large Detector . . . . .	65

3.3.1	Particle flow . . . . .	65
3.3.2	Design goals . . . . .	65
3.3.3	Detector overview . . . . .	66
<b>4</b>	<b>Fitting algorithms for determining SUSY parameters</b>	<b>69</b>
4.1	Parameter fitting with <code>Fittino</code> . . . . .	69
4.2	<code>SPheno</code> . . . . .	73
4.3	<code>FeynHiggs</code> . . . . .	74
4.4	<code>MicrOMEGAs</code> . . . . .	75
4.5	<code>Astrofit</code> and <code>DarkSUSY</code> . . . . .	76
4.6	Tools to analyse the chi-squared distributions . . . . .	76
4.7	Other fitting codes . . . . .	78
<b>5</b>	<b>Dark matter relic density</b>	<b>81</b>
5.1	Stau coannihilation measurements at ILC . . . . .	82
5.1.1	Gauginos . . . . .	86
5.1.2	Sleptons . . . . .	86
5.1.3	Sneutrinos . . . . .	88
5.1.4	Mixings . . . . .	89
5.2	Method to extract relic density . . . . .	90
5.3	Results . . . . .	91
5.4	Conclusion . . . . .	94
<b>6</b>	<b>Stau coannihilation scenario</b>	<b>97</b>
6.1	Motivation . . . . .	97
6.2	Benchmarks . . . . .	98
6.3	Prospects for measurements at ILC . . . . .	109
6.4	Expected measurements from LHC . . . . .	109
6.5	Parameter fits . . . . .	111
6.5.1	Fitting setup . . . . .	111
6.5.2	Fitted models . . . . .	111
6.5.3	Fit inputs or observables . . . . .	112
6.6	Fit results . . . . .	115
6.6.1	GUT model fits to STC10' observables . . . . .	115
6.6.2	pMSSM-13 fits to STC10' . . . . .	117
6.6.3	STC10' relic density predictions . . . . .	135
6.6.4	pMSSM-4 fit to STC10' observables . . . . .	136
6.6.5	pMSSM-13 fits to STC10'- $\Omega_{75}$ and STC10'- $\Omega_{50}$ . . . . .	138
6.6.6	pMSSM-14 fits to STC10'-LH150 . . . . .	144
6.6.7	Comparison to direct and indirect DM detection experiments . . . . .	145
6.6.8	Effect of $Sign(\mu)$ . . . . .	149
6.7	From the weak scale to the GUT scale . . . . .	150
6.7.1	Method . . . . .	152
6.7.2	Results . . . . .	152
6.8	Outlook . . . . .	155
<b>7</b>	<b>Light higgsino scenario</b>	<b>157</b>
7.1	Motivation . . . . .	157
7.1.1	Previous study of very degenerate higgsinos at ILC . . . . .	161

7.1.2	Previous study on running of SUSY parameters . . . . .	162
7.2	Higgsino benchmarks . . . . .	162
7.3	Expected measurements from ILD . . . . .	172
7.3.1	Event selection . . . . .	173
7.3.2	Mass measurement . . . . .	174
7.3.3	SUSY cross section measurements . . . . .	178
7.3.4	Higgs measurements . . . . .	180
7.3.5	Expected measurements from LHC . . . . .	180
7.4	Parameter fits . . . . .	182
7.4.1	Fitting setup . . . . .	182
7.4.2	Fitted models . . . . .	183
7.4.3	Fit inputs . . . . .	183
7.5	GUT scale fit results . . . . .	184
7.5.1	Results of fitting NUHM2 to ILC1 observables . . . . .	184
7.5.2	Results of fitting NUHM2 to ILC2 observables . . . . .	185
7.5.3	Results of fitting NUHM2 to nGMM1 observables . . . . .	188
7.5.4	CMSSM and NUHM1 fits . . . . .	190
7.6	Weak scale fit results . . . . .	191
7.6.1	ILC1 pMSSM-10 fit . . . . .	191
7.6.2	Effect of including gluino mass measurement on ILC1 pMSSM-10 fit . . . . .	193
7.6.3	ILC1 pMSSM-4 fit . . . . .	196
7.6.4	ILC2 pMSSM-10 fit . . . . .	200
7.6.5	ILC2 pMSSM-4 fit . . . . .	201
7.6.6	nGMM1 pMSSM-10 fit . . . . .	204
7.6.7	nGMM1 pMSSM-10 fit with mass difference measurements . . .	208
7.6.8	nGMM1 pMSSM-4 fit . . . . .	209
7.6.9	Effect of fit input precisions . . . . .	212
7.6.10	Dark matter in higgsino fits . . . . .	212
7.7	Testing gaugino mass unification . . . . .	214
7.7.1	Method . . . . .	214
7.7.2	ILC1 running . . . . .	215
7.7.3	ILC2 running . . . . .	216
7.7.4	nGMM1 running . . . . .	216
7.8	Outlook . . . . .	218
<b>8</b>	<b>Conclusion</b>	<b>221</b>
<b>A</b>	<b>Tree-level estimates of SUSY parameters</b>	<b>225</b>
<b>B</b>	<b>Example files</b>	<b>229</b>
B.1	Les Houches input file for SPheno with STC10' parameters . . . . .	229
B.2	SPheno output file for the STC10' benchmark . . . . .	230
B.3	Fittino input file for a pMSSM-10 fit to ILC1 observables . . . . .	247



# Chapter 1

## Introduction

Many decades of particle physics experiments have provided us with a very successful model of the subatomic world known as the Standard Model of particle physics. The discovery of the Higgs-like particle at the LHC in 2012 provided a candidate for the last missing particle of the Standard Model. The theory describes particle interactions with unprecedented precision, yet some phenomena cannot be explained by the Standard Model alone. For example, the existence of dark matter or neutrino masses is not predicted by the Standard Model which points to physics beyond the Standard Model (BSM).

There are many proposals for theories to explain dark matter, neutrino masses and a plethora of other effects. One of the most theoretically motivated models of BSM physics is supersymmetry (SUSY), which elegantly addresses the problem of the light Higgs mass: if the Standard Model held up to the Planck scale, then loop-corrections to the Higgs mass would diverge. With certain requirements, supersymmetry removes this issue by introducing a cancelling effect coming from new particles called sparticles. These sparticles should have the same mass and couplings as the Standard Model particles but half-integer spin more or less than the Standard Model counterpart.

As we have not observed supersymmetric partners with the same mass as the Standard Model particles, supersymmetry must be a broken symmetry, meaning that the masses must be heavier. However, due to this, there are many different models of supersymmetry with many free parameters. Since we want the cancellation of the Higgs mass loops then the masses should not exceed a few TeV. The LHC is looking for sparticles and successfully excluding many models. There are limitations to the LHC searches, however, as hadron collisions have large QCD backgrounds. This means that not all interactions can be recorded, and low-energetic particles can be missed.

To close any loopholes left open by the LHC, a machine is needed which can record and store all the collisions because there are no QCD backgrounds. This is what an electron-positron collider would provide. There is a very advanced proposal for an electron-positron collider called the International Linear Collider (ILC). The ILC is planned to be operating at the highest ever centre-of-mass energy, 500 GeV, for a lepton collider. It will run with polarised beams and the centre-of-mass energy is tunable to as low as 200 GeV. The ILC will be able to measure the Higgs mass with 15 MeV precision after 20 years of operation, and measure many Higgs couplings,

including the Higgs self-coupling. Additionally the ILC can measure the top quark mass with enough precision to check whether the electroweak vacuum is stable. Any deviations in the Higgs and top measurements from the Standard Model expectation will be evidence for BSM physics. Depending on the type of deviation we may even be guided as to what kind of BSM physics causes the deviation.

The precise measurements of the known particles are enough to justify building the ILC. However, there is another avenue for discovery which is direct detection. As all particles can be recorded and the background rates are relatively low, it will be possible to detect decay products of SUSY particles even if they have little visible energy. In fact, the ILC would enable high-precision measurements of the mass, coupling and spin of almost any kind of particle within its kinematic reach.

In the case of supersymmetric discoveries, would we know if the particles we have found fill the amount of dark matter in the universe? If we know the masses of some of the sparticles, will we be any wiser about the rest of the supersymmetric spectrum? What kind of measurements are sufficient to make further predictions? These kinds of questions can be answered by fitting the parameters of the theory to the observed sparticle properties. It is important to extract the full available information from the measurements in order to gain guidance for designing future experiments and for testing theoretical models. Additionally, before the detector is built, it is important to make sure that the detector will be able to make the measurements with the required precisions. This is the motivation for this thesis.

Supersymmetry parameter fits can be done with algorithms which probe the large parameter space efficiently. In some simplified models of supersymmetry, there are 4-19 free parameters which have to be matched to the observables. This can be done via Markov Chain Monte Carlo methods using `Fittino`. There have been studies before on parameter determination at the LHC and at a linear collider, however, these results are based on earlier estimates of the possible measurements of the supersymmetric particles or on tree-level theory calculations of the observables. In this thesis, we use up-to-date realistic assumptions about the detector performance and thus realistic prospects of making the measurements, and the most accurate calculations of the theoretical observables.

Two kinds of scenarios were investigated in this thesis. For models which fill the dark matter density in the universe, the lightest particle should be a neutralino. If it is a bino neutralino, as is the case in many models motivated by Grand Unification, then another particle should exist, namely a slightly heavier sfermion, which coannihilates with the neutralino. This is the motivation to expect coannihilation models to exist. As the coannihilating particles have similar masses, the decay products are soft, so the LHC may have missed their signal. This thesis investigates one type of such model, the stau coannihilation model. It is possible to measure the stau and the neutralino properties with permille-level precision at the ILC. If such discoveries and measurements were made, then the SUSY model parameters can be fitted and the properties of some of the unobserved particles be inferred.

The other kind of model investigated in this thesis is motivated by the hierarchy problem, which hints that the higgsino mass parameter should be small. This leads to light higgsinos which could also be discovered at the ILC. In this case the measurement

---

precisions would be in the percent-level range. Yet with these measurements, predictions of the unseen particles can be made. Additionally, as the small higgsino mass parameter can be realised naturally in some Grand Unified models, it is possible to get some guidance from the experimental measurements that indeed supersymmetry may be realised as a Grand Unified Theory.

This thesis discusses all the aforementioned material in more detail in the following order. Chapter 2 describes the theoretical foundations of the project, namely the Minimally Supersymmetric Standard Model (MSSM) and its properties, as well as its relevance for dark matter and Grand Unified Theories. Ch. 3 describes the experimental premises, namely the ILC. The physics motivation and detector and accelerator designs are discussed. The methods for fitting supersymmetry parameters to measurements are detailed in Ch. 4, which includes both the fitting tool itself and the calculators which connect SUSY theory to the observations.

The coannihilation scenarios are explored in Chapters 5 and 6. In both chapters, a scenario is discussed where gauginos, all sleptons and sneutrinos would be observed at the ILC with  $\sqrt{s} = 500$  GeV. The lightest neutralino is mostly bino and has 96 GeV mass and the light stau is mostly right-handed and has 107 GeV mass, leading to the coannihilation of the two. In this model, the dark matter relic density is saturated. In Ch. 5, the hypothetical SUSY observations from the ILC are used to calculate the dark matter relic density with **MicrOMEGAs**. Toy calculations are performed and the unobserved sparticle masses are used as nuisance parameters to check whether the dark matter relic density is found correctly.

In Ch. 6, the supersymmetry parameters of GUT scale CMSSM, NUHM1, NUHM2 models and a 10 or 13 parameter weak scale phenomenological MSSM model are fitted to the same stau coannihilation scenario as above, including polarised SUSY cross sections and light Higgs mass and branching fraction observations. Via the fits, conclusions about the masses of the unobserved particles can be made. The importance of the precision of the SUSY inputs was investigated. Additionally, the dark matter relic density was investigated using the fitted parameters. To generalise the statements about dark matter, two further benchmark models were considered where the relic density is only partially filled. To update the study, a fourth benchmark was considered, which respects the current exclusion limits from the LHC.

Chapter 7 discusses the higgsino scenario in which the hierarchy problem is solved. We considered three benchmark scenarios, in which only three higgsinos are observable at the ILC, with mass differences of 3-20 GeV. SUSY parameter fits were performed, where CMSSM, NUHM1, NUHM2 and pMSSM-10 parameters were fitted to higgsino masses, polarised cross sections and the light Higgs mass and branching fractions. Predictions for the unobserved particles and dark matter properties are made. In addition, the high-scale properties of the model were studied via the renormalisation group running of the fitted parameters. The conclusions are presented in Ch. 8.



# Chapter 2

## Supersymmetry

The studies in this thesis are based on hypothetical discoveries of supersymmetric particles. To understand the work, it is necessary to discuss the theoretical foundations of supersymmetry. This chapter covers the Standard Model of particle physics and some of its deficiencies. Supersymmetry can solve some of the issues and thus the basics of supersymmetry are discussed, focusing on the phenomenological aspects i.e. masses and cross sections. The types of supersymmetry model used in this thesis are defined, after which the special role of the lightest supersymmetric particle as a dark matter candidate is discussed. The chapter is concluded with a summary of the experimental exclusion limits from LEP and LHC.

### 2.1 The Standard Model of particle physics

The Standard Model of particle physics (SM) provides a very good description of particle physics phenomena. The Standard Model gives a framework for studying three of the four fundamental forces of nature, namely electromagnetism, weak interaction and strong interaction. It has made predictions which experiments have verified, and vice versa. Phenomena such as electron orbits in atoms, nuclear beta decay and the existence of a bound state with three up quarks can be described. The following is a discussion of the particles and interactions in the Standard Model.

#### 2.1.1 Particles and interactions

The Standard Model contains the electrically charged leptons  $e, \mu$  and  $\tau$ , the electrically neutral neutrinos  $\nu_e, \nu_\mu$  and  $\nu_\tau$ , and quarks  $u, d, c, s, b$  and  $t$  with fractional electric charges. Collectively these are called fermions. All fermions have half-integer spin and each of these has an anti-particle with opposite quantum numbers. The fermion masses are listed in Tab. 2.1.

These matter particles interact with each other via the exchange of gauge bosons. All electrically charged particles interact under the electromagnetic force, which is mediated by an electrically neutral, massless spin-1 particle, the photon  $\gamma$ . The fermions have a chirality, left-handed and right-handed, of which the left-handed components

interact under the weak force via massive spin-1 particles,  $W^+$ ,  $W^-$  and  $Z$ . Furthermore, the quarks carry colour charge, which means that they interact with the strong force via the gluon, which is a massless, electrically neutral spin-1 particle. There is a massive spin-0 particle, the Higgs boson, which interacts with all massive particles. Neutrinos are considered massless in the Standard Model. The gauge boson masses are listed in Tab. 2.2.

	particle	label	mass [GeV]	electric charge
leptons	electron neutrino	$\nu_e$	$< 2 \times 10^{-9}$	0
	electron	$e$	$0.511 \times 10^{-3}$	-1
	muon neutrino	$\nu_\mu$	$< 0.19 \times 10^{-9}$	0
	muon	$\mu$	0.106	-1
	tau neutrino	$\nu_\tau$	$< 18.2 \times 10^{-9}$	0
	tau	$\tau$	$1.77686 \pm 0.00012$	-1
quarks	up	$u$	$(2.2^{+0.6}_{-0.4}) \times 10^{-3}$	$+\frac{2}{3}$
	down	$d$	$(4.7 \pm^{+0.5}_{-0.4}) \times 10^{-3}$	$-\frac{1}{3}$
	charm	$c$	$1.28 \pm 0.03$	$+\frac{2}{3}$
	strange	$s$	$(96^{+8}_{-4}) \times 10^{-3}$	$-\frac{1}{3}$
	top	$t$	$173.1 \pm 0.6$ GeV	$+\frac{2}{3}$
	bottom	$b$	$4.18^{+0.04}_{-0.03}$	$-\frac{1}{3}$

Table 2.1: Fermions of the Standard Model. All the masses are from PDG 2016 review [1]. Planck 2015 data imposes that the sum of the neutrino masses should be less than 0.23 eV [2]. The electron and muon mass uncertainties are less than  $\mathcal{O}(10^{-8})$  GeV, see [1] for the exact uncertainties. The quark masses are the  $\overline{MS}$  masses except the top mass is the direct measurement from Tevatron and LHC Run-1 and Run-2 data [1].

### 2.1.2 Standard Model as a gauge theory

The Standard Model can be described by quantum field theory where particles are excitations of a field in flat space with discrete quantum numbers. The Lagrangian contains the fields as well as the strengths of the interactions. The Standard Model is described by a theory which is invariant under local transformations of the  $SU(3)_C \times SU(2)_L \times U(1)_Y$  gauge group. The Standard Model Lagrangian is given by

$$\mathcal{L}_{SM} = \mathcal{L}_{\text{QCD}} + \mathcal{L}_{\text{EW}} + \mathcal{L}_{\text{Higgs}} \quad (2.1)$$

where  $\mathcal{L}_{\text{QCD}}$  describes quantum chromodynamics,  $\mathcal{L}_{\text{EW}}$  electroweak interaction and  $\mathcal{L}_{\text{Higgs}}$  the Higgs sector. A more detailed discussion of each of these follows. This discussion is based loosely on [4] and [5].

	particle	label	mass (GeV)	electric charge
bosons	photon	$\gamma$	$< 1 \times 10^{-27}$	0
	W-boson	$W^\pm$	$80.385 \pm 0.015$	$\pm 1$
	Z-boson	$Z$	$91.1876 \pm 0.0021$	0
	gluon	$g$	0	0
	Higgs	$h$	$125.09 \pm 0.24$	0

Table 2.2: Gauge bosons of the Standard Model with mass values from PDG 2016 review [1], except the Higgs mass from ATLAS and CMS combined measurements from  $\sqrt{s} = 8$  TeV LHC data [3].

### Electroweak interaction

The electroweak theory describes the electromagnetic interaction and the weak interaction as proposed by Glashow [6], Salam [7] and Weinberg [8] independently in the 1960s. The electroweak interaction can be expressed as a unified  $SU(2)_L \times U(1)_Y$  symmetric Lagrangian given by

$$\mathcal{L}_{EW} = -\frac{1}{4}W_{\mu\nu}^a W^{a\mu\nu} - \frac{1}{4}B_{\mu\nu}B^{\mu\nu} + \sum_{\text{fermions } \psi} \bar{\psi}i\gamma^\mu D_\mu\psi. \quad (2.2)$$

Here the weak vector boson field tensor  $W_{\mu\nu}^a$  is given by

$$W_{\mu\nu}^a = \partial_\mu W_\nu^a - \partial_\nu W_\mu^a + g\epsilon_{abc}W_\mu^b W_\nu^c, \quad (2.3)$$

where  $\epsilon_{abc}$  is the totally antisymmetric Levi-Civita symbol,  $g$  is the  $SU(2)_L$  coupling strength and  $a = 1, 2, 3$ . The electromagnetic field tensor  $B_{\mu\nu}$  is simply

$$B_{\mu\nu} = \partial_\mu B_\nu - \partial_\nu B_\mu. \quad (2.4)$$

The left-handed states are contained in  $SU(2)_L$  doublets of the form

$$\begin{pmatrix} \nu \\ e \end{pmatrix}_L \quad \text{or} \quad \begin{pmatrix} u \\ d \end{pmatrix}_L \quad (2.5)$$

with third component of isospin  $I^3 = \pm\frac{1}{2}$  for the top and bottom entries. The right-handed states are isospin singlets. The covariant derivative  $D_\mu$  acting on a Dirac spinor  $\psi$  is

$$D_\mu = \partial_\mu - iYg'B_\mu - igW_\mu^a T^a. \quad (2.6)$$

$Y$  is the weak hypercharge which is associated with the  $U(1)_Y$  symmetry and  $g'$  denotes the  $U(1)_Y$  coupling. The charges are related by  $Y = (Q - I^3)$ .  $T^a$  are the generators of the  $SU(2)$  group. Notice that, since  $T^a = \sigma^a/2$  ( $\sigma^a$  are the Pauli matrices) for isospin doublets and  $T^a = 0$  for isospin singlets, the last term of Eq. 2.6 vanishes on the right-handed states, i.e. the weak force acts on left-handed chiral states only.

The physical vector bosons are given by combinations of the fields

$$\begin{aligned} W_\mu^\pm &= \frac{1}{\sqrt{2}}(W_\mu^1 \mp iW_\mu^2), \\ Z_\mu &= \cos \theta_W W_\mu^3 - \sin \theta_W B_\mu, \\ A_\mu &= \sin \theta_W W_\mu^3 + \cos \theta_W B_\mu, \end{aligned} \quad (2.7)$$

The weak mixing angle  $\sin \theta_W$  appearing here is an important concept. It gives the mixing of the neutral fields and relates the weak and the electromagnetic couplings by  $g' = g_W \cos \theta / \sin \theta$ . This arises from electroweak symmetry breaking.

### Quantum chromodynamics

Quantum chromodynamics (QCD), invented by Fritzsch, Gell-Mann and Leutwyler [9] in the 1970s, describes the strong interaction which binds quarks together. Quarks carry one of red, green and blue colour (in an abstract sense) as they are in the triplet representation of  $SU(3)_C$  and any stable state is a colour neutral state. Quarks are bound together via gluons, a colour octet of  $SU(3)_C$ , which carry a combination of colour and anticolour. The symmetry describing QCD is  $SU(3)_C$  and the Lagrangian invariant under this symmetry is

$$\mathcal{L}_{QCD} = \bar{q}(i\gamma_\mu D^\mu - m_q)q - \frac{1}{4}G_k^{\mu\nu}(G_k)_{\mu\nu} \quad (2.8)$$

with the gluon field strength tensor  $G_k^{\mu\nu}$  given by the gluon fields  $G_\mu$  as

$$G_k^{\mu\nu} = \partial^\mu G_k^\nu - \partial^\nu G_k^\mu + g_s f_{klm} G_l^\mu G_m^\nu. \quad (2.9)$$

The  $f_{klm}$  are the structure constants of  $SU(3)$  and  $g_s$  is the strong coupling constant. The covariant derivative  $D_\mu$  acting on the quark fields is

$$D^\mu = \partial^\mu - \frac{ig_s \lambda_k}{2} G_k^\mu, \quad (2.10)$$

with  $\lambda_k$  the Gell-Mann matrices.

### Higgs mechanism

The Higgs mechanism in the Standard Model breaks the local  $SU(2)_L \times U(1)_Y$  down to  $U(1)_{em}$  by an isospin doublet of two complex scalar fields. This theory was proposed by Brout and Englert [10], Higgs [11], and Guralnik, Hagen and Kibble [12] in 1964. For simplicity, consider first the simple case of symmetry breaking for a real scalar field. For a real scalar field  $\phi$  the interacting Lagrangian is given by

$$\begin{aligned} \mathcal{L} &= \frac{1}{2}(\partial_\mu \phi)(\partial^\mu \phi) - V(\phi) \\ &= \frac{1}{2}(\partial_\mu \phi)(\partial^\mu \phi) - \frac{1}{2}\mu^2 \phi^2 - \frac{1}{4}\lambda \phi^4, \end{aligned} \quad (2.11)$$

where  $\mu$  and  $\lambda$  are free parameters. If  $\mu^2 < 0$  then the potential has minima at

$$\phi = \pm v = \pm \sqrt{\frac{-\mu^2}{\lambda}} \neq 0, \quad (2.12)$$

and  $v$  denotes the vacuum expectation value (VEV). When the physical system chooses one of these vacua, then the symmetry of the Lagrangian Eq. 2.11 is spontaneously broken. Consider the case when the vacuum is  $\phi = +v$ . The field  $\phi$  can be expanded about the vacuum  $v$  by writing  $\phi(x) = v + \eta(x)$ . Substituting this into Eq. 2.11 and using  $\mu^2 = -\lambda v^2$  gives

$$\mathcal{L}(\eta) = \frac{1}{2}(\partial_\mu \eta)(\partial^\mu \eta) - \lambda v^2 \eta^2 - \lambda v \eta^3 - \frac{1}{4} \lambda \eta^4 - \frac{1}{4} \lambda v^4. \quad (2.13)$$

This Lagrangian describes the field  $\eta$  with mass  $m_\eta = \sqrt{2\lambda v^2}$  and its triple and quartic self-interactions proportional to  $\lambda v$  and  $\lambda$  respectively.

Now consider a complex scalar field  $\phi = \phi_1 + i\phi_2$  written in terms of two real scalar fields  $\phi_1$  and  $\phi_2$ . The Lagrangian is now

$$\mathcal{L} = (\partial_\mu \phi)^*(\partial^\mu \phi) - \frac{1}{2} \mu^2 (\phi^* \phi) - \frac{1}{4} \lambda (\phi^* \phi)^2, \quad (2.14)$$

which is invariant under a  $U(1)$  phase transformation. The potential  $V$  has an infinite set of minima at

$$\phi_1^2 + \phi_2^2 = \frac{-\mu^2}{\lambda} = v^2. \quad (2.15)$$

Without loss of generality one can choose the vacuum to be  $(\phi_1, \phi_2) = (v, 0)$ . Expanding the field about the vacuum,  $\phi_1 = \eta(x) + v$ ,  $\phi_2 = \xi(x)$ , and using  $\mu^2 = \lambda v^2$  the Lagrangian can be written as

$$\mathcal{L} = \frac{1}{2}(\partial_\mu \eta)(\partial^\mu \eta) - \frac{1}{2} m_\eta^2 \eta^2 + \frac{1}{2}(\partial_\mu \xi)(\partial^\mu \xi) - V_{int}(\eta, \xi), \quad (2.16)$$

where  $m_\eta = \sqrt{2\lambda v^2}$  and

$$V_{int}(\eta, \xi) = \lambda v \eta^3 + \frac{1}{4} \lambda \eta^4 + \frac{1}{4} \lambda \xi^4 + \lambda v \eta \xi^2 + \frac{1}{2} \lambda \eta^2 \xi^2. \quad (2.17)$$

Now we have a massless scalar field, a Goldstone boson,  $\xi$ , and a massive field  $\eta$ . The Goldstone boson may be removed by adding the appropriate term to the partial derivative  $\partial_\mu$  i.e. choosing the ‘‘unitary gauge’’.

The SM Higgs field generates mass for the gauge bosons of the local  $SU(2)_L \times U(1)_Y$  gauge symmetry. There are three massive gauge bosons and at least one massive scalar particle. The simplest model which satisfies these criteria has two complex scalar fields in a weak isospin doublet. We write

$$\phi = \begin{pmatrix} \phi^+ \\ \phi^0 \end{pmatrix} = \frac{1}{\sqrt{2}} \begin{pmatrix} \phi_1 + i\phi_2 \\ \phi_3 + i\phi_4 \end{pmatrix}. \quad (2.18)$$

Now the Lagrangian is

$$\mathcal{L} = (D_\mu \phi)^\dagger (D^\mu \phi) - V(\phi), \quad (2.19)$$

where  $D_\mu = \partial_\mu + ig_W T^a W_\mu^a + ig' Y B_\mu$  as in Eq. 2.6 and the potential  $V$  is

$$V(\phi) = \mu^2 \phi^\dagger \phi + \lambda (\phi^\dagger \phi)^2. \quad (2.20)$$

Now if  $\mu^2 < 0$  then the potential has minima

$$\phi^\dagger \phi = \frac{1}{2}(\phi_1^2 + \phi_2^2 + \phi_3^2 + \phi_4^2) = \frac{v^2}{2} = -\frac{\mu^2}{2\lambda}. \quad (2.21)$$

Because there needs to be a massless photon after symmetry breaking, the VEV needs to develop for the neutral component  $\phi^0$  only. Thus expanding about the vacuum,

$$\phi = \frac{1}{\sqrt{2}} \begin{pmatrix} \phi_1 + i\phi_2 \\ v + \eta(x) + i\xi(x) \end{pmatrix}. \quad (2.22)$$

Writing the Lagrangian in terms of these fields will introduce three Goldstone bosons, which are eaten by the weak vector bosons. Then the doublet can be written in terms of the VEV and the field  $\eta(x)$  which is relabelled as  $h(x)$  to highlight this is the Higgs field.

$$\phi = \frac{1}{\sqrt{2}} \begin{pmatrix} 0 \\ v + h(x) \end{pmatrix}. \quad (2.23)$$

Then one can write the Lagrangian Eq. 2.19 in terms of the VEV and the Higgs field as

$$\begin{aligned} \mathcal{L}_{Higgs}^{EW} &= \frac{1}{8}g^2(h^2 + 2vh + v^2)(W^+W^+ + W^-W^-) \\ &+ \frac{1}{8}(g^2 + g'^2)(h^2 + 2vh + v^2)Z_\mu Z^\mu - \mu^2 h^2 - \lambda v h^3 + \frac{1}{4}\lambda h^4. \end{aligned} \quad (2.24)$$

Notice that we have rotated into the basis of the physical fields  $W^\pm$ ,  $Z_\mu$  and  $B_\mu$  as in Eq. 2.7. Finally the masses and couplings of gauge bosons can be read off:  $m_W = \frac{1}{2}gv$ ,  $m_\gamma = 0$  and  $m_Z = \frac{1}{2}v\sqrt{g^2 + g'^2}$ . By defining  $\frac{g'}{g} = \tan \theta_W$ , one gets the following prediction:  $\frac{m_W}{m_Z} = \cos \theta_W$ . From the measurements of  $m_W$  and  $g_W$  we obtain  $v = 246$  GeV.

We have found how the boson masses are generated by the Higgs mechanism. Fermion masses are generated by adding so-called Yukawa terms to the unbroken Lagrangian. With the notation  $L$  for an  $SU(2)$  doublet containing the left-handed chiral fermions and  $R$  for an  $SU(2)$  singlet containing a right-handed chiral fermions, the mass-generating terms are:  $\lambda_d(\bar{L}\phi R + (\bar{L}\phi R)^\dagger)$  giving mass to the down-type fermions and  $\lambda_u(\bar{L}_L\phi_c R + (\bar{L}_L\phi_c R)^\dagger)$  giving mass to the up-type fermions after the Higgs field obtains a VEV.  $\lambda_{d,u}$  are referred to as the Yukawa couplings.

The properties of the SM Higgs are fixed by the measurement of the Higgs VEV via the gauge boson masses and the measurement of the Higgs mass from the LHC. The 125 GeV Higgs has a total width of 4 MeV [13], and it decays mostly into  $\bar{b}b$  and  $WW^*$  as can be read from Fig. 2.1. It remains to be checked by experiment whether the SM predictions for the Higgs properties are valid.

One of the remaining checks for the validity of the Standard Model is measuring the value of the parameter  $\lambda$  appearing in Higgs self-coupling term  $\lambda v h^3$  and quartic coupling term  $\frac{1}{4}\lambda h^4$ . Its value in the Standard Model is set by the relation of the Higgs mass and  $v$ . The parameter  $\lambda$  can be determined by measuring the double-Higgs production cross section, best in  $e^+e^-$  collisions at an energy higher than 500 GeV [14].

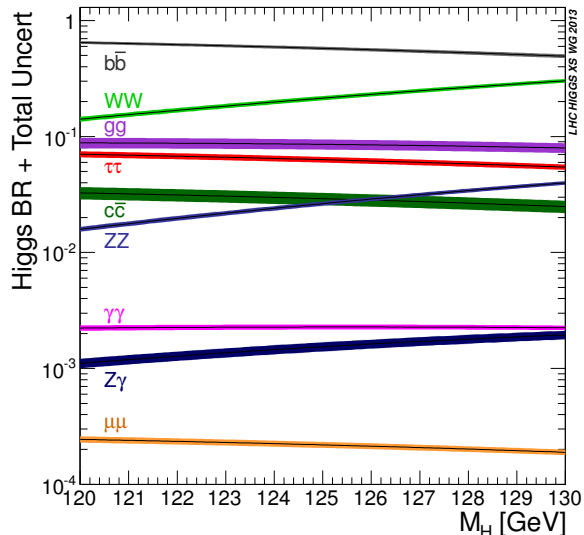


Figure 2.1: Branching ratios of the SM Higgs boson as a function of its mass. Figure from [15].

## 2.2 Problems of the Standard Model

Despite the successes of the Standard Model, it cannot explain dark matter, gravity, matter-antimatter asymmetry, neutrino masses and a few other observations. We shall briefly go through some of these problems and return to them later in describing how they could be solved by supersymmetry.

### 2.2.1 Dark matter

The evidence for the existence of dark matter (DM) is compelling. The rotation curves of galaxies, meaning the speed of stars with respect to their distance to the galactic centre, do not follow the expectation based on ordinary matter only [16, 17]. This might be due to dark matter [18–20] or Modified Newtonian Dynamics [21]. The latter option is not favoured as another stellar phenomenon requires dark matter: the famous Bullet Cluster. The Bullet Cluster is a system of two colliding galaxy clusters, in which dark matter was found by its lensing effect on other sky objects [22, 23].

Dark matter could in principle be moving fast, consisting of e.g. neutrinos. This type of dark matter is called hot dark matter. If dark matter was hot, the fast-moving particles would have smoothed out any density fluctuations which cause the observed structures in the universe. Therefore, a favoured explanation for dark matter observations is cold dark matter (CDM), which is moving slowly [24–27]. Examples of cold dark matter candidates are Weakly Interacting Massive Particles (WIMPs), Massive Astrophysical Compact Halo Objects (MACHOs) e.g. black holes, and axions. Cold dark matter now forms part of the so called standard model of cosmology, the  $\Lambda$ CDM model. The lambda stands for a positive cosmological constant, or dark energy, which accounts for the accelerated expansion of the universe. It is known that the amount of ordinary matter, or baryonic matter, is only 4.9% of the total mass-energy of the universe [28]:

25.9% is dark matter and 69.1% is dark energy [28].

The amount of cold dark matter can and has been measured from the temperature spectrum of the cosmic microwave background (CMB). At the time of writing, the most precise measurement of the dark matter relic density at present time,  $\Omega_{\text{CDM}}h^2$ , has been made by the Planck experiment, combining CMB measurements with polarisation data. The 2015 Planck result  $\Omega_{\text{CDM}}h^2 = 0.1197 \pm 0.0022$  [28].

The exact nature of dark matter is currently unknown. There are general arguments which suggest that dark matter which undergoes freeze-out should not have more mass than  $\sim \sqrt{T_0 \times M_P} \sim 1$  TeV [29]. Here  $T_0$  is the present CMB temperature 2.73 K and  $M_P \sim 1.2 \times 10^{19}$  GeV. This means that dark matter should be accessible at current or near-future colliders [30]. This is indeed the motivation for the work in Chapters 5 and 6.

## 2.2.2 Hierarchy problem

It is surprising that the fermion masses range over 11 orders of magnitude from 1 eV neutrino masses to 173 GeV top quark mass. It seems unnatural that this should be the case. However, this is just one example of a hierarchy problem.

Another version has to do with the Higgs mass. The Higgs mass receives corrections from loops such as those the fermion loop Fig. 2.2. The corrections are of the order of  $\lambda_f^2 \Lambda_{UV}^2$ , where  $\Lambda_{UV}$  is a cut-off scale required for renormalisation and defined by the onset of some new physics. If new physics was not present below the Planck scale, then  $\Lambda_{UV} = 10^{19}$  GeV. This would mean enormous corrections to the Higgs mass. But the Higgs mass is measured to be 125.1 GeV so the question arises why is the Higgs so light.

The Higgs mass divergence from fermions can be rectified by introducing loop corrections with scalars (and vice versa). Corrections from scalars have the opposite sign with respect to corrections from fermions. If the coupling and mass of the scalar is equal to the fermion coupling and mass then the corrections cancel exactly. This is the case in theories with unbroken supersymmetry. Since we have not observed scalars of the same mass as the SM fermions, supersymmetry is broken. However, if the supersymmetry breaking scale is not too heavy, meaning not in the multi-TeV range, then the Higgs mass may be stabilised. A more detailed discussion of the hierarchy problem can be found in Ch. 7.1.

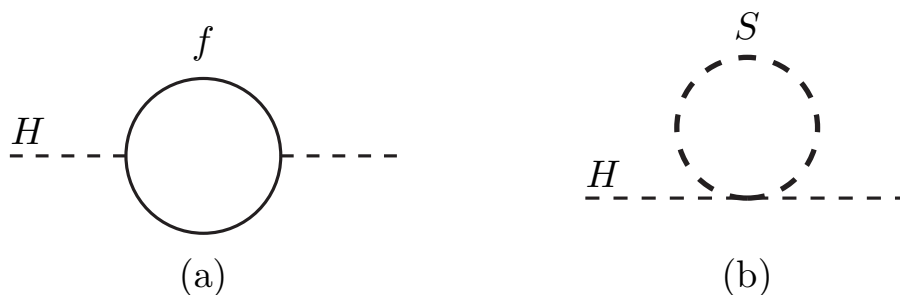


Figure 2.2: Contributions to Higgs mass from a) fermion loop and b) scalar loop [31].

### 2.2.3 Anomalous magnetic moment of the muon

The magnetic moment  $\vec{\mu} = g_\mu \frac{q}{2m_\mu} \vec{s}$  of a muon depends on the Landé  $g$ -factor or gyromagnetic ratio  $g_\mu$  (see e.g. [32]). According to Dirac theory,  $g_\mu = 2$ . Loop corrections modify the expected value and it is common to talk about the anomalous magnetic moment of the muon, the deviation from the simple tree-level value 2, defined as  $a = \frac{g_\mu - 2}{2}$ . This is a dimensionless quantity. The anomalous magnetic moment  $a_\mu$  gets contributions from all possible particles in the loop diagrams and therefore it is sensitive to new particles via their loop contributions.

There is a long-standing discrepancy between the Standard Model prediction for the muon anomalous magnetic moment and the measured value from Brookhaven National Laboratory experiment E821 [33]. The measured value is  $a_\mu(\text{Exp}) = 116592080(54)(33) \times 10^{-11}$ . The theoretical prediction for the SM anomalous magnetic moment of the muon consists of three parts:  $a_\mu = a_\mu^{\text{QED}} + a_\mu^{\text{EW}} + a^{\text{hadronic}}$  where the theoretical uncertainty on the hadronic contribution is by far largest of the three [1]. An example diagram can be seen in Fig. 2.3. Adding the latest values of the three contributions together,  $a_\mu(\text{SM}) = 116591803(1)(42)(26) \times 10^{-11}$  [1]. This leads to an overall deviation from the Standard Model of  $3.6\sigma$  [1].

There are two ways that the discrepancy may be solved. Firstly, two new experiments are expected to improve the measurement of  $a_\mu$  soon: E989 at Fermilab [34], which started to take data in 2017, and a possible experiment at J-PARC at KEK [35]. The Fermilab experiment will provide a factor four improvement on the uncertainty on  $a_\mu$  in the next four years [34].

The other way to solve the discrepancy is via new physics that contributes to the muon vertex. In general the size of the contribution will be  $\propto (m_\mu/M_{NP})^2$ , where  $M_{NP}$  is the scale of the new physics. There may be new dark photons which would be a cosmologically motivated solution [36, 37]. Another possibility is that there may be supersymmetric particles in which case the contribution would be  $\propto (m_\mu/M_{SUSY})^2$  [38, 39]. Specifically, there could be a chargino-sneutrino or neutralino-smuon contribution to the muon vertex, see Fig. 2.4. This possibility has been widely studied, as the deviation implies that the SUSY particle masses would have to be accessible at the LHC [40]. The precise measurement of  $a_\mu$  excludes certain supersymmetry models [41].

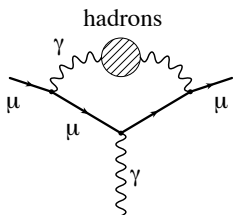


Figure 2.3: Hadronic correction to muon magnetic moment. Figure from [39].

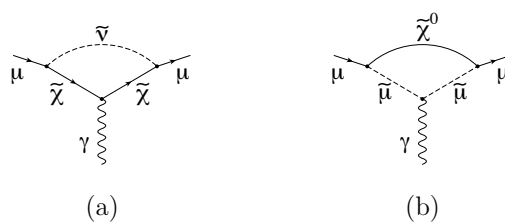


Figure 2.4: SUSY correction to muon magnetic moment. Figure from [39].

### 2.2.4 Other open problems

The Standard Model makes no attempt to include gravity as the Standard Model is a theory in flat spacetime while general relativity is a theory about dynamical curved spacetime. However, objects like black holes and processes in the very early universe require a quantum description of gravity. Most famously string theory (see e.g. [42,43]) and also loop quantum gravity [44] provide theories of quantum gravity. String theory requires supersymmetry, however supersymmetry can exist without string theory.

Another big question in physics is why is there more matter than antimatter. Matter and antimatter should be generated in equal amounts, however experiment shows that the amounts are not equal in today's universe. There was one part in a billion more matter than antimatter at the beginning of the universe. Any theory that tries to explain the asymmetry is called a theory of baryogenesis. The theory should satisfy three conditions, known as the Sakharov conditions [45]: 1) baryon number changing processes must be present, 2) matter and antimatter need to obey slightly different physics so  $C$  and  $CP$  are not exact symmetries, and 3) baryon number changing processes have to take place out of thermal equilibrium in order not to wash out the asymmetry. There are two main types of theory, GUT baryogenesis [46] and electroweak baryogenesis [47], named after the energy scales at which baryogenesis is hypothesised to occur. The Standard Model itself could explain baryogenesis in principle but the amount of  $CP$ -violation in the CKM matrix in the Standard Model is not large enough to account for the observed baryon asymmetry [48]. The Minimal Supersymmetric Standard Model (MSSM), however, could contain the needed  $CP$ -violation [49, 50].

In the SM, neutrinos are massless but neutrino experiments have shown that neutrinos oscillate and therefore have non-zero masses. The first evidence for neutrino oscillations came from the Super Kamiokande experiment in 1998 [51]. The current most stringent limit on neutrino masses comes from Planck high and low multipole WMAP data combined with baryon acoustic oscillation data giving a limit on the sum of neutrino masses  $\Sigma_i m_i < 0.23$  eV at 95% CL [28]. There is a direct measurement of the mass of the electron anti-neutrino from the Troitsk experiment giving an upper limit of about 2.1 eV on the electron antineutrino mass [52]. Popular modifications of the SM to explain neutrino oscillations include the seesaw mechanism with either right-handed neutrinos [53–55] or  $Y = 2$ ,  $SU(2)_L$  triplet Higgs [56–58].

## 2.3 Supersymmetry basics

Supersymmetry promises to solve some of the problems of the Standard Model mentioned in the last section: Supersymmetry is an appealing candidate for solving the hierarchy problem. It can also provide a dark matter candidate and solve the muon magnetic moment anomaly. Supersymmetry is strongly predictive because it requires that each particle in the SM is accompanied by a SUSY particle with half a spin difference but otherwise the same properties, including mass and coupling. Supersymmetry in four dimensions was first found by Wess and Zumino [59].

The supersymmetry transformation  $Q$  is an extension of the Poincaré symmetry of

spacetime.  $Q$  transforms bosons into fermions and vice versa,

$$Q |\text{boson}\rangle = |\text{fermion}\rangle, \quad Q |\text{fermion}\rangle = |\text{boson}\rangle. \quad (2.25)$$

The transformation  $Q$  must satisfy the following commutation and anti-commutation relations with the generator of spacetime translations  $P^\mu$ :

$$\{Q, Q^\dagger\} = P^\mu, \quad (2.26)$$

$$\{Q, Q\} = \{Q^\dagger, Q^\dagger\} = 0, \quad (2.27)$$

$$[P^\mu, Q] = [P^\mu, Q^\dagger] = 0. \quad (2.28)$$

The supersymmetry operator acts on supermultiplets, which consist of a fermion and a boson. The members of a supermultiplet are called superpartners. Due to Eq. 2.28, the superpartners have the same mass, and by the lack of evidence for same-mass superpartners, SUSY must be broken. Since the supersymmetry generator  $Q$  commutes with the generators of gauge transformations, the SM and SUSY partner must have the same gauge quantum numbers (electric charge, weak isospin and colour).

The Minimal Supersymmetric Standard Model (MSSM) introduces one superpartner for each Standard Model particle. The superpartners of the SM fermionic fields are named with the prefix “s-” e.g. selectron. The SM fermions live in chiral supermultiplets listed in Tab. 2.3, which contain the spin-0 partners of the SM fermions. The superpartners of the SM bosonic fields are named with the suffix “-ino” e.g. higgsino. The gauge bosons live in gauge supermultiplets alongside with the spin- $\frac{1}{2}$  gauginos, see Tab. 2.4. The superpartner fields are denoted by a tilde on top of the corresponding SM field. It should be noted that the superpartners of the SM fields are not necessarily mass eigenstates as we will discuss later.

The MSSM requires an extended Higgs sector with two electroweak Higgs doublets as can be read from Tab. 2.3. One reason is that the down and up type masses are generated with the Higgs field its complex conjugate respectively. Since complex conjugated fields are not allowed in the superpotential (to be defined below), two Higgs fields  $H_d$  and  $H_u$  are needed to generate mass for up and down type particles separately. Additionally, two Higgs doublets are needed to maintain anomaly cancellation which would be violated by the superpartners of a single Higgs doublet field [31]. Both the extended Higgs sector and the mixing of the superpartners of the bosons are discussed in more detail below.

The supersymmetric Lagrangian contains kinetic and interaction terms for both the chiral and gauge fields.

The chiral superfields give rise to terms in the Lagrangian of the form

$$\mathcal{L}_{chiral} = -D^\mu \phi^{*i} D_\mu \phi_i + i\psi^\dagger \bar{\sigma}^\mu D_\mu \psi_i - \frac{1}{2} W^{ij} \psi_i \psi_j + W_{ij}^* \psi^{\dagger i} \psi^{\dagger j} - W^i W_i^*, \quad (2.29)$$

where the first two terms are conventional kinetic terms for chiral fields and

$$W^{ij} = \frac{\delta^2}{\delta\phi_i \delta\phi_j} W, \quad (2.30)$$

particles	label	spin 0	spin 1/2	$SU(3)_C, SU(2)_L, U(1)_Y$
squarks, quarks	$Q$	$(\tilde{u}_L \tilde{d}_L)$	$(u_L d_L)$	$(\mathbf{3}, \mathbf{2}, \frac{1}{6})$
	$\bar{u}$	$\tilde{u}_R^*$	$u_R^\dagger$	$(\bar{\mathbf{3}}, \mathbf{1}, -\frac{2}{3})$
	$\bar{d}$	$\tilde{d}_R^*$	$d_R^\dagger$	$(\bar{\mathbf{3}}, \mathbf{1}, \frac{1}{3})$
sleptons, leptons	$L$	$(\tilde{\nu} \tilde{e}_L)$	$(\nu e_L)$	$(\mathbf{1}, \mathbf{2}, -\frac{1}{2})$
	$\bar{e}$	$\tilde{e}_R^*$	$e_R^\dagger$	$(\mathbf{1}, \mathbf{1}, 1)$
higgses, higgsinos	$H_u$	$(H_u^+ H_u^0)$	$(\tilde{H}^+ \tilde{H}_u^0)$	$(\mathbf{1}, \mathbf{2}, +\frac{1}{2})$
	$H_d$	$(H_d^0 H_d^-)$	$(\tilde{H}_d^0 \tilde{H}_d^-)$	$(\mathbf{1}, \mathbf{2}, -\frac{1}{2})$

Table 2.3: Chiral or matter supermultiplets in the MSSM. Table from [31]. The  $U(1)_Y$  quantum number  $Y_W = (Q - I_3)$  as above.

particles	spin 1/2	spin 1	$SU(3)_C, SU(2)_L, U(1)_Y$
gluino, gluon	$\tilde{g}$	$g$	$(\mathbf{8}, \mathbf{1}, 0)$
winos, W bosons	$\tilde{W}^0 \tilde{W}^\pm$	$W^\pm W^0$	$(\mathbf{1}, \mathbf{3}, 0)$
bino, B boson	$\tilde{B}^0$	$B^0$	$(\mathbf{1}, \mathbf{1}, 0)$

Table 2.4: Vector or gauge supermultiplets in the MSSM. Table from [31].

which is the derivative of the superpotential  $W$  defined as

$$W = \frac{1}{2} M^{ij} \phi_i \phi_j + \frac{1}{6} y^{ijk} \phi_i \phi_j \phi_k. \quad (2.31)$$

$W^i$  is simply the first-order derivative of  $W$  with respect to the field  $\phi_i$ . For gauge supermultiplets the Lagrangian terms are

$$\mathcal{L}_{gauge} = -\frac{1}{4} F_{\mu\nu}^a F^{a\mu\nu} + i \lambda^{\dagger a} \bar{\sigma}^\mu D_\mu \lambda^a + \frac{1}{2} D^a D^a. \quad (2.32)$$

$D^a$  is the auxiliary field. The interaction terms between the gauge and chiral fields are

$$\mathcal{L}_{int} = -\sqrt{2} g (\phi^* T^a \psi) \lambda^a - \sqrt{2} g \lambda^{\dagger a} (\psi^\dagger T^a \phi) + g (\phi^* T^a \phi) D^a. \quad (2.33)$$

The unbroken SUSY Lagrangian contains the superpotential

$$W_{\text{MSSM}} = \bar{u}_y \mathbf{y}_u Q H_u - \bar{d}_y \mathbf{y}_d Q H_d - \bar{e}_y \mathbf{y}_e L H_d + \mu H_u H_d. \quad (2.34)$$

The colour and weak isospin indices have been suppressed. The only new parameter in the unbroken SUSY Lagrangian compared to the SM is the higgsino mass parameter  $\mu$ .

As an aside, note that these are not the only possible invariant terms of the superpotential. We have not allowed terms which violate baryon number, lepton number, or both. We have imposed  $R$ -parity conservation

$$R = (-1)^{3(B-L)+2s}, \quad (2.35)$$

consequences of which will be discussed in Sec. 2.3.1.

To induce supersymmetry breaking, we have to add terms to the Lagrangian by hand. The soft SUSY breaking part of the MSSM Lagrangian contains many new parameters and it is given by

$$\begin{aligned}
 \mathcal{L}_{\text{soft}}^{\text{MSSM}} = & -\frac{1}{2}(M_1\tilde{B}\tilde{B} + M_2\tilde{W}\tilde{W} + M_3\tilde{g}\tilde{g} + c.c.) \\
 & - (\tilde{u}\mathbf{a}_u\tilde{Q}H_u - \tilde{d}\mathbf{a}_d\tilde{Q}H_d + \tilde{e}\mathbf{a}_e\tilde{L}H_d + c.c.) \\
 & - \tilde{Q}^\dagger\mathbf{m}_Q^2\tilde{Q} - \tilde{L}^\dagger\mathbf{m}_L^2\tilde{L} + \tilde{u}\mathbf{m}_u^2\tilde{u}^\dagger - \tilde{d}\mathbf{m}_d^2\tilde{d}^\dagger - \tilde{e}\mathbf{m}_e^2\tilde{e}^\dagger \\
 & - m_{H_u}^2 H_u^* H_u - m_{H_d}^2 H_d^* H_d - (bH_u H_d + c.c.).
 \end{aligned} \tag{2.36}$$

There are four types of terms. The first row contains mass terms for the superpartners of the gauge bosons.  $M_1$  is the bino mass parameter,  $M_2$  the wino mass parameter, and  $M_3$  is the gluino mass parameter. In the second row we have trilinear terms describing the Higgs-squark-squark interactions with  $\mathbf{a}_\mathbf{x}$  the trilinear coupling matrices with size  $3 \times 3$ . These are in one-to-one correspondence with the Yukawa couplings of the Standard Model. Then we have the squark mass terms like  $\tilde{Q}^\dagger\mathbf{m}_Q^2\tilde{Q}$  where the matrices are also of size  $3 \times 3$ . Finally we have the Higgs squared masses and  $b$ -terms with mixed Higgs fields. It should be noted that right-handed neutrinos are not included in the MSSM. The Lagrangian breaking SUSY ‘‘softly’’ is jargon for the terms having positive mass dimension and not having quadratic divergencies of the scalars. The terms can give mass to all scalars and gauginos.

### 2.3.1 Consequences of $R$ -parity conservation

If all the possible supersymmetric terms were allowed in the superpotential Eq. 2.34, some of them would induce lepton or baryon number violation. This would introduce proton decay. Experimentally this is not observed and it is theoretically easy to set the relevant parameters to zero by imposing a multiplicatively conserved quantity called  $R$ -parity. The quantum number  $R$  is defined as

$$R = (-1)^{3(B-L)+2s}, \tag{2.37}$$

where  $B$  is the baryon number,  $L$  is the lepton number and  $s$  is the spin. For a Standard Model particle  $R = 1$  and for a SUSY particle  $R = -1$ . If  $R$ -parity is conserved, there are dramatic restrictions to the model. The SM and SUSY particles cannot mix. Additionally, as each vertex has to contain an even number of SUSY particles, the SUSY particles are produced in pairs. The lightest SUSY particle, the LSP, is stable. Since a stable LSP would provide a dark matter candidate,  $R$ -parity conservation is often conjectured.  $R$ -parity conservation is assumed throughout this thesis.

Searches for  $R$ -parity violating SUSY particles have been performed at HERA e.g. [60], Tevatron e.g. [61] and LEP e.g. [62]. There are current efforts at the LHC as well - see [63] for example. It would be possible to search for  $R$ -parity violation at the ILC, see [64] for a recent study.

### 2.3.2 Electroweak symmetry breaking in the MSSM

We will next discuss electroweak symmetry breaking in the MSSM. This gives one of the important equations motivating us to study higgsinos.

In the MSSM, the scalar potential for the Higgs fields is given by

$$\begin{aligned}
 V = & (|\mu|^2 + m_{H_u}^2)(|H_u^0|^2 + |H_u^+|^2) + (|\mu|^2 + m_{H_d}^2)(|H_d^0|^2 + |H_d^-|^2) \\
 & + [b(H_u^+ H_d^- - H_u^0 H_d^0) + c.c.] \\
 & + \frac{1}{8}(g^2 + g'^2)(|H_u^0|^2 + |H_u^+|^2 - |H_d^0|^2 - |H_d^-|^2) \\
 & + \frac{1}{2}g^2 |H_u^+ H_d^{0*} + H_u^0 H_d^{-*}|^2.
 \end{aligned} \tag{2.38}$$

Without loss of generality we can set  $H_u^+ = 0$ , which then in the potential minimum  $\partial V/\partial H_u^+ = 0$  implies  $H_d^- = 0$ . Then we are left with

$$\begin{aligned}
 V = & (|\mu|^2 + m_{H_u}^2)|H_u^0|^2 + (|\mu|^2 + m_{H_d}^2)|H_d^0|^2 - (bH_u^0 H_d^0 + c.c.) \\
 & + \frac{1}{8}(g^2 + g'^2)(|H_u^0|^2 - |H_d^0|^2)^2.
 \end{aligned} \tag{2.39}$$

To check that the scalar potential has a proper minimum one has to check that it is bounded from below and that the origin is a local maximum to get non-zero values for the higgs VEVs,  $\langle H_u^0 \rangle \neq 0$ ,  $\langle H_d^0 \rangle \neq 0$ . We denote the VEVs by

$$v_u = \langle H_u^0 \rangle, \quad v_d = \langle H_d^0 \rangle. \tag{2.40}$$

These are not independent but satisfy the relation

$$v_u^2 + v_d^2 = v^2 = 2m_Z/(g^2 + g'^2) \approx (174 \text{ GeV})^2. \tag{2.41}$$

Notational conventions are used to denote the ratio of the VEVs as

$$\tan \beta \equiv v_u/v_d. \tag{2.42}$$

In order to minimize the potential we set  $\partial V/\partial H_u^0 = \partial V/\partial H_d^0 = 0$ . Manipulating the result gives

$$\sin(2\beta) = \frac{2b}{m_{H_u}^2 + m_{H_d}^2 + 2|\mu|^2}, \quad \text{and} \tag{2.43}$$

$$m_Z^2 = \frac{|m_{H_d}^2 - m_{H_u}^2|}{\sqrt{1 - \sin^2(2\beta)}} - m_{H_u}^2 - m_{H_d}^2 - 2|\mu|^2. \tag{2.44}$$

Rewriting Eq. 2.44 gives

$$\frac{1}{2}m_Z^2 = \frac{m_{H_d}^2 - m_{H_u}^2 \tan^2 \beta}{\tan^2 \beta - 1} - \mu^2. \tag{2.45}$$

This is a striking equation because this relates the  $\mu$ -term of the unbroken SUSY Lagrangian to the  $Z$ -boson mass. In the large  $\tan \beta$  limit the equation approximates as  $\frac{1}{2}M_Z^2 \approx -m_{H_u}^2 - \mu^2$ . If the theory should be natural, meaning not to include too much fine-tuning, then the up-type squared Higgs mass term should get a small

negative value along with a  $\mu$ -parameter of the order of the  $Z$ -mass. As we will see later, this equation motivates us to study light higgsinos in Ch. 7.

We have ignored the scalar quark and lepton contributions to the scalar potential as these should have positive mass-squared terms and hence do not obtain vacuum expectation values.

### 2.3.3 Masses in the MSSM

The equations for the sparticle masses in the MSSM are detailed below, starting with the Higgs bosons. The masses of neutralinos, charginos and sleptons are discussed in detail, mentioning the loop corrections as well.

#### Higgs bosons

As mentioned in the previous section, the MSSM Higgs sector consists of two complex Higgs doublets so there are 8 degrees of freedom. Three give the longitudinal components of the gauge bosons  $W^\pm, Z$  and five remain. These give the light and heavy neutral CP-even Higgses  $h_0$  and  $H_0$ , pseudoscalar Higgs  $A_0$  and charged Higgses  $H^\pm$ .

The masses of the physical Higgses are given by

$$\begin{aligned} m_{A_0}^2 &= 2|\mu|^2 + m_{H_u}^2 + m_{H_d}^2, \\ m_{h_0, H_0}^2 &= \frac{1}{2} \left( m_{A_0}^2 + m_Z^2 \mp \sqrt{(m_{A_0}^2 - m_Z^2)^2 + 4m_Z^2 m_{A_0}^2 \sin^2(2\beta)} \right), \\ m_{H^\pm}^2 &= m_{A_0}^2 + m_W^2. \end{aligned} \quad (2.46)$$

The mixing in the neutral sector is defined by

$$\begin{pmatrix} h_0 \\ H_0 \end{pmatrix} = \begin{pmatrix} \cos \alpha & \sin \alpha \\ -\sin \alpha & \cos \alpha \end{pmatrix} \begin{pmatrix} H_{uR}^0 \\ H_{dR}^0 \end{pmatrix} \quad (2.47)$$

where  $H_{uR}^0$  and  $H_{dR}^0$  stand for the real parts of the neutral Higgs field components. It is conventional to choose  $\alpha$  to be negative.

#### Neutralinos and charginos

The neutral partners of the SM bosons ( $\tilde{B}, \tilde{W}^3, \tilde{H}_d^0, \tilde{H}_u^0$ ) mix to give four neutral mass eigenstates  $\tilde{\chi}_i^0$ ,  $i = 1, 2, 3, 4$  called neutralinos. The mixing is parametrised by the neutralino mass matrix  $\mathcal{M}_N$ . It is a  $4 \times 4$  real matrix

$$\mathcal{M}_N = \begin{pmatrix} M_1 & 0 & -m_Z c_\beta s_W & m_Z s_\beta s_W \\ 0 & M_2 & m_Z c_\beta c_W & -m_Z s_\beta c_W \\ -m_Z c_\beta s_W & m_Z c_\beta c_W & 0 & -\mu \\ m_Z s_\beta s_W & -m_Z s_\beta c_W & -\mu & 0 \end{pmatrix} \quad (2.48)$$

in the  $(\tilde{B}, \tilde{W}^3, \tilde{H}_d^0, \tilde{H}_u^0)$  basis. In the matrix  $c_\beta = \cos \beta$ ,  $s_\beta = \sin \beta$ ,  $c_W = \cos \theta_W$  and  $s_W = \sin \theta_W$ . This mixing matrix tells us that at tree-level, the neutralino masses are

given by four SUSY parameters  $M_1, M_2, \mu$  and  $\tan \beta$ . In general the parameters  $M_1, M_2$  and  $\mu$  can be complex but one of them can be made real without loss of generality by rotating the higgsino fields. If the remaining two are complex, then this implies new CP-violating effects, so in most analyses and in all of this thesis, all three parameters are restricted to be real.

The neutralino masses are obtained by diagonalising the mass matrix by a  $4 \times 4$  unitary matrix  $N$ ,

$$\text{Diag}(m_{\tilde{\chi}_1^0}, m_{\tilde{\chi}_2^0}, m_{\tilde{\chi}_3^0}, m_{\tilde{\chi}_4^0}) = N^* \mathcal{M}_N N^\dagger. \quad (2.49)$$

By definition the neutralinos are sorted by mass such that  $\tilde{\chi}_1^0$  is the lightest. It should be noted that the measurement of two neutralino masses and one chargino mass is sufficient to determine the full matrix [65, 66].

The charged superpartners of the SM bosonic fields  $(\tilde{W}^+, \tilde{H}_u^+)$  and  $(\tilde{W}^-, \tilde{H}_d^-)$  mix to give two positively charged charginos  $\tilde{\chi}_i^+$  and two negatively charged charginos  $\tilde{\chi}_i^-$ , with  $i = 1, 2$ . The mixing is parametrised by the chargino mass matrix

$$M_C = \begin{pmatrix} M_2 & \sqrt{2}s_\beta m_W \\ \sqrt{2}c_\beta m_W & \mu \end{pmatrix}, \quad (2.50)$$

and the mass eigenstates are found by diagonalising  $\mathcal{M}_C$ ,  $\text{Diag}(\tilde{\chi}_1^\pm, \tilde{\chi}_2^\pm) = U^* \mathcal{M}_C V^{-1}$ , where  $U$  and  $V$  are two unitary  $2 \times 2$  matrices. The chargino masses are then given by

$$m_{\tilde{\chi}_1^\pm}^2, m_{\tilde{\chi}_2^\pm}^2 = \frac{1}{2} \left[ |M_2|^2 + |\mu|^2 + 2m_W^2 \mp \sqrt{(|M_2|^2 + |\mu|^2 + 2m_W^2)^2 - 4|\mu M_2 - m_W^2 \sin 2\beta|^2} \right]. \quad (2.51)$$

Certain hierarchies of the parameters in the neutralino and chargino mass matrices lead to distinct phenomenologies. It is common to refer to the neutralinos and charginos as being bino-like, wino-like or higgsino-like if  $M_1, M_2$  and  $\mu$  have relative sizes as plotted in Fig. 2.5. For example, if  $M_1 < M_2 \ll \mu$ , then the lightest neutralino  $\tilde{\chi}_1^0$  is approximately equivalent to the bino field, thus the name bino-like  $\tilde{\chi}_1^0$ . It should be noted that, due to the structures of the neutralino and chargino mass matrices, the wino-like neutralino and chargino are close in mass and similarly the higgsino-like neutralinos and chargino are close in mass.

The above discussion holds at tree-level. The neutralino masses receive loop corrections from sfermions and the gauginos themselves as was first quantified in [67] and [68]. Assume that  $\mu \ll M_1, M_2$ , quark masses are neglected and the squarks have a common mass parameter and the sleptons have a common mass parameter. In this approximation the dominant corrections to the bino mass parameter  $M_1$  comes from quark-squark, chargino-charged Higgs and neutralino-neutral Higgs loops. Considering the full one-loop corrections, in a certain subset of MSSM points with high-scale unification, the correction to the LSP mass can be as large as +10% if  $M_1$  is small [69]. Two-loop coloured corrections can modify the neutralino masses by  $\mathcal{O}(0.1\%)$  [70].

The corrections to the LSP mass in the case of  $M_1 < M_2 \ll \mu$  are quantified in Ref. [69]. The corrections are most often in the region of +1-3% for LSP masses between 100

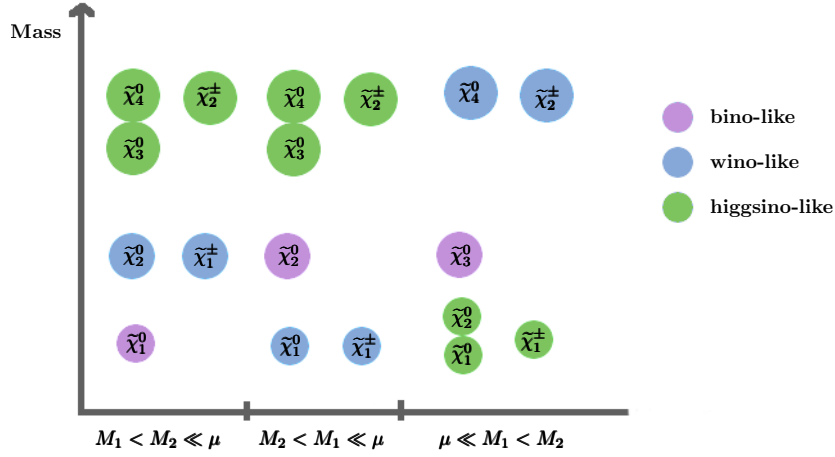


Figure 2.5: Mixings and mass hierarchy of neutralinos and charginos

and 200 GeV. Corrections to  $\tilde{\chi}_1^\pm$  mass can be as high as +10% for a mass of 150 GeV, and minimally +3%.

At tree-level the neutralino and chargino masses are invariant under the inversion of the sign of  $M_1$ ,  $M_2$  and  $\mu$ . At one-loop level the masses are modified by less than 0.1% due to squark masses changing under the inversion of the sign of  $\mu$  [67].

Corrections to the wino mass parameter  $M_2$  come mainly from quark-squark loops, Higgs loops and gauge boson loops. In analogy to the LSP, for the lightest chargino the dominant contribution can be up to +10% if  $M_2$  is small [69]. Two-loop coloured corrections to the chargino mass can be of the order of 0.1% [71].

The gluino mass is given by the  $M_3$  parameter with significant contributions from gluon-gluino and squark-quark loops at one-loop order [72]. Two-loop corrections can give 1-2% modifications with respect to the one-loop mass [73, 74].

### Sfermions

Mixing may occur in the sfermion sector too. In the most generic case in the MSSM, the mass terms in Eq. 2.36 can cause mixing between the sfermion generations. If these mixing angles are allowed to be large then there could be flavour-changing and  $CP$ -violating effects beyond those allowed by low-energy measurements of flavour-changing processes. If the sfermion mass matrices are assumed to be proportional to the identity matrix, then the undesired flavour-changing and  $CP$ -violating terms are eliminated. This is the “flavour-blind” hypothesis. The only allowed mixing contributions would come from Yukawa couplings, which are negligible for first and second generation sfermions. Then the only mixings would be in the third-generation pairs  $(\tilde{t}_L, \tilde{t}_R)$ ,  $(\tilde{b}_L, \tilde{b}_R)$ ,  $(\tilde{\tau}_L$  and  $\tilde{\tau}_R)$ . The first and second generation SUSY fields correspond to the mass eigenstates.

In more detail, assuming a flavour diagonal slepton mass matrix, the mass matrix of staus in the  $(\tilde{\tau}_L, \tilde{\tau}_R)$  basis is

$$\mathcal{M}_{\tilde{\tau}}^2 = \begin{pmatrix} M_{\tilde{\tau}_L}^2 & m_\tau(A_\tau - \mu \tan \beta) \\ m_\tau(A_\tau - \mu \tan \beta) & M_{\tilde{\tau}_R}^2 \end{pmatrix}, \quad (2.52)$$

where

$$M_{\tilde{\tau}_L}^2 = M_{L(3)}^2 + m_Z \cos 2\beta \left(-\frac{1}{2} + \sin^2 \theta_W\right) + m_\tau \quad (2.53)$$

and

$$M_{\tilde{\tau}_R}^2 = M_{E(3)}^2 + m_Z \cos 2\beta (\sin^2 \theta_W) + m_\tau. \quad (2.54)$$

$M_{L(3)}^2$  and  $M_{E(3)}^2$  are the soft SUSY breaking parameters for  $\tilde{\tau}_L$  and  $\tilde{\tau}_R$  respectively. The  $A_\tau$  is the soft SUSY breaking trilinear scalar coupling. If all parameters are real, then the mass matrix can be diagonalised by  $2 \times 2$  orthogonal matrices. The mass eigenvalues are

$$m_{\tilde{\tau}_{1,2}}^2 = \frac{1}{2} (M_{\tilde{\tau}_L}^2 + M_{\tilde{\tau}_R}^2 \mp \sqrt{(M_{\tilde{\tau}_L}^2 - M_{\tilde{\tau}_R}^2)^2 + 4m_\tau^2 (A_\tau - \mu \tan \beta)^2}). \quad (2.55)$$

The mass eigenstates are

$$\begin{aligned} \tilde{\tau}_1 &= \cos \theta_{\tilde{\tau}} \tilde{\tau}_L + \sin \theta_{\tilde{\tau}} \tilde{\tau}_R, \\ \tilde{\tau}_2 &= -\sin \theta_{\tilde{\tau}} \tilde{\tau}_L + \cos \theta_{\tilde{\tau}} \tilde{\tau}_R. \end{aligned} \quad (2.56)$$

The stau mixing angle  $\theta_{\tilde{\tau}}$  is given by

$$\cos \theta_{\tilde{\tau}} = \frac{-m_\tau (A_\tau - \mu \tan \beta)}{\sqrt{(M_{\tilde{\tau}_L}^2 - m_{\tilde{\tau}_1}^2)^2 + m_\tau^2 (A_\tau - \mu \tan \beta)^2}}, \quad (2.57)$$

$$\sin \theta_{\tilde{\tau}} = \frac{M_{\tilde{\tau}_L}^2 - m_{\tilde{\tau}_1}^2}{\sqrt{(M_{\tilde{\tau}_L}^2 - m_{\tilde{\tau}_1}^2)^2 + m_\tau^2 (A_\tau - \mu \tan \beta)^2}} \quad (2.58)$$

If the stau mixing angle  $\theta_{\tilde{\tau}}$  is 0 degrees then  $\tilde{\tau}_1$  is entirely left-handed, if  $\theta_{\tilde{\tau}} = 45^\circ$  or  $135^\circ$  degrees then the couplings are equal, if  $\theta_{\tilde{\tau}} = 90^\circ$  then  $\tilde{\tau}_1$  entirely right-handed, and if  $\theta_{\tilde{\tau}} = 180^\circ$  then  $\tilde{\tau}_1$  entirely left-handed.

The tau sneutrino has a mass [75]

$$m_{\tilde{\nu}_\tau}^2 = M_{L(3)}^2 + \frac{1}{2} m_Z^2 \cos 2\beta. \quad (2.59)$$

If mixing within the first generation and the second generation is neglected, as is reasonable, then the first and second generation slepton masses are given by equations of the form

$$\begin{aligned} m_{\tilde{e}_L}^2 &= m_{L(1)}^2 + m_e^2 + M_Z^2 \cos(2\beta) \left(-\frac{1}{2} + \sin^2 \theta_W\right), \text{ or} \\ m_{\tilde{\nu}_e}^2 &= m_{L(1)}^2 + M_Z^2 \cos(2\beta) \left(-\frac{1}{2}\right). \end{aligned} \quad (2.60)$$

The interested reader can find the full list in [75].

One-loop corrections to slepton masses are small but not irrelevant [76]. The corrections to the first and second generation sleptons can be in the  $\pm 1\%$  range, while the corrections for the third generation, due to Yukawa coupling corrections, can be in the  $\pm 2\%$  range [69].

The squark masses can be calculated in a similar fashion to the slepton masses. It is usually assumed that only the third generation has mixing. The mixing matrix is analogous to the stau mixing matrix Eq. 2.52.

### 2.3.4 SUSY cross sections, decays and polarisation

Sparticle production at colliders follows the rules set in the Lagrangian. The allowed vertices are equivalent to those of the Standard Model. The cross sections for left-handed and right-handed sleptons are different, and the cross sections for neutralinos and charginos depend on their mixing.

In electron-positron collisions, pair production of smuons, staus and their sneutrinos occurs via the  $s$ -channel exchange of a  $Z$  boson or a photon. This process is possible for opposite-handed incoming electrons and positrons. The production of selectrons can proceed additionally via the  $t$ -channel exchange of neutralinos, as is shown in Fig. 2.6. In this case, the production of a  $\tilde{e}_L\tilde{e}_R$  pair is possible. Electron sneutrinos can also be produced via the  $t$ -channel exchange of charginos. The cross sections for first and second generation sleptons are fairly model-independent but the production of staus depends on the stau mixing angle. In general, however, the production cross section of sleptons of 100-200 GeV mass is several hundred femtobarns at an  $e^+e^-$  centre-of-mass energy of 500 GeV.

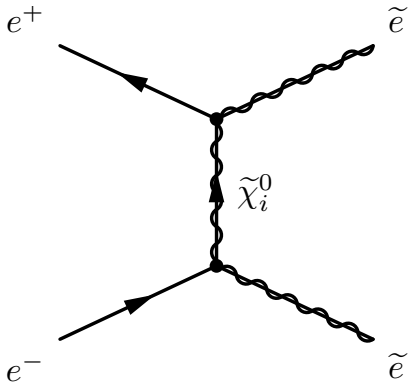


Figure 2.6: Example Feynman diagram of  $\tilde{e}$  pair-production in  $e^+e^-$  collisions.

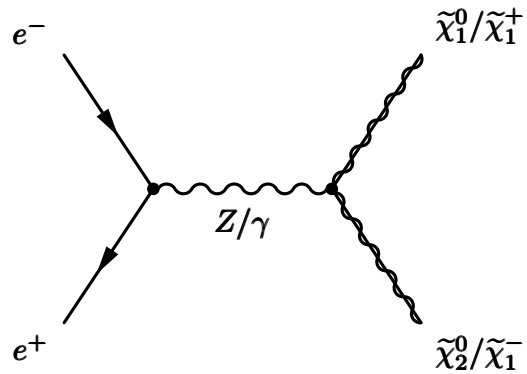


Figure 2.7: Example Feynman diagram of neutralino production in  $e^+e^-$  collisions.

Pair production of charginos  $\tilde{\chi}_1^+\tilde{\chi}_1^-$  and  $\tilde{\chi}_2^+\tilde{\chi}_2^-$  in  $e^+e^-$  collisions proceeds via the  $s$ -channel exchange of a  $Z$  or a  $\gamma$ , or via the  $t$ -channel exchange of a left-chiral electron sneutrino. For the  $Z$  or  $\tilde{\nu}_e$  exchange, the final state  $\tilde{\chi}_1^\pm\tilde{\chi}_2^\mp$  is possible. The chargino production cross section is typically  $\mathcal{O}(100 \text{ fb})$  at  $\sqrt{s} = 500 \text{ GeV}$ .

Neutralinos are also produced in pairs via the  $Z$ -exchange, see Fig. 2.7 or selectron exchange. The cross sections depend on the mixings: for example pair production of binos is suppressed the  $s$ -channel. The  $t$ -channel exchange can be kinematically suppressed due to heavy selectrons. For higgsino-like neutralinos of the same kind, the coupling to  $Z$  is also suppressed but the mixed production is larger. Thus the rates of neutralino-production are very model-dependent.

The production cross sections can be enhanced or decreased via the choice of beam polarisation. In general, left-chiral states are favoured in the left-chiral beam polarisation and right-chiral states in the right-chiral beam polarisation. The production modes involving the  $W$ -bosons can be enhanced by choosing left-chiral beam polarisation. The cross section can be suppressed by two orders of magnitude by the choice of beam polarisation. The partially polarised cross section can be obtained from the

fully polarised cross sections by calculating

$$\begin{aligned} \sigma = & \frac{1 + P^{e^-}}{2} \frac{1 + P^{e^+}}{2} \sigma_{RR} + \frac{1 + P^{e^-}}{2} \frac{1 - P^{e^+}}{2} \sigma_{RL} \\ & + \frac{1 - P^{e^-}}{2} \frac{1 + P^{e^+}}{2} \sigma_{LR} + \frac{1 - P^{e^-}}{2} \frac{1 - P^{e^+}}{2} \sigma_{LL}, \end{aligned} \quad (2.61)$$

where  $P^{e^\pm} = \frac{N_R - N_L}{N_L + N_R}$  with  $N_L$  and  $N_R$  referring to the number of left-handed and right-handed polarised electrons or positrons in the beam [77].

Naturally, choosing the centre-of-mass energy can switch on and off SUSY processes. It is useful to operate near the kinematic threshold to maximise the production cross section, which sharply increases above threshold and slowly decreases with increasing centre-of-mass energy.

Sparticle decays depend on the assumption of  $R$ -parity. If  $R$ -parity is conserved, then a sparticle decays into another sparticle along with some Standard Model particles. The decay chains end in the LSP.

First and second generation sleptons decay as  $\tilde{l}_{R,L} \rightarrow l\tilde{\chi}_i^0$  or  $\tilde{l}_L \rightarrow \nu_l\tilde{\chi}_i^\pm$  as long as the neutralino or chargino is lighter than the slepton. The decays to the Higgs are negligible due to the tiny Yukawa couplings. Decays via weak vector bosons are not allowed without flavour violating couplings [75]. Staus decay as  $\tau\tilde{\chi}_i^0, \nu_\tau\tilde{\chi}_i^\pm$  and possibly  $H^\pm\tilde{\nu}_\tau, H^0\tilde{\tau}_1$  or  $A^0\tilde{\tau}_1$ . Tau sneutrino decays are similar [75].

Charginos decay in two-body modes if they are kinematically allowed. The possible decay products for the light chargino are  $W\tilde{\chi}_i^0, H^\pm\tilde{\chi}_i^0, \tilde{q}_L\tilde{q}', \tilde{l}_L\nu_l$  and  $\tilde{\nu}_l l$  [75]. The heavy chargino decays into the neutral bosons and a light chargino. If these decays are kinematically suppressed, then decays via virtual vector bosons are favoured. In this case the decay proceeds as  $\tilde{\chi}^\pm \rightarrow \tilde{\chi}_i^0 + f\bar{f}'$ . If these are suppressed too, then the chargino lifetime is increased [75].

Neutralinos have many possible two-body decay modes, including decays into gauge bosons and a neutralino or chargino to conserve electric charge. Otherwise, the decays into quark-squark, lepton-slepton or neutrino-sneutrino pairs are possible. In the case of suppressed two-body decays, three-body decay modes take over. The possibilities are  $\tilde{\chi}_i^0 \rightarrow \tilde{\chi}_j^0 + f\bar{f}, \tilde{\chi}_j + f\bar{f}'$ , or  $\gamma\tilde{\chi}_j^0$  if three-body decays are suppressed [75].

## 2.4 Renormalisation group flow

In the Standard Model the bare parameters in the Lagrangian receive corrections from self-energy loops. To renormalise the parameters is to take the corrections into account by introducing a cut-off scale, a scale above which the theory is no longer valid. This introduces an energy scale dependence to the value of the parameter. A well-known example is the decreasing of the QCD coupling  $\alpha_s$  with increasing energy scale, also known as asymptotic freedom. The energy dependence of a parameter is governed by the renormalisation group equations (RGEs) which can be written as a set of coupled differential equations.

Similarly in the MSSM, the parameters evolve with the RGEs. The one-loop RGE equations for MSSM gauge sector parameters are

$$\beta_{M_a} \equiv \frac{d}{dt} M_a = \frac{1}{8\pi^2} b_a g_a^2 M_a \quad (2.62)$$

where  $b_a = (\frac{33}{5}, 1, -3)$  and  $t = \ln(Q/Q_0)$  with  $Q$  the RG scale. Here  $g_a$  are the Standard Model gauge couplings -  $g_2 = g$  and  $g_1 = \sqrt{5/3}g'$  - which have their own renormalisation group running. The one-loop renormalisation group equations for the couplings  $g_1, g_2$  and  $g_3$  are

$$\beta_{g_a} \equiv \frac{d}{dt} g_a = \frac{1}{16\pi^2} b_a g_a^3 \quad (2.63)$$

where  $(b_1, b_2, b_3) = (41/10, -19/6, -7)$  in the Standard Model. In the MSSM, the new SUSY particles in loops modify the coefficients  $b_i$  to  $(b_1, b_2, b_3) = (33/5, 1, -3)$ .

All of the parameters in MSSM have a renormalisation group running. The 1-loop equations are listed for example in [31].

The SM couplings nearly unify, and in the MSSM the couplings are modified and the unification is more accurate, see Fig. 2.8. The unification scale is usually taken to be where  $g_1$  and  $g_2$  unify, and usually  $g_3$  is slightly bigger (smaller in terms of the reciprocal squared  $\alpha_3$ .) The GUT scale is  $M_{GUT} \sim 2 \times 10^{16}$  GeV, but this slightly increases as the SUSY masses increase. The near-unification of the gauge couplings is usually taken as motivation to assume gaugino mass unification, as is the case in constrained SUSY models discussed in the next section.

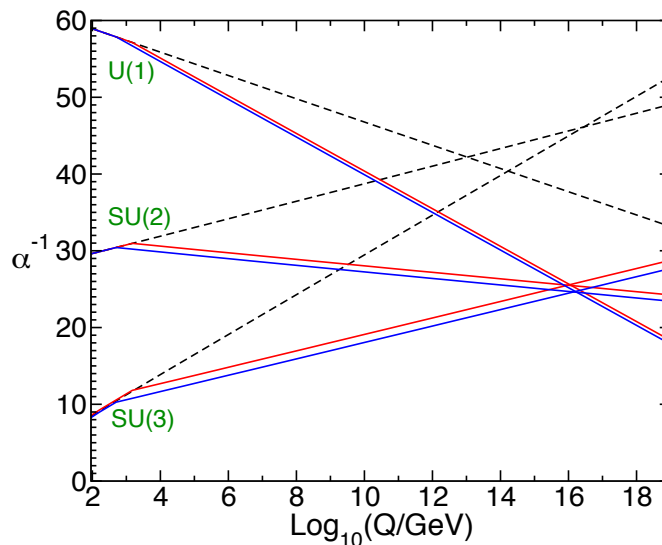


Figure 2.8: The running of gauge couplings in the Standard Model (dashed) and in two different MSSM models (red and blue). The gauge couplings are expressed as  $\alpha_a = g_a^2/4\pi$ ,  $a = 1, 2, 3$ . Figure from Ref. [31].

## 2.5 Constrained models

Constrained models assume some known form of supersymmetry breaking. This means that instead of the 105 free MSSM parameters there are only 4-6 free parameters de-

fixed at the GUT scale. There are a few types of constrained model. Supergravity-mediated supersymmetry breaking (SUGRA) is the most studied one. Among others are anomaly mediated supersymmetry breaking (AMSB), gauge-mediated supersymmetry breaking (GMSB) and a hybrid model called mirage-mediated supersymmetry breaking (MM).

Supergravity-inspired models [78–84], known as SUGRA or constrained MSSM (CMSSM) models assume that gravity is responsible for supersymmetry breaking. This introduces non-renormalisable interaction terms to the Lagrangian. A minimal version of the normalisation leaves only four parameters undetermined, namely a common scalar mass parameter  $M_0$ , a common gaugino mass parameter  $M_{1/2}$ , a common trilinear coupling  $A_0$ , all defined at the GUT scale,  $\tan\beta$  defined at the weak scale, and  $\text{sign}(\mu)$ .

CMSSM can be extended to NUHM1 or NUHM2 which stand for non-universal Higgs mass model 1 and 2 respectively. NUHM1 has the extra high-scale parameter  $M_H^0$  to differentiate the Higgs masses from the other scalar masses. NUHM2 further splits the Higgs sector parameter into  $M_{H_u}^0$  and  $M_{H_d}^0$  to give six parameters in total. The Higgs sector in NUHM2 can be alternatively defined at the weak scale with  $m_A$  and  $\mu$ .

Anomaly-mediated supersymmetry breaking derives from models with extra dimensions. These extra dimensions are spatially separated from the physical dimensions. If the supersymmetry breaking effects come only via supergravity, then this is called anomaly-mediated supersymmetry breaking [85, 86]. In its simplest form AMSB has negative mass-squared terms for sleptons, so it needs to be combined with another theory to make a viable scenario [31].

Mirage mediation on the other hand is a hybrid model of anomaly mediation and moduli i.e. gravity mediation [87, 88]. In this type of model, the gaugino mass unification scale differs from the gauge coupling unification scale. The gaugino mass unification scale  $\mu_{mir}$  is given by  $\mu_{mir} = M_{GUT}e^{-8\pi^2/\alpha}$  where  $\alpha$  determines the proportions of anomaly and gravity mediation to the soft terms. The model is defined by the parameters  $M_{3/2}, \alpha, \tan\beta, \text{Sign}(\mu), n_i, l_a$  where  $M_{3/2}$  is the gravitino mass,  $n_i$  are called modular weights, and  $l_a$  are some power terms. The  $l_a$  are universal for all generations and  $n_i$  can be reduced to three weights, one for the non-Higgs scalars, and one for each Higgs doublet - see [89] for an explanation. The latter two are parameters for the Higgs sector,  $c_{H_u}$  and  $c_{H_d}$ , defined at the GUT scale, which can be exchanged for the weak scale parameters  $\mu$  and  $m_A$ . The theoretical motivation for mirage mediation models stems from string theory, from the reduction of the extra dimensions via flux compactifications [90–92].

There is a further common supersymmetry breaking scenario, gauge-mediated supersymmetry breaking (GMSB) [93–98]. In this scenario there are new messenger chiral supermultiplets, which interact with the matter particles via the SM bosons and SUSY fermions. These messenger multiplets are responsible for supersymmetry breaking. Because the messengers have not been discovered, their masses have to be large. The distinctive phenomenology from GMSB models is that the gravitino may be the LSP, leading to the lightest neutralino to decay into the gravitino and a visible SM particle.

Two types of SUSY breaking scenario are discussed in this thesis: a supergravity-inspired model with two extra Higgs parameters, i.e. the NUHM2 model, and the

mirage-mediation model were used to design the higgsino benchmarks in Ch. 7.

## 2.6 Phenomenological MSSM

The unconstrained MSSM has 105 new parameters, some of which violate lepton number, violate CP in new ways and increase rates of flavour changing neutral currents. The simplest way to remove these new effects and to only allow the effects which exist in the Standard Model is to set many of the parameters to zero or equal to each other. This is convenient because SUSY calculations and parameter scans are greatly simplified.

To motivate this, for example, flavour off-diagonal terms are restricted by the measurement of the  $\mu \rightarrow e\gamma$  process. This process is measured to be very rare [1] and SUSY flavour mixing diagrams would enhance the rate beyond the allowed value. Thus, we have reason to set slepton flavour mixing terms and off-diagonal trilinear coupling terms to zero. Furthermore, fluctuations in the  $K^0 - \bar{K}^0$  system restricts the squark mixing matrices and trilinear couplings. Therefore, it is usual to set all the flavour mixing to zero and only allow mixings in the third generation.

Thus, by setting the sfermion mass matrices diagonal, i.e. removing flavour mixing from MSSM, setting the trilinear couplings proportional to the Yukawa matrices and removing any complex phases from the soft parameters and  $\mu$ , then there are only 14 parameters remaining. If the third generation masses are split from the first and second generation masses, then this adds another 5 parameters. Then we have arrived at the 19 parameters of the phenomenological MSSM (pMSSM) [99] listed in Tab. 2.5 along with the names of the parameters.

## 2.7 Dark matter in supersymmetry

As alluded to in Sec. 2.3.1, if  $R$ -parity is conserved, then the lightest sparticle is a dark matter candidate. Most often the lightest superpartner is a neutralino. If the neutralino is to account for the dark matter relic density, its properties are restricted.

From the cosmological side, the Weakly Interacting Massive Particle assumed to explain the dark matter observation could be the lightest neutralino in  $R$ -parity conserving SUSY, or some other stable, neutral and colourless particle which couples to the SM via a mediator. Since the topic of this thesis is SUSY, we concentrate on SUSY here, and the interested reader can find more information on the mediator approach in Ref. [100].

In SUSY, the neutral and colourless particles are the neutralinos and the sneutrinos. Dark matter cannot consist of sneutrinos: LEP limits on the decays of the  $Z$  to invisible particles sets a limit that the sneutrino mass should be larger than half of the  $Z$  mass [101]. This combined with direct dark matter searches excludes the possibility of sneutrinos as the LSP in the MSSM [102], unless additional flavour violating terms are added to the superpotential [103, 104]. This leaves us with the lightest neutralino

Parameter	Name
$M_1$	Bino mass parameter
$M_2$	Wino mass parameter
$M_3$	Gluino mass parameter
$\mu$	Higgsino mass parameter
$\tan \beta$	Ratio of Higgs VEVs
$m_A$	Pseudoscalar Higgs mass
$A_t$	Trilinear top coupling
$A_b$	Trilinear bottom coupling
$A_\tau$	Trilinear tau coupling
$M_{L(1)} = M_{L(2)}$	Left-handed 1st and 2nd generation slepton mass
$M_{L(3)}$	Left-handed 3rd generation slepton mass
$M_{E(1)} = M_{E(2)}$	Right-handed 1st and 2nd generation slepton mass
$M_{E(3)}$	Right-handed 3rd generation slepton mass
$M_{Q(1)} = M_{Q(2)}$	Left-handed 1st and 2nd generation squark mass
$M_{Q(3)}$	Left-handed 3rd generation squark mass
$M_{U(1)} = M_{U(2)}$	Right-handed 1st and 2nd generation squark mass
$M_{U(3)}$	Right-handed 3rd generation squark mass
$M_{D(1)} = M_{D(2)}$	Right-handed 1st and 2nd generation squark mass
$M_{D(3)}$	Right-handed 3rd generation squark mass

Table 2.5: Parameters of pMSSM-19

to consider. To understand why the properties of the neutralino cannot be arbitrary, let us first discuss how the dark matter relic density is calculated in a model.

### 2.7.1 Relic density calculations

The amount of dark matter today in a model with a stable neutralino LSP can be calculated as follows. During the expansion of the universe, the rates of interactions of DM and SM particles are in equilibrium until some freeze-out temperature where the DM decouples from the SM, see Fig. 2.9. This is the process with which the relic density gets fixed. Calculating the relic density  $\Omega_{LSP}h^2$  involves solving a Boltzmann equation for the present day relic abundance  $Y(T_0)$ . The Boltzmann equation is given by

$$\frac{dY}{dT} = \sqrt{\frac{\pi g_*(T)}{45}} M_p \langle \sigma v \rangle (Y(T)^2 - Y_{eq}(T)^2) \quad (2.64)$$

where  $g^*$  is an effective number of degrees of freedom,  $M_p$  is the Planck mass and  $Y_{eq}(T)$  is the thermal equilibrium abundance [105]. Particle physics comes in in the relativistic thermally averaged annihilation cross section  $\langle \sigma v \rangle$ . This cross section is the sum of all LSP annihilation and coannihilation channels and is given by

$$\langle \sigma v \rangle = \frac{\sum_{i,j} g_i g_j \int_{(m_i+m_j)^2} ds \sqrt{s} K_1(\sqrt{s}/T) p_{ij}^2 \sum_{k,l} \sigma_{ij;kl}(s)}{2T (\sum_i g_i m_i^2 K_2(m_i/T))^2}. \quad (2.65)$$

Here  $g_i$  is the number of degrees of freedom,  $\sigma_{ij;kl}$  is the total annihilation cross section of SUSY particles  $i, j$  with masses  $m_i, m_j$  into SM particles  $k, l$  with masses  $m_k, m_l$ .  $p_{ij}(\sqrt{s})$  is the momentum of the incoming particles in their centre-of-mass frame, and  $K_1$  and  $K_2$  are the modified Bessel functions of the second kind of order 1 and 2 [106]. This means that, if all the sparticle masses and couplings are known,  $\langle \sigma v \rangle$  can be calculated.

The present day relic density is then given by  $\Omega_{LSP} = \rho_{\chi}^0 / \rho_{crit} = m_{LSP} 8\pi G Y_0 / 3H^2$ , or  $\Omega_{LSP} h^2 = 2.755 \times 10^8 \frac{m_{\chi}}{\text{GeV}} Y_0$  [106].

### 2.7.2 Lightest SUSY particle as dark matter

In supersymmetry the relic density is not automatically the observed value but model parameters need to be chosen appropriately. Using the formalism above and using typical SUGRA-type properties for the LSP (mixing is bino-like, mass is in the usually considered  $\mathcal{O}(100 \text{ GeV})$ ), the relic density turns out to be too big [108]. This problem may be fixed by introducing coannihilation of the LSP with a slightly heavier sparticle. The stronger the annihilation or coannihilation process, the smaller the relic density. Coannihilation is important if the cross sections of the coannihilating particle are large,  $\sigma_{\tilde{\chi}_1^0 X} / \sigma_{\tilde{\chi}_1^0 \tilde{\chi}_1^0}$  and  $\sigma_{XX} / \sigma_{\tilde{\chi}_1^0 \tilde{\chi}_1^0}$ , and depending on the ratio of number densities determined by a Boltzmann factor  $\exp((m_X - m_{\tilde{\chi}_1^0})/T_f)$ ,  $T_f$  being the freeze-out temperature [29]. Practically a mass difference of the order of 5-15% can cause the coannihilation channels to dominate over the annihilation channels [109]. Depending on the coannihilating particle, there are different coannihilation mechanisms: chargino coannihilation, stau coannihilation and stop coannihilation.

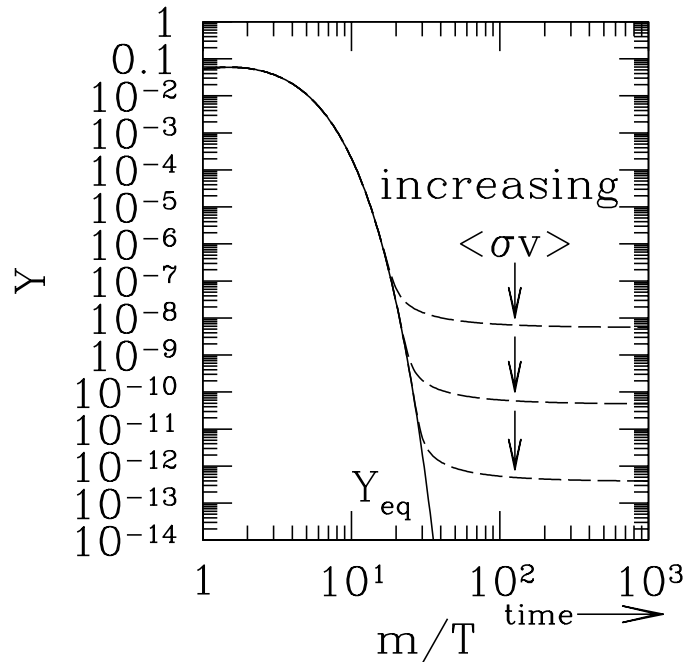


Figure 2.9: The number density of DM with respect to its mass over temperature. As the temperature cools, we move up in the x-axis. The number density starts out large, and when the universe cools, the density decreases until a point determined by the thermally averaged DM annihilation cross section  $\langle\sigma v\rangle$ . The larger the  $\langle\sigma v\rangle$  the smaller the number density and relic density. Figure from [107].

Nearly degenerate particles are not needed if the annihilation can happen with a resonance of either the light Higgs  $h$ , heavy Higgs  $H$  or pseudoscalar Higgs  $A$  or with the  $Z$  boson. These mechanisms are called funnels, e.g.  $h$ -funnel. There is also the focus point region [110] which means that there are some boundary conditions to the GUT relations forcing the renormalisation group to take  $m_H^2$  to  $m_Z$  at EW scale independent of the GUT scale value. This is the focussing. The focussing does not apply to sleptons and squarks hence they can have multi TeV masses without introducing fine tuning. This thesis considers the coannihilation case in Chs. 5 and 6, in particular the stau coannihilation case, since it is the most challenging coannihilation type to study at the LHC.

In scalar tau coannihilation, two types of processes set the relic density. In the neutralino pair annihilation, many final states are possible, listed in [?]. They include pair production of neutral Higgses, associated production of the neutral Higgses, pair production of the charged Higgses, and associated production of a  $W$  and a charged Higgs. Any of the neutral Higgses can be produced in association with a  $Z$ , and SM bosons and fermions can be produced in pairs. Most of these interactions can be mediated by a neutral Higgs in the  $s$ -channel or a neutralino or chargino in the  $t$ - and  $u$ -channels. The annihilation cross section depends on the masses of the particles involved and the strength of the couplings.

The coannihilation processes in stau coannihilation proceeds as  $\tilde{\chi}_1^0\tilde{\tau} \rightarrow \gamma\tau, Z\tau, h\tau$  or  $W^-\nu_\tau$ . Additionally, there can be contributions to the relic density from the  $\tilde{\tau}$  pair annihilation process  $\tilde{\tau}\tilde{\tau} \rightarrow \tau\tau$ , for example.

The other kind of scenario in this thesis is the light higgsino scenario, where the LSP is higgsino-like. Light higgsinos have a very large annihilation rate, leading to a low relic density. To obtain the observed relic density, the mass of the higgsino dark matter should be of the order of 1 TeV [111]. This means that in the scenarios relevant for the ILC at  $\sqrt{s} = 500$  GeV and considered in Ch. 7, the higgsino LSP contributes only a fraction of the dark matter relic density, and the rest must be explained by other particles or non-thermal production mechanisms [112].

### 2.7.3 Non-collider signatures of dark matter

Apart from searching for dark matter production in colliders, there are other avenues for studying the dark matter properties. Direct and indirect searches for dark matter are based on the assumptions that dark matter scatters off Standard Model particles or annihilates with itself into Standard Model particles. Experiments for these processes are dubbed searches for direct and indirect signals of dark matter. The theory behind these is summarised below.

#### WIMP annihilation cross section

The LSP can annihilate with itself into Standard Model particles. These processes may cause some excess in the spectrum of particles observed to reach the Earth. The excess can in principle consist of any kind of Standard Model particles, however photon signals propagate nearly freely, and dark matter annihilation can cause a unique spectral line in the photon spectrum, making it easy to distinguish dark matter signals from conventional photon sources, see e.g. Ref. [113].

The experimental upper limits on photon fluxes are usually quoted in terms of the thermally averaged, velocity-weighted WIMP annihilation cross section  $\langle\sigma v\rangle$ . The cross section part of this quantity can be calculated in from the total one-loop process  $\tilde{\chi}_1^0\tilde{\chi}_1^0 \rightarrow \gamma\gamma$  [114].

#### WIMP-nucleon scattering

The LSP can couple to nuclei via the electroweak force, and therefore there are experiments to look for signals of the LSP scattering off the nucleus. The interactions are governed by the spin-independent WIMP-nucleus scattering cross section

$$\sigma_{SI,A} = \frac{4\mu_N^2}{\pi} [Zf_p + (A - Z)f_n]^2 \quad (2.66)$$

where  $\mu_A$  is the WIMP-nucleus reduced mass  $\mu_A = M_\chi M_A / (M_\chi + M_A)$  with  $M_\chi$  the WIMP mass and  $M_A$  nucleus with atomic mass  $A$  [115].  $Z$  is the number of protons in the nucleus and  $f_{p,n}$  are the effective spin-independent couplings of the WIMP to the proton  $p$  or neutron  $n$ . For many models  $f_p \approx f_n$ , and factoring out the dependence on the target material gives the spin-independent cross section for WIMP-nucleon scattering

$$\sigma_{SI} = \frac{4\mu_n^2 f_n^2}{\pi} \quad (2.67)$$

The WIMP may have spin-dependent interactions, however the terms from WIMP-proton and WIMP-neutron interactions frequently cancel each other, reducing the relevance of these interactions to experiments [115].

While it is outside of the scope of this thesis to detail the current experimental limits on dark matter from direct and indirect detection experiments, it is worthwhile to go through the status of SUSY from collider experiments, as this serves as direct motivation for building an electron-positron collider.

## 2.8 Status of SUSY at LEP and LHC

The theoretical SUSY parameter space is reduced by past and current experiments, as discussed in the motivation for e.g. setting  $CP$ -violating parameters to zero. We will summarise the exclusion limits from high-energy experiments that most affect the possible scenarios remaining to be studied at a high-energy  $e^+e^-$  collider. These are the LHC and LEP limits.

### 2.8.1 Results from LHC

The LHC is performing incredibly well and is setting limits on many types of BSM model including limits on all SUSY particles. The LHC has large SUSY cross sections for coloured particles as can be seen from Fig. 2.10. The slepton production cross sections are smaller than the electroweakino production cross sections. As the total energy of the colliding partons is not known, the searches are conducted by looking for events with large missing transverse energy or momentum as this would be the signature of an invisible LSP. Additionally some number of jets and/or leptons is required.

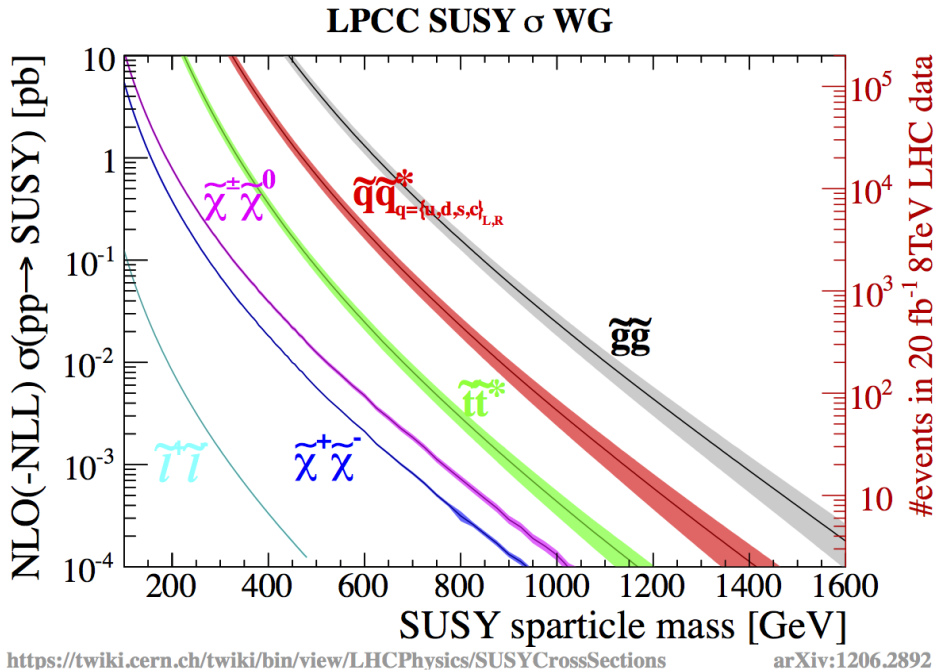


Figure 2.10: LHC SUSY cross sections [116]. The neutralino cross section is for high-ginos, and the wino cross section would be about four times this value [117, 118].

The searches are limited by the huge QCD backgrounds and the simultaneous overlay of multiple hard interactions in the same bunch crossing. Due to these, not all events can be recorded and trigger requirements need to be set, which puts a lower limit on the amount of energy that the visible particles have to have. This is to say that the decay products of the SUSY particles need to have energy above a certain value. If the decay products are too soft, then they would be missed and would add to the invisible energy in the event. In the extremely soft decay scenarios, the missing energy can be interpreted as containing a small amount of energy from SM decay products leading to upper limits on the visible energy of the decay products of the SUSY particles.

One of the relevant exclusion ranges for future  $e^+e^-$  colliders is related to the electroweak gauge sector. With respect to neutralinos and charginos, there are limits from the LHC for  $\sqrt{s} = 13$  TeV and an integrated luminosity of  $35.9 \text{ fb}^{-1}$  from CMS shown in Fig. 2.11 ([119]) and up to  $36.1 \text{ fb}^{-1}$  from ATLAS shown in Fig. 2.12 ([120]).

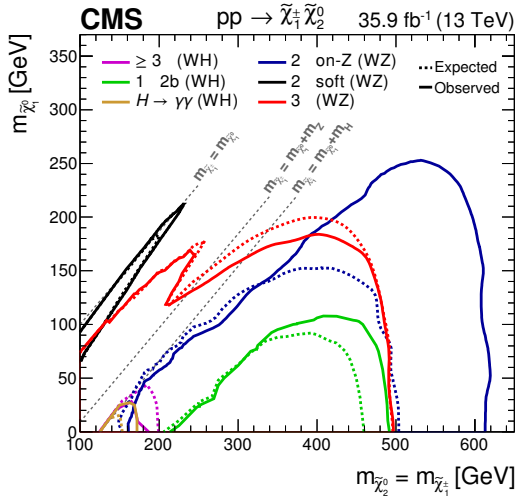


Figure 2.11: CMS summary of electroweakino searches from  $\sqrt{s} = 13$  TeV,  $\mathcal{L} = 35.9 \text{ fb}^{-1}$  [119].

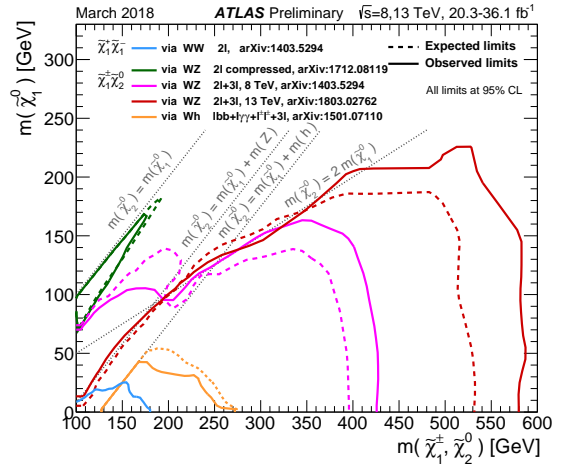


Figure 2.12: ATLAS electroweakino search summary from  $\sqrt{s} = 8, 13$  TeV,  $\mathcal{L} = 20.3 - 36.1 \text{ fb}^{-1}$  [120].

On a first look at Figs. 2.11 and 2.12 it seems that most of the parameter space at low masses is already excluded by the searches for  $pp \rightarrow \tilde{\chi}_2^0 \tilde{\chi}_1^\pm \rightarrow$  two or three leptons and missing transverse energy. The highest reach is up to 600 GeV from the two-lepton search. At the lower masses the sensitive search is for three leptons or two soft leptons.

However, the exclusion limits are shown assuming a purely wino LSP. This means that the electroweakino production cross section in the plot is assumed to be about four times higher than it would be for higgsinos [117, 118]. This means that the integrated luminosity would have to be about 16 times the current integrated luminosity [121] to rule out higgsinos.

The higgsino case is plotted in detail in Figs. 2.15 and 2.13. Both figures show that despite requiring triggering for soft decay products, the LHC has managed to successfully exclude many possible higgsino models down to a mass difference of 7 GeV for CMS and 1.5 GeV for ATLAS, and reaching up to higgsino masses of 170 GeV or 140 GeV for CMS and ATLAS respectively [122, 123]. Thus, as it stands at the time of

writing, there remain some gaps in the LHC searches for electroweakinos in the regime with higgsino mass above 140 GeV and mass difference below 7 GeV if the ATLAS and CMS results are combined by eye.

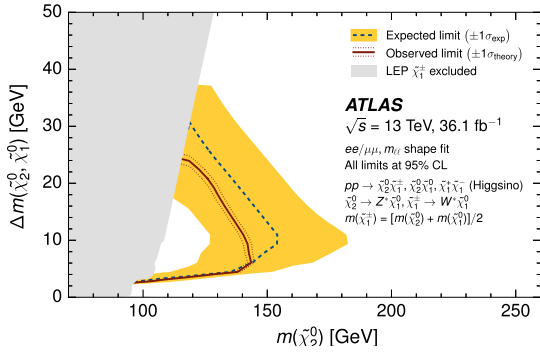


Figure 2.13: ATLAS limit on pure higgsinos from  $\sqrt{s} = 13$  TeV,  $\mathcal{L} = 36.1$  fb $^{-1}$  [123].

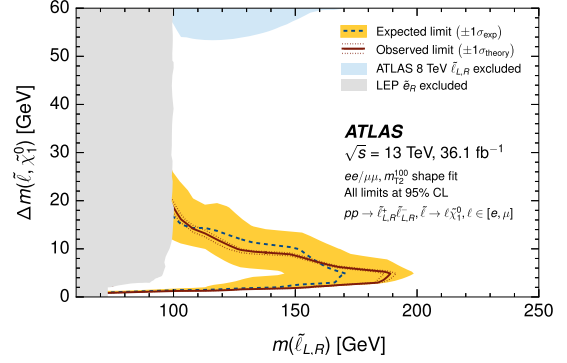


Figure 2.14: ATLAS limit on mass-degenerate selectrons and smuons from  $\sqrt{s} = 13$  TeV,  $\mathcal{L} = 36.1$  fb $^{-1}$  [123].

The other type of exclusions which are particularly relevant for a lepton collider are the slepton exclusion limits. The assumption in the slepton lower limits from the LHC is a 100% branching fraction for one decay mode. In general, however, there can many possible decay modes of one slepton. Additionally, the LHC sensitivity is mostly in the large mass gap region, although analysis strategies are improving to close this gap with mono-jet and mono-photon and soft lepton searches. ATLAS results in the small mass gap region can be found in [123]. The limit assumes the same mass for  $\tilde{e}_L$ ,  $\tilde{e}_R$ ,  $\tilde{\mu}_L$  and  $\tilde{\mu}_R$ , which combine to exclude those sleptons if they have mass below 190 GeV and less than 10 GeV mass difference to the LSP. For the larger mass gap scenarios, for example, for a 100 GeV LSP, selectrons of mass between 160 GeV and 300 GeV are excluded [124]. In general, the slepton limits are stronger for the left-chiral sleptons as can be seen from Fig. 2.16 for CMS [125], due to their preferred production in  $pp$  collisions.

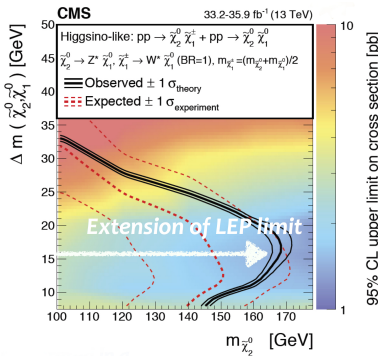


Figure 2.15: CMS exclusion limit for pure higgsinos from  $\sqrt{s} = 13$  TeV,  $\mathcal{L} = 33.2 - 35.9$  fb $^{-1}$  [122].

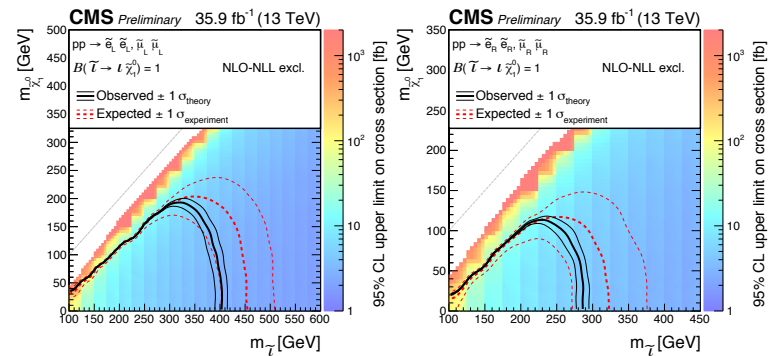


Figure 2.16: CMS exclusion limit for  $\tilde{e}_L$  and  $\tilde{\mu}_L$  (left) and for  $\tilde{e}_R$  and  $\tilde{\mu}_R$  (right) from  $\sqrt{s} = 13$  TeV,  $\mathcal{L} = 35.9$  fb $^{-1}$  [125].

The LHC has the largest sensitivity to coloured new particles as the production cross sections are large due to the strong interaction of the particles with quarks and gluons.

The limit for gluinos is particularly strong, about 2 TeV with  $36 \text{ fb}^{-1}$  at  $\sqrt{s} = 14 \text{ TeV}$  if the LSP is massless [126]. If the LSP is around 1 TeV or heavier, then there is no limit on the gluino mass. Limits for scalar quarks are strong, however these are for the best case scenario: first and second generation left-handed and right-handed squarks are degenerate and the gluino is heavy leading to an eight times larger production cross section compared to a single squark. Similarly here the LSP mass plays a crucial role, and for LSP masses above 500 GeV, no limit on squark masses can be set [126]. For third generation squarks the picture is similar, however the production cross section is suppressed by a factor 100 due to the lack of top and bottom quarks in the proton. Additionally, the decay products of top and bottom squarks are experimentally harder to reconstruct, thus leading to weaker exclusion limits. In summary, the gluino limit is the strongest but there are regions of the rest of the coloured sector which are uncovered by the current exclusions.

There is of course also an extensive search program for the extended Higgs sector. The searches are most sensitive to charged Higgses. The limits on the mass can be translated into limits in the  $\tan \beta - m_A$  plane in Figs. 2.17 and 2.18 for two different models [127]. The limits are weak for small  $\tan \beta$  and large  $m_A$ , and depending on the interpretation for a  $\tan \beta = 10$  model the limit is 300 – 800 GeV in the most recent ATLAS results with  $\sqrt{s} = 13 \text{ TeV}$  and  $\mathcal{L} = 36.1 \text{ fb}^{-1}$ .

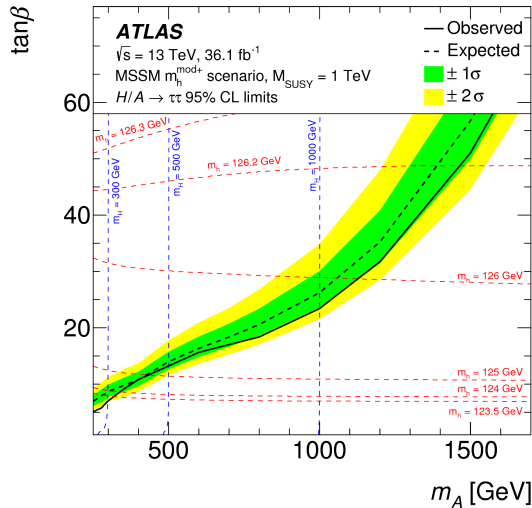


Figure 2.17: ATLAS heavy Higgs searches lead to exclusion limits in the  $\tan \beta - m_A$  plane [127].

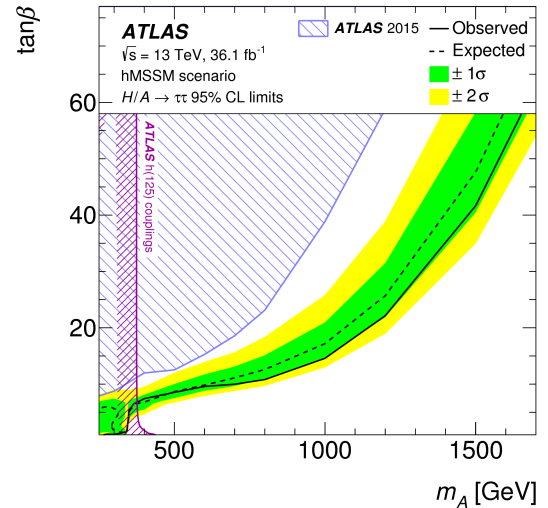


Figure 2.18: ATLAS heavy Higgs searches lead to exclusion limits in the  $\tan \beta - m_A$  plane [127].

## 2.8.2 Future constraints from high-luminosity LHC

The LHC will continue running with its current setup with an instantaneous luminosity of about  $1 - 1.5 \times 10^{34} \text{ cm}^{-2}\text{s}^{-1}$  until about 2023. This will result in a data set of  $300 \text{ fb}^{-1}$  collected. It has been planned and approved that after that there will be an upgrade of the instantaneous luminosity of the proton beams, increasing it by a factor 5 to 7, resulting in the High-Luminosity LHC (HL-LHC) [128]. This will be achieved by improving the final focusing magnets, by introducing crab crossing to reduce the

effect of the crossing angle, and upgrading the collimation and cryogenics. Whereas now the pileup, i.e. number of simultaneous hard scattering events, is on average 35, after the luminosity upgrade it will increase to 200 [128]. This poses a challenge for the detector system: detector granularity needs to be increased, radiation hardness improved, timing components need to be faster and trigger acceptance needs to be increased [129]. The tracker upgrade is of particular importance, so that interesting physics events can be identified despite the large pileup [129].

The luminosity upgrade is motivated by collecting as much data as possible. More data will help in particular with precision measurements of the Higgs boson properties. It is expected that the Higgs couplings will be measured in the  $\kappa$ -framework [130] to a few percent or pessimistically to 10% depending on the assumptions [131]. Either the new detectors can be parametrised or current results can be extrapolated. There will be sensitivity to rare decays of the Higgs, including its decay into two muons, whereby a  $7\sigma$  excess is expected [132]. There will be only enough data to set upper limits on  $h \rightarrow c\bar{c}$  rates [133]. The limit is 15 times the SM expectation. Similarly the Higgs self-coupling analysis, so the di-higgs production search, is expected to gain a significance of  $1.05\sigma$  at ATLAS [134] and  $1.6\sigma$  at CMS [135] in the Standard Model case for the best channel  $hh \rightarrow \gamma\gamma b\bar{b}$ .

Furthermore, the BSM searches will be sensitive even to higher mass scales with the HL-LHC data set. For example, the search for electroweakinos in the channel  $pp \rightarrow \tilde{\chi}_2^0 \tilde{\chi}^\pm \rightarrow \tilde{\chi}_1^0 Z \tilde{\chi}_1^0 W^\pm$  would discover any previously unexcluded charginos with masses up to 800 GeV for a  $\tilde{\chi}_1^0$  mass of 0 – 200 GeV as in Fig. 2.19 [136]. The monojet search for WIMPs will have sensitivity to LSP masses up to 800-1000 GeV depending on the assumptions [137]. All of the projections are dependent on the assumed efficiencies which are difficult to estimate due to the increased pileup in the HL-LHC. The searches for soft decay products in the mass-degenerate regime depend on this strongly.

Even after the HL-LHC measurements there will be room for discoveries or improving any measurements, and for that a future collider is needed: the lepton type for improving on precisions and closing phase space gaps in the BSM search, and the hadron type for extending the mass reach of direct searches.

### 2.8.3 Results from LEP

In some cases the LEP exclusion limits are still stronger than the current LHC exclusion limits. This is true in particular because the LEP searches are nearly model-independent, whereas the LHC searches have assumptions due to the unknown initial state and beam remnants. For example, this can be seen in the slepton limits plotted in Fig. 2.14, where the LEP limit covers nearly the entire range of possible decay product energies.

The LEP exclusion plot for right-handed slepton pairs is shown in Fig. 2.20. The strongest limits are on the first and second generation, but also the exclusion on a right-chiral  $\tilde{\tau}_1$  reaches up to 87-93 GeV [138]. The limit for a stau with any mixing angle and any mass with a mass difference  $\Delta M(\tilde{\tau}_1 - \tilde{\chi}_1^0) \geq m_\tau$  is 26.3 GeV [139].

LEP provides lower mass limits on the chargino mass above 103.5 GeV if sneutrinos are heavier [140] and 91.9 GeV for any LSP mass [?]. The chargino exclusion for

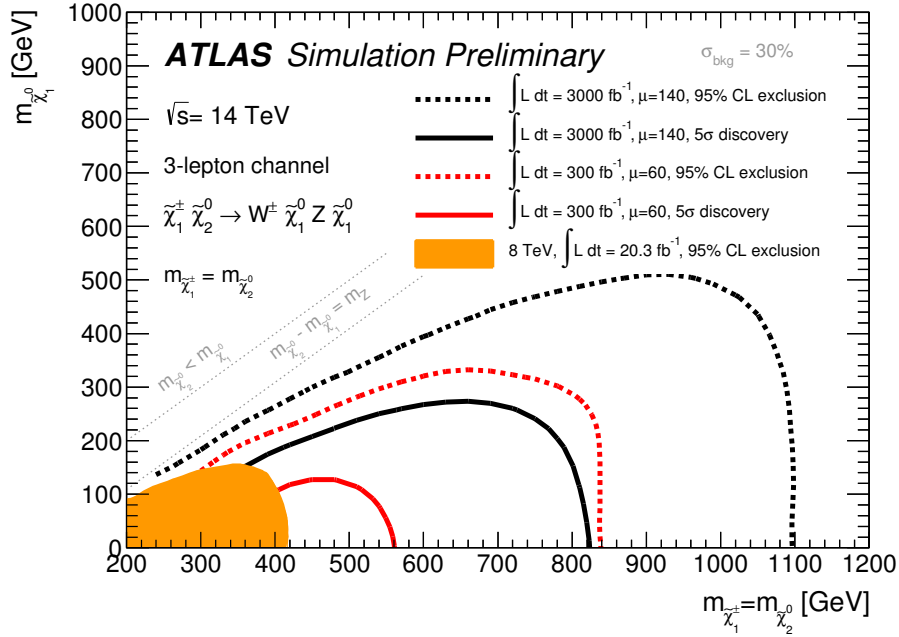


Figure 2.19: ATLAS HL-LHC projection for chargino-neutralino production in the boson-mediated decay channel. The number of interactions per bunch crossing is assumed to be 60 (140) for the 300 (3000)  $\text{fb}^{-1}$  data set. [136]

higgsino-like  $\tilde{\chi}_1^\pm$  is plotted in Fig. 2.21, from which it can be seen that the exact value of the limit depends on the LSP mass [?]. There are limits on other kinds of SUSY particles too, which the interested reader can find from Ref. [141].

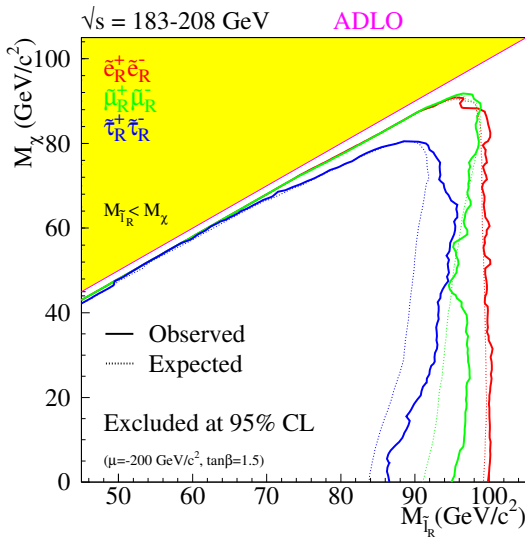


Figure 2.20: LEP slepton exclusion limits for pair-production of  $\tilde{e}_R$ ,  $\tilde{\mu}_R$  and  $\tilde{\tau}_R$  with  $\sqrt{s} = 183 - 208$  GeV [142].

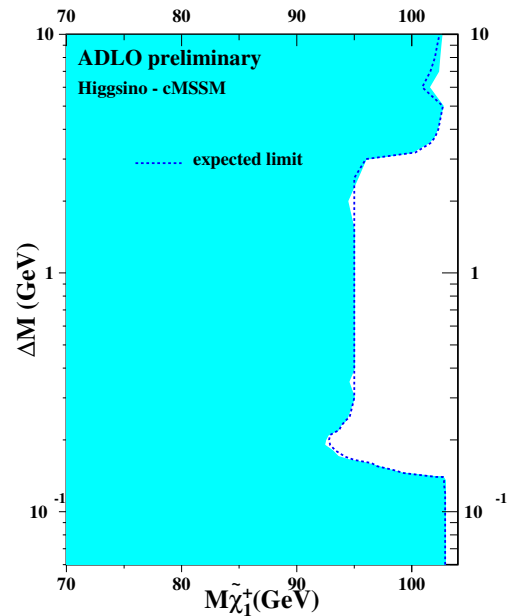


Figure 2.21: LEP higgsino exclusion limits for data up to  $\sqrt{s} = 208$  GeV [?].



# Chapter 3

## International Linear Collider

Traditionally hadron and lepton colliders have contributed to particle physics in a complementary way. Hadron colliders have broken records for the energy of the collisions, while lepton colliders have accessed high scales by making precision measurements. There is a long-standing plan for a future lepton collider, namely the International Linear Collider or ILC [143]. The plan for the ILC has been built from combining different national projects for a linear collider. Those predecessors were Teraelectronvolt Energy Superconducting Linear Accelerator (TESLA) [144] in Germany, Next Linear Collider (NLC) in the US [145] and Global Linear Collider (GLC) in Japan [146]. The ILC is a linear electron-positron collider which has superconducting radio-frequency cavities to accelerate the particles. In addition, both beams are polarised, on average 80% polarisation for electrons and 30% polarisation for positrons. The beams have a centre-of-mass energy  $\sqrt{s} = 200 - 500$  GeV, with the possibility to upgrade to 1 TeV. There are planned to be two detectors, the ILD (for International Large Detector) and SiD (for Silicon Detector), which would operate alternately in a push-pull system. The details of the physics motivation for the ILC, as well as the accelerator and detector design for the ILD for are discussed below.

### 3.1 Physics at the ILC

The physics goals of the ILC are varied and impressive. As a precision measurement experiment, the ILC will pin down, for example, the Higgs couplings and the top mass, and strengthen the model-independent limits for WIMPs or SUSY particles. To understand why it is possible to measure these processes more accurately at the ILC than at the LHC, the advantages of the ILC are discussed. Then we will go into more detail on the Higgs, top and beyond the Standard Model physics at the ILC.

#### 3.1.1 Advantages of lepton colliders over hadron colliders

There are five major advantages of electron-positron colliders over proton-proton colliders. These are cleanliness, democracy, calculability, polarisation and a known initial state [147].

**Cleanliness:** The background from the beam in lepton colliders is much more benign than at hadron colliders. This is simply because the large proton-proton cross section leads to around 30 interactions per bunch crossing in the current LHC phase. The background rate at the ILC is around 1 event per bunch crossing. Another benefit of lepton interactions is the reduced jet activity due to the electroweak production modes. A visualisation of the differences in the interactions can be seen in Fig. 3.1 in a simulated higgsino and a Higgs event display from ILD and CMS respectively. The large background at the LHC implies the need to cut down the rate of events by trigger systems. Triggering is not required at the ILC. Additionally the detector materials must sustain high rates of radiation, which puts limitations on the achievable resolution.

**Democracy:** Different flavours are produced democratically in  $e^+e^-$  collisions as the initial state has a zero sum of charge and flavour, and the photon and  $Z$  have similar size couplings to all fermions. On the contrary, pp collisions have net electric charge and more up-flavour than down-flavour. Most interactions are soft, light-flavour QCD interactions in which the interesting and rare processes are difficult to observe. Thus it is necessary to trigger for relevant events at the LHC, meaning some signals could be hidden and only select decay modes can be studied at once.

**Calculability:** Electroweak interactions are well understood theoretically and there are no problems with the convergence of the perturbation series. QCD, on the other hand, includes non-perturbative effects and uncertainties in the proton structure function. The theoretical uncertainties from QCD limit the potential for precision measurements at the LHC, while the tiny theoretical uncertainties in electroweak processes enable the sensitivity of ILC measurements to higher-order corrections from new physics.

**Polarisation:** Tuning the beam polarisation enables reducing background and enhancing signal as needed. For example, the Higgsstrahlung process  $e^+e^- \rightarrow Zh$  is enhanced by the  $\mathcal{P}(e^-, e^+) = (-80\%, +30\%)$  beam polarisation combination. On the other hand, new physics searches such as SUSY searches benefit from the suppression of the Standard Model background in the polarisation  $\mathcal{P}(e^-, e^+) = (+80\%, -30\%)$ . It should be noted that even if the desired signal  $S$  and background  $B$  have the same polarisation dependence, the significance of a discovery is proportional to  $S/\sqrt{B}$ , so enhancing both the signal and the background by a factor two improves the significance by  $\sqrt{2}$ . An in-depth review of the benefits of electron and positron beam polarisation on the physics reach of the ILC is presented in [77] and in [148].

**Known initial state:** Due to electrons and positrons being elementary particles, the colliding energy can be known up to some uncertainty on the beam energy spread (discussed below). This allows the kinematic constraining of the decay products, leading to more information about possible invisible particles in the event. The total energy is increased by the energy from simultaneous  $e\gamma$  or  $\gamma\gamma$  events, which will be discussed below.

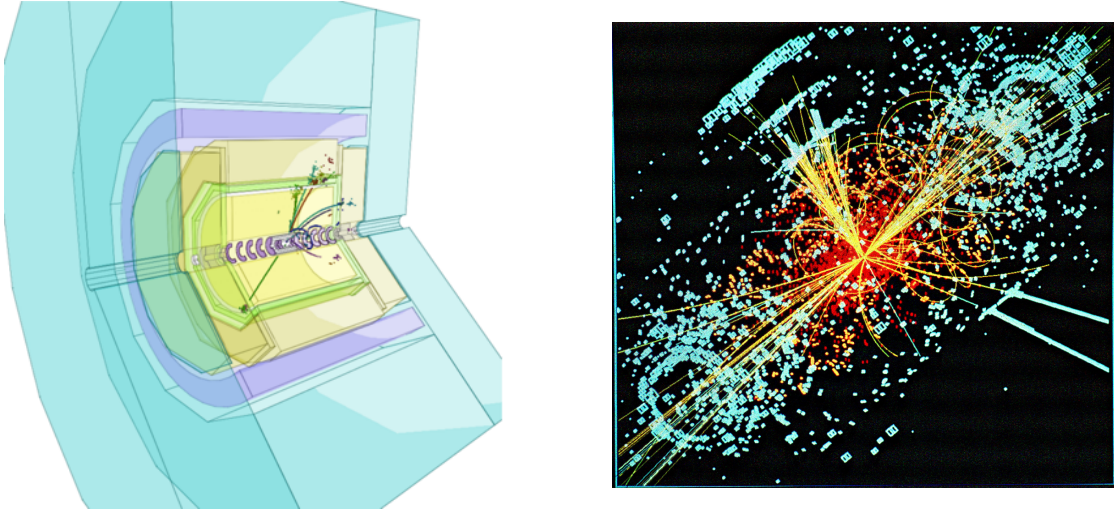


Figure 3.1: Left: Simulated higgsino pair production with one higgsino decaying to hadrons and an LSP, and the other decaying into an electron and an LSP in the ILD detector, [149]. Right: Simulated Higgs boson production and decay into two hadrons and two electrons in the CMS detector, image from [150]. The difference in the amount of activity in the detectors is striking.

### 3.1.2 Operating scenarios

The ILC has been designed based on the following criteria required for high-precision physics measurements: tunable centre-of-mass energy  $\sqrt{s} = 200 - 500$  GeV with less than 0.1% allowed spread of beam energy, instantaneous luminosity  $L = 2 \times 10^{34}$   $\text{cm}^{-2}\text{s}^{-1}$  at  $\sqrt{s} = 500$  GeV, an 80% average polarisation for the electrons, and a 30% positron polarisation [151].

There are different possible ways of dividing the ILC operation time between different centre-of-mass energies and beam polarisations. Various scenarios have been designed based on the requirement for precise measurements of the Higgsstrahlung  $e^+e^- \rightarrow Zh$  at  $\sqrt{s} = 250$  GeV, top mass scan at  $\sqrt{s} = 350$  GeV and top Yukawa coupling, Higgs total width and self-coupling at  $\sqrt{s} = 500$  GeV [152]. All the key measurements and required centre-of-mass energies are listed in Tab. 3.1. The integrated luminosity at each centre-of-mass energy depends on the physics goals.

For optimal reach for new particles, a large  $4 \text{ ab}^{-1}$  data set at  $\sqrt{s} = 500$  GeV should be obtained as early on in the operation as possible, as is in the running scenario H20 in Fig. 3.2 [152]. In this scenario, the optimal sharing of the data set between different beam polarisation configurations is shown in Tab. 3.2: at  $\sqrt{s} = 500$  GeV an even split for LR and RL beam configurations is envisaged, with only 10% running time for each of LL and RR configurations. This is determined on the one hand by wanting to measure the Higgs processes which benefit from the LR configuration and new physics which benefit from the suppression of the Standard Model background in the RL or same-handed polarisations. If the initial ILC could only reach  $\sqrt{s} = 250$  GeV, then a possible timeline is shown in Fig. 3.3. If the emphasis is on the 350 GeV operation then the scenario I20 in Tab. 3.3 is suitable. In the case of direct observation of new particles, threshold scans can be considered, and the running scenario will be settled upon once the machine is closer to being operational.

250 GeV	Higgs mass and $J^{PC}$ Inclusive cross section $\sigma(e^+e^- \rightarrow Zh)$ Coupling $g_{ZZH}$
340-350 GeV	Top threshold scan for mass Top CP and couplings
350-500 GeV	Coupling $g_{WWH}$ Triple gauge couplings Higgs total width Top Yukawa coupling
500 GeV	BR of Higgs decay modes Higgs self-coupling via Zh
1 TeV	Rare Higgs decays Higgs self-coupling in W-fusion Quartic gauge couplings

Table 3.1: Key measurements at the ILC and the required centre-of-mass energy.

Below is a more detailed review of the physics potential of the ILC, first going through the “guaranteed” measurements of the Higgs and the top and finally the beyond the Standard Model capabilities. All of the examples below are based on simulations of a realistic detector, the International Large Detector (ILD) for the ILC accelerator. The experimental setup is described after the physics case, which guides the specifications required for the accelerator and the detector.

energy	LR	RL	LL	RR	Total
250 GeV	1350	450	100	100	2000
350 GeV	135	45	10	10	200
500 GeV	1600	1600	400	400	4000

Table 3.2: Running scenario H-20 [152]. Values are integrated luminosity in  $\text{fb}^{-1}$ . The LR stands for beam polarisation  $\mathcal{P}(e^- = -80\%, e^+ = +30\%)$ , RL for  $\mathcal{P}(e^- = +80\%, e^+ = -30\%)$ , LL  $\mathcal{P}(e^- = -80\%, e^+ = -30\%)$  and RR for  $\mathcal{P}(e^- = +80\%, e^+ = +30\%)$ .

### 3.1.3 Higgs physics

As can be seen from Tab. 3.1, precision Higgs measurements, i.e. Higgs mass and coupling measurements, are one of the biggest motivations for building the ILC. Different

energy	LR	RL	LL	RR	Total
250 GeV	337.5	112.5	25	25	500
350 GeV	1147.5	382.5	85	85	1700
500 GeV	1600	1600	400	400	4000

Table 3.3: Running scenario I-20 [152]. Values are integrated luminosity in  $\text{fb}^{-1}$ . The LR stands for beam polarisation  $\mathcal{P}(e^- = -80\%, e^+ = +30\%)$ , RL for  $\mathcal{P}(e^- = +80\%, e^+ = -30\%)$ , LL  $\mathcal{P}(e^- = -80\%, e^+ = -30\%)$  and RR for  $\mathcal{P}(e^- = +80\%, e^+ = +30\%)$ .

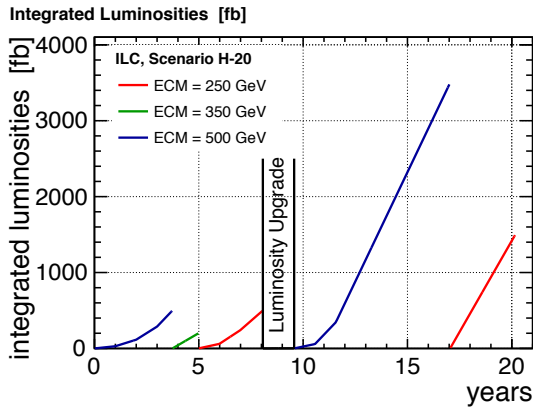


Figure 3.2: A timeline showing the scheduled data collecting in the H20 scenario [152].

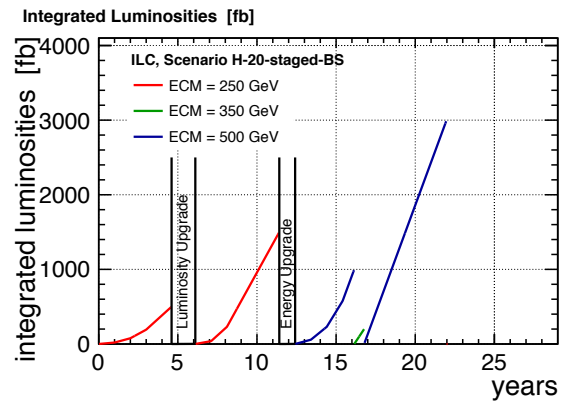


Figure 3.3: Staged operating scenario if ILC was built initially to reach only  $\sqrt{s} = 250$  GeV [153].

measurements benefit from different centre-of-mass energies: The Higgsstrahlung process  $e^+e^- \rightarrow Zh$  can be best measured around  $\sqrt{s} = 250$  GeV as can be seen from Fig. 3.4 which shows the cross section versus  $\sqrt{s}$  and the corresponding Feynman diagram. The Higgsstrahlung process can be used to measure the Higgs mass. The key is that, in this mode, the Higgs boson can be reconstructed from the decay products of the  $Z$ -boson alone. The Higgs mass is the mass  $M_X$  against which the  $Z$ -boson recoiled,

$$M_X^2 = (p_{CM} - (p_{\mu^+} + p_{\mu^-}))^2, \quad (3.1)$$

where  $p_{\mu^+, \mu^-}$  are the four-momenta of the two muons and  $p_{CM}$  is the four-momentum of the incoming particles in their centre-of-mass frame which is known up to the beam spectrum. This allows us to measure the mass of the Higgs without measuring the Higgs itself. The result is the measurement of the Higgs mass with ultimate precision of 15 MeV in the H20 scenario [154, 155]. This precision restricts any possible Beyond the Standard Model contributions to the Higgs mass.

Additionally, the Higgs couplings can be measured in a model-independent way. The key is measuring the total cross section of Higgsstrahlung, which is proportional to  $g_{HZZ}^2$ . The Feynman diagram for this process is in Fig. 3.4, and the same figure shows that the process is maximally likely at  $\sqrt{s} = 250$  GeV. It is possible to measure this cross section without assumptions on the Higgs decay rates. Simply the decay products of the  $Z$ -boson are reconstructed, and with the knowledge of the  $Z$  branching fractions from LEP, the total cross section can be extracted from the  $Z \rightarrow l^+l^-$  ( $l = e, \mu$ ) or  $Z \rightarrow q\bar{q}$  channels. The total cross section can be measured with sub-percent precision [154, 155].

The next step is to measure the same Higgs decay process in the two different production modes, Higgsstrahlung and  $W$ -fusion. Both of these rates are proportional to the Higgs branching fraction and the inverse of the Higgs width. Taking the ratio leaves the dependence on  $g_{HZZ}$  and  $g_{HWW}$ , and knowing the former implies knowing the latter. Now measuring the rate  $e^+e^- \rightarrow H\nu\bar{\nu} \rightarrow WW^*\nu\bar{\nu}$ , which depends on  $g_{HWW}$  and the Higgs width  $\Gamma_H$  allows determining  $\Gamma_H$ . After that, all Higgs couplings can be extracted from the rates of the exclusive Higgs decay channels. In practice, all this is done simultaneously, and the results of the model-independent Higgs coupling fit are plotted in Fig. 3.6 for the running scenario H20 [155]. For comparison with the LHC, model-dependent results are plotted in Fig. 3.5, showing that the ILC projections are more accurate than the high-luminosity LHC projections, except in the  $h\gamma\gamma$  coupling, where LHC has the advantage of higher statistics than the ILC. In this case, a combination of ILC and LHC results brings the  $h\gamma\gamma$  coupling to the percent-level where the other projections lie.

The model-independent values can be translated into precisions on the Higgs branching ratios (via the relation  $\text{BR} \propto g^2$ ), which are listed in Tab. 3.4 for the H20 operating scenario. The Higgs couplings are modified in beyond the Standard Model scenarios. For example, light gauginos would reduce the size of the  $hWW$  and  $hZZ$  couplings. Therefore, when fitting SUSY parameters to observations, it can be useful to use the Higgs coupling measurements as input alongside SUSY measurements. The branching fractions precisions of Tab. 3.4 are used in the analyses in this thesis.

Besides the Higgs mass and couplings being interesting, there is also the Higgs self-coupling. It is crucial for the electroweak symmetry breaking mechanism. In the

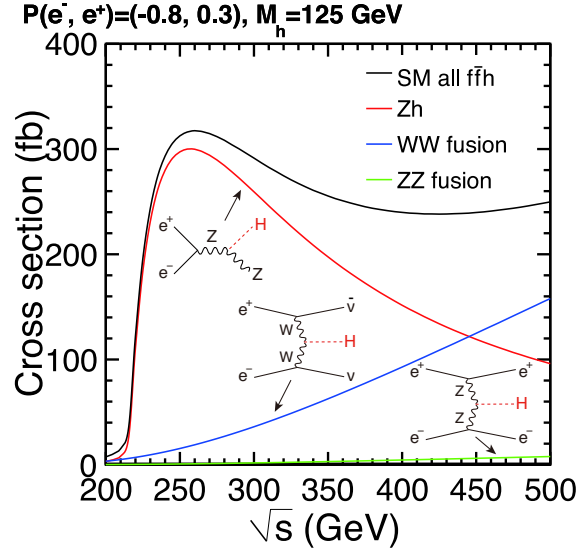


Figure 3.4: Higgs production cross sections vs. centre-of-mass energy [147].

SM the Higgs couples to itself but this has not been experimentally verified. The channel which depends on the Higgs self-coupling  $\lambda$  is  $e^+e^- \rightarrow hh$  i.e. the di-Higgs production channel. At the LHC the self-coupling diagram interferes destructively with the background diagrams which depend on  $Vhh$  and  $VVhh$  couplings. Therefore, the signal at the LHC for Higgs-self coupling is indeed a reduced cross section of  $pp \rightarrow hh$ . At the ILC a measurement of the Higgs self-coupling can be made with 26% precision in the SM case with  $2 \text{ fb}^{-1}$  for both of the the opposite-handed polarisations  $\mathcal{P}(\pm 80\%, \mp 30\%)$  [14]. The Higgs self-coupling is modified in BSM scenarios as the new particles contribute to the  $\lambda$ . Maximally the modification can be a factor of a few with respect to the Standard Model value without being excluded already [156].

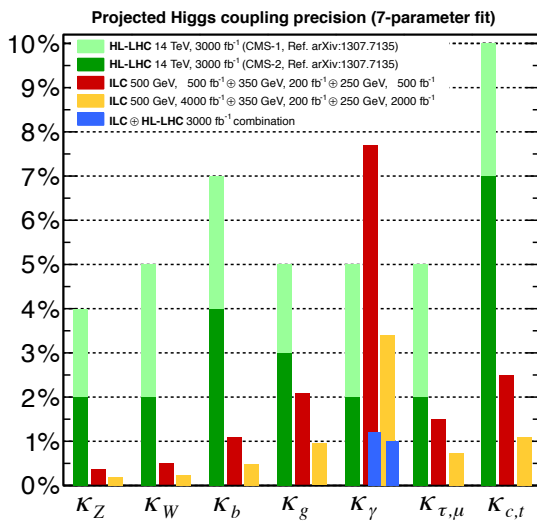


Figure 3.5: Higgs coupling precisions in the model dependent fit for different ILC and HL-LHC data sets [155].

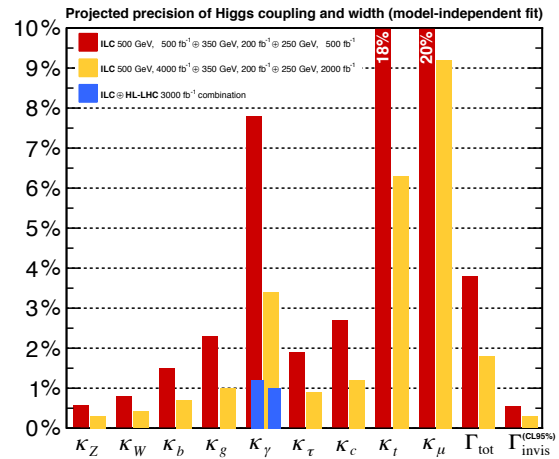


Figure 3.6: Higgs coupling precisions in the model independent fit for different ILC and HL-LHC data sets [155].

Obs.	init. $\Delta\text{BR}$	H20 $\Delta\text{BR}$
$BR(h \rightarrow ZZ)$	1.16%	0.62%
$BR(h \rightarrow WW)$	1.62%	0.84%
$BR(h \rightarrow b\bar{b})$	3.0%	1.4%
$BR(h \rightarrow gg)$	4.6%	2.0%
$BR(h \rightarrow \gamma\gamma)$	2.4%	2.0%
$BR(h \rightarrow \tau\tau)$	3.8%	1.8%
$BR(h \rightarrow c\bar{c})$	5.4%	2.4%
$m_h$	25 MeV	15 MeV

Table 3.4: Model independent Higgs branching fractions uncertainties for an initial phase  $500 \text{ fb}^{-1}$  at 500 GeV,  $200 \text{ fb}^{-1}$  at 350 GeV and  $500 \text{ fb}^{-1}$  at 250 GeV. The H20 scenario has an additional  $3500 \text{ fb}^{-1}$  and  $1500 \text{ fb}^{-1}$  at 250 GeV. 40% with +-, 40% with -+ and 10% - and 10% ++ polarisations with respect to the initial data set. Values scaled from the coupling fit in Ref. [155].

If the centre-of-mass energy of the ILC would be only 250 GeV, then the measurement of the  $g_{hWW}$  coupling would be difficult. On the other hand, as shown in [157], an Effective Field Theory fit considering only 22 of the 84 possible dimension 6 contributions can be performed. If the fit includes electroweak precision observables and Higgs measurements with  $\mathcal{L} = 2000 \text{ fb}^{-1}$ , then the resulting Higgs coupling precisions have maximally twice the uncertainty of the Higgs coupling fit to H20 data [157]. There would be very good model distinguishing power - see Ref. [157] for more details. The top Yukawa coupling measurement would be forfeit, as would the Higgs self-coupling measurement. This thesis is concentrated on the scenario where  $\sqrt{s} = 500 \text{ GeV}$  data is available, so we will not discuss the scenarios involving Higgs physics if  $\sqrt{s} = 250 \text{ GeV}$  in further detail.

### 3.1.4 Top physics

The top quark plays an important role as the heaviest particle in the Standard Model. It gives the largest contribution to the Higgs mass radiative corrections, which is important from the naturalness of any possible SUSY theory, discussed in more detail in Ch. 7. Also, the top quark causes important corrections to many electroweak precision measurements. If the top mass uncertainty is reduced, then the sensitivity of electroweak precision observables to new physics is increased [158]. Furthermore, the top quark enters the loop corrections of many SUSY particles, enhancing the importance of knowing the top mass precisely. The current direct top quark measurement is  $m_t = 173.1 \pm 0.6 \text{ GeV}$  [1].

The problem with the top mass measurement is that the experiments measure a quantity called the Monte Carlo mass which is the parameter in the simulation which best predicts what the detector measures, see e.g. [162]. This however does not have a clear

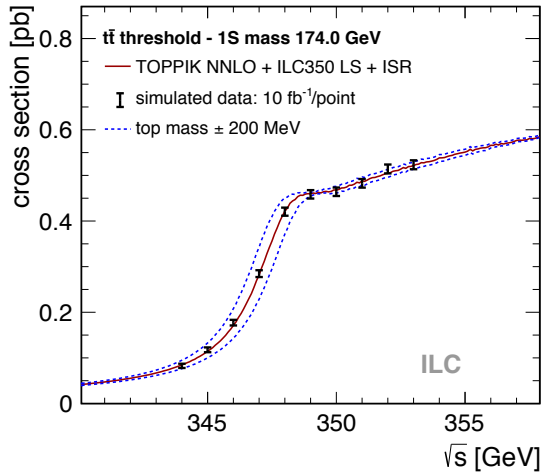


Figure 3.7: Top quark mass scan at ILC. Figure from [155], however the original work for CLIC, or ILC accelerator with CLIC detector in [159].

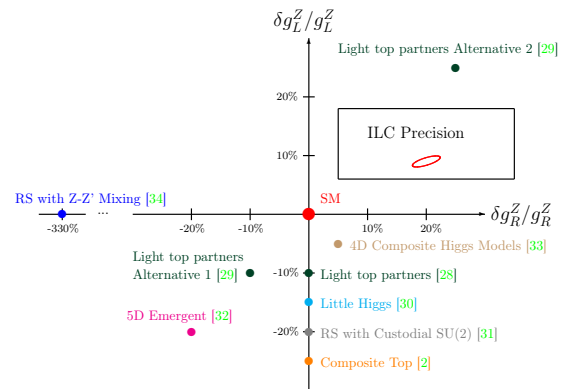


Figure 3.8: Top quark coupling sensitivity at ILC with  $\sqrt{s} = 500$  GeV,  $\mathcal{L} = 250\text{fb}^{-1}$  for  $\mathcal{P} = (\pm 80\%, \mp 30\%)$  [160], who used the original version of this plot in [161].

theoretical definition. The theoretical definition is called the pole or bare mass. A scan of the  $t\bar{t}$  cross section around the production threshold gives a measurement of the so called 1S mass which corresponds to the real part of the pole mass. The 1S mass can be translated into the  $\overline{MS}$  mass for example with a 10 MeV uncertainty [163]. This is in contrast with the LHC where the theoretical uncertainty is about 500 MeV [164]. Statistical uncertainty at the ILC is 17 MeV for the top mass, 26 MeV for the width and 4.2% for the top quark Yukawa coupling with a  $200\text{fb}^{-1}$  scan around the threshold with the polarisation division according to Tab. 3.2 [155, 159, 165].

While the top mass has been measured already, its couplings to the weak vector bosons have not been measured before. These couplings give crucial insights to possible contributions from new physics. As the weak interaction depends on the polarisation of the incoming particles, the polarised beams at the ILC give a unique insight into the left-handed and right-handed couplings of the top to the  $Z$ -boson. The precision on the left-handed top quark coupling to  $Z$  will be 0.6% and right-handed will be 1.0% [160, 161, 166, 167]. This precision allows to uniquely discriminate between many models of Beyond the Standard Model physics, as can be seen from Fig. 3.8 where each dot represents a different type of BSM model [160]. The polarisation of the incoming beams as well as the centre-of-mass energy above the pair production threshold 350 GeV are crucial for the top quark measurements.

### 3.1.5 Beyond the Standard Model measurements

As the ILC will operate without triggers, all events can be recorded. This enables model-independent searches for supersymmetry and other extensions of the Standard Model. The generic features of SUSY searches as well as the search for Weakly Interacting Massive Particles (WIMPs) are summarised below as examples of direct measurements of beyond the Standard Model physics at the ILC.

For a SUSY particle to be detected at the ILC via its visible decay products, the simple requirement is that the particle can be produced from electrons and positrons at the centre-of-mass energy. This has been quantified in [168], where it is argued that in any  $R$ -parity conserving scenario there is an LSP and a next-to-lightest particle (NSLP). The NSLP will be pair-produced, and if it has visible decay products, it will be detected with  $\mathcal{L} = 500 \text{ fb}^{-1}$ ,  $P(+80\%, -30\%)$  at  $\sqrt{s} = 500 \text{ GeV}$ . Only in a small range of the kinematic phase space, in which the NSLP mass is within a few GeV of half of the centre-of-mass energy, the NSLP decay products will not be detected over the background, see Fig. 3.9.

Even in cases with very soft SUSY decay products, e.g. in the case of nearly mass-degenerate higgsinos, it is possible to measure the SUSY masses and cross section times branching ratios to a few percent precision [169]. This higgsino study will be elaborated on in Sec. 7.1.1. Similarly, in the case of a complicated SUSY model where all sleptons, sneutrinos and gauginos are accessible simultaneously like in the stau-coannihilation models it is possible to measure all the masses with permille or percent precisions [170]. Cross sections and some of the mixing properties can be extracted provided that the Standard Model background is sufficiently suppressed [170, 171]. More details of the stau-coannihilation scenario measurement prospects can be found in Sec. 5.1.

In order to determine whether the new particle is indeed a SUSY particle, the coupling and spin have to be measured. The coupling measurement can proceed via a threshold scan where for a spin-1/2 particle the size of the cross section increases as  $\beta = \sqrt{1 - 4(M_{\text{SUSY}}/E_{\text{cms}})^2}$  with respect to the centre-of-mass energy  $E_{\text{cms}}$ , while for a spin-0 particle it increases as  $\beta^3$  [170].

Many more studies on supersymmetry have been performed in addition to the stau coannihilation and higgsino scenarios. Those include studies on gauginos decaying to on-shell gauge bosons [172],  $R$ -parity violating SUSY decays [64] and heavy Higgs production [173]. As all events can be recorded, the discovery potential at the ILC is huge.

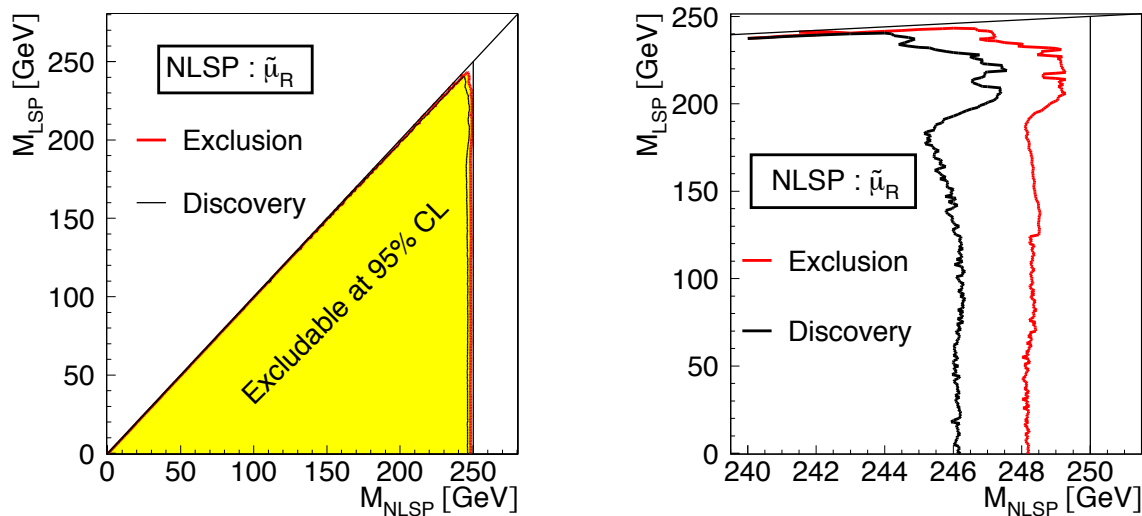


Figure 3.9: Exclusion reach of NLSP w.r.t the LSP with  $\mathcal{L} = 500 \text{ fb}^{-1}$  for  $P(+80\%, -30\%)$  at  $\sqrt{s} = 500 \text{ GeV}$  [169].

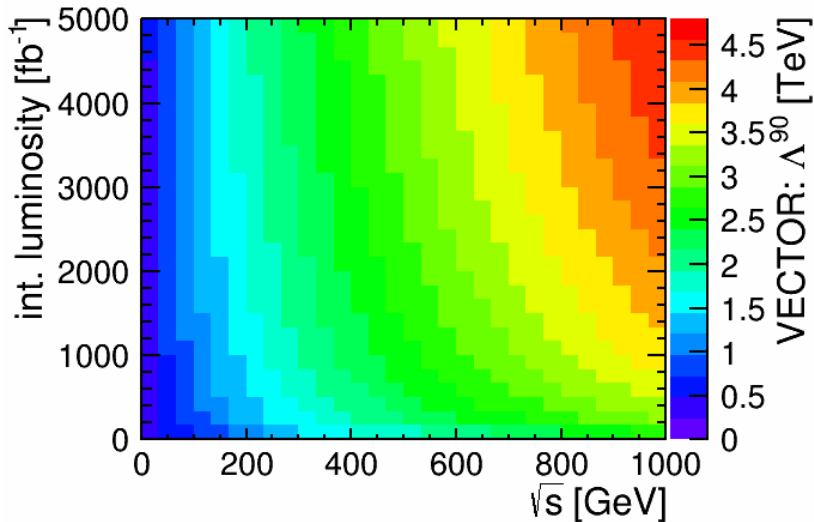


Figure 3.10: The sensitivity for a vector-like mediator decaying into WIMPs for the polarisation sharing as in H20 with  $\sqrt{s} = 500$  GeV [174].

In addition to SUSY particles, other more generic Beyond the Standard Model particles can be detected. This is exemplified by the search for the Weakly Interacting Massive Particles (WIMPs), which themselves are invisible but can be detected by measuring the energy of the initial state radiation photon in the  $e^+e^- \rightarrow \chi\chi\gamma$  process. The discovery or exclusion of the WIMPs can be parameterised in an Effective Field Theory formalism where the mediator is integrated out and the scale is parameterised by  $\Lambda = M_{\text{mediator}}/\sqrt{g_f g_\chi}$  with  $g_{f,\chi}$  the couplings of the mediator to the electron and positron, and the WIMP respectively. For a  $4 \text{ fb}^{-1}$  data set and a vector-type mediator the discovery reach goes up to  $\Lambda \sim 3$  TeV at the  $\sqrt{s} = 500$  GeV ILC [174]. This can be read out from Fig. 3.10, where the sensitivity is plotted as a function of the data set and centre-of-mass energy based on an extrapolation of the analysis in [175].

In the studies for BSM signals, beam polarisation plays a crucial role as it can be used to suppress the Standard Model background. Furthermore, the polarisation combinations are a strong tool for distinguishing between different models. It should be noted that the larger the centre-of-mass energy, the heavier the particles that can be accessed.

### 3.1.6 Electroweak precision measurements

In addition to Higgs, top and possibly BSM measurements, the ILC can make new measurements of electroweak precision observables, such as gauge boson masses, effective leptonic weak mixing angle, strong coupling, triple gauge couplings, and oblique corrections. Their values can be modified by SUSY particles, see e.g. [176]. Electroweak precision observables, thus, constrain the SUSY parameter space. This is beyond the scope of this thesis, and including electroweak precision observables could be an extension of the work presented here.

The setup planned for making these measurements, i.e. the ILC accelerator and the ILD detector are described in the following sections.

## 3.2 International Linear Collider

The International Linear Collider has been designed to gain the ultimate precision on the physics observables described above. The leading criteria are a high centre-of-mass energy, high instantaneous luminosity and beam polarisation. A high centre-of-mass energy is required to allow for kinematic access to top and Higgs processes and possible BSM signatures. To be able to measure these relatively rare processes, a high instantaneous luminosity is required. Additionally, for separating signal processes from backgrounds, and for characterising the chiral properties of the particles, beam polarisation is a useful tool. First the design goals are listed, after which a brief overview of the accelerator components and beam backgrounds is given. This section is based on [151], unless specified otherwise.

### 3.2.1 Design goals

The ILC is designed to break the energy frontier of lepton collisions set by LEP. It is known that top pair production requires  $\sqrt{s} = 350$  GeV, and Higgs self-coupling measurement at least 500 GeV. To fully benefit from threshold scans and maximal cross sections for different processes, the centre-of-mass energy should be tunable.

In order to measure the electroweak processes of the SM and possible BSM physics, a high beam luminosity is required,  $1.8 \times 10^{34} \text{ cm}^{-2}\text{s}^{-1}$ . The instantaneous luminosity is given by

$$\mathcal{L} = \frac{n_b N^2 f_{rep}}{4\pi\sigma_x\sigma_y} H_D, \quad (3.2)$$

where  $n_b$  is the number of bunches,  $N$  is the number of particles per bunch, and  $f_{rep}$  is the pulse repetition rate. The denominator contains the bunch size in the transverse directions,  $\sigma_x$  and  $\sigma_y$  [177].  $H_D$  is an enhancement factor originating from the mutual focussing of the beams at the interaction point, explained in Sec. 3.2.3. It can be seen from the equation, that to maximise the instantaneous luminosity, a high repetition rate and as many particles as possible per bunch are required, while the dimensions of the bunch should be minimised.

Beam polarisation is an essential tool for characterising BSM signals and enhancing the signal or suppressing the background. It is envisaged that an 80% polarisation for the electron beam and a 30% polarisation for the positron beam should be obtainable.

### 3.2.2 Accelerator overview

The beam electrons are produced by a photocathode direct current gun. The material of the photocathode is gallium-arsenite. The produced electrons are inherently polarised with a 90% polarisation but have a low energy of 140 keV and a wide spread in the transverse and longitudinal directions. To maximise the luminosity as explained above, the electrons pass through a damping ring where they emit synchrotron radiation which reduces the beam cross section. Then the electrons traverse a bunch

compressor before being accelerated to full energy in superconducting radio frequency cavities.

When the electrons have reached the full beam energy, they are forced to radiate photons in an undulator. These high-energy photons convert into electron-positron pairs when aimed at a rotating titanium alloy target. These positrons have a polarisation of 30%. Once they are extracted, they also pass through the damping ring and are then accelerated in the main part of the accelerator. The technology for the positron undulator source is believed to be feasible to operate, despite demonstrations lacking for a sufficient cooling mechanism, stable creation of the positron pulse shape and a functioning photon dump. The other type of positron source which could be an alternative, the electron-driven positron source, has not been demonstrated either.

The main part of the accelerator, the superconducting radio frequency cavities, is operated at 2 K temperature and 1.6 GHz frequency. The average accelerating gradient is 31.5 MV/m. These cavities are a large source of expenditure in the total ILC budget. Therefore, significant efforts have been and are being undertaken to improve the production of the cavities, in particular with respect to impurities on the inner surface. There is a new, promising technique whereby the cavity inner surface is doped with nitrogen to reduce impurities [178]. This may allow for production of consistently high gradient cavities, possibly even as high as 45 MV/m gradients [179].

After acceleration, the beams are focussed in the beam delivery system. This last section of the accelerator also contains equipment to measure the beam size, position and energy. Furthermore, it has structures to remove some of the beam-induced background. The beams are brought into collision in the interaction region. At this point, the beam parameters are as listed in Tab. 3.5.

After the collision, the beams are dumped in pressurised water containers which are designed to absorb even the 14 MW of a 500 GeV beam. The main part of the container is made from stainless steel. The front has a titanium window, through which the beam goes into the water. The main challenges of the beam dumps are the shielding of the outside from the radiated water and the integrity of the beam entrance window [151]. As it is expected that the window has a short lifetime, there needs to be systems to replace it periodically and to ensure that any unexpected leaks from the beam dump, which would be highly radioactive, are contained.

### 3.2.3 Beam backgrounds

Despite the old adage that a lepton collider does not suffer from beam backgrounds in the same way as a hadron collider does, there are a few backgrounds at the ILC which need to be considered. The main sources and their effects are listed in Tab. 3.6.

A difficult background source is beamstrahlung photons, which can have any energy and angle with respect to the beam. These photons are caused by the pinch effect of the beams on each other; the beam electron trajectories bend in the electromagnetic field of the other beam causing photon radiation as in Fig. 3.11.

Further background sources are radiative Bhabha scattering events, which are mostly not detected as the outgoing particles tend to point in the direction of the beam pipes.

Quantity	Symbol	Unit	Value		
Centre of mass energy	$\sqrt{s}$	GeV	250	350	500
Luminosity pulse repetition rate		Hz	5	5	5
Bunch population	$N$	$\times 10^{10}$	2	2	2
Number of bunches	$n_b$		1312	1312	1312
Linac bunch interval	$\Delta t_b$	ns	554	554	554
RMS bunch length	$\sigma_z$	$\mu m$	300	300	300
RMS horizontal bunch size at IP	$\epsilon_x$	nm	729	684	474
RMS vertical bunch at IP	$\epsilon_y$	nm	7.7	5.9	5.9
Fractional RMS energy loss via beamstrahlung	$\delta_{BS}$	%	0.97	1.9	4.5
Luminosity	$L$	$\times 10^{34} \text{ cm}^{-2}\text{s}^{-1}$	0.75	1.0	1.8
Fraction of luminosity in top 1% of $\sqrt{s}$	$L_{0.01}$	%	87	77	58

Table 3.5: ILC baseline parameters in the Technical Design Report [151].

A background that is harder to remove is the  $\gamma\gamma \rightarrow$  hadrons or muons background (depicted in Fig. 3.12), which is caused by the photons from the various sources interacting with each other to produce hadrons or muons. There are some methods to remove these from signal events via a jet-clustering algorithm [180]. However, it is currently under study how to mitigate low- $p_T$  events from getting absorbed in for example  $\tilde{\chi}_1^\pm \rightarrow \tilde{\chi}_1^0 q\bar{q}'$  events [181].

Source	# particles per bunch	mean E [GeV]
Disrupted primary beam	$2 \times 10^{10}$	244
Beamstrahlung photons	$2.5 \times 10^{10}$	
$e^+e^-$ pairs from beam-beam interactions	$7.5 \times 10^4$	2.5
Radiative Bhabhas	$3.2 \times 10^6$	195
$\gamma\gamma \rightarrow$ hadrons (muons)	0.5(1.3) events	—

Table 3.6: ILC beam backgrounds [182].

### 3.2.4 Polarimeters

Beam polarisation is a great tool for characterising BSM physics signals. To interpret the data correctly, it is important to know the beam polarisation accurately. There will be a real-time measurement of the polarisation both before and after the beam collision. The beam polarisation will be flipped every one or few bunch trains in order to reduce systematic uncertainties via cancellation [152].

The target precision for the luminosity-weighted polarisation is  $10^{-3}$ . This can be

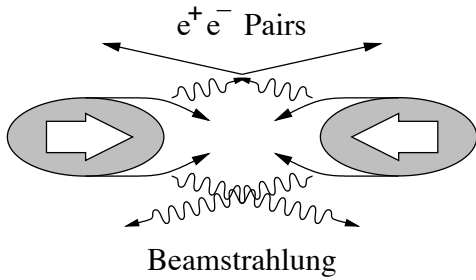


Figure 3.11: Illustration of the beamstrahlung effect in ILC bunches [183].

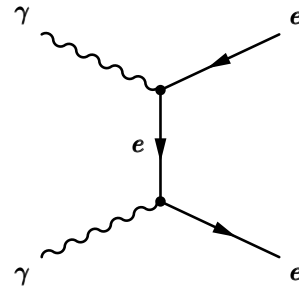


Figure 3.12: An example of a  $\gamma\gamma$  background process.

reached with Compton polarimeters: photons interact with the beam electrons and the outgoing electron energy depends on the product of the longitudinal polarisation of the electron and the circular polarisation of the photon. This dependence can be seen from Fig. 3.13 [184]. The measurement of the electron polarisation is based on measuring the asymmetry in the Compton cross sections for opposite sign laser polarisations. This dependence is shown in the same figure.

Practically the measurement is done by shining a circularly polarised laser beam on the electron beam. The energy of the scattered electrons is measured via a Cherenkov detector. The laser polarisation is flipped on a pulse-by-pulse basis enabling a measurement of the Compton cross section asymmetry. The two polarimeters serve different purposes: The upstream polarimeter gives information on the change of polarisation during a bunch train and the downstream polarimeter gives information on the polarisation loss from the beam-beam interaction [185].

In order to find out what the polarisation is at the interaction point, the information from the two polarimeters has to be interpolated taking into account spin transport effects. This can be done theoretically. A cross-check on the result is provided by making an independent measurement of the beam polarisations from collision data. A long-term average of the polarisation can be obtained from measurements of the cross sections of e.g.  $W$ -pair production in the total cross section or differential cross section form [186, 187].

A measurement with precision 0.1% for the luminosity-weighted average polarisation is the achievable target, see e.g. [186, 188], however a better value would bring benefits. The benefits of the polarised beams are summarised in [77] and in [148].

### 3.2.5 Location and cost

In the TDR phase, many locations were considered. At the time of writing there is only one candidate site, which is in Japan in a mountainous region in the north of the main island Honshu. The site is called Kitakami in the region of Iwate [189]. The Japanese ministry for Education, Culture, Sports, Science and Technology, MEXT, is reviewing the Technical Design Report and aiming to reach a decision whether Japan will propose to host the ILC.

The special challenges of the mountainous and earthquake susceptible area in Japan

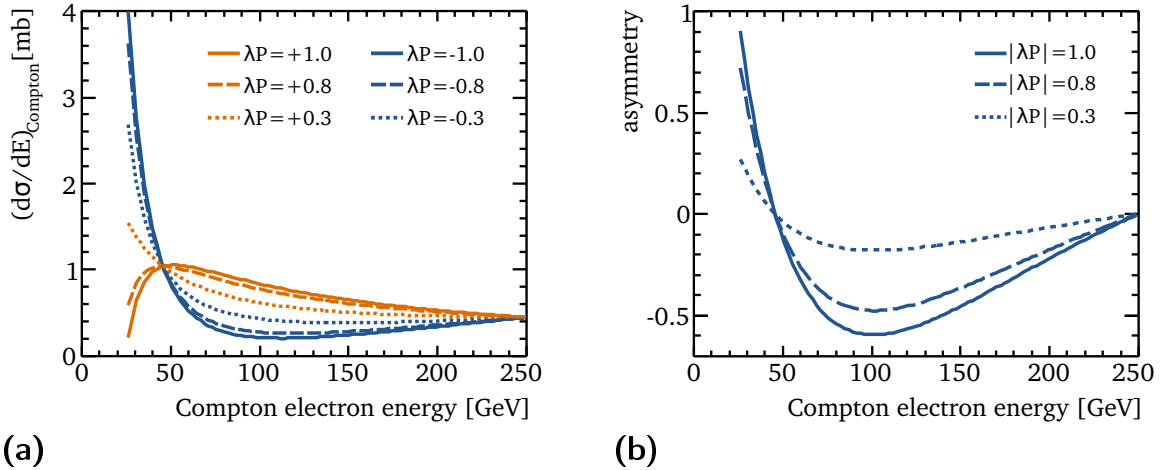


Figure 3.13: a) The energy spectrum of the Compton electrons for different products of the electron and photon polarisations. b) The difference in the sizes of the cross sections for opposite sign laser polarisations vs. energy depends on the electron polarisation. Figures from Ref. [184].

are access to the accelerating tunnel and the stability of the alignment. The access is planned to happen via vertical tunnels, and all of the equipment will be stored underground. As far as detector alignment is concerned, the rock in the proposal site Kitakami is solid granite, and the accelerator and detectors will be equipped with advanced laser or other alignment technologies [143].

The total cost of the ILC in the TDR design is about 7.8 billion ILCU (2012 value of USD) [143]. The largest costs come from the cryomodules and the conventional facilities including buildings and tunnels, adding up to 73% of the total.

### 3.2.6 Political situation

Since the Linear Collider Workshop in Morioka in December 2016, there has been a significant change of plans with respect to the TDR times. It is now proposed that initially, funding is sought for a 250 GeV accelerator instead of a 500 GeV accelerator. This is motivated by requests from the Japanese ministry to reduce the project budget. Currently it is understood that the final integrated luminosities gathered will be the same as previously planned:  $2 \text{ ab}^{-1}$  at  $\sqrt{s} = 250 \text{ GeV}$  and  $4 \text{ ab}^{-1}$  at  $\sqrt{s} = 500 \text{ GeV}$  and  $200 \text{ fb}^{-1}$  at  $\sqrt{s} = 350 \text{ GeV}$ . The total project timeline would be extended from 20 years to 22 years if the instantaneous luminosity can be increased [153]. The new operating timeline would be as is shown in Fig. 3.3.

The physics case for the  $\sqrt{s} = 250 \text{ GeV}$  ILC is impressive as is discussed in [157] and [153]. Nevertheless, it is less appealing than the case for a  $\sqrt{s} = 500 \text{ GeV}$  accelerator. It is clear that crucial measurements of the Higgs self-coupling and top mass and Yukawa coupling will not be possible at this lower centre-of-mass energy. Additionally, the international appeal of the ILC project will be reduced, as there are other options for an electron-positron collider with less than 500 GeV centre-of-mass energy. There is the proposal for a 100 km circumference tunnel at CERN which could be used to host

an electron-positron Future Circular Collider (FCC-ee) [190–193]. Other competitors exist too, the Circular Electron Positron Collider (CEPC) with 250 GeV centre-of-mass [194, 195] and Compact Linear Collider (CLIC) with a proposed 380 GeV initial stage [196, 197]. Out of these options, only CLIC has the potential for an energy upgrade in the future. CERN is due to evaluate the proposals for CLIC and FCC based on the European Strategy for Particle Physics update in 2018/2019. It is expected that the Japanese government will make a statement about the future of the ILC before the European Strategy update.

### 3.3 International Large Detector

To enable the high-precision measurements described above, the detector has to be suitably designed. One of the two proposed ILC detectors, the International Large Detector (ILD), is discussed in more detail here, first outlining the design principles and then summarising the current design choices. This section is based on Ref. [182]

#### 3.3.1 Particle flow

The ILD has been designed with the aim of particle flow reconstruction [198, 199]. The basic principle is that each particle is measured in the detector component which has the best resolution for that type of particle. For charged particles the best component is the tracker while for neutral particles the calorimeter is used. On average, 65% of jet energy comes from charged particles, and the achievable resolution of the tracker is higher than of the calorimeter. Thus the overall jet energy resolution via particle flow is much better than from calorimeters alone. On the other hand, for a successful measurement of the energy of the neutral particles, the energy from the charged particles in the calorimeters has to be removed, for which a high granularity calorimeter is required. The aim is to resolve each particle individually. The separation of the neutral and charged clusters is limited by confusion at high jet energies. Confusion means that parts of neutral calorimeter showers can be combined with charged showers and thus the energy measured is lower than should be as the neutral clusters are replaced with the charged track measurement. Additionally, parts of charged calorimeter clusters can be assigned to be neutral, meaning that there is additional energy since those clusters are counted twice. At low energies, the limiting factor is the natural resolution of the calorimeter. For an overall correct measurement of the energy in the calorimeter, the jet energy should not be lowered by the material in the tracker and, therefore, the tracker has to contain as little material as possible.

#### 3.3.2 Design goals

Benchmark values have been set in the ILC Technical Design Report for the properties of the detector components. For the separation of the hadronic decays of the  $W$ - and  $Z$ -bosons, a jet energy resolution of the order of the natural width of the bosons is desired,  $\sigma_E/E \sim 3 - 4\%$ . For the tracking system, the Higgs recoil mass measurement

$e^+e^- \rightarrow hZ \rightarrow h\mu^+\mu^-$  has motivated the tracking resolution requirement of  $\sigma_{1/p_T} = 2 \times 10^{-5} \text{ GeV}^{-1} \oplus \frac{1 \times 10^{-3}}{p_T \sin \theta}$ . The tracking requirement is of utmost importance also for measuring the charged decay products of SUSY particles, whose energy and momentum are directly related to the mass of the SUSY particle. The imposed requirement ensures that any mass measurement is limited by the knowledge of the beam spectrum rather than the track resolution. Further requirements are set by the need to detect vertices which are not consistent with the interaction point of the beams, which can be caused by the decays of heavy quarks or of SUSY particles with a detectable lifetime, for example. For this purpose, an impact parameter resolution goal has been set as per Tab. 3.7, in which all the aforementioned goals are listed. A hermetic detector is crucial for BSM measurements.

Component	Parameter	Goal
Jet energy resolution	$\sigma_E/E$	3 – 4%
Track resolution	$\sigma_{1/p_T}$	$2 \times 10^{-5} \text{ GeV}^{-1} \oplus \frac{1 \times 10^{-3}}{p_T \sin \theta}$
Impact parameter resolution	$\sigma_{r\phi}$	$5 \mu\text{m} \oplus \frac{10}{p(\text{GeV}) \sin^{2/3} \theta} \mu\text{m}$

Table 3.7: ILD design goals [182].

### 3.3.3 Detector overview

In a quick summary, the ILD has an onion like structure as shown in Fig. 3.14. From the interaction point outwards, the particles go through the following set of detector: the vertex detector, time projection chamber (TPC), electromagnetic calorimeter (ECAL), hadronic calorimeter (HCAL), coil and an iron yoke/muon detector. Each of these serves a specific purpose.

The vertex detector provides flavour tagging via measuring displaced vertices. The aim is to have as good a point resolution as possible, below  $3 \mu\text{m}$  and very small material budget, below 0.15% radiation length per layer. The vertex detector is a multi-layer pixel vertex detector. Its first layer is located at radius 1.6 cm and it does not have endcaps.

The time projection chamber (TPC) is made out of gas, a field cage and an anode and a cathode. It has a very small material budget. The TPC provides continuous tracking and gives measurements for below 7 degrees polar angle from the beam direction. It has up to 224 points per track allowing for particle identification based on the energy loss in the tracker. The working principle is that charged particles ionise the TPC gas which is proposed to consist mostly of argon. These ions are collected at the endplates of the TPC by applying an electric field between the TPC endplates. The collected ions go through a Gas Electron Multiplier which is a thin foil with an electric field and holes in it. As the ions go through, the signal multiplies. The signal is then read out. The tracker system is augmented by silicon trackers on the inside and outside of the TPC, and tracking discs to increase the angular coverage down to 5 degrees.

The electromagnetic calorimeter measures the electromagnetic decay products i.e. electrons and photons. The ECAL needs to be able to separate photons from nearby particles and reconstruct the shower shape, as discussed above. There are two technology options for the active material: silicon pad diodes and scintillating strips with silicon photo-sensor readout. The pixel size will be  $5 \times 5 \text{ mm}^2$ , in order to optimise between cost and jet energy resolution. The ECAL barrel is highly granular, with up to 30 layers. It has a cylindrical shape and uses tungsten as the absorber material. There is a forward part of the ECAL as well.

Similarly the HCAL is very granular with 48 layers of scintillating  $3 \times 3 \text{ cm}^2$  tiles with analog readout, or with gas based  $1 \times 1 \text{ cm}^2$  tiles with digital or semi-digital readout. There are two technology options: scintillator tiles with silicon photo-sensors and analog readout, and gas resistive plate chambers (RPCs) with semi-digital readout (2 bits).

The luminosity monitor (LumiCAL), beamstrahlung monitor (BeamCAL) and neutral hadron calorimeter (LHCAL) enable the detection of particles in a solid angle  $4\pi$ , as many BSM physics processes cause signals at low angles. Additionally these components are used for the measurements of the luminosity and beam quality.

The outermost part is the iron yoke which shields the outside of the detector from the magnetic field. It is instrumented with the tail-catcher/muon tracker in order to measure any high-energetic hadrons which were not fully contained in the calorimeter system. It is not possible to build the calorimeter system large enough to contain all showers and yet have a strong but affordable magnet outside it. Another reason for including this detector component is that while muons leave tracks in the tracking system, the muon tracker helps to identify the muons from other particles [200]. The yoke is instrumented with 14 layers in the barrel and 12 layers in the endcap. The sensitive layers will either be scintillator strips or resistive plate chambers.

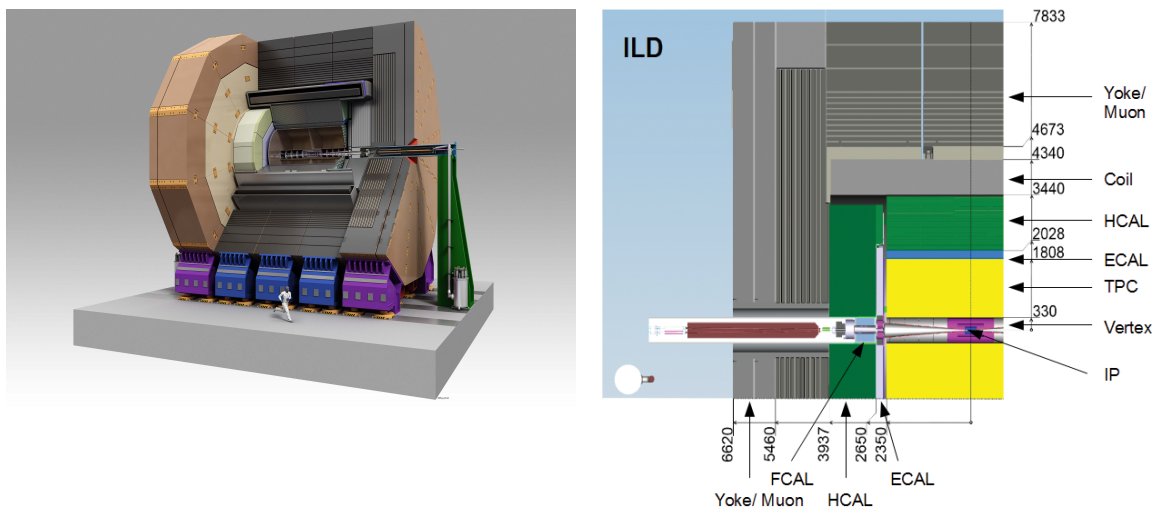


Figure 3.14: Sketches of the ILD detector from Ref. [143].

The detector has triggerless operation to the huge advantage for precision measurements and BSM reach. This is possible due to the low beam backgrounds.

The ILD will cost between 250 and 440 Million ILCU (2012 value USD) excluding

labour, with the most expensive parts being the yoke and the calorimeter system roughly 25% and 40% of the total budget cost respectively [143].

# Chapter 4

## Fitting algorithms for determining SUSY parameters

The computational tools used in this thesis for the SUSY parameter determination are described below. The main tool, `Fittino` [201], was developed to scan the large space of SUSY parameters in order to find the point which best matches some real or hypothetical set of experimental measurements. The sampling method has to be efficient to scan pMSSM-13 and has to provide a rigorous statistical interpretation of the fit results. The reason why the parameters cannot be found analytically is that only some of the tree-level relations between the parameters and the observables can be inverted. As soon as loop-level contributions are included, a computational approach is needed while gaining the additional constraints induced by loop processes. These loop processes are calculated by external codes which were written for some specific calculation types. Thus, the process of finding SUSY parameters from SUSY observables relies on two important choices: what fitting algorithm is used and what calculators are employed for calculating the predicted observables. A description of the fitting tool and the calculators follows.

### 4.1 Parameter fitting with `Fittino`

`Fittino` is a scanning algorithm designed for SUSY parameter fitting written in C++ [201]. `Fittino` scans the SUSY parameter space, in fact any version from CMSSM, NUHM1, NUHM2 or pMSSM-19 spaces or their subspaces, using a Markov Chain Monte Carlo (MCMC) method to pick the scanned points [202]. It is an efficient method as it converges fast towards the true parameter point, not wasting time to scan parameter space far away from the minimum. The overall idea is to find what parameters give the observables that best fit the experimentally measured inputs. The aim of the MCMC algorithm is to minimise a chi-squared value between the observables in the parameter point with respect to the measured observables and their uncertainties. A point in the MCMC is accepted or rejected with a certain probability calculated from this chi-squared value, and so the program scans the parameter space more accurately near the true parameter point than further away from it. After the fit, confidence intervals for the parameters and predicted observables can be extracted.

The experimental inputs to `Fittino` are the observables from the ILC and possibly from other experiments, as defined by the user. The observables may include SUSY and SM masses, kinematic edge positions, simple mass limits, cross sections, branching fractions, sums of branching fractions, and cross sections times branching fractions. For all of these, uncertainties need to be defined for the calculation of the chi-squared value. It is possible to consider flavour observables, limits from LEP and LHC for SUSY searches and Higgs measurements as well.

The user defines which model type and which parameters in that model are fitted. The choice of model includes among others CMSSM, NUHM1, NUHM2 and pMSSM, and any combination of parameters within those models can be fitted. Some parameters can be fixed. For the fixed parameters one has to set the values. For the fitted parameters, starting values have to be set if the model is a GUT model. For pMSSM, starting values can be set or these can be calculated from a set of input observables and uncertainties described in Appendix A.

To summarise, the user is required to define the model type, fitted and fixed parameters, and observables. The Markov Chain is then initialised by a random generator seed or by hand with the flag `RandomGeneratorSeed` in the input file. The fits in this thesis are initialised by the random seed which is generated from a sum of the system uptime, free swap space, PID of the `Fittino` process and system time. The random generator using the seed is the strong `TRandom3` generator in `ROOT` [201, 203].

There are many other possible flags in the initialisation of the fits. For these, we refer the reader to the `Fittino` manual [201] and the example input file in Appendix B.

The logic for the parameter fitting is sketched out in Fig. 4.1 as described in detail in Ref. [202]. `Fittino` uses Markov Chain Monte Carlo to sample the SUSY parameter space to find the point which best matches the observables. Mathematically the aim is to minimise the chi-squared between observations and theory predictions for the observables,

$$\chi^2 = (\mathbf{M} - \mathbf{O}(\mathbf{P}))^T cov_M^{-1} (\mathbf{M} - \mathbf{O}(\mathbf{P})) + \text{penalties for exceeding limits.} \quad (4.1)$$

Here  $\mathbf{M}$  is a vector of the measurements (observables),  $\mathbf{O}(\mathbf{P})$  is a vector of the SUSY observables given a point  $\mathbf{P}$  in parameter space [202]. Observables  $\mathbf{O}(\mathbf{P})$  are calculated with various external codes as explained shortly. The uncertainties and correlations are included in the covariance matrix  $cov$ . If correlations between the observables are neglected, as is the case in this thesis, the chi-squared is simplified to

$$\chi^2 = \sum_i \left( \frac{\mathbf{M}_i - \mathbf{O}(\mathbf{P})_i}{\sigma_{\mathbf{M}_i}} \right)^2 + \text{penalties for exceeding limits.} \quad (4.2)$$

where  $\sigma_{\mathbf{M}_i}$  stands for the uncertainty on the measurement  $\mathbf{M}_i$  [202]. If upper or lower limits on particle masses are included, then if those limits are exceeded, an additional component is added to the overall chi-squared. The component is proportional to the size of the deviation from the limit, scaled by a factor inversely proportional to the uncertainty on that limit [202]. These limits are not used in this thesis but could be used in a simplistic way to include LEP or LHC limits.

This chi-squared value determines which parameter point  $\mathbf{P}$  is sampled next. The logic applied in `Fittino` for this is the Metropolis algorithm [204]. The first point  $x_i$ ,

$i = 1$ , in the Markov Chain, corresponding to the first parameter point  $\mathbf{P}_i$ , is picked from a Gaussian distribution for each of the input SUSY parameters with the given uncertainties if the flag `UseGivenStartValues` is on. Then a chi-squared value of this point  $\chi_i^2$  is calculated. The first point is always accepted into the Markov Chain.

The next point  $\mathbf{P}_{i+1}$  is picked from Gaussian probability density functions for each parameter. The proposal distribution has the variance as determined by the uncertainty of the parameter in the input file. If adaptive widths are switched on with the flag `UpdateWidths`, then the variance is updated every 1000 accepted points. The variance is simply the variance of the parameter in all the 1000 points, scaled by some arbitrary factor, in this thesis one half.

For the proposed point  $x_{i+1}$  a likelihood is calculated by

$$\mathcal{L}_{i+1} = \exp\left(-\frac{\chi_{i+1}^2}{2}\right). \quad (4.3)$$

If  $\mathcal{L}_{i+1} > \mathcal{L}_i$  then the point is accepted and the next parameter point is picked. If  $\mathcal{L}_{i+1} < \mathcal{L}_i$  then the point is accepted with the probability  $\mathcal{L}_{i+1}/\mathcal{L}_i$ . If the point  $x_{i+1}$  is rejected, then  $x_i$  is added to the Markov Chain again. A new point is picked based on the last accepted point and the process repeats until the desired length of the Markov Chain is obtained.

The parameters in the Markov Chain are limited to a certain range to ensure all calculated points are still within the soft SUSY breaking range. The parameters are in most cases limited to  $[0, 10000]$  GeV. The ranges for each parameter can be read out from Tab. 4.1 for the MSSM, Tab. 4.2 for CMSSM, NUHM1 and NUHM2.

parameter	range
$Q_{EWSB}$	[91.2, 10000]
$M_1$	[0, 10000]
$M_2$	[0, 10000]
$M_3$	[0, 10000]
$\tan\beta$	[0, 1000]
$\mu$	[0, 10000]
$m_{sfermions}$	[0, 10000]
$A_{t,b,\tau}$	[-10000, 10000]

Table 4.1: Allowed `Fittino` probing ranges in GeV, except  $\tan\beta$  unitless, of the parameters in the MSSM.

For the calculation of the theoretical observables  $\mathbf{O}(\mathbf{P})_i$  in Eq. 4.2, `Fittino` calls other programs via SUSY Les Houches Accord (SLHA) interface files [205]. These are programs created specifically for calculating the SUSY particle spectrum and cross sections, Higgs mass and couplings, dark matter relic density, dark matter cross sections,

parameter	range CMSSM	range NUHM1	range NUHM2
$Q_{EWSB}$	[91.2, 10000]	[91.2, 10000]	[91.2, 10000]
$M_0$	[0, 10000]	[0, 10000]	[0, 10000]
$M_{1/2}$	[0, 10000]	[0, 10000]	[0, 10000]
$A_0$	[-100000, 100000]	[-100000, 100000]	[-100000, 100000]
$\tan\beta$	[0, 100]	[0, 100]	[0, 100]
$M_H^0$	–	$[-1 \times 10^7, 1 \times 10^7]$	–
$m_A$	–	–	$[-1 \times 10^7, 1 \times 10^7]$
$\mu$	–	–	[0, 100000]

Table 4.2: Allowed `Fittino` probing ranges in GeV, except  $\tan\beta$  unitless, of the parameters in the CMSSM, NUHM1 and NUHM2 models.

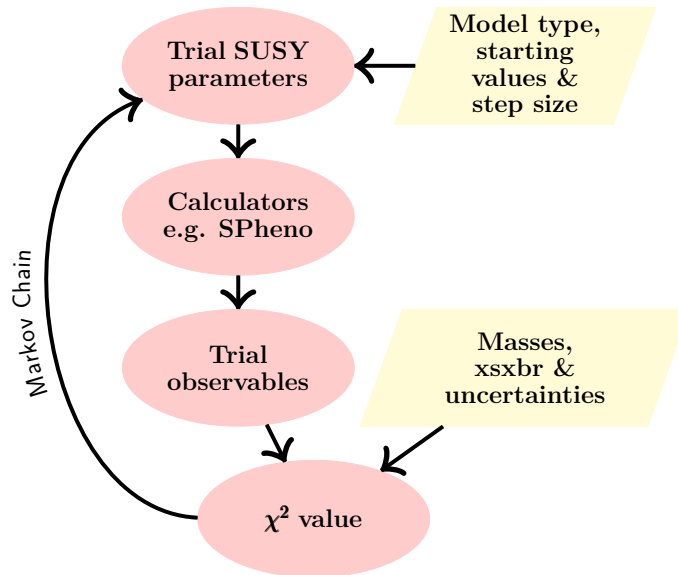


Figure 4.1: Schematic of `Fittino`

flavour observables etc. The calculation accuracy of the programs should be of the same order or better than the input observables from the ILC, else the ILC precisions are not exploited maximally.

We have used `SPheno3.3.9beta` or `SPheno3.3.9beta3` [206] for the SUSY and SM masses, cross sections and branching ratios, except for the Higgs sector masses and branching ratios, for which we use `FeynHiggs2.10.4` [207]. The dark matter relic density is calculated with `MicrOMEGAs`, and the spin-independent WIMP-nucleon interaction cross section and the thermally averaged WIMP annihilation cross section is calculated with `Astrofit` [208] which internally calls `DarkSUSY` [114]. These are some of the best calculation tools at the moment. Nevertheless, in the case of real discoveries of SUSY their precisions would be improved by focussing the phenomenology efforts on higher-order corrections relevant for the observations.

It would be possible to constrain SUSY parameters via the inclusion of low-energy measurements. This could be done with `superISO` [209], however the interface between `Fittino` and `superISO` has to be updated. Additionally, work is going on to include current LHC analysis interpreted in non-simplified models via `Smodels` [210]. Also, current LHC measurements of the Higgs sector could be implemented with the `HiggsBounds` software [211]. None of these are used in this thesis as the interfaces have not been available, and computing time would be increased significantly if these were used.

There are prospects for improving `Fittino`. The authors are implementing second-order MCMC, meaning that not only the latest chi-squared value is used to decide on the next parameter point, but that two latest values are used [212]. Additionally, LHC exclusion limits could be interpreted faster via neural networks [212].

The calculators used are described below.

## 4.2 SPheno

`SPheno` is a program which calculates the supersymmetric particle spectrum [206,213]. The code is in `Fortran95`. `SPheno` takes the SUSY model type and SUSY and SM parameter values as input. It outputs the SUSY masses, mixing matrices and branching ratios, Higgs mass and branching ratios, running couplings, and on request polarised  $e^+e^-$  cross sections and some flavour observables. The masses are calculated to one-loop order except partially to two-loop order for the neutral Higgs masses. The program also calculates the renormalisation group running of supersymmetric parameters. `Fittino` calls `SPheno` via the Les Houches SUSY format [205]. `SPheno` is implemented for many different SUSY models, including those used in this thesis, i.e. NUHM2 with weak scale Higgs inputs, mirage mediation with weak scale Higgs input, pMSSM, CMSSM and NUHM1 among others.

The workings of the program are as follows. Standard Model parameters (quark masses etc.) and the SUSY model and parameters are input. First, tree-level values for gauge and Yukawa couplings are calculated. Then two-loop RGEs are used to run these to the GUT scale, where boundary conditions for the SUSY parameters are imposed, assuming a high-scale model is being considered. Then the parameters are evolved to

the electroweak scale where then the SUSY particle and Higgs masses are calculated in the first step with tree-level values, with the exception of the neutral  $CP$ -even Higgs for which third generation quark and squark loop contributions are taken into account. After the tree-level calculation, all radiative corrections are applied to the gauge and Yukawa couplings. The running up, imposing boundary conditions, running down and calculating the SUSY particle and Higgs masses is repeated until the final mass value does not change much between iterations. If at any point in the iteration the sparticle pole masses are found to be negative squared, then the program terminates. If not, after the iteration stabilises, particle decay widths, branching ratios, cross sections and low energy observables are calculated in that order. In the whole of this procedure, great care has been taken in using and switching between the appropriate renormalisation schemes  $\overline{DR}$  and  $\overline{MS}$  [206].

The assumption in the **SPheno** algorithm is that the SUSY mass scale is close to the electroweak scale. In many interesting models nowadays, due to the LHC exclusion limits, the SUSY mass scale is heavier than the electroweak scale. Therefore, new techniques have been developed to ensure consistency of the running between the electroweak scale and the SUSY scale, namely that this part of the RGE is purely from the Standard Model. An explanation of the new **SPheno4.0.0** version with "two scale matching" is in [214]. This method became available less than a year ago (May 2017) and thus is not used in this thesis. Another reason is that negative mass squared values appear if this scheme is used for the stau coannihilation benchmark in Ch. 5 and 6. The differences between these two methods can cause up to 0.5-1 GeV difference in the Higgs mass [214].

Different **SPheno** versions were used in this thesis: **SPheno3.3.9beta3** for the stau coannihilation and **SPheno3.3.9beta** for the higgsino study.

Comparing the mass spectra from **SPheno3.3.9beta** and **Isasugra** [215] for the ILC1 benchmark (introduced later in the thesis) with light higgsinos around 100 GeV shows differences of 3-5 GeV for the LSP and  $\tilde{\chi}_2^0$  masses.  $\tilde{\chi}_1^\pm$  masses on the other hand agree within 14 MeV. These calculator differences are much larger than the expected ILC measurement uncertainties. Therefore the results of the fit will depend strongly on the chosen calculator and have to be interpreted bearing this in mind. It can be reasonably assumed that the phenomenological calculations will be made more accurate with time and especially after any SUSY discoveries.

For the purposes of this thesis, **SPheno** is used to generate the particle spectrum of the model point and those masses are assumed to be the measured central values from the ILC. This allows a proper study on the accuracy of the fit, even if some of the detector simulations leading to the input uncertainties were made on **Isajet** spectra.

### 4.3 FeynHiggs

**FeynHiggs** is a specialist **Fortran** code to calculate the Higgs sector masses and decays in supersymmetric models [207]. **FeynHiggs** having two-loop calculation with additional resummation of possibly large logarithms from scalar tops, is claimed, e.g. in [216], to give the most precise calculation of the Higgs sector masses.

`FeynHiggs`, when called from `Fittino`, reads in the SUSY particle masses from the Les Houches file from `SPheno`. `FeynHiggs` uses these masses to calculate the Higgs sector masses and branching fractions. `FeynHiggs` itself does contain a full spectrum calculator which works on parameter input only but it is not deemed as accurate as `SPheno`.

The Higgs observables are also strongly dependent on the calculator. `FeynHiggs2.10.4` disagrees with `SPheno3.3.9beta3` on the light higgs mass in the STC10' benchmark (introduced later) by 2.2 GeV. Therefore, all the fit results should be interpreted within that specific Higgs calculator until the calculators agree with a precision of the order of the ILC permille-level SUSY measurements. More details about the Higgs calculator precisions can be found in e.g. [214].

## 4.4 MicrOMEGAs

`MicrOMEGAs2.4.5` [217] calculates the dark matter relic density  $\Omega h^2$  and other cosmological observables from SUSY parameters or from the physical SUSY spectrum. `Fittino` gives the `SPheno` spectrum to `MicrOMEGAs`. Only the dark matter relic density is used or saved by `Fittino`.

`MicrOMEGAs` assumes the standard  $\Lambda$ -CDM model for the evolution of the universe. The relic density is calculated by solving the evolution equation for the relic abundance as described in Ch. 2.7. The evolution equation depends on the thermally-averaged dark matter annihilation and coannihilation cross sections, which `MicrOMEGAs` calculates at tree-level. Then numerical integration is required to find the present day relic density. `MicrOMEGAs` gives a value for the relative contributions of each of the annihilation and coannihilation channels.

Similarly to the theoretical uncertainties in the SUSY spectrum and Higgs calculators, dark matter calculators come with uncertainties too. There are inherent uncertainties from the methods or assumptions of calculating the relic density. More crucially, the SUSY spectrum uncertainties are carried over to the relic density calculator, possibly multiplying a 1% uncertainty on the masses to a 10% uncertainty on the relic density [218]. Different relic density calculators give different values, e.g. `MicrOMEGAs2.4.5` disagrees with `DarkSUSY` [114] by 4% on the relic density in the stau coannihilation benchmark STC10'.

Current relic density codes, including `MicrOMEGAs` have the same shortcoming which is relevant for the study in this thesis: the cross sections are calculated at leading order only. However, they can receive large loop corrections from SUSY particles. Some discussion of these is in e.g. [219–221] with the worst case correction around 15% for  $\tilde{\chi}_1^0 \tilde{\chi}_1^0 \rightarrow W^+ W^-$  if the LSP is wino [221] and unaccounted for QCD corrections about 20% [220]. Coannihilation channels have their own contributions, and e.g. in chargino coannihilation one can have 15% SUSY-QCD corrections [222]. In stau coannihilation processes, which are discussed in Ch. 5 and Ch. 6, the loop corrections can change the cross section by  $\sim 10\%$  [223].

There is a public code `DM@NLO` [224], which it is an extension of `MicrOMEGAs` to include leading-order loop corrections to the dark matter relic density. This program currently

contains only squark coannihilation cross sections and thus is not relevant for the stau coannihilation scenario. There exists a private code `SLOOPS` [221] which also performs SUSY loop cross section calculations, which can be used for dark matter calculations.

The predicted relic density can depend on the renormalisation scheme [218]. The loop contributions and any uncertainties from renormalisation group evolution are ignored in the following.

## 4.5 `Astrofit` and `DarkSUSY`

`Astrofit` is used in this thesis to calculate the WIMP-nucleon scattering cross section and the thermally-averaged WIMP annihilation cross section into photons (discussed in Ch. 2). These are not used to constrain the `Fittino` fit but simply to compare the predictions from the fit to current and future indirect and direct WIMP detection experiments. In fact, `Astrofit` uses functions from the `DarkSUSY5.0.5` code [114] to perform these calculations. `Astrofit` communicates with `Fittino` via Les Houches files.

The direct detection cross sections i.e. the WIMP-nucleon scattering cross sections depend on the coupling of the WIMP to the nucleus, the reduced neutralino-nucleus mass and the number of protons and neutrons in the nucleus [114] for the spin-independent scattering cross section which dominates over the spin-dependent scattering cross sections in heavy element dark matter experiments.

The indirect detection aims to detect WIMP annihilation via e.g. enhanced neutrino fluxes from the Sun or unusual spectra of gamma rays or positron rays from the Galactic halo [114]. The standard measure to compare indirect detection experiments is the thermally averaged WIMP annihilation cross section, familiar from the relic density calculation.

If desired, `Astrofit` could be used to constrain the `Fittino` fit, as `Astrofit` has the capacity to store experimental bounds from direct and indirect dark matter detection experiments. In this thesis what is done instead is simply to check the direct and indirect detection bounds before commencing with the fits. These detection bounds are not used to constrain the fit to study simply what is the significance of the ILC in constraining the dark matter observables.

## 4.6 Tools to analyse the chi-squared distributions

The first step in analysing the `Fittino` fit results is to check whether the fit has converged. This means that the results should not change if the Markov Chain is extended or started from a different point. Some methods to check both have been discussed in [202]. For the convergence test, the paper suggests performing two scans with different start values within  $2\sigma$  of the previously estimated fit minimum. The fit is accepted if the differences in the two-dimensional confidence areas of the two fits agree up to binning the  $2\sigma$  confidence interval into 25 bins.

In this thesis the starting values are picked assuming that tree-level analysis would bring the starting values close to the true model point. The technique is summarised in [201] for an SPS1a-type scenario and for a light higgsino scenario in [169]. The starting values are picked by `Fittino` from a Gaussian with the model parameters as mean and 1% of that as the variance. In order to try to ensure that the fit does not simply get stuck in the minimum, an additional measure has been employed: the main data set has been composed of different Markov Chains where some of the parameter start values are 10% away from the true point.

The consistency of the results can be checked by running the fit twice on the same input files. It is found that the results do slightly depend on the length and starting point of the fits. Furthermore, the scanned parameters can be plotted as a function of their position in the Markov Chain. This can give an understanding of which parameters are stable throughout the Markov Chain, like in Fig. 4.2.

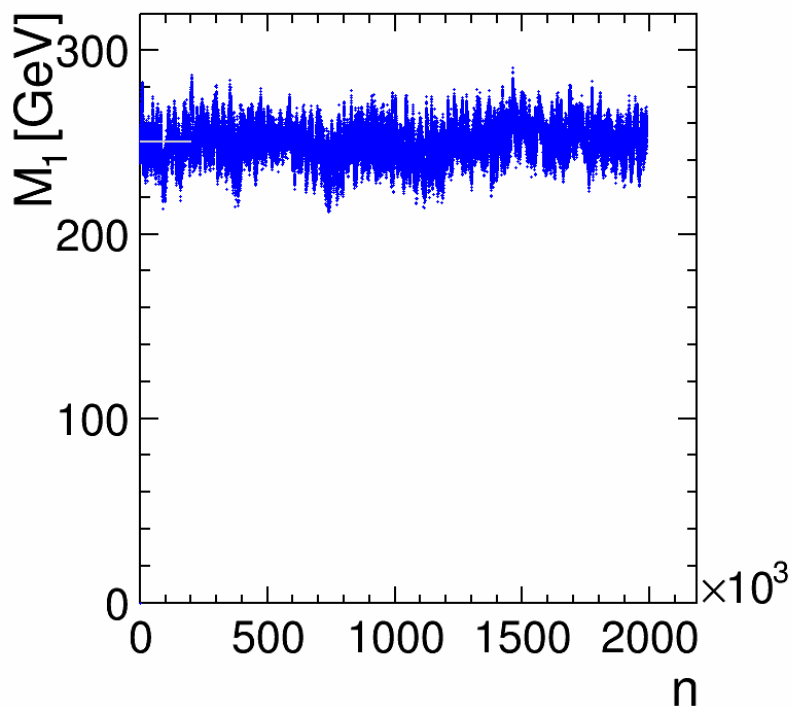


Figure 4.2: Example of the probing pattern of the Markov Chains: probed value of  $M_1$  in GeV vs. the position of that iteration in the Markov Chain. Here the scanning of ten different Markov Chains are plotted one after the other. The model parameter value is indicated with the grey line.

Ref. [202] suggests that several million points are required for the pMSSM scan. The results in this thesis are composed of 1-4 million points, specified for each result separately.

The `Fittino` algorithm output is a `ROOT` tree which contains the probed parameter points and the input observables calculated for this point and the corresponding chi-squared. In addition it contains any predictions for the observables which were not used to constrain the fit but which the user requested the fit saves by including them

in the `Fittino` input file with the `nofit` tag.

The chi-squared distributions can be interpreted with frequentist statistics and exploited in the following way to get the determined parameter ranges and predicted observable ranges.

First of all, the best fit point is the set of parameters which gives the smallest chi-squared value according to Eq. 4.2.

Then the one-dimensional  $1\sigma$  and  $2\sigma$  confidence intervals for a parameter are the ranges of that parameter where the maximal deviation of the  $\chi^2$  is less than 1 or 4 from the best fit point:  $\Delta\chi^2 = \chi^2 - \chi_{\text{best}}^2 < 1$  (4). For this purpose, the other dimensions are integrated out. The results are quoted as the best fit point + distance to the  $1\sigma$  maximum – distance to the  $1\sigma$  minimum. If the underlying  $\Delta\chi^2$  distribution is parabolic, then the  $1\sigma$  and  $2\sigma$  ranges can be associated with the 68% and 95% confidence intervals. This is not the case in most of the fit results. A visual example of a possible  $\Delta\chi^2$  distribution of a parameter is in Fig. 4.3.

The correlations of two parameters can be studied by plotting the  $\Delta\chi^2$  distribution on a plane. In this case, the plotted  $\Delta\chi^2$  value corresponds to the lowest  $\chi^2$  that the fit found for that bin on the 2D plane, thus integrating out the remaining dimensions. In these figures, we quote, following [202], the 1D- $1\sigma$  confidence interval corresponding to  $\Delta\chi^2 < 1$  and the 2D- $2\sigma$  confidence interval corresponding to  $\Delta\chi^2 < 5.99$ , as shown in Fig. 4.4.

The predictions for observables, such as the masses of heavy SUSY particles, can be extracted from the fit. For this purpose, the  $\Delta\chi^2$  distribution of the observable is plotted in a histogram. Then the  $1\sigma$  and  $2\sigma$  confidence intervals can be found as above. This gives a conservative prediction for the observables, as any correlations between the underlying parameters are ignored.

## 4.7 Other fitting codes

As mentioned above, `Fittino` is only one of a few options for the fitting algorithm. The scanning results from `Fittino` can be interpreted in a frequentist way as explained above, or a Bayesian way. The essential difference is that the Bayesian approach aims to give a statement of the degree of confidence in a prior given the observed data. This can be formulated as the probability  $P(\theta|d)$  of parameter distribution  $\theta$  given the data  $d$ ,

$$P(\theta|d) = \frac{P(d|\theta)P(\theta)}{P(d)}. \quad (4.4)$$

Here  $P(\theta)$  is the prior distribution of the parameters,  $P(d)$  is the Bayesian evidence or model likelihood and  $P(d|\theta)$  is the probability of the data given the parameter distribution. This approach gives a probability for the model to be correct assuming that the priors were reasonable. Under an appropriate proposal probability density and using flat priors, the sampling density of the scan is proportional to likelihood and to the posterior probability. It is especially important in this approach to ensure that the fit sampling probability is in equilibrium, requiring a large number of sampled points [202]. In the frequentist approach used in this thesis, there is no need to choose

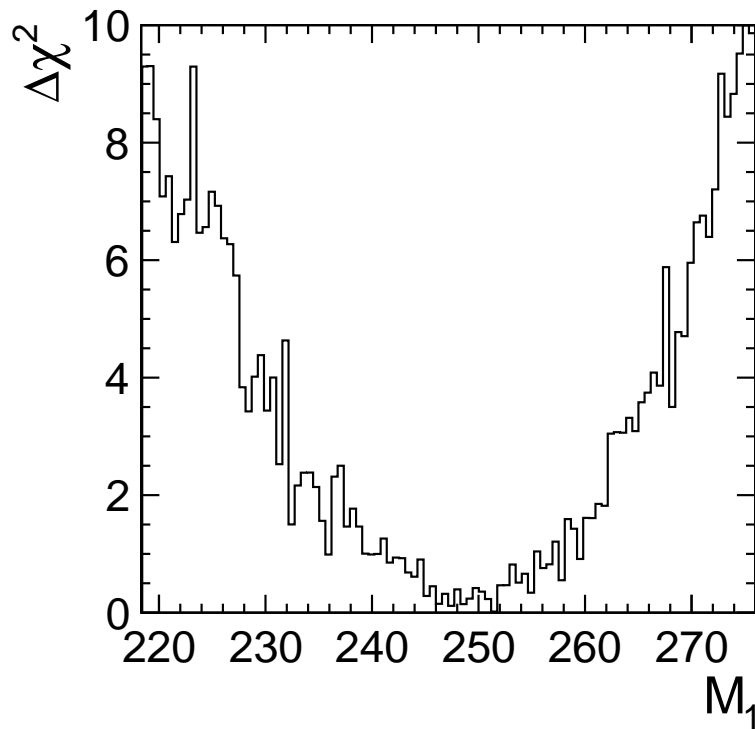


Figure 4.3: Example of the  $\Delta\chi^2$  distribution of a parameter

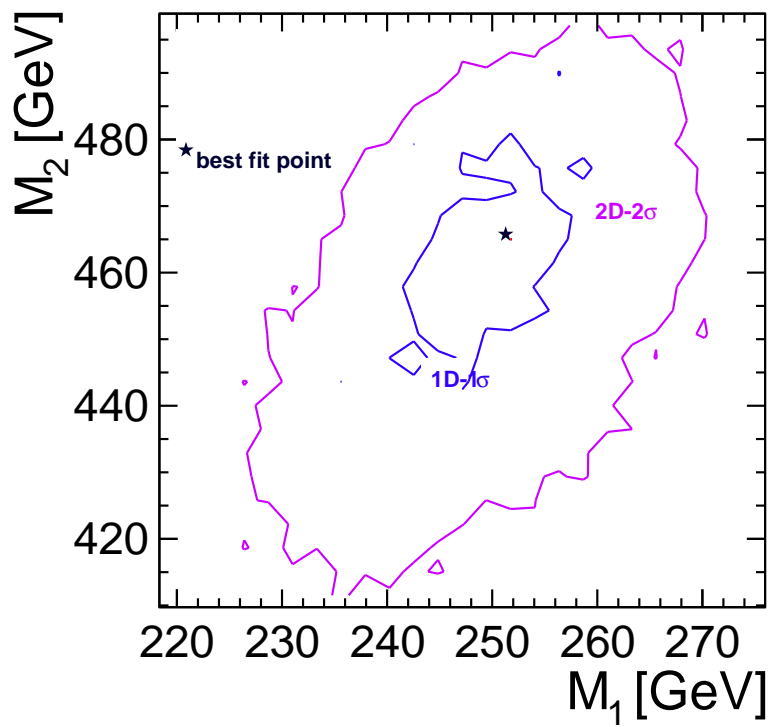


Figure 4.4: Example of the correlation of two parameters and the corresponding 1D-1 $\sigma$  and 2D-2 $\sigma$  ranges.

priors, and a less uniform scanning is allowed. The downside of the frequentist approach is that measurements and parameters have to be assumed to be linear at least locally [202].

Apart from Markov Chains, there are other scanning methods which will be only mentioned here. Those are nested sampling via **MultiNEST** [225, 226], genetic algorithms [227], simulated annealing [228], differential evolution [229] and neural networks [230]. There are also tools which combine some of these techniques: **Mastercode** [216, 231, 232] with nested sampling; **GAMBIT**, Global And Modular BSM Inference Tool [233] using a variety of scanning methods [234], **SuperBayeS** [235] using **MultiNEST** or Markov Chain Monte Carlo; Rizzo et al [236] studies using a simple grid scanning of the SUSY space.

# Chapter 5

## Dark matter relic density

Dark matter is an undisputed constituent of the universe, although its nature is yet to be determined. A candidate theory is supersymmetry, as has been discussed in detail in Sec. 2.7. To recap, not all supersymmetric models provide an explanation of dark matter, however:  $R$ -parity must be conserved to have a stable lightest SUSY particle, and the requirements from astrophysics can be satisfied by a neutralino LSP. Moreover, the coupling properties and mass of the LSP must be right to obtain the right relic density as measured by cosmology. The bino LSP with electroweak-scale mass provides a too weak interaction rate so that there would be too much bino dark matter today if that was the only contributor. The relic density can be reduced by enhancing the annihilation with another particle. This is called a coannihilation scenario. The condition for coannihilation to be significant, the masses of the two particles have to be similar.

The coannihilating particle can be any of the sfermions or an electroweakino. An interesting choice, which is not excluded by the LHC and could be discovered at the ILC, is stau coannihilation. A scenario which has received considerable attention is the Stau Coannihilation Scenario 8 (STC8) [237], which is inherited from the SPS1a scenario [238]. In STC8, the LSP and the scalar tau would be in reach of the ILC with  $\sqrt{s} = 500$  GeV along with the whole slepton and sneutrino sector, as well as  $\tilde{\chi}_2^0$  and  $\tilde{\chi}_1^\pm$ . This scenario has a bino LSP and a mostly right-handed  $\tilde{\tau}_1$  with a mass difference of 11 GeV. The coloured sector is heavy, with the exception of  $\tilde{t}_1$  and  $\tilde{b}_1$  which would cause an excess with large  $\sqrt{s} = 13$  TeV data sets at the LHC [170].

The prospects for measuring the gauginos and sleptons at the ILC have been investigated in Refs. [170, 171]. It was shown that the ILC could measure the properties of the accessible sparticles with percent-level precision.

SUSY parameters have been fitted previously with `Fittino` [201] to the hypothetical SPS1a' observations from ILC and LHC [202]. It was shown with toy fits that the observations of the whole SUSY spectrum from ILC and LHC together are enough to predict the dark matter relic density correctly with 1-2 permille precision.

In this chapter, we attempt to predict the relic density directly from the observables and using only ILC measurements in STC8. It was discussed in Sec. 2.7 that the full spectrum of sparticles is required to calculate the relic density, however, it may not be necessary to know all the values. If the relic density can be predicted correctly without

LHC measurements, then this would allow a much heavier coloured sector than was assumed in Ref. [202].

The considered benchmark STC8 is introduced in Sec. 5.1, where also the ILC prospects for SUSY measurements are summarised. The method for extracting the relic density with `MicrOMEGAs` from ILC SUSY measurements is presented in Sec. 5.2, and the results of the study are presented in Sec. 5.3, and conclusions are drawn in Sec. 5.4.

The standard cosmology is assumed in this chapter and all the results hold assuming the standard cosmology. Modifications of the standard cosmology may allow to circumvent the conclusions made in the next sections.

## 5.1 Stau coannihilation measurements at ILC

The scenario considered here is the Stau Coannihilation scenario 8 (STC8) [237], which is a 13-parameter point in the pMSSM. The number 8 in STC8 comes from the mass scale of the stop quark, 800 GeV. The parameters of STC8 are listed in Table 5.1. The parameters are similar to SPS1a [238] but the coloured particles are heavier due to LHC exclusions and modified due to the observed Higgs mass.

The STC8 spectrum is shown in Fig. 5.1 as calculated by `SPheno3.1.4` [206, 213]. All sleptons, sneutrinos,  $\tilde{\chi}_1^0$ ,  $\tilde{\chi}_2^0$  and  $\tilde{\chi}_1^\pm$  would be pair produced at the ILC with  $\sqrt{s} = 500$  GeV. Upgrading to  $\sqrt{s} = 1$  TeV would give access to the heavy Higgses,  $\tilde{\chi}_3^0$ ,  $\tilde{\chi}_4^0$  and  $\tilde{\chi}_2^\pm$ .

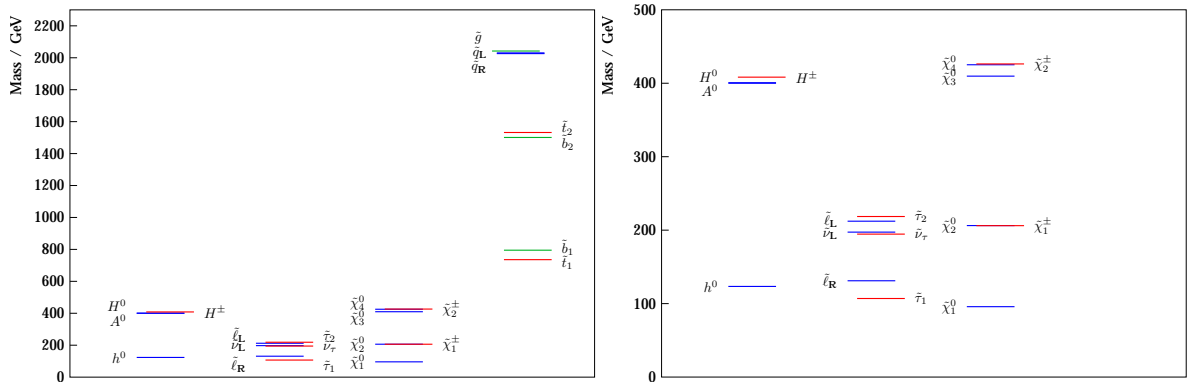


Figure 5.1: STC8 spectrum, all sparticles (left) and those with mass less than 500 GeV (right) [237].

The masses of the LSP and the  $\tilde{\tau}_1$  are 96 GeV and 107 GeV respectively, yielding a mass difference of 11 GeV. The composition of the LSP is  $\tilde{\chi}_1^0 = -0.99\tilde{B} + 0.03\tilde{W}^0 - 0.16\tilde{H}_d^0 + 0.04\tilde{H}_u^0$  and the stau mixing angle  $\theta_\tau = 71^\circ$ . The slepton, sneutrino and gaugino masses are listed in Tab. 5.2 along with the slepton and gaugino branching fractions. All the sleptons and gauginos are accessible at the ILC with  $\sqrt{s}=500$  GeV, and the coloured sector is heavy.

The decays of the sparticles are easy to understand: the sleptons decay almost entirely into the LSP and the lepton corresponding to the decaying particle. The  $\tilde{\chi}_1^\pm$  decays into  $\tilde{\tau}_1\nu_\tau$  with a 68% branching fraction, while the remaining fraction consists of mostly

parameter	model value
$\tan \beta$	10
$\mu$	400 GeV
$m_A$	400 GeV
$A_{\tau,t,b}$	-2400 GeV
$M_E$	119 GeV
$M_L$	205 GeV
$M_Q(1, 2)$	2000 GeV
$M_Q(3)$	1500 GeV
$M_U(1, 2) = M_D(1, 2)$	2000 GeV
$M_U(3)=M_D(3)$	800 GeV
$M_1$	100 GeV
$M_2$	210 GeV
$M_3$	2000 GeV
$m_t$	173.1 GeV

Table 5.1: STC8 SUSY parameters [237].

decays into sneutrinos. The largest fraction of  $\tilde{\chi}_2^0$  decays is into  $\tilde{\tau}_1^\pm \tau^\mp$  with a 73.3% contribution, and totally invisible states with sneutrinos and the LSP make up most of the rest of the remaining decays.

The relic density of the model is  $\Omega_{STC8} h^2 = 0.113$  as calculated with `Micromegas2.4.5` [239], which is close to the Planck measurement [28] (94% of Planck value). The channels which contribute to the relic density the most are  $\tilde{\chi}_1^0 \tilde{\chi}_1^0 \rightarrow l^+ l^-$  with 73%,  $\tilde{\chi}_1^0 \tilde{\tau}_1 \rightarrow \gamma \tau$  with 16% and  $\tilde{\chi}_1^0 \tilde{\tau}_1 \rightarrow Z \tau$  with 3% contributions. Fig. 5.2 shows some of the Feynman diagrams which contribute to these processes. It can be seen from the diagrams and Fig. 5.3 that the relic density is sensitive to the LSP mass,  $\tilde{\tau}_1$  mass, binoness  $N_{11}$  of the LSP and the stau mixing angle  $\theta_\tau$ . If, for example, the  $\tilde{\tau}_1$  mass is increased, meaning the LSP- $\tilde{\tau}_1$  mass gap is increased, then the coannihilation gets less effective and the relic density increases ( $1/\Omega$  decreases). If the stau mixing angle  $\theta_\tau$  increases, meaning that the  $\tilde{\tau}_1$  gets more right-handed, the relic density increases as the annihilation and coannihilation gets more ineffective.

An analysis of this scenario has been conducted in [170] using the fast detector simulation of ILD [240] and polarised electron and positron beams  $\mathcal{P}(e^-, e^+)(+80\%, -30\%)$ . The kinematically accessible sparticles can be measured from the kinematics of their decay products. The analysis finds that both the LSP mass and  $\tilde{\tau}_1$  mass can be measured with a 100 MeV or one permille accuracy with ILC  $\sqrt{s} = 500$  GeV from a data set of  $\mathcal{L} = 500 \text{ fb}^{-1}$  and beam polarisations  $\mathcal{P}(e^-, e^+)(\pm 80\%, \mp 30\%)$ . The masses of all other kinematically accessible particles can be measured with precisions of 1-5%.

		BR [%]	STC8			BR [%]	STC8
observable	STC8	$\tilde{e}_R \rightarrow \tilde{\chi}_1^0 e$	100	$\tilde{\chi}_1^+ \rightarrow \tilde{e}_L^+ \nu_e$	—		
$m_{\tilde{\chi}_1^0}$	95.80	$\tilde{\mu}_R \rightarrow \tilde{\chi}_1^0 \mu$	100	$\tilde{\chi}_1^+ \rightarrow \tilde{\mu}_R^+ \nu_\mu$	0.2		
$m_{\tilde{\tau}_1}$	106.95	$\tilde{e}_L \rightarrow \tilde{\chi}_1^0 e$	95.3	$\tilde{\chi}_1^+ \rightarrow \tilde{\mu}_L^+ \nu_\mu$	—		
$m_{\tilde{\chi}_2^0}$	206.23	$\tilde{\mu}_L \rightarrow \tilde{\chi}_1^0 \mu$	95.3	$\tilde{\chi}_1^+ \rightarrow \tilde{\tau}_1 \nu_\tau$	67.9		
$m_{\tilde{\chi}_1^\pm}$	206.12	$\tilde{e}_L \rightarrow \tilde{\chi}_2^0 e$	1.7	$\tilde{\chi}_1^+ \rightarrow \tilde{\nu}_e e^+$	6.6		
$m_{\tilde{\tau}_2}$	218.57	$\tilde{\mu}_L \rightarrow \tilde{\chi}_2^0 \mu$	1.7	$\tilde{\chi}_1^+ \rightarrow \tilde{\nu}_\mu \mu^+$	6.6		
$m_{\tilde{e}_L}$	212.19	$\tilde{e}_L \rightarrow \tilde{\chi}_1^\pm \nu_e$	3.0	$\tilde{\chi}_1^+ \rightarrow \tilde{\nu}_\tau \tau^+$	11.3		
$m_{\tilde{e}_R}$	131.09	$\tilde{\mu}_L \rightarrow \tilde{\chi}_1^\pm \nu_\mu$	3.0	$\tilde{\chi}_1^+ \rightarrow \tilde{\chi}_1^0 W^+$	7.2		
$m_{\tilde{\mu}_L}$	212.22	$\tilde{\nu}_{eL} \rightarrow \tilde{\chi}_1^0 \nu_e$	100	$\tilde{\chi}_2^0 \rightarrow \tilde{e}_R^\pm e^\mp$	2.6		
$m_{\tilde{\mu}_R}$	131.01	$\tilde{\nu}_{\mu L} \rightarrow \tilde{\chi}_1^0 \nu_\mu$	100	$\tilde{\chi}_2^0 \rightarrow \tilde{e}_L^\pm e^\mp$	—		
$m_{\tilde{\nu}_\tau}$	194.60	$\tilde{\tau}_1 \rightarrow \tilde{\chi}_1^0 \tau$	100	$\tilde{\chi}_2^0 \rightarrow \tilde{\mu}_R^\pm \mu^\mp$	2.4		
$m_{\tilde{\nu}_e}, m_{\tilde{\nu}_\mu}$	197.31	$\tilde{\tau}_2 \rightarrow \tilde{\chi}_1^0 \tau$	81.3	$\tilde{\chi}_2^0 \rightarrow \tilde{\mu}_L^\pm \mu^\mp$	—		
$m_h$	123.39	$\tilde{\tau}_2 \rightarrow \tilde{\chi}_2^0 \tau$	3.4	$\tilde{\chi}_2^0 \rightarrow \tilde{\tau}_1^\pm \tau^\mp$	73.3		
$\Omega h^2$	0.113	$\tilde{\tau}_2 \rightarrow \tilde{\chi}_1^\pm \nu_\tau$	6.2	$\tilde{\chi}_2^0 \rightarrow \tilde{\nu}_e \nu_e$	5.7		
$\Omega/\Omega_{\text{Planck}}$	94%	$\tilde{\tau}_2 \rightarrow \tilde{\tau}_1 Z$	9.1	$\tilde{\chi}_2^0 \rightarrow \tilde{\nu}_\mu \nu_\mu$	5.7		
		$\tilde{\nu}_{\tau L} \rightarrow \tilde{\chi}_1^0 \nu_\tau$	94.2	$\tilde{\chi}_2^0 \rightarrow \tilde{\nu}_\tau \nu_\tau$	9.5		
		$\tilde{\nu}_{\tau L} \rightarrow \tilde{\tau}_1 W$	5.8	$\tilde{\chi}_2^0 \rightarrow \tilde{\chi}_1^0 Z$	1.2		

Table 5.2: The light sparticle masses and branching fractions of sleptons and gauginos in STC8, using SPheno3.1.4. All the masses are in units of GeV.

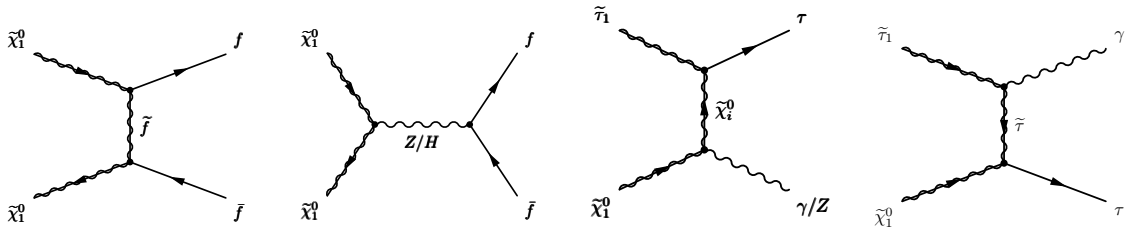


Figure 5.2: Some LSP annihilation and stau coannihilation diagrams, strengths of which set the relic density in STC8.

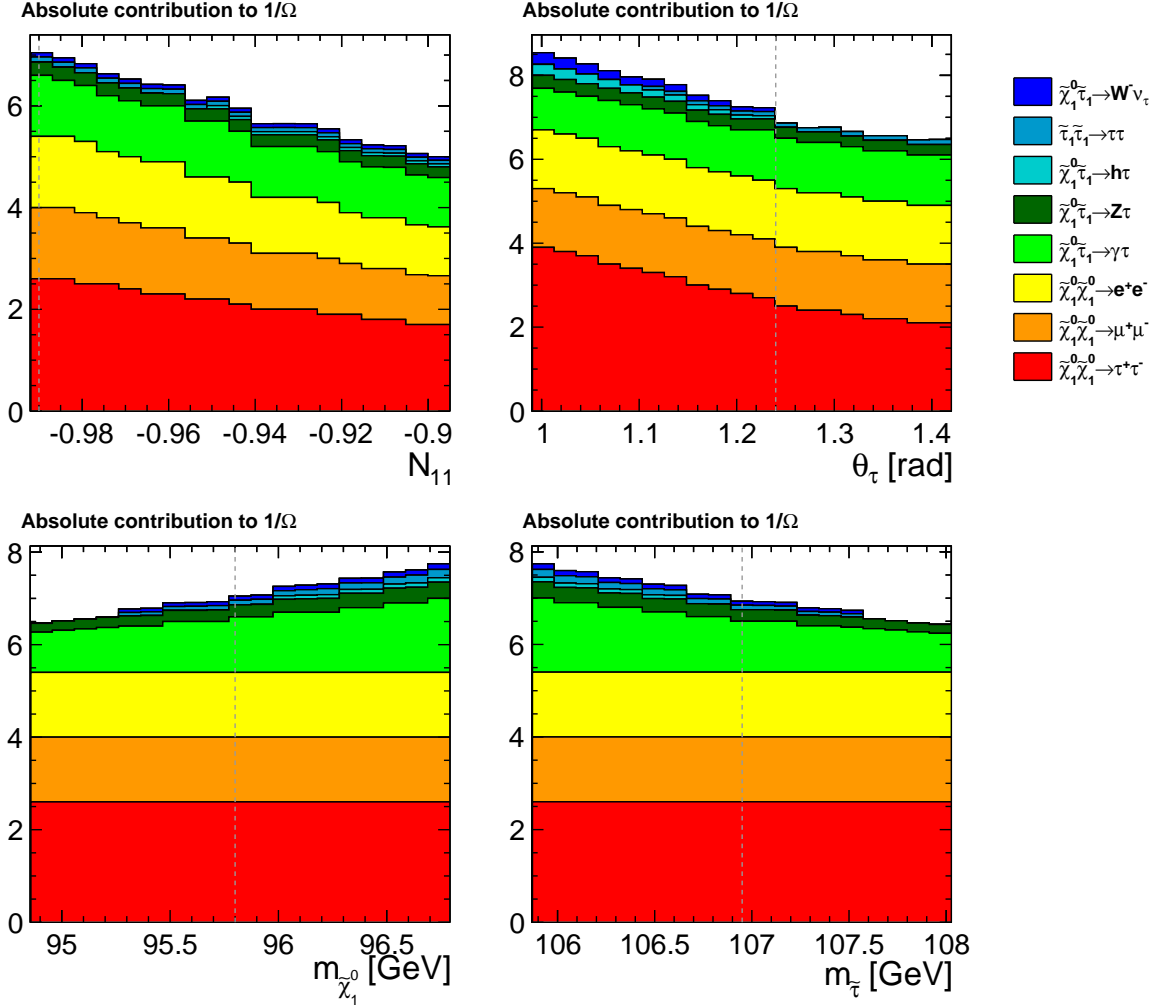


Figure 5.3: The absolute contributions from different annihilation and coannihilation channels to  $1/\Omega$  as given by MicrOMEGAs [239] for STC8. The dashed lines indicate the model value in STC8. If the LSP- $\tilde{\tau}_1$  mass difference gets smaller then the coannihilation channels get more effective. If the bineness of the LSP gets smaller then the rates of all interactions get smaller - note that the other couplings were not increased so unitarity of the neutralino mixing matrix was not maintained. If the stau mixing angle increases from 71 degrees (1.24 rad) then the  $\tilde{\tau}_1$  becomes more right-handed and the annihilation and coannihilation get weaker.

In the 20-year operation scenario H20, the uncertainties would reduce to around half due to the increased integrated luminosity in the long running scenario. The details of the measurements and results from Ref. [170] are recapped below.

### 5.1.1 Gauginos

Gauginos are produced in the pairs  $\tilde{\chi}_2^0\tilde{\chi}_1^0$  or  $\tilde{\chi}_1^+\tilde{\chi}_1^-$ . In STC8,  $\tilde{\chi}_2^0$  decays predominantly (70% BR) to  $\tilde{\tau}_1\tau$ . The  $\tilde{\tau}_1$  further decays to  $\tau\tilde{\chi}_1^0$ , leading to the overall process  $e^+e^- \rightarrow \tilde{\chi}_1^0\tilde{\chi}_2^0 \rightarrow \tilde{\chi}_1^0\tilde{\chi}_1^0\tau\tau$ . There is not a simulation study for this, but simple assumptions lead to the estimate that the  $\tilde{\chi}_2^0$  mass could be measured with 0.5-1.0% precision [241]. An alternative channel is  $\tilde{\chi}_1^0\tilde{\chi}_2^0 \rightarrow \tilde{\chi}_1^0\tilde{\chi}_1^0\mu\mu$  which gives an uncertainty on the  $\tilde{\chi}_2^0$  mass of about 0.5% for  $500 \text{ fb}^{-1}$  and  $\mathcal{P}(e^-, e^+) = (-80\%, +60\%)$  [242].

For chargino pair production the most likely final state is  $\tau\tau$  with missing energy. This suffers from background from the neutralino pair production. The rarer decays  $\tilde{\chi}_1^\pm \rightarrow \tilde{\chi}_1^0 W^\pm$  and  $\tilde{\chi}_1^\pm \rightarrow \tilde{\nu}_e e, \tilde{\nu}_\mu \mu$  provide channels with which it should be possible to measure the chargino and sneutrino masses to 1% [170].

A direct probe for the invisible  $\tilde{\chi}_1^0$  pair-production is the mono-photon search  $e^+e^- \rightarrow \tilde{\chi}_1^0\tilde{\chi}_1^0\gamma$ . The initial state photon is required for tagging the otherwise invisible process. This search requires a good hermeticity of the detector in order to have an accurate estimate of the rate of the background process  $e^+e^- \rightarrow e^+e^-\gamma$ . The energy of the photon has to be measured accurately. From the shape of the distribution of the photon energy in a large data set, the  $\tilde{\chi}_1^0$  mass can be deduced. The most recent update of the model-independent mono-photon analysis can be found in Ref. [174]. In a previous study, the LSP mass was found to get a precision of 1 GeV or 2% [175].

### 5.1.2 Sleptons

In STC8 the sleptons decay to the corresponding lepton and the LSP. To understand the mass measurement as presented in [170], consider the process  $e^+e^- \rightarrow \tilde{X}\tilde{Y} \rightarrow XY\tilde{\chi}_1^0\tilde{\chi}_1^0$  at a centre-of-mass energy well above threshold. The kinematic endpoints of the energies of the Standard Model particles X and Y, assuming X and Y are massless, can be written as

$$\begin{aligned} E_l^{\max(\min)} &= \frac{M_{\tilde{l}}}{2} \left( 1 - \left( \frac{M_{\tilde{\chi}_1^0}}{M_{\tilde{l}}} \right)^2 \right) (\gamma_{(\pm)} \gamma_{\beta}) \\ &= \frac{M_{\tilde{l}}}{2} \left( 1 - \left( \frac{M_{\tilde{\chi}_1^0}}{M_{\tilde{l}}} \right)^2 \right) \left( E_{\tilde{l}}^{\text{lab}}{}_{(\pm)} \frac{|\vec{p}^{\text{lab}}|}{M_{\tilde{l}}} \right), \end{aligned} \quad (5.1)$$

where  $l = X, Y$ . If the sleptons are alike,  $\tilde{X} = \tilde{Y}$ , then  $E_{\tilde{l}}^{\text{lab}} = E_{\text{cms}}/2$  and  $|\vec{p}^{\text{lab}}| = \sqrt{(E_{\text{cms}}/2)^2 - M_{\tilde{l}}^2}$ . Thus for slepton pair production of the same flavour

$$E_l^{\max(\min)} = \frac{E_{\text{cms}}}{4} \left( 1 - \left( \frac{M_{\tilde{\chi}_1^0}}{M_{\tilde{l}}} \right)^2 \right) \left( 1_{(\pm)} \sqrt{1 - 4 \left( \frac{M_{\tilde{l}}}{E_{\text{cms}}} \right)^2} \right). \quad (5.2)$$

Provided that  $E_{cms}$  is known, as it is at the ILC, both the  $\tilde{\chi}_1^0$  and the slepton mass can be determined from these two endpoints. In the case of stau decays, we have taus which decay further with additional invisible energy. If we have the LSP mass from other channels then the maximum edge gives us the  $\tilde{\tau}_1$  mass.

The search for sleptons relies on two opposite-sign lepton candidates and less than 10 charged particles in the event with a zero sum of charges. There should be more than 200 GeV missing energy and less than 300 GeV visible energy. The right-handed sparticles can be best searched for in the mostly right-handed beam polarisation configuration,  $\mathcal{P}(e^-, e^+) = (+80\%, -30\%)$ , and conversely left-handed beam polarisation configuration for left-handed sleptons. Since the right-handed sleptons are light, their decay products will be more boosted than the decay products of the heavier left-handed sleptons. Thus, a cut on the relative transverse momentum of the visible decay products is applied to separate between left-handed and right-handed sleptons. It should be noted that the production cross section for  $\tilde{e}_R \tilde{e}_R$  is a factor 70 larger than  $\tilde{e}_L \tilde{e}_L$  due to the neutralino exchange in the  $t$ -channel in the  $l_R \tilde{l}_R$  production. Nevertheless, both edges of both signal processes can be detected [170].

The signal and background distributions for the selectron search can be seen in Fig. 5.4 and the smuon search in Fig. 5.5. The edges can be detected by finding the fastest lepton in subsets of the full data set. Those energies will give an average. The average can be calibrated via toy Monte Carlo. The resulting statistical precisions are  $\delta m_{\tilde{e}_R} = 0.17\%$ ,  $\delta m_{\tilde{e}_L} = 1\%$ ,  $\delta m_{\tilde{\mu}_R} = 0.40\%$  and  $\delta m_{\tilde{\mu}_L} = 1\%$  [170].

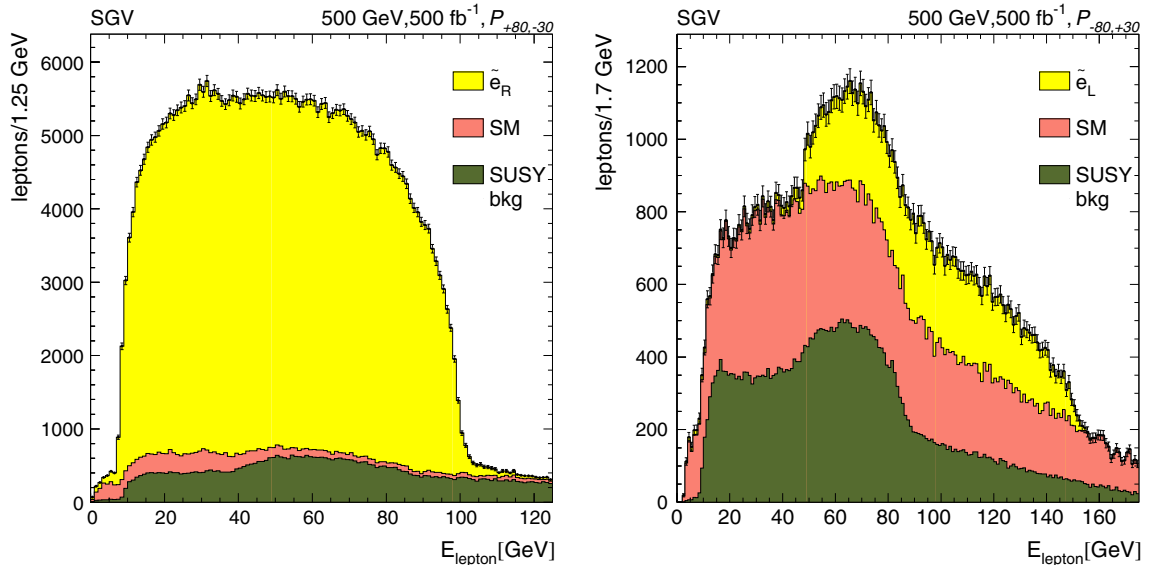


Figure 5.4: STC8 selectron search [170]. The plots show the distribution of electron energy from  $\tilde{e}_R$  (left) and  $\tilde{e}_L$  decays (right). In both cases, the higher and lower edge can be determined.

The search for staus proceeds in a similar manner to the selectron and smuon search. The difference is the smaller mass difference of the stau with the LSP, and the decays of the tau into jets. This makes the background from  $\gamma\gamma$  events and  $VV \rightarrow \tau\nu\tau\nu$  more severe. These backgrounds can be reduced by stronger mass and energy cuts, and additional angular cuts. The lower kinematic endpoint would overlap with the  $\gamma\gamma$  event region, so after the cuts, the lower endpoint is no longer detectable, as can

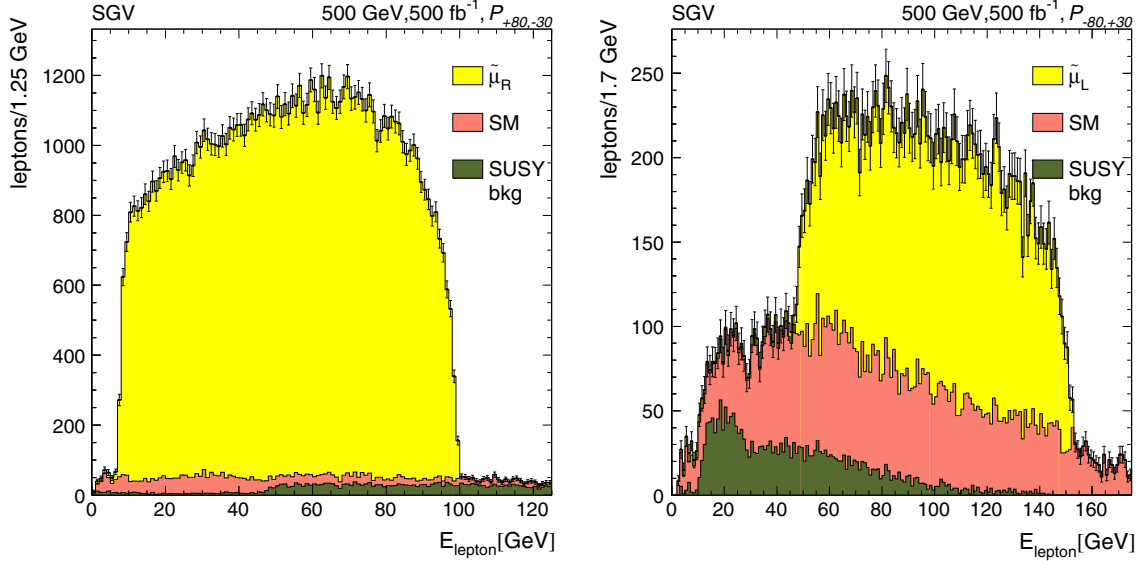


Figure 5.5: STC8 smuon search [170]. The plots show the distribution of muon energy from  $\tilde{\mu}_R$  (left) and  $\tilde{\mu}_L$  decays (right). For both particles, both edges can be measured.

be seen from Fig. 5.6. The upper endpoint however can be measured with roughly 0.1 GeV uncertainty. Using the equation for the stau mass,

$$m_{\tilde{\tau}_1}^2 = \frac{m_{LSP}^2}{1 - \frac{2E_{max}}{\sqrt{s}}}, \quad (5.3)$$

one can calculate an uncertainty on the  $\tilde{\tau}_1$  mass based on the edge precision and LSP mass precision. This gives a 169 MeV (0.16%) uncertainty on the stau mass assuming a 147 MeV uncertainty on the LSP mass and 120 MeV on the stau kinematic endpoint. The  $\tilde{\tau}_2$  mass is measured with 2.5% precision with  $500 \text{ fb}^{-1}$  for  $\mathcal{P}(e^-, e^+) = (+80\%, -30\%)$  [170].

### 5.1.3 Sneutrinos

Sneutrinos decay mainly to neutrinos and LSP. This channel is totally invisible but there is a 5% probability for a visible  $\tilde{\nu}_\tau \rightarrow \tilde{\tau}_1 W$  decay. Another option is to search for sneutrino pair production with an initial state radiation photon and invisible decay products. The effect is that the signal is enhanced because the cross section  $\sigma(e^+e^- \rightarrow \tilde{\nu}_\tau \tilde{\nu}_\tau) = 10\sigma(e^+e^- \rightarrow \tilde{\chi}_1^0 \tilde{\chi}_1^0)$ . There is not a detailed study on either but the invisible decay with an initial state radiation corresponds to the standard WIMP search. It can be estimated that the sneutrino mass could be measured with 1% percent precision with  $500 \text{ fb}^{-1}$  and polarisation  $\mathcal{P}(e^-, e^+) = (-80\%, +30\%)$  suppressing the right-handed sleptons [170].

Alternatively,  $\tilde{\chi}_1^\pm$  decays to sneutrinos give an avenue for measuring the sneutrino masses.  $\tilde{\chi}_1^\pm \rightarrow \tilde{\nu}_e e(\tilde{\nu}_\mu \mu)$  decays have kinematic endpoints in the lepton energy spectrum. As long as these endpoints do not overlap with the selectron and smuon decay signals, then the sneutrino mass is estimated to be measured with 1% precision with  $\mathcal{L} = 500 \text{ fb}^{-1}$  with  $\mathcal{P}(e^-, e^+) = (-80\%, +30\%)$  [170].

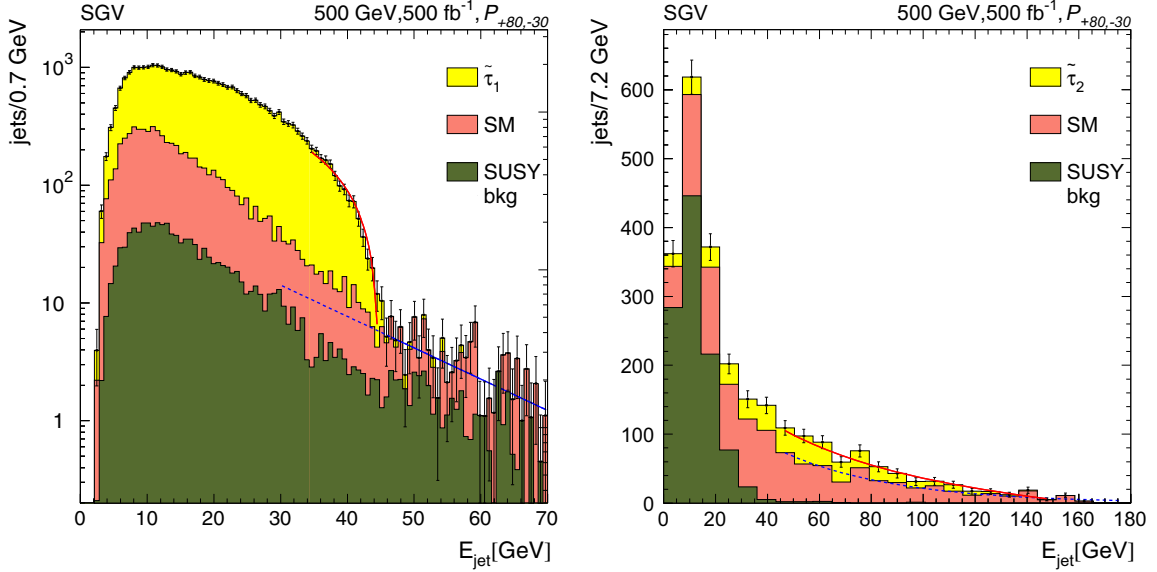


Figure 5.6: STC8 stau search [170]. The upper endpoint of both  $\tilde{\tau}_1$  and  $\tilde{\tau}_2$  decays can be measured.

### 5.1.4 Mixings

As discussed in the preceding sections, to calculate the relic density requires knowing the couplings of the relevant sparticles, the LSP and stau in particular. As there can be many diagrams contributing to one process, it is most often not straightforward to deduce the mixing structure of sparticles. In general, the mixing affects the cross sections and branching fractions of SUSY particles. The easiest and most studied case is the stau, as it has only one parameter determining its mixing, the stau mixing angle  $\theta_\tau$ . A method for determining it is presented in [243]. The stau mixing angle can be determined from the cross section  $\sigma(e_L^+ e_R^- \rightarrow \tilde{\tau}_1 \tilde{\tau}_1)$  to  $\cos 2\theta_\tau = -0.987 \pm 0.02$  (stat.)  $\pm 0.06$  (syst.) in an SPS1a inspired scenario [243]. This corresponds to a 4% statistical and 13% systematic uncertainty in this scenario considered. In another paper Ref. [171], the stau mixing can be measured with 7% uncertainty.

The neutralino mixing matrix elements are not all independent. The neutralino mixing matrix is a real orthogonal matrix with  $N \times (N-1)/2 = 6$  degrees of freedom for  $N = 4$ . It is not straightforward to convert the mixing matrix elements into the independent mixing angles. Therefore, all the neutralino mixing matrix elements are treated as independent. For more details about the interdependence of the elements see [66] and [244]. There are some ways to measure the neutralino mixing matrix elements as they appear in cross sections. For example, if one measures the polarisation of the tau from the  $\tilde{\tau}_1 \rightarrow \tau \tilde{\chi}_1^0$  decay and the cross section  $\sigma(\tilde{\tau}_1 \tilde{\tau}_1)$  then these two measurements can be used to disentangle the stau mixing and the higgsino-gaugino mixing of the LSP [245]. This measurement of the polarisation of the tau is difficult because the tau does not have a fixed energy. There is not a study on the quantitative prospects of measuring neutralino mixing matrix elements at the ILC. Therefore the study in the next section can and will give hints as to what precision would be sufficient for a successful relic density calculation.

Additionally, the relic density diagrams are affected by the trilinear coupling of the  $\tilde{\tau}$ ,

$A_\tau$ . A method is presented in [243] for extracting  $A_\tau$ . If we measure both  $m_{\tilde{\tau}_1}$  and  $m_{\tilde{\tau}_2}$  and their mixing angle and the polarisation of a  $\tau$  in a  $\tilde{\tau}$  decay then we can determine  $\tan\beta$  and the trilinear coupling. This paper assumes a strong higgsino component of the LSP. Also the tau trilinear coupling is a factor 10 smaller than in STC8, -254 GeV vs. -2400 GeV. The paper quotes a 100% uncertainty on the trilinear coupling in some cases, which translates to a  $\sim 250$  GeV uncertainty in absolute terms.

Apart from the  $\tilde{\tau}$  mixing angle and neutralino mixing there are also two chargino mixing angles. The chargino mass matrix is diagonalised by two  $2 \times 2$  matrices  $U$  and  $V$ , which are parametrised by  $\cos 2\phi_L$  and  $\cos 2\phi_R$ . One needs to measure the cross section  $\tilde{\chi}_1^+ \tilde{\chi}_1^-$ ,  $\tilde{\chi}_1^\pm \tilde{\chi}_2^\mp$  and  $\tilde{\chi}_2^+ \tilde{\chi}_2^-$  production with a right-handedly polarised electron beam [246]. The left-handedly polarised electron beam is needed to distinguish between possible solutions of the chargino mixing angles  $\cos 2\phi_L$  and  $\cos 2\phi_R$ . The mixing angles can be measured even if the production of  $\tilde{\chi}_2^+ \tilde{\chi}_2^-$  is not accessible. The paper quotes  $\cos 2\phi_L = 0.645 \pm 0.02$ ,  $\cos 2\phi_R = 0.844 \pm 0.005$ . Of course in the case of the STC8, at  $\sqrt{s} = 500$  GeV, the heavier chargino is not accessible. With a combination of ILC and LHC searches, the LHC would be able to measure the mass of the  $\tilde{\chi}_2^\pm$  with about 10% precision after  $300 \text{ fb}^{-1}$  [170].

In the next section the information gained from SUSY mass measurements will be used to calculate the dark matter relic density of the LSP to check if all of dark matter is composed of the LSP.

## 5.2 Method to extract relic density

It is possible to calculate the relic density for a full SUSY model as discussed in Sec. 2.7.1. The required input is the full SUSY model either via the SUSY parameter definition or explicitly giving all the masses and mixings. We follow the latter approach and use `MicrOMEGAs2.4.5` [239] for this study.

The ILC measurements from the previous sections are used as input. Toy calculations were performed with the mass and/or mixing values drawn randomly from Gaussian distributions with the measured mean and standard deviation. These toy values were drawn 10 000 times for each observable. For the heavy particles, which were not assumed to have been observed, including the heavy Higgs bosons and coloured sparticles, the toy values were drawn from uniform distributions instead.

In the first step, only some masses and mixings were varied and the rest were fixed to the STC8 model values. Later the unobserved particle properties were treated as nuisance parameters and varied uniformly. In all of the following it is assumed that the measured values fall on the model values, so any effects from miscalibration of the measurements are not considered.

For each toy set of values, `MicrOMEGAs2.4.5` [239] was executed and the calculated relic density was saved. The distribution of calculated values was scaled to the model STC8 relic density. The resulting histogram was plotted and its mean and standard deviation were computed with `ROOT` [203].

### 5.3 Results

Let us first consider the LSP and  $\tilde{\tau}_1$  properties only, keeping the rest of the spectrum fixed to the model values. The mass of the LSP and the value of the  $\tilde{\tau}_1$  endpoint can be measured to permille level at the ILC with  $\sqrt{s} = 500$  GeV,  $\mathcal{L} = 500$  fb $^{-1}$  and polarisation  $\mathcal{P}(e^-, e^+) = (+80\%, -30\%)$ : 0.15% for the LSP mass and 0.24% for the  $\tilde{\tau}_1$  endpoint or, equivalently, a 0.16% uncertainty on the mass of the  $\tilde{\tau}_1$  as summarised in Tab. 5.3. If the LSP mass and the  $\tilde{\tau}_1$  endpoint are varied according to Gaussian distributions with the model mass value as the mean and the respective experimental uncertainties, then the calculated relic density has a narrow distribution centred around the model relic density, as shown in Fig. 5.7. The standard deviation of the distribution is 0.3%.

A 1% uncertainty on either the LSP or  $\tilde{\tau}_1$  mass causes a 10% uncertainty on the relic density. This is large compared to the effect of a 1% uncertainty on the  $\tilde{e}_R$  or  $\tilde{\mu}_R$  masses. This leads to a 0.7% uncertainty on the relic density. The  $\tilde{e}_L$  and  $\tilde{\mu}_L$  masses are even less important, 1% mass uncertainty implying a  $1 \times 10^{-4}$  effect. The sneutrinos are also not important, a 10% mass uncertainty merely contributes a 0.3% effect. The neutral Heavy higgses have a comparable importance to the sneutrinos but other masses can be neglected as can be seen later.

observable	uncertainty	observable	uncertainty
$m_{\tilde{\chi}_1^0}$	0.15%	$m_{\tilde{\chi}_1^\pm}$	1%
$m_{\tilde{\tau}_1}$	0.16%	$m_{\tilde{\nu}_e, \tilde{\nu}_\mu, \tilde{\nu}_\tau}$	1%
$m_{\tilde{e}_R}$	0.17%	$m_{\tilde{e}_L}$	1%
$m_{\tilde{\mu}_R}$	0.40%	$m_{\tilde{\mu}_L}$	1%
$m_{\tilde{\chi}_2^0}$	0.5%	$N_{11,12,13,14}$	1% each
$m_{\tilde{\tau}_2}$	2.5%	$\theta_\tau$	1%
		$A_\tau$	20%
		$U_{mix}, V_{mix}$	20% each

Table 5.3: Uncertainties at the ILC with  $\sqrt{s} = 500$  GeV. Values in the left column are from the analysis in [170] for  $\mathcal{L} = 500$  fb $^{-1}$  and  $\mathcal{P}(e^-, e^+) = (\pm 80\%, \mp 30\%)$ . Values in the right column are assumptions. These uncertainties correspond to those in Fig. 5.9.

Fig. 5.7 shows the relic density distribution if the stau mixing angle  $\theta_\tau$  and neutralino mixing matrix elements  $N_{11}, N_{12}, N_{13}, N_{14}$ , are all varied by 1%. It should be noted that the  $N_{1i}$ ,  $i = 1, 2, 3, 4$  are not independent but, due to unitarity, satisfy  $\sum_i N_{1i}^2 = 1$  and  $\sum_j N_{j1}^2 = 1$ . Ignoring this inconsistency, the variation of the neutralino mixing elements and stau mixing angle by 1% results in a 3.3% uncertainty on the relic density, which is of the same order as the Planck precision. Thus, to predict the relic density with a precision comparable to the current Planck measurement, the ILC has to measure the mixings with 1% accuracy at least. However, an uncertainty of one percent for the mixings is ambitious as discussed in Sec. 5.1.4:  $\theta_\tau$  could be determined from the

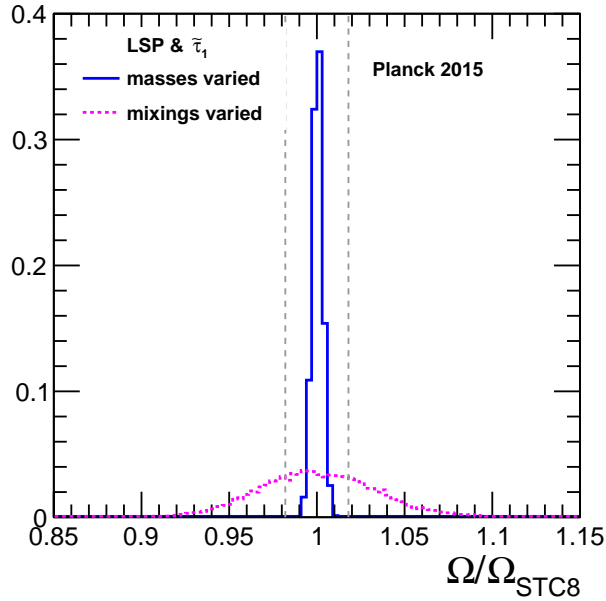


Figure 5.7: Distribution of predicted  $\Omega$  when LSP mass and  $\tilde{\tau}_1$  endpoint are varied (solid blue line) and when  $\tilde{\chi}_1^0$  and  $\tilde{\tau}_1$  mixings are varied (dashed pink line). The mixings need to be measured to 1% to get a 3.3% uncertainty on  $\Omega$ .

polarised production cross sections of  $\tilde{\tau}_1$  pairs [243] which could be measured to a three percent uncertainty with  $\mathcal{L} = 500 \text{ fb}^{-1}$  in a similar scenario [171]. There is not a study on the precisions of the neutralino mixing elements from the experimental point of view. If the mixings were measured to 2% accuracy instead of 1%, then the uncertainty on the relic density would double. A 10% precision on the mixings would lead to a factor 10 larger uncertainty on  $\Omega_{LSP} h^2$  than the uncertainty from 1% mixing variations.

If the LSP and  $\tilde{\tau}_1$  masses and mixings are varied simultaneously, the uncertainty on the relic density is 3.4% (pink dashed curve in Fig. 5.8) compared with 3.3% if only the mixings are varied (pink dashed curve in Fig. 5.7). Hence the mixings dominate the uncertainty. It is particularly important to measure the largest mixing matrix element  $N_{11}$  of the LSP as precisely as possible. This can be seen from Fig. 5.8, where the effect of varying the value of  $N_{11}$  is shown. If  $N_{11}$  is fixed to its model value, then the uncertainty on the relic density is reduced by approximately two thirds.

Thus far, true model values have been used for sparticle masses and mixings apart from the LSP and  $\tilde{\tau}_1$ . If the other masses and mixings were allowed to vary, would the relic density still be predicted correctly? This question is answered by Fig. 5.9. Let us assume that the sleptons, sneutrinos and  $\tilde{\chi}_1^0, \tilde{\chi}_2^0$  and  $\tilde{\chi}_1^\pm$  were discovered with the ILC at  $\sqrt{s} = 500 \text{ GeV}$ . Then assuming the uncertainties in Tab. 5.3 and fixing the properties of the squarks, higgsinos and heavy Higgses to the model values, the relic density is predicted correctly with a 3.4% uncertainty. If the properties of the unobserved squarks, higgsinos and heavy Higgses were allowed to vary uniformly within the ranges in Tab. 5.4, then the central value of the dark matter distribution is shifted to the lower values by about one standard deviation from the true model value. The

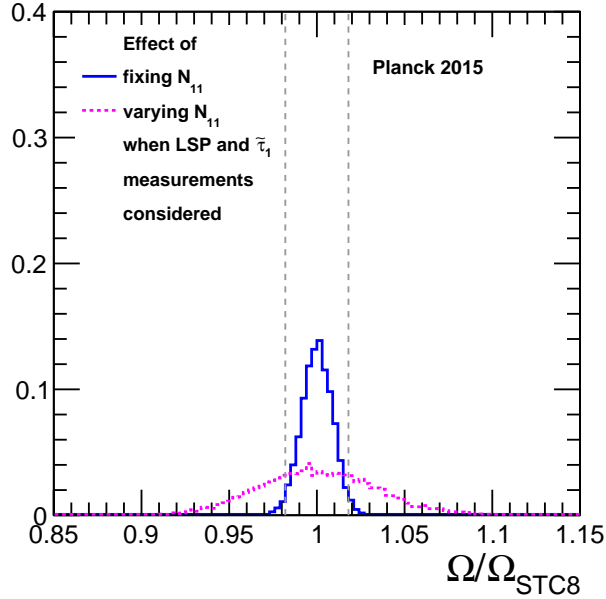


Figure 5.8: The LSP and  $\tilde{\tau}_1$  masses and mixings varied together (dashed pink curve). If  $N_{11}$  is fixed (solid blue curve), the uncertainty shrinks by two thirds. In other words, the uncertainty on the main coupling of the LSP accounts for two thirds of the uncertainty on  $\Omega$ .

shift is small, so any possible contribution to the relic density from other types of dark matter would have to be small.

observable	range	observable	range
$m_{\tilde{\chi}_3^0, \tilde{\chi}_4^0}$	0.25 – 2 TeV	$m_{\tilde{\chi}_2^\pm}$	0.25 – 2 TeV
$m_{H_0, A_0, H^\pm}$	0.4 – 2 TeV	$m_{\tilde{d}_R, \tilde{u}_R, \tilde{s}_R, \tilde{c}_R}$	$= m_{\tilde{d}_L} - 100$ GeV
$m_{\tilde{d}_L, \tilde{u}_L, \tilde{s}_L, \tilde{c}_L}$ all equal	1 – 50 TeV	$m_{\tilde{g}}$	1 – 50 TeV
$m_{\tilde{t}_1, \tilde{t}_2, \tilde{b}_1, \tilde{b}_2}$ independent	0.6 – 50 TeV	$A_{t,b}$	–5000 – 5000
$\theta_{t,b}$	$-\pi/2 \rightarrow \pi/2$		

Table 5.4: STC8 particles not observed at the ILC with  $\sqrt{s} = 500$  GeV. All variables are varied uniformly within the indicated ranges. These assumptions are used in Fig. 5.9.

The reduction of the relic density would be removed by the observation of the heavy Higgses and the  $\tilde{\chi}_3^0, \tilde{\chi}_4^0$  and  $\tilde{\chi}_2^\pm$ . These would be pair produced and hence observed at the ILC with  $\sqrt{s} = 1$  TeV. Some could be observed in mixed production even at  $\sqrt{s} = 550$  GeV. Assuming a 1% uncertainty on the masses of the heavy Higgses,  $\tilde{\chi}_3^0, \tilde{\chi}_4^0$  and  $\tilde{\chi}_2^\pm$ , and keeping the previously used assumptions for the lighter sparticles, the relic density distribution has the same uncertainty as before, as can be seen from Fig. 5.10. All of the assumptions corresponding to this figure are listed in Tabs. 5.5 and 5.6. It does not matter whether the squark masses are varied or not. The centre of the relic

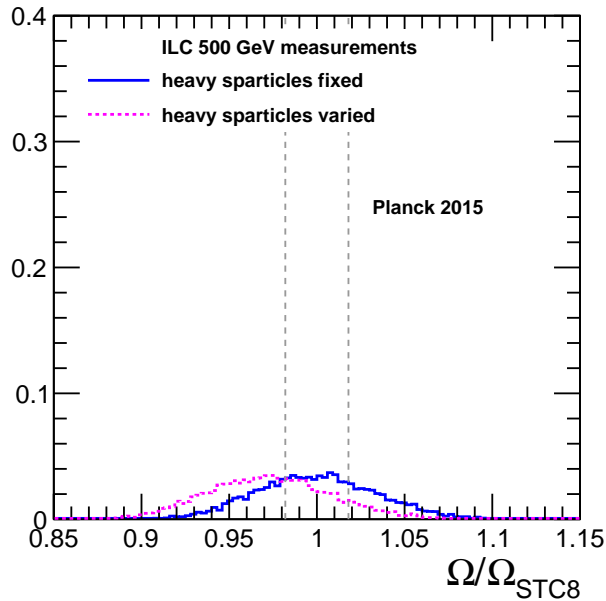


Figure 5.9: The distribution marked with a blue solid line contains variations of all possible observables from the 500 GeV ILC according to Tab. 5.3 and the rest of the spectrum is fixed. In the dashed pink distribution the same observations are assumed and the rest of the spectrum is allowed to vary uniformly according to Tab. 5.4. This lowers the mean predicted value by  $1\sigma$ .

density distribution falls on the model value in both cases and the uncertainty is the same as before. The uncertainty is still dominated by the 1% precision on  $N_{11}$ .

It was conservatively assumed that the precisions on the light particles would not improve with data from the  $\sqrt{s} = 1$  TeV ILC. This is not the case in reality: the precisions on masses would improve. In addition, the discovery of the full neutralino sector would decrease the uncertainty on the mixing properties of the LSP, which is the largest contributor to the relic density uncertainty. Currently there does not exist an analysis on the precisions of the 1 TeV measurements.

An observable that was not considered is the mixing angle of the  $CP$ -even Higgses. This would be well constrained after the discovery of the heavy Higgses and the determination of  $\tan\beta$  from the neutralino or chargino sector. Also the mixings of the  $\tilde{\chi}_2^0$ ,  $\tilde{\chi}_3^0$  and  $\tilde{\chi}_4^0$  were fixed to their true values. This was done because the mixing properties of the neutralinos are interlinked by the orthogonality of the neutralino mixing matrix, making it difficult to simultaneously vary all the elements consistently.

## 5.4 Conclusion

The ILC could discover SUSY scenarios with small mass differences. Scenarios with a stable bino LSP and an almost mass degenerate  $\tilde{\tau}$ ,  $\tilde{t}$  or  $\tilde{\chi}^\pm$  are among possible candidates which could explain the dark matter relic density that the Planck mission has measured. A stau coannihilation study was presented in this chapter. In the

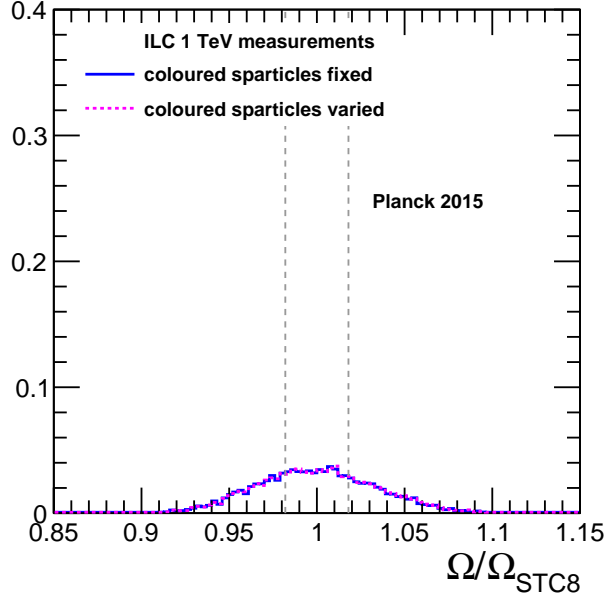


Figure 5.10: The assumptions used for this figure are listed in Tabs. 5.5 and 5.6. All sparticles except the squarks are assumed to be observed. The relic density is predicted to have the true value with a 3.4% uncertainty irrespective of whether the squarks are observed (red) or not (blue).

observable	uncertainty	observable	uncertainty
$m_{\tilde{e}_R}$	0.17%	$m_{\tilde{\mu}_R}$	0.40%
$m_{\tilde{e}_L}$	1%	$m_{\tilde{\mu}_L}$	1%
$m_{\tilde{\tau}_1}$	0.16%	$m_{\tilde{\tau}_2}$	2.5%
$\theta_\tau$	1%	$A_\tau$	20%
$m_{\tilde{\nu}_e, \tilde{\nu}_\mu, \tilde{\nu}_\tau}$	1%	$m_{\tilde{\chi}_1^\pm}$	1%
$m_{\tilde{\chi}_1^0}$	0.15%	$m_{\tilde{\chi}_2^0}$	0.5%
$N_{12,13,14}$	1% each	$Umix, Vmix$	20% each
$m_{\tilde{\chi}_3^0, \tilde{\chi}_4^0}$	1%	$m_{\tilde{\chi}_2^\pm}$	1%
$m_{H_0, A_0, H^\pm}$	1%		

Table 5.5: STC8 particles observed at the 1 TeV ILC. These assumptions are used in Fig. 5.10.

observable	range	observable	range
$m_{\tilde{d}_L, \tilde{u}_L, \tilde{s}_L, \tilde{c}_L}$ all equal	$1 \rightarrow 50$ TeV	$m_{\tilde{d}_R, \tilde{u}_R, \tilde{s}_R, \tilde{c}_R}$	$= m_{\tilde{d}_L} - 100$ GeV
$m_{\tilde{t}_1, \tilde{t}_2, \tilde{b}_1, \tilde{b}_2}$ independent	$0.6 \rightarrow 50$ TeV	$m_{\tilde{g}}$	$1 \rightarrow 50$ TeV
$\theta_{t,b}$	$0 \rightarrow \pi/2$	$A_{t,b}$	$0 \rightarrow -5000$

Table 5.6: STC8 particles not observed at the 1 TeV ILC. These assumptions are used in Fig. 5.10.

benchmark point considered, all sleptons, sneutrinos,  $\tilde{\chi}_1^0$ ,  $\tilde{\chi}_2^0$  and  $\tilde{\chi}_1^\pm$  could be discovered at the ILC at  $\sqrt{s} = 500$  GeV. Assuming these discoveries, the mixings of the  $\tilde{\tau}_1$  and the LSP would have to be measured to the percent-level precision to predict the relic density with an accuracy comparable to the current cosmological accuracy. The main mixing of the LSP dominates the uncertainty on the relic density prediction, since the masses of the LSP and the  $\tilde{\tau}_1$  would be measured so precisely. The squarks and the gluino do not have to be observed. Measuring the full neutralino and Higgs sectors with the ILC at  $\sqrt{s} = 1$  TeV would confirm or exclude the existence of other types of dark matter than the LSP.

As the mixing of the neutralino and of the  $\tilde{\tau}_1$  are important for the relic density but are not observables themselves directly, there is motivation to study the relic density via a SUSY parameter fit. The parameter fit allows us to consider the observables, e.g. the cross sections, without having to solve the complicated relationships of the observables for the mixings. This is one of the motivations for the parameter fits of STC models in the next chapter.

Another limitation of the study in this chapter is that the relic density calculator **MicrOMEGAs** calculates the SUSY cross sections at tree-level. This means that the importance of any unobserved particles is underestimated. Loop corrections to stau coannihilation diagrams can change the cross section by  $\sim 10\%$  [223]. The full set of one-loop SUSY corrections has been calculated with the program **SLOOPS** [223]. It would be possible to interface **SLOOPS** with **MicrOMEGAs** to improve improve the accuracy of the study. With the permille-level precision of the ILC measurements these loop corrections should be taken into account. Additionally, renormalisation group running uncertainties should be taken into account.

# Chapter 6

## Stau coannihilation scenario

In this chapter, four stau coannihilation benchmarks are studied by fitting pMSSM-13, pMSSM-4 or constrained SUSY models to ILC measurements. First the study is motivated, the benchmarks introduced and the prospects for SUSY measurements at ILC discussed. Then the fitting setup is laid out, after which results for the parameter fits are presented. Finally, it is investigated whether the high-scale behaviour of the fitted models can be tested and an outlook is given for directions of further study.

### 6.1 Motivation

We have learnt in the previous chapter that if certain measurements of SUSY particles are made, then it is possible to calculate the relic density and check whether the LSP is the only dark matter particle. This is not straightforward because the neutralino mixing properties play a crucial role and these are not directly observables themselves. Therefore, a fit of the mixing properties to suitable observables like polarised cross sections would be useful.

This chapter goes further: if we have the measurements of sleptons, sneutrinos and gauginos, what do we learn about the unobserved part of the spectrum? Could we decide which type of SUSY model these particles originate from? Would the results elucidate dark matter properties, not just the relic density but other astrophysical observables? What other predictions could be made?

To investigate the potential for conclusions from ILC coannihilation measurements, we have investigated several benchmark points, all with stau coannihilation but not all saturating the relic density. These benchmarks are introduced in the next section. The prospects for measurements in each benchmark are presented in Sec. 6.3 and the fit results of GUT models, pMSSM-13 and pMSSM-4 are presented in Sec. 6.5. As we will see in the case of another scenario in Ch. 7, the measurements may be sensitive to GUT scale information assuming no other new physics enters below the GUT scale. The prospects for this type of prediction from stau coannihilation are discussed in Sec. 6.7.

## 6.2 Benchmarks

The original STC8 benchmark was defined in [237]. The overall idea is that the benchmark provides an explanation of dark matter and the muon anomalous magnetic moment, and gives signals both at the ILC and the LHC. The benchmark parameter values originate from the mSUGRA model SPS1a [238] but STC8 is defined purely at the weak scale as a 13-parameter pMSSM point. SPS1a parameters were modified to avoid the exclusion limits from the LHC  $\sqrt{s} = 8$  TeV data set. STC8 has the correct Higgs mass and is consistent with flavour experiments as well as the LHC  $\sqrt{s} = 8$  TeV data set.

The parameters of STC are  $M_1$ ,  $M_2$ ,  $M_3$ ,  $\mu$ ,  $\tan\beta$ ,  $m_A$ , universal mass for the right-handed sleptons  $M_{E(1,2,3)}$ , a universal mass for the left-handed sleptons  $M_{L(1,2,3)}$ , a universal first and second generation squark mass  $M_{Q(1,2)} = M_{U(1,2)} = M_{D(1,2)}$ ,  $M_{Q(3)}$ ,  $M_{U(3)}$ ,  $M_{D(3)}$  and a common third-generation trilinear coupling  $A_t = A_b = A_\tau$ . Flavour mixing is set to zero, and flavour diagonal mixing is only allowed in the third generation. The values of the parameters were chosen to fine-tune the Higgs mass and the relic density to 100% of its observed value.

For the results in this chapter we have modified the STC8 benchmark. The reason is that the physical spectrum for the original benchmark was produced with an old `SPheno` version 3.1.4 [213] which decouples SUSY from SM at one single scale. This is not appropriate in STC because the electroweak and coloured sectors are at very different scales. Therefore, we use a newer version `SPheno 3.3.9beta3` which induces the need to modify the SUSY parameters slightly in order to get the same physical spectrum as in the original benchmark point. The parameters of both the original benchmark from Ref. [170] and the new adapted benchmark STC10' are listed in Tab. 6.1. All the sfermion mass parameters are modified slightly except  $M_{Q(1,2)}$ . Also  $A_t$  is modified.

In addition to studying the STC10' point with fully saturated relic density, we investigated coannihilation benchmarks in which the relic density is only partially filled by the LSP. In order to make a more generic statement on the prospects for predictions from the ILC, two new benchmark points were designed, STC10'- $\Omega 75$  and STC10'- $\Omega 50$ . Omega and the number indicate what approximate proportion of the relic density  $\Omega_{\text{Planck}} = 0.1199$  is filled by the LSP: in  $\Omega 75$  the percentage is around 75% and in  $\Omega 50$  51% as calculated by `MicrOMEGAs 2.4.5` [239]. The parameters for STC10'- $\Omega 75$  and STC10'- $\Omega 50$  are listed in Tab. 6.1. Both benchmarks have the same parameters as the STC10' apart from the trilinear coupling  $A_t$  and the right-handed slepton mass parameter  $M_{E(1,2,3)}$ . These parameters modify  $\tilde{\tau}_1$  mass which defines the efficiency of the coannihilation. If only one parameter was modified at a time, then the relic density would increase (with increasing  $M_{E(1,2,3)}$  or decreasing  $|A_t|$ ) or negative sfermion masses would occur (with decreasing  $M_{E(1,2,3)}$  or increasing  $|A_t|$ ). Thus both parameters were modified simultaneously. The right-handed slepton mass parameter is reduced from 118 to 110 GeV. The trilinear coupling is reduced from -2850 GeV to -2300 GeV in STC10'- $\Omega 75$  and to -2600 GeV in STC10'- $\Omega 50$ .

A fourth benchmark was introduced to bring this study more up-to date with respect to LHC limits on left-handed sleptons. The masses of the left-handed selectron and

parameter	STC8	STC10'	STC10'- $\Omega_{75}$	STC10'- $\Omega_{50}$
$\tan \beta$	10	10	10	10
$\mu$	400	400	400	400
$M_1$	100	100	100	100
$M_2$	210	210	210	210
$M_3$	2000	2000	2000	2000
$m_A$	400	400	400	400
$A_t = A_b = A_\tau$	-2400	<b>-2850</b>	<b>-2300</b>	<b>-2600</b>
$M_{Q(1,2)} = M_{U(1,2)} = M_{D(1,2)}$	2000	2000	2000	2000
$M_{Q(3)}$	1500	1450	1450	1450
$M_{U(3)}$	<b>800</b>	<b>1100</b>	1100	1100
$M_{D(3)}$	<b>800</b>	<b>1000</b>	1000	1000
$M_{L(1,2,3)}$	205	207	207	207
$M_{E(1,2,3)}$	119	<b>118</b>	<b>110</b>	<b>110</b>

Table 6.1: The definitions of stau coannihilation scenarios. The difference between the original STC8 benchmark and the modified ones denoted by a prime is the trilinear coupling and the slepton parameters. The right-handed third generation parameters were modified to correspond to the STC10 scenario in Ref. [170]. The  $M_{Q(3)}$  parameter was modified by 50 GeV as well. The versions for the reduced relic density, denoted by  $\Omega_{75}$  and  $\Omega_{50}$  are different in the trilinear coupling and  $M_{E(1,2,3)}$ .

smuon are excluded by LHC [124, 125], see also Sec. 2.8.1. This is not a problem as the parameter governing those masses,  $M_{L(1,2,3)}$ , can be split into two,  $M_{L(1,2)}$  and  $M_{L(3)}$ . The third-generation parameter is left the same to keep the mixing properties of the staus as before but  $M_{L(1,2)}$  takes the value 140 GeV, making  $\tilde{e}_L$  and  $\tilde{\mu}_L$  light enough to escape LHC limits. Now we have a pMSSM-14 instead of pMSSM-13. The parameters and their values are listed in Tab. 6.2.

parameter	STC10'-LH150
$\tan \beta$	10
$\mu$	400
$M_1$	100
$M_2$	210
$M_3$	2000
$m_A$	400
$A_t = A_b = A_\tau$	-2300
$M_Q(1, 2) = M_U(1, 2) = M_D(1, 2)$	2000
$M_Q(3)$	1450
$M_U(3)$	1100
$M_D(3)$	1000
$M_L(1, 2)$	140
$M_L(3)$	207
$M_E(1, 2, 3)$	118

Table 6.2: Parameters for a benchmark which avoids current LH slepton limits from LHC.

### SUSY masses

To understand the physical spectra in all the STC benchmarks, one can look at Tab. 6.3. The original benchmark STC8 was produced with `SPheno 3.1.4`. STC8 has all sleptons, sneutrinos,  $\tilde{\chi}_1^0$ ,  $\tilde{\chi}_2^0$  and  $\tilde{\chi}_1^\pm$  detectable with ILC  $\sqrt{s} = 500$  GeV. Going through them from lightest to heaviest, the lightest one is of course the bino neutralino with 96 GeV mass, and the lighter stau has 107 GeV mass. Right-handed selectron and smuon come next at 131 GeV and the rest are around 200 GeV. The adapted STC10' benchmark, part of whose mass spectrum is plotted in Fig. 6.1, has very similar masses to STC8.

With respect to STC10', the biggest difference in the reduced relic density points STC10'- $\Omega_{75}$  and STC10'- $\Omega_{50}$  is in the  $\tilde{\tau}_1$ . The  $\tilde{\tau}_1$  is only 9 GeV and 6 GeV heavier than the LSP in the STC10'- $\Omega_{75}$  and STC10'- $\Omega_{50}$  benchmarks respectively, enhancing the coannihilation as the mass difference gets smaller. The LSP mass remains the same within a 130 MeV range. The  $\tilde{e}_R$  and  $\tilde{\mu}_R$  masses are lowered in the reduced relic

density benchmarks. They are 7 GeV lower in STC10'- $\Omega$ 75 and STC10'- $\Omega$ 50 than in the original points, however the mass hierarchy remains the same and thus the the branching ratios are similar. The two of the sneutrinos get a lower mass but these have invisible decays in all benchmarks and can only be accessed via  $\tilde{\chi}_1^\pm$  decays to sneutrinos as discussed in Ch. 5.

observable	STC8	STC10'	STC10'- $\Omega$ 75	STC10'- $\Omega$ 50	STC10'-LH150
$m_{\tilde{\chi}_1^0}$	95.80	95.93	95.87	95.88	95.83
$m_{\tilde{\tau}_1}$	<b>106.95</b>	<b>107.36</b>	<b>104.46</b>	<b>101.91</b>	<b>111.41</b>
$m_{\tilde{\chi}_2^0}$	206.23	206.23	206.14	206.19	205.41
$m_{\tilde{\chi}_1^\pm}$	206.12	206.13	206.02	206.08	205.53
$m_{\tilde{\tau}_2}$	218.57	219.49	219.02	219.04	219.53
$m_{\tilde{e}_L}$	212.19	214.08	214.15	214.10	<b>150.62</b>
$m_{\tilde{e}_R}$	131.09	130.09	<b>123.00</b>	<b>122.99</b>	129.59
$m_{\tilde{\mu}_L}$	212.22	214.09	214.16	214.11	<b>150.70</b>
$m_{\tilde{\mu}_R}$	131.01	130.07	<b>122.98</b>	<b>122.96</b>	129.49
$m_{\tilde{\nu}_\tau}$	194.60	196.7	197.4	197.0	197.6
$m_{\tilde{\nu}_e}, m_{\tilde{\nu}_\mu}$	197.31	199.4	199.3	199.3	128.7
$m_h$	123.39	125.59	124.20	125.28	124.15
$m_{\tilde{t}_1}$	736	1010	1025	1042	1042
$m_{\tilde{b}_1}$	795	1008	1008	1008	1008
$m_{\tilde{g}}$	2042	2041	2041	2041	2041
$\Omega h^2$	0.113	0.1156	0.0894	0.0608	0.1337
$\Omega/\Omega_{\text{Planck}}$	94%	96%	75%	51%	112%

Table 6.3: Light sparticle masses in the various versions of the stau coannihilation benchmark.  $\Omega_{\text{Planck}}$  is 0.1199 [28]. The spectrum was calculated with `SPheno 3.1.4` for STC8 and with `SPheno 3.3.9beta3` for the other benchmarks. Higgs mass from `FeynHiggs 2.10.4` and relic density from `MicrOMEGAs 2.4.5`.

Finally for STC10'-LH150 the important SUSY masses are listed the last column of Tab. 6.3. Here the  $\tilde{\tau}_1$  mass difference to LSP is 16 GeV, making the relic density in slight excess of the observed amount. The key feature of this benchmark, though, is the lower left-handed selectron and smuon masses which at 150 GeV are not excluded by the LHC (c.f. 2.8.1). The mass hierarchy is the same as in the other benchmarks apart from  $\tilde{\nu}_e$  and  $\tilde{\nu}_\mu$  which now are as light as  $\tilde{e}_R$  and  $\tilde{\mu}_R$ , as can be seen from Fig. 6.2. This has some small impact on the branching ratios of the chargino and neutralinos which will be discussed below.

### SUSY cross sections

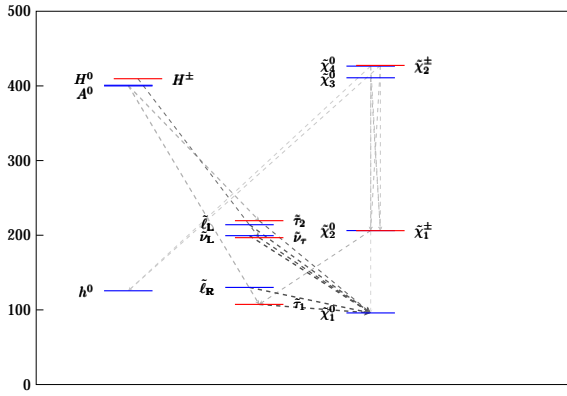


Figure 6.1: STC10' spectrum of masses below 500 GeV and arrows indicating branching fractions above 10%.

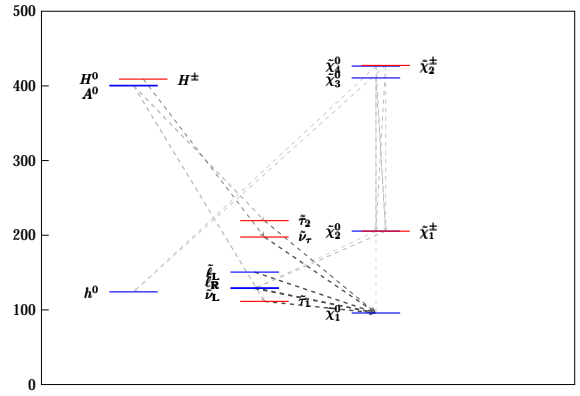


Figure 6.2: STC10'-LH150 spectrum of masses below 500 GeV and arrows indicating branching fractions above 10%.

The light SUSY particles will be produced in plentiful amounts at the ILC with  $\sqrt{s} = 500$  GeV. One can see the pair production cross sections with respect to the centre-of-mass energy and beam polarisation in Fig. 6.3. At  $\sqrt{s} = 500$  GeV, and for the polarisation combination  $\mathcal{P}(e^-, e^+) = (+80\%, -30\%)$ , the right-handed sleptons are produced with a 100 fb cross section. Even the smallest cross section, which is for the  $\tilde{\tau}_2$  pair production, is around 3 fb. Similarly, most electroweakino production cross sections are of the order 10 fb with some reaching several hundred fb if the polarisation is changed to  $\mathcal{P}(e^-, e^+) = (-80\%, +30\%)$ . As a general rule of thumb, the right-handed particles are produced more abundantly with  $\mathcal{P}(+80, -30)$  and left-handed particles with  $\mathcal{P}(e^-, e^+) = (-80\%, +30\%)$  beam polarisation combination.

The centre-of-mass energy does not need to be 500 GeV to discover some of the particles in this SUSY model. For LSP pair production and  $\tilde{\tau}_1$  pair production 250 GeV is enough. It is clear, however, that with the lower limits on charginos and staus from LEP, the higher the centre-of-mass energy, the more possible models can be discovered. All in all, if these particles exist with light enough masses to be produced, there are great prospects for studying these particles at the ILC [170].

### SUSY branching fractions

Despite the complicated and compressed spectrum in the STC models, the branching ratios are easy to understand. The slepton decays are listed in Tab. 6.4. The right-handed sparticles decay directly into the LSP and the corresponding lepton. The left-handed sparticles decay 95% of the time into a lepton and the LSP, with the remaining 5% divided between the  $\tilde{\chi}_1^\pm$  and  $\tilde{\chi}_2^0$  channels. The sneutrinos decay entirely to the LSP and a neutrino, except for  $\tilde{\nu}_\tau$  which has a 6% contribution from the  $\tilde{\nu}_\tau \rightarrow \tilde{\tau}_1 W$  channel. Broadly speaking, all the four considered models are the same within a few percentage points. The only exception is STC10'-LH150 where the mass hierarchy forces  $\tilde{e}_L$  and  $\tilde{\mu}_L$  to decay entirely to the LSP and a lepton.

The charginos have more decay channels available - see Tab. 6.5. In all the benchmarks except STC10'-LH150, the likeliest channel for the light chargino decay is  $\tilde{\chi}_1^\pm \rightarrow \tilde{\tau}_1 \nu_\tau$  with a share of about 70%. The next most probable channel is  $\tilde{\chi}_1^\pm \rightarrow \tilde{\nu}_\tau \tau^\pm$  with a branching fraction of 11%. The proportion of direct decay into the LSP with an

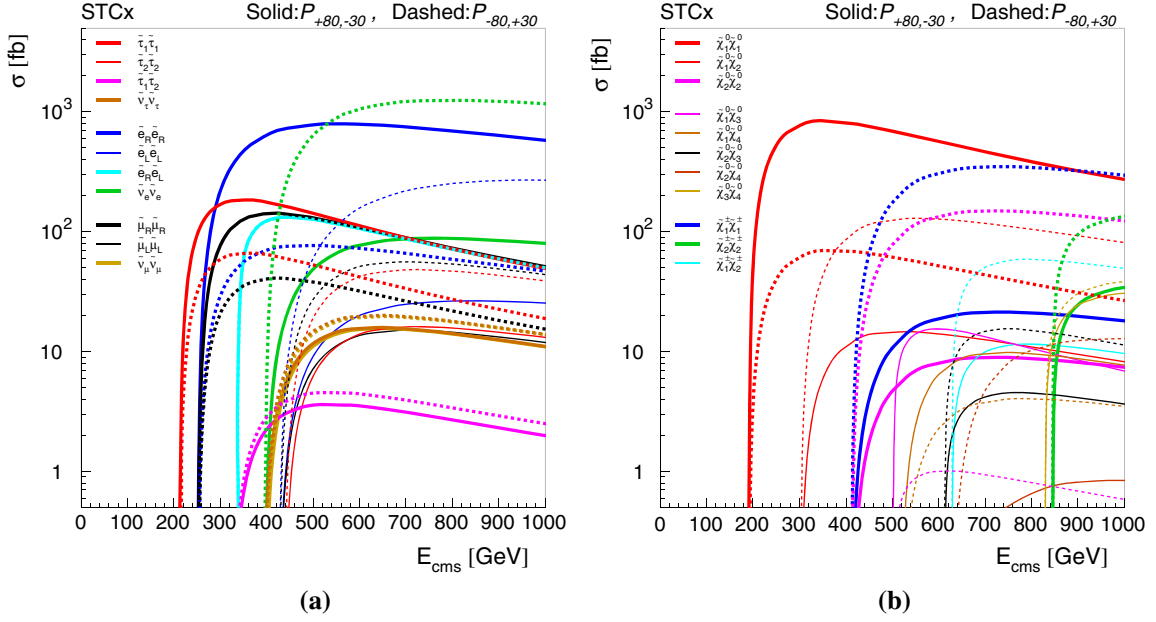


Figure 6.3: Plot of SUSY production cross sections for STC models in  $e^+e^-$  collisions as presented in Ref. [170]. At  $\sqrt{s} = 500$  GeV there are many processes available. At  $\sqrt{s} = 250$  GeV the phenomenology is restricted to  $\tilde{\tau}_1\tilde{\tau}_1$ ,  $\tilde{e}_R\tilde{e}_R$ ,  $\tilde{\mu}_R\tilde{\mu}_R$  and  $\tilde{\chi}_1^0\tilde{\chi}_1^0$  pair production.

associated  $W$ -boson is 7.2%. In STC10'-LH150, the decays into left-handed sfermions are enabled, both the selectron and smuon channel occupying 16% of the decay width. In STC10'-LH150, the electron and muon sneutrino channels are the likeliest decay channels with a 31% share each, while the  $\tilde{\chi}_1^\pm \rightarrow \tilde{\tau}_1\nu_\tau$  is suppressed to 4.5% compared with a 70% share in the other models.

The neutralino decays are listed in Tab. 6.6. Similarly here, the models are alike apart from STC10'-LH150. The most probable channel for  $\tilde{\chi}_2^0$  decays is  $\tilde{\tau}\tau$  with a  $\sim 75\%$  branching fraction, except when the decays into left-handed sleptons are enabled in STC10'-LH150. There the neutralino mainly decays into an  $\tilde{\nu}_e$  or  $\tilde{\nu}_\mu$  and a neutrino, or selectron or smuon and the corresponding lepton.  $\tilde{\chi}_3^0$  mainly decays into a chargino and a  $W$ , although decays into lighter neutralinos with an associated  $Z$  have a 30% probability.

### Higgs mass and branching fractions

The Higgs mass is adjusted to its measured value [3] in the STC10' point but for the purposes of the other points it is fixed to agree with the current LHC measurement if the 2 GeV theoretical uncertainty on the calculation of the SUSY Higgs mass is considered. The values are listed in Tab. 6.3. The branching fractions in each model are listed in Tab. 6.7. The light Higgs branching fractions are different from the branching fractions of the Standard Model Higgs with the same mass. This can be seen by using `FeynHiggs 2.10.4` [207] to calculate the Higgs mass and branching fractions based on the SUSY mass spectrum from `SPheno` and the branching fractions for a SM Higgs of the same mass as in the SUSY model. In STC10', the branching fractions into bosons are suppressed by 19% with respect to the Standard Model case. The  $c\bar{c}$  branching fraction is suppressed by 22%, while the  $b\bar{b}$  and  $\tau\tau$  are both enhanced by 11%. These

BR [%]	STC8	STC10'	STC10'- $\Omega 75$	STC10'- $\Omega 50$	STC10'-LH150
$\tilde{e}_R \rightarrow \tilde{\chi}_1^0 e$	100	100	100	100	100
$\tilde{\mu}_R \rightarrow \tilde{\chi}_1^0 \mu$	100	100	100	100	100
$\tilde{e}_L \rightarrow \tilde{\chi}_1^0 e$	95.3	92.4	92.1	92.3	100
$\tilde{\mu}_L \rightarrow \tilde{\chi}_1^0 \mu$	95.3	92.4	92.1	92.3	100
$\tilde{e}_L \rightarrow \tilde{\chi}_2^0 e$	1.7	2.7	2.8	2.7	—
$\tilde{\mu}_L \rightarrow \tilde{\chi}_2^0 \mu$	1.7	2.7	2.8	2.7	—
$\tilde{e}_L \rightarrow \tilde{\chi}_1^\pm \nu_e$	3.0	4.9	5.1	4.9	—
$\tilde{\mu}_L \rightarrow \tilde{\chi}_1^\pm \nu_\mu$	3.0	4.9	5.1	5.0	—
$\tilde{\nu}_{eL} \rightarrow \tilde{\chi}_1^0 \nu_e$	100	100	100	100	100
$\tilde{\nu}_{\mu L} \rightarrow \tilde{\chi}_1^0 \nu_\mu$	100	100	100	100	100
$\tilde{\tau}_1 \rightarrow \tilde{\chi}_1^0 \tau$	100	100	100	100	100
$\tilde{\tau}_2 \rightarrow \tilde{\chi}_1^0 \tau$	81.3	80.1	79.7	78.5	80.9
$\tilde{\tau}_2 \rightarrow \tilde{\chi}_2^0 \tau$	3.4	4.0	4.0	3.9	4.7
$\tilde{\tau}_2 \rightarrow \tilde{\chi}_1^\pm \nu_\tau$	6.2	7.3	7.4	7.1	8.5
$\tilde{\tau}_2 \rightarrow \tilde{\tau}_1 Z$	9.1	8.7	8.9	10.5	6.0
$\tilde{\nu}_{\tau L} \rightarrow \tilde{\chi}_1^0 \nu_\tau$	94.2	93.2	91.1	88.4	96.6
$\tilde{\nu}_{\tau L} \rightarrow \tilde{\tau}_1 W$	5.8	6.8	8.9	11.6	3.3

Table 6.4: Branching fractions of sleptons in the various STC models. All but first column are from SPheno3.3.9beta3. The first column is from SPheno3.1.4.

BR [%]	STC8	STC10'	STC10'- $\Omega 75$	STC10'- $\Omega 50$	STC10'-LH150
$\tilde{\chi}_1^+ \rightarrow \tilde{e}_L^+ \nu_e$	—	—	—	—	16.3
$\tilde{\chi}_1^+ \rightarrow \tilde{\mu}_R^+ \nu_\mu$	0.2	0.1	0.1	0.1	0.1
$\tilde{\chi}_1^+ \rightarrow \tilde{\mu}_L^+ \nu_\mu$	—	—	—	—	16.2
$\tilde{\chi}_1^+ \rightarrow \tilde{\tau}_1 \nu_\tau$	67.9	72.4	70.9	72.0	4.5
$\tilde{\chi}_1^+ \rightarrow \tilde{\nu}_e e^+$	6.6	4.8	5.3	5.0	30.9
$\tilde{\chi}_1^+ \rightarrow \tilde{\nu}_\mu \mu^+$	6.6	4.8	5.3	5.0	30.9
$\tilde{\chi}_1^+ \rightarrow \tilde{\nu}_\tau \tau^+$	11.3	9.2	8.6	8.9	0.5
$\tilde{\chi}_1^+ \rightarrow \tilde{\chi}_1^0 W^+$	7.2	8.6	9.6	9.0	0.6
$\tilde{\chi}_2^+ \rightarrow \tilde{e}_L^+ \nu_e$	4.6	4.5	4.5	4.5	5.9
$\tilde{\chi}_2^+ \rightarrow \tilde{\mu}_L^+ \nu_\mu$	4.6	4.5	4.5	4.5	5.9
$\tilde{\chi}_2^+ \rightarrow \tilde{\tau}_2 \nu_\tau$	5.1	4.9	4.9	4.9	4.7
$\tilde{\chi}_2^+ \rightarrow \tilde{\nu}_e e^+$	1.7	1.7	1.7	1.7	2.1
$\tilde{\chi}_2^+ \rightarrow \tilde{\nu}_\mu \mu^+$	1.7	1.7	1.7	1.7	2.1
$\tilde{\chi}_2^+ \rightarrow \tilde{\nu}_\tau \tau^+$	2.5	2.3	2.3	2.3	2.2
$\tilde{\chi}_2^+ \rightarrow \tilde{\chi}_1^0 W^+$	7.8	7.6	7.6	7.6	7.3
$\tilde{\chi}_2^+ \rightarrow \tilde{\chi}_2^0 W^+$	2.8	28.5	28.5	28.5	27.2
$\tilde{\chi}_2^+ \rightarrow \tilde{\chi}_1^+ Z$	25.0	25.2	25.2	25.2	24.2
$\tilde{\chi}_2^+ \rightarrow \tilde{\chi}_1^+ h^0$	18.8	19.0	19.0	19.0	18.3

Table 6.5: Branching fractions of charginos in the various STC models in percentages. All but first column are from `SPheno3.3.9b3`. The first column is from `SPheno3.1.4`. The decays of the sleptons in STC10'-LH150 are effectively as they would be in a simplified model.

BR [%]	STC8	STC10'	STC10'- $\Omega 75$	STC10'- $\Omega 50$	STC10'-LH150
$\tilde{\chi}_2^0 \rightarrow \tilde{e}_R^\pm e^\mp$	2.6	2.6	3.3	3.1	0.2
$\tilde{\chi}_2^0 \rightarrow \tilde{e}_L^\pm e^\mp$	—	—	—	—	19.1
$\tilde{\chi}_2^0 \rightarrow \tilde{\mu}_R^\pm \mu^\mp$	2.4	2.6	3.4	3.2	0.36
$\tilde{\chi}_2^0 \rightarrow \tilde{\mu}_L^\pm \mu^\mp$	—	—	—	—	18.9
$\tilde{\chi}_2^0 \rightarrow \tilde{\tau}_1^\pm \tau^\mp$	73.3	77.4	75.5	76.4	5.3
$\tilde{\chi}_2^0 \rightarrow \tilde{\nu}_e \nu_e$	5.7	4.0	4.5	4.2	27.8
$\tilde{\chi}_2^0 \rightarrow \tilde{\nu}_\mu \nu_\mu$	5.7	4.0	4.5	4.2	27.8
$\tilde{\chi}_2^0 \rightarrow \tilde{\nu}_\tau \nu_\tau$	9.5	7.7	7.2	7.4	4.3
$\tilde{\chi}_2^0 \rightarrow \tilde{\chi}_1^0 Z$	1.2	1.3	1.5	1.4	0.1
$\tilde{\chi}_3^0 \rightarrow \tilde{\chi}_1^\pm W^\mp$	58.4	58.8	58.7	58.7	58.4
$\tilde{\chi}_3^0 \rightarrow \tilde{\chi}_1^0 Z$	10.3	10.2	10.2	10.2	10.1
$\tilde{\chi}_3^0 \rightarrow \tilde{\chi}_2^0 Z$	23.2	23.5	23.4	23.4	23.3
$\tilde{\chi}_3^0 \rightarrow \tilde{\chi}_1^0 h^0$	2.2	2.2	2.2	2.2	2.2
$\tilde{\chi}_3^0 \rightarrow \tilde{\chi}_2^0 h^0$	1.2	1.2	1.2	1.2	1.2

Table 6.6: Branching fractions of neutralinos in the various STC models. All but first column are from `SPheno3.3.9b3`. The first column is from `SPheno3.1.4`.

BR [%]	STC10'	STC10'- $\Omega 75$	STC10'- $\Omega 75$	STC10'-LH150
$h \rightarrow ZZ$	0.0234	0.0207	0.0228	0.0206
$h \rightarrow WW$	0.1908	0.1744	0.1874	0.1731
$h \rightarrow b\bar{b}$	0.6335	0.6489	0.6360	0.6494
$h \rightarrow gg$	0.0542	0.0561	0.0550	0.0561
$h \rightarrow \gamma\gamma$	0.0019	0.0019	0.0019	0.0018
$h \rightarrow \tau\tau$	0.0713	0.0723	0.0716	0.0730
$h \rightarrow c\bar{c}$	0.0232	0.0242	0.0235	0.0243

Table 6.7: Branching fractions of the light Higgs in the STC models. All values are from `FeynHiggs2.10.4`.

deviations are plotted in Fig. 6.4 showing the predicted ILC precisions after the H20 operating scheme. The individual branching fractions disagree with the SM maximally by  $30\sigma$  in the  $ZZ$  channel and minimally by  $6\sigma$  in the  $\tau\tau$  channel. As a goodness-of-fit test, the  $\chi^2/d.o.f.$  value  $\sum_i (\text{BF}_i^{\text{SUSY}} - \text{BF}_i^{\text{SM}}/\sigma_i^{\text{ILC}})^2/d.o.f.=240$  for the 7 degrees of freedom in the H20 scenario. Thus, measurements of SUSY particles would not be needed to confirm that the light Higgs is not the SM Higgs. If the ILC had an initial stage of  $\sqrt{s} = 250$  GeV with  $2000 \text{ fb}^{-1}$  and the polarisation divide as in H20 (see Ch. 3 and Ref. [153]), then the goodness-of-fit value is 104. Also in this case the SM Higgs would be ruled out.

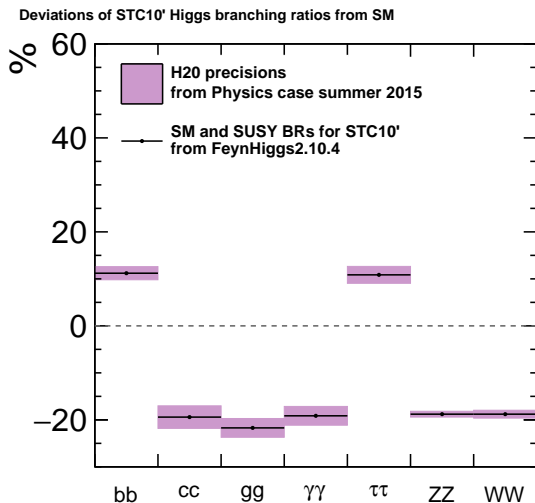


Figure 6.4: Deviations of the Higgs BRs in the STC10' model. All branching fractions are suppressed by 20% except  $bb$  and  $\tau\tau$ , which are both enhanced by 15%.

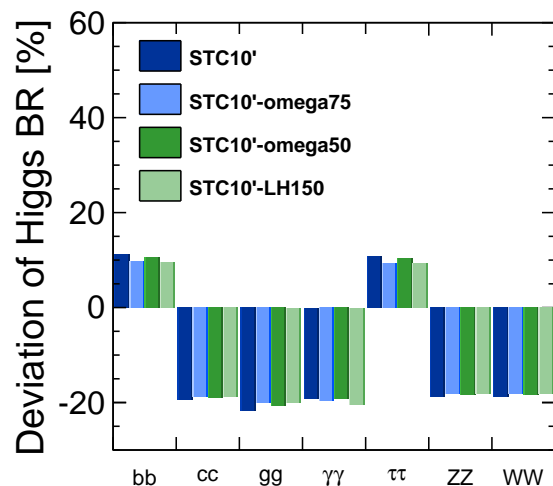


Figure 6.5: Comparison of the Higgs BR deviations in the different benchmarks. For all the benchmarks, the branching fractions are the same as in STC10' within about 2%.

The Higgs branching ratios are very similar in all the models, see Fig. 6.5. The largest differences between the models are within two percentage points.

As the Higgs branching fraction deviations are quite large in the STC10' benchmark point, the source of the deviations was investigated. The deviations originate from the light extended Higgs sector. If  $m_A$  is moved up from 400 GeV to 1 TeV, the Higgs branching ratios change, and the  $\chi^2$  for this model with respect to the  $m_A = 400$  GeV observables is 3604.2. The Higgs mass moves up by 190 MeV and the Higgs branching ratios get modified: the maximal deviation is still in the  $gg$  channel but its size is reduced to -4.8%. All channels see deviations but less so than in STC10' with  $m_A = 400$  GeV. It would be possible to adjust the benchmarks to accommodate this, and in fact, the current limits of the heavy Higgs mass from ATLAS and CMS for  $\tan\beta = 10 - 15$  require  $m_A > 300 - 800$  GeV [127, 247], as briefly mentioned in Sec. 2.8.1.

### Dark matter properties

The model values for the relic density, spin-independent WIMP-nucleon scattering

cross section (direct detection) and thermally averaged WIMP annihilation cross section (indirect detection) are listed in Tab. 6.8. The direct and indirect detection cross sections are plotted in Figs. 6.6 and 6.7 along with the current and future exclusion plots from WIMP experiments. For the direct detection plot in Fig. 6.6 the model cross sections have been scaled by  $\xi = \Omega_{LSP}/\Omega_{Planck} = \Omega_{LSP}/0.1199$ . Similarly for the indirect detection in Fig. 6.7, the cross section has been scaled by  $\xi^2$ .

observable	STC10'	STC10'- $\Omega_{75}$	STC10'- $\Omega_{50}$	STC10'-LH150
$\Omega h^2$	0.1156	0.0894	0.0608	0.1337
$\Omega/\Omega_{Planck}$	96%	75%	51%	112%
$\langle\sigma v\rangle[10^{-27}\text{cm}^3\text{s}^{-1}]$	2.10	1.76	2.11	1.53
$\xi^2\langle\sigma v\rangle[10^{-27}\text{cm}^3\text{s}^{-1}]$	1.95	0.979	0.542	1.90
$\sigma^{SI}[10^{-9}\text{pb}]$	2.24	2.27	2.24	2.28
$\xi\sigma^{SI}[10^{-45}\text{cm}^2]$	2.16	1.69	1.14	2.41

Table 6.8: Relic density from MicrOMEGAs2.4.5, and direct and indirect detection cross sections from Astrofit in the various versions of the stau coannihilation benchmark.  $\Omega_{Planck}$  is 0.1199 [28].

From the direct detection plot it can be seen that LUX2016 should have detected some signal in the STC10' models. This clearly did not happen [248], meaning that these models are excluded if the cosmological assumptions in the interpretation of the LUX data are correct. If the assumptions are true, then the direct detection cross section should somehow be suppressed in order to avoid this exclusion. The indirect detection experiments need another factor 10 in sensitivity before the STC10' would cause a signal.

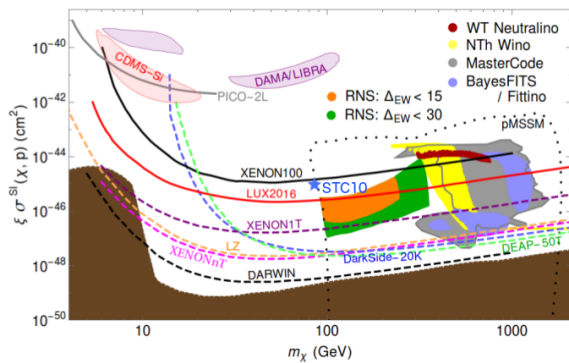


Figure 6.6: Exclusion limits for direct detection (WIMP spin-independent nucleon scattering cross section times fraction of Planck relic density satisfied by the LSP) vs. LSP mass. Figure from [112] with the STC10' point added.

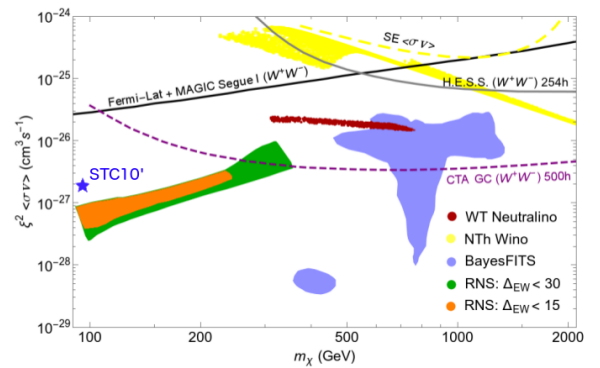


Figure 6.7: Exclusion limits for indirect WIMP detection (WIMP annihilation cross section times the square of the fraction of Planck relic density satisfied by LSP) vs. LSP mass. Figure from [112] with the STC10' point added.

## Flavour observables

With reference to Tab. 6.9, the measured rates  $b \rightarrow s\gamma$  and  $B_s \rightarrow \mu^+\mu^-$  are satisfied by all the four points. The rate of  $B \rightarrow \tau\nu$  is not, it is too small by  $2.3\sigma$ . The anomalous magnetic moment of the muon  $a_\mu$  is correct by design, except  $1\sigma$  too high for the LH150 point. These flavour observables are not discussed further in this chapter except for the outlook in the last section.

flavour obs.	PDG2017	STC10'	STC10'- $\Omega_{75}$	STC10'- $\Omega_{50}$	STC10'-LH150
$BR(b \rightarrow s\gamma)[10^{-4}]$	$(3.49 \pm 0.19)$	3.60	3.70	3.65	3.70
$BR(B_s \rightarrow \mu\mu)[10^{-9}]$	$(2.4_{-0.7}^{+0.9})$	3.36	3.31	3.33	3.31
$BR(B \rightarrow \tau\nu)[10^{-4}]$	$(1.09 \pm 0.24)$	0.786	0.786	0.786	0.786
$a_\mu[10^{-9}]$	$(2.88 \pm 0.80)$	2.54	2.60	2.60	3.86

Table 6.9: Flavour observables in the different models from SuperISO [209].

### 6.3 Prospects for measurements at ILC

The prospects for measurements at ILC for the STC8 original benchmark point were discussed in Ch. 5. The mass measurement precisions are printed again in Tab. 6.10. Masses of the accessible particles can be measured to 1% or better with  $\sqrt{s} = 500$  GeV for a data set of  $500 \text{ fb}^{-1}$  for both polarisations  $\mathcal{P}(e^-, e^+) = (\pm 80\%, \mp 30\%)$ .

The prospects for measurements in the STC10'- $\Omega_{75}$  and STC10'- $\Omega_{50}$  should be analogous to STC10' as the phenomenology is nearly the same. The only differences will be brought by the softer decay products in the reduced relic density points as the mass of the  $\tilde{\tau}_1$  gets closer to the mass of the LSP. The background changes to be softer as well. In principle the analysis is similar and it should be reasonable to expect a comparable precision of the  $\tilde{\tau}_1$ -LSP edge as in the original benchmark point. For the other mass measurements a similar argument applies.

While measuring SUSY masses, cross section measurements can be made by counting the event rates. The prospects were discussed in Ch. 5. The projections for cross section measurements at the ILC are listed in Tab. 6.11. The production cross sections uncertainties are expected to be around 1-5% for  $2 \times 500 \text{ fb}^{-1}$  - see Tab. 6.11 for the precise numbers.

### 6.4 Expected measurements from LHC

The STC8 and STC10 points were designed to cause a signal at the LHC or HL-LHC. The  $\tilde{b}_1 \rightarrow b\tilde{\chi}_1^0$  decay would give a  $5\sigma$  discovery signal after  $9 \text{ fb}^{-1}$  in STC8 and  $300 \text{ fb}^{-1}$  in STC10. Additional signals will be seen in the multilepton channel and the inclusive hadronic channel with  $b$ -tag [170]. A measurement of the  $\tilde{b}_1$  mass will be possible in

observable	uncertainty	observable	uncertainty
$m_{\tilde{\chi}_1^0}$	0.15%	$m_{\tilde{\chi}_1^\pm}$	1%
$m_{\tilde{\tau}_1}$	0.16%	$m_{\tilde{\nu}_e, \tilde{\nu}_\mu, \tilde{\nu}_\tau}$	1%
$m_{\tilde{e}_R}$	0.17%	$m_{\tilde{e}_L}$	1%
$m_{\tilde{\mu}_R}$	0.40%	$m_{\tilde{\mu}_L}$	1%
$m_{\tilde{\chi}_2^0}$	0.5%		
$m_{\tilde{\tau}_2}$	2.5%		

Table 6.10: Uncertainties of SUSY mass measurements at the ILC with  $\sqrt{s} = 500$  GeV after  $500 \text{ fb}^{-1}$  for both  $\mathcal{P}(e^-, e^+) = (\pm 80\%, \mp 30\%)$ . Values in the left column are from the analysis in [170]. Values in the right column are estimates from the same paper. This table corresponds to Tab. 5.3 used in the previous chapter, except that the inputs on the mixing angles used in that chapter are not considered here.

Polarisation	Process	Uncertainty
(-80%, +30%)	$\sigma(e^+e^- \rightarrow \tilde{\chi}_1^0 \tilde{\chi}_2^0) \times BR(\tilde{\chi}_2^0 \rightarrow \tilde{\mu}_R \mu) \times BR(\tilde{\mu}_R \rightarrow \mu \tilde{\chi}_1^0)$	20%* [242]
	$\sigma(e^+e^- \rightarrow \tilde{\chi}_1^0 \tilde{\chi}_2^0) \times BR(\tilde{\chi}_2^0 \rightarrow \tilde{\tau}_1 \tau) \times BR(\tilde{\tau}_1 \rightarrow \tau \tilde{\chi}_1^0)$	2%** [241]
	$\sigma(e^+e^- \rightarrow \tilde{\tau}_1 \tilde{\tau}_1 \rightarrow \tau \tilde{\chi}_1^0 \tau \tilde{\chi}_1^0)$	3.1% [171]
( +80%, -30%)	$\sigma(e^+e^- \rightarrow \tilde{\mu}_R \tilde{\mu}_R)$	0.8% [249]
	$\sigma(e^+e^- \rightarrow \tilde{e}_R \tilde{e}_R)$	0.4% [249]

Table 6.11: Precisions of cross section measurements from ILC  $\sqrt{s} = 500$  GeV after  $500 \text{ fb}^{-1}$  for  $\mathcal{P}(e^-, e^+) = (\pm 80\%, \mp 30\%)$ . \*The original study was done for  $\mathcal{P} = (-80\%, 60\%)$  where the cross section is 25% larger than for  $\mathcal{P} = (-80\%, 30\%)$ . 20% was the upper limit on the precision from the quoted study so this is adopted as the best case scenario for the current polarisation. \*\*The quoted study assumed zero polarisation for both beams, and changing to LR polarisation increases the cross section so the results of the quoted study can be adopted here.

STC10 with a HL-LHC data set of  $3000 \text{ fb}^{-1}$ . The measured mass would have a 15% uncertainty for the  $\tilde{b}_1$  [170].

## 6.5 Parameter fits

The overarching theme of this thesis continues here: What is the largest possible amount of information that can be inferred from SUSY precision measurements at the ILC? We have investigated this in the various stau coannihilation scenarios introduced in the previous sections. This section describes the technical details of the parameter fits: what is the software setup, which models are fitted and which input observables are used.

### 6.5.1 Fitting setup

SUSY parameters were fitted to the projected observables from the ILC using `Fittino1` [201]. The SUSY particle spectrum, cross sections and branching ratios were calculated with `SPheno 3.3.9beta3` [206, 213] and Higgs sector masses and branching ratios with `FeynHiggs 2.10.4` [207]. The dark matter relic density was calculated with `MicrOMEGAs 2.4.5` [239], but the direct and indirect detection cross sections were calculated with `Astrofit` [208]. The details of the used software are discussed in Ch. 4.

The fits were started from near the true model point. As discussed in Ch. 4, it would be possible to find starting values for the fit parameters from ILC observables only (using the method in Ref. [201]), except for the coloured sector parameters. Then, assuming a long enough Markov Chain, the fit would find the absolute minimum, if there is one, and eventually scan it thoroughly. Here this phase is skipped and it is assumed that an initial parameter sweep would direct us to start the fit near the model parameter values.

The fits consist of 1-4 million Markov Chain points combined from fits of the length 100 000 points per chain. The constituent fits have slightly different input parameters: the central values of most parameters are the model values but two parameters are shifted up or down by 5 or 10%. The input uncertainty of the parameters is always 1%. Then the fit picks starting values using these probability distributions as discussed in Ch. 4.

### 6.5.2 Fitted models

A priori we do not know which model the measured SUSY properties originate from. It is commonly thought that the pMSSM takes into account the limited computing power available and yet would accommodate most  $CP$ -conserving, non-flavour violating MSSM models. With no hint of coloured sector particles but sleptons having been observed, clearly the slepton and squark sectors need to have their own parameters. However, as the sleptons are found at similar masses, it is reasonable to fit universal

slepton parameters for the left-handed sleptons and for the right-handed sleptons, as long as the minimum  $\chi^2$  from the fit is still reasonably small. Due to the dependence of the Higgs mass on the third generation squarks, the third generation squarks should be split from the first and second generation squarks. There is not much need for separate squark mass parameters for the first and second generation.

With the above reasoning, we fit the following model of pMSSM-13:  $M_1, M_2, M_3, \mu, \tan \beta, m_A, M_{Q(1,2)} = M_{U(1,2)} = M_{D(1,2)}, M_{Q(3)}, M_{U(3)}, M_{D(3)}, M_{L(1,2,3)}, M_{E(1,2,3)}$ , and  $A_{t=b=\tau}$ . Other trilinear couplings are set to zero. If there is a hint that some of the slepton generations are not unified then one can fit pMSSM-14, where the third generation left-handed slepton mass is independent of the first two generations, i.e.  $M_{L(1,2,3)} \rightarrow M_{L(1,2)}, M_{L(3)}$ . All the parameters are defined and fitted at the energy scale  $Q = 1$  TeV.

If the sleptons are discovered at low mass while the squarks are excluded at that mass, then it is clear that a constrained model is not the truth. To quantify the disagreement, the constrained models CMSSM, NUHM1 and NUHM2 were fitted. The parameters are the following: CMSSM  $M_0, M_{1/2}, A_0, \tan \beta$  (and  $\text{Sign}\mu$ ); NUHM1  $M_0, M_{1/2}, A_0, \tan \beta, MH^0$ ; NUHM2  $M_0, M_{1/2}, A_0, \tan \beta, \mu$  and  $m_A$ . These parameters are defined and fitted at the GUT scale (gauge coupling unification scale) except for  $\tan \beta, m_A$  and  $\mu$  which are defined and fitted at  $Q = 100$  GeV.

### 6.5.3 Fit inputs or observables

The fits have been performed with three different kinds of input options: SUSY masses, Higgs observables and SUSY cross sections times branching fractions. Care has been taken that the inputs and precisions are as realistic as possible.

The fit inputs in most fits consist of the ILC SUSY masses and Higgs mass and branching fraction measurements. The SUSY masses are assumed to be measured with their model values and with the relative uncertainties from Tab. 6.12. The precisions in the table were determined with  $2 \times 500 \text{ fb}^{-1}$  data set from the ILC. These fit inputs are called “All SUSY+h” or “All SUSY” depending whether Higgs mass and branching fractions were used. Another version of the fits was done with a subset of the SUSY mass inputs using only the LSP,  $\tilde{\tau}_1, \tilde{e}_R$  and  $\tilde{\mu}_R$  masses and the Higgs measurements. These fit inputs, which correspond to the scenario where the ILC initial operating energy is 250 GeV, are called “Min SUSY+h”.

The input precisions would vary during the time of the ILC operation, and  $\mathcal{L} = 2 \times 500 \text{ fb}^{-1}$  at  $\sqrt{s} = 500$  GeV will not be the final data set. Thus, some fits were done using a scaled set of precisions to investigate the dependence on the precisions themselves. Those fits correspond to data sets of  $2 \times 20 \text{ fb}^{-1}$ , and  $2 \times 2000 \text{ fb}^{-1}$ . The corresponding precisions for the fit inputs are listed in Tab. 6.13.

The Higgs mass and branching ratios were used with the true SUSY model values from `FeynHiggs` and the precisions from ILC H20 projections as introduced in Ch. 3.1.3 and listed in Tabs. 6.12 and 6.13 for each fit. Some of the fits use the SUSY cross sections times branching fraction measurements from Tab. 6.11.

observable	All SUSY+h	All SUSY	Min SUSY+h
$m_{\tilde{\chi}_1^0}$	0.15%	0.15%	0.15%
$m_{\tilde{\tau}_1}$	0.16%	0.16%	0.16%
$m_{\tilde{\chi}_1^\pm}$	1%	1%	—
$m_{\tilde{\chi}_2^0}$	0.5%	0.5%	—
$m_{\tilde{e}_R}$	0.17%	0.17%	0.17%
$m_{\tilde{\mu}_R}$	0.40%	0.40%	0.40%
$m_{\tilde{e}_L}$	1%	1%	—
$m_{\tilde{\mu}_L}$	1%	1%	—
$m_{\tilde{\nu}_e, \tilde{\nu}_\mu, \tilde{\nu}_\tau}$	1%	1%	—
$m_{\tilde{\tau}_2}$	2.5%	2.5%	—
$m_h$	15 MeV	—	15 MeV
$BR(h \rightarrow ZZ)$	0.62%	—	0.62%
$BR(h \rightarrow WW)$	0.84%	—	0.84%
$BR(h \rightarrow b\bar{b})$	1.4%	—	1.4%
$BR(h \rightarrow gg)$	2.0%	—	2.0%
$BR(h \rightarrow \gamma\gamma)$	2.0%	—	2.0%
$BR(h \rightarrow \tau\tau)$	1.8%	—	1.8%
$BR(h \rightarrow c\bar{c})$	2.4%	—	2.4%
# observables	20	12	13

Table 6.12: Fit input uncertainties for STC fits. Dash means that the observable was not used. Note that the sneutrino masses constitute three observables.

Observable	All SUSY+h	All SUSY5x+h	All SUSY0.5x+h
$m_{\tilde{\chi}_1^0}$	0.15%	0.75%	0.08%
$m_{\tilde{\tau}_1}$	0.16%	0.80%	0.08%
$m_{\tilde{\chi}_1^\pm}$	1%	5%	0.5%
$m_{\tilde{\chi}_2^0}$	0.5%	2.5%	0.5%
$m_{\tilde{e}_R}$	0.17%	0.85%	0.09%
$m_{\tilde{\mu}_R}$	0.40%	2.0%	0.20%
$m_{\tilde{e}_L}$	1%	5%	0.5%
$m_{\tilde{\mu}_L}$	1%	5%	0.5%
$m_{\tilde{\nu}_e, \tilde{\nu}_\mu, \tilde{\nu}_\tau}$	1%	5%	0.5%
$m_{\tilde{\tau}_2}$	2.5%	12.5%	1.3%
$m_h$	15 MeV	15 MeV	15 MeV
$BR(h \rightarrow ZZ)$	0.62%	0.62%	0.62%
$BR(h \rightarrow WW)$	0.84%	0.84%	0.84%
$BR(h \rightarrow b\bar{b})$	1.4%	1.4%	1.4%
$BR(h \rightarrow gg)$	2.0%	2.0%	2.0%
$BR(h \rightarrow \gamma\gamma)$	2.0%	2.0%	2.0%
$BR(h \rightarrow \tau\tau)$	1.8%	1.8%	1.8%
$BR(h \rightarrow c\bar{c})$	2.4%	2.4%	2.4%

Table 6.13: Fit input uncertainties for fits testing the importance of the precision measurements. The first column corresponds to  $2 \times 500 \text{ fb}^{-1}$  for  $\mathcal{P}(\pm 80\%, \mp 30\%)$  at  $\sqrt{s} = 500 \text{ GeV}$  as in Ref. [170]. If the selection efficiency is assumed to be constant for a smaller and larger data set then the statistical uncertainties in columns 3 and 4 correspond to data sets of  $2 \times 20 \text{ fb}^{-1}$  and  $2 \times 2000 \text{ fb}^{-1}$  respectively. The Higgs precisions are not scaled in order to study the effect of the SUSY precisions only.

Standard Model parameters are fixed according to the example Les Houches input files in Appendix B.

It should be noted that none of the dark matter observables discussed in Sec. 6.2 are used as inputs. Rather their predicted values are saved in the fit for comparison to the model values. The flavour observables are not used or saved due saving computing power and due to the interface of `Fittino` to `SuperISO` [209] being outdated.

## 6.6 Fit results

This section answers which parameters can be fitted, which unobserved particle masses can be predicted, which dark matter properties can be predicted, and what can be said about physics beyond the TeV scale. Next, the results for the GUT model fits (CMSSM, NUHM1 and NUHM2) are discussed, before proceeding on to the pMSSM fit results.

### 6.6.1 GUT model fits to STC10' observables

The STC10' benchmark points are defined in the pMSSM without any assumption of GUT unification. It is interesting to check whether a more constrained model than the pMSSM would describe the hypothesised ILC measurements.

It is easy to see that GUT models should fit the STC observations badly. As the most common GUT models CMSSM, NUHM1 and NUHM2 all assume a unified sfermion mass  $M_0$ , this implies that along with the sleptons, the squarks should be discovered. In fact, just the knowledge of a single slepton mass would require all sfermions to have that mass. In addition, as the supersymmetric gauge sector should be unified in these models, after the bino and wino discovery, the gluino should be found at 4 times the bino mass (famous relation  $M_1 : M_2 : M_3 = 1 : 2 : 4$ ). This mass, around 400 GeV, is strongly excluded by the LHC searches (see e.g. [250, 251]). Additional limits come from  $b \rightarrow \gamma s$  decays, see e.g. [252].

The remaining question is then how badly do these GUT models fit the observations? To answer this, we performed a fit of each of CMSSM, NUHM1 and NUHM2 to the hypothetical STC10' SUSY mass measurements including all sleptons, sneutrinos and  $\tilde{\chi}_1^0, \tilde{\chi}_2^0$  and  $\tilde{\chi}_1^\pm$ . Additionally, the standard Higgs mass and branching ratios were used. It should be noted that none of the limits on the coloured sector or the extended Higgs sector were explicitly used. The inputs correspond to the All SUSY+h column in Tab. 6.12. The fit length was  $10^6$  points combined from 10 separate fits with the same starting values.

The best  $\chi^2$  values for the fits can be found in Tab. 6.14. The best  $\chi^2$  value for each of the CMSSM, NUHM1 and NUMH2 fit is roughly the same,  $2.6 \times 10^5$ . There are 20 input observables and 4 free parameters in the CMSSM fit. This makes the reduced chi-squared  $\chi^2/\text{d.o.f.} = 16100$ .

The largest individual contributions from the observables to the  $\chi^2$  are from the Higgs mass ( $463^2$ ) and from the LSP mass ( $118^2$ ). Both the SUSY measurements as well

as the Higgs measurements are in disagreement with this best fit point. It should be emphasised again that this poor fit of CMSSM is obtained without explicit inclusion of the squark exclusion limits and heavy Higgs limits.

For the NUHM1 model there are 5 free parameters and thus the  $\chi^2/\text{d.o.f.}$  is slightly worse than in the CMSSM case. In NUHM2, there are 6 free parameters and the goodness-of-fit is worse than in the other models. In both of these cases, introduced freedom in the Higgs sector does not lower the best fit  $\chi^2$  indicating further that the observables are sensitive to the squarks not being at the sfermion energy scale.

$\chi^2/\text{d.o.f.}$	All SUSY+h
CMSSM	257700/16 = 16100
NUHM1	257300/15 = 17200
NUHM2	257600/14 = 18400

Table 6.14: The best  $\chi^2$  values for fits of constrained models to STC10'. The fit inputs including all SUSY masses and Higgs measurements contain 13 mass and 7 branching fraction inputs, all assumed to be independent measurements. The number of fitted parameters is 4 for CMSSM, 5 for NUHM1 and 6 for NUHM2 so then dof is 20-4/5/6=16, 15, 14.

best fit	$M_{1/2}$	$M_0$	$A_0$	$\tan\beta$	$M_{H^0}$	$\mu$	$m_A$
CMSSM	281	111	-960	12.2	<i>n/a</i>	<i>n/a</i>	<i>n/a</i>
NUHM1	282	113	-967	12.4	430	<i>n/a</i>	<i>n/a</i>
NUHM2	282	112	-962	12.3	<i>n/a</i>	502	391

Table 6.15: Best fitted parameters in fits of constrained models to STC10' SUSY masses and Higgs observables.

The best fit parameters for each of the constrained model fits are listed in Tab. 6.15. The best fit parameters are very similar as is expected from the similarity of the resulting  $\chi^2$  values. The best fit  $M_{1/2}$  values are excluded by the gluino lower mass bound from the LHC. If the gluino mass bound had been included in the list of observables, then the best  $\chi^2$  would be much larger as the best  $M_{1/2}$  would have been pushed upwards.

The best fit masses are plotted in Fig. 6.8 for the CMSSM fit with all SUSY masses and Higgs mass and BR measurements as fit input. The figure shows that the best fit scalar top mass is around 200 GeV leading to the decays into bottom or charm quarks and the LSP, which is in a challenging region for the LHC searches [253]. The squarks are around 600 GeV heavy and are excluded by the LHC [126] along with the gluino [126]. The Higgses and higgsinos are also around 600 GeV which the LHC limits starting to probe with the charged Higgs limits [127]. The sleptons are forced to be light as the fit inputs dictate. If the LHC exclusion limits were included, then the minimum  $\chi^2$  would be even bigger as it is not possible to accommodate a split slepton-squark

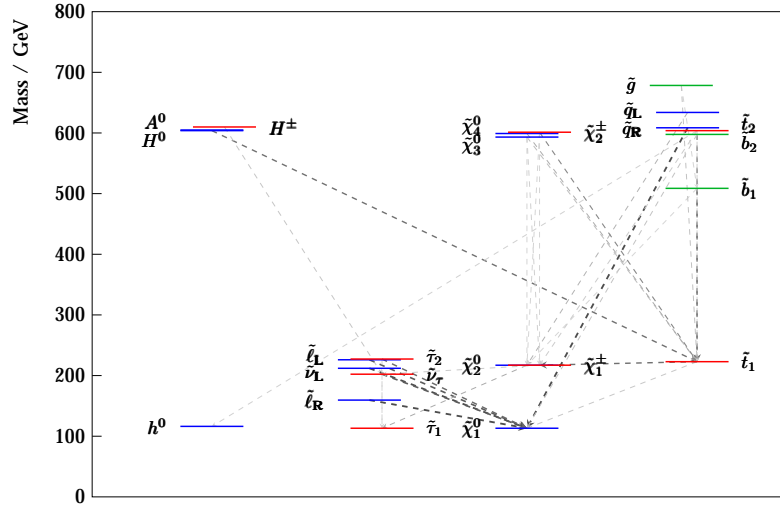


Figure 6.8: Best fit spectrum from CMSSM fit to STC10' All SUSY+h observables. This spectrum can be compared with the model spectrum of STC10' in Fig. 6.1.

spectrum with a unified sfermion mass parameter  $M_0$ . The NUHM1 and NUHM2 fits produce the same kind of best fit spectrum. As expected, the GUT models do not fit the observables, so the next step is to consider a pMSSM model.

### 6.6.2 pMSSM-13 fits to STC10'

Here we describe the results of fitting pMSSM-13 parameters to STC10' observables. First we will go through the results for the fit where only the ILC SUSY mass inputs and Higgs mass and branching fractions are input (All SUSY+h). Then the importance of including the Higgs observables will be discussed (All SUSY fit). Further, it is investigated what importance the precision of the ILC SUSY measurements have on the fit results (All SUSY0.5x+h and All SUSY5x+h fits). Then the benefits gained from including SUSY cross section measurements (AllSUSY+xs+h) are discussed.

#### Parameters and correlations

All 13 parameters of STC10' were fitted to the full set of expected SUSY mass measurements and Higgs precision measurements from the ILC. The fitted parameters are listed in Tab. 6.16 using 4 million Markov Chain points. A visual representation of the results for the fitted parameters is in Fig. 6.9. The best fit parameters agree with the model values, and have a small  $\chi^2 = 0.4345$ .  $M_1$ ,  $M_{L(1)}$  and  $M_{E(1)}$  are constrained to within 2 GeV at  $1\sigma$  confidence.  $M_2$  is constrained to a 9 GeV range at  $1\sigma$ , while  $m_A$  is within 12 GeV. The higgsino parameter  $\mu$  is constrained only to within 120 GeV. It was expected that all of these parameters would be constrained to some extent, as the gaugino masses depend on  $M_1$ ,  $M_2$ ,  $\tan\beta$  and  $\mu$  at tree-level. The slepton and

sneutrino masses depend on  $M_{L(3)}$  and  $M_{E(3)}$ ,  $\tan\beta$  and  $A_t$  at tree-level, and the Higgs sector depends on  $m_A$  and  $\tan\beta$ . The wide coverage of the probed region is due to the longer fit containing subfits with starting values far from the minimum.

The coloured sector parameters all are constrained to within maximally a 1 TeV range. This might seem surprising as there is no tree-level dependence of the observables used here on the coloured sector parameters. However, the coloured sector does enter the gaugino masses at one-loop level, as mentioned in Ch. 2. The effect of the first and second generation squark mass parameter  $M_{U(1)}$  on  $\tilde{\chi}_1^0$ ,  $\tilde{\chi}_2^0$ ,  $\tilde{\chi}_3^0$ ,  $\tilde{\tau}_1$  and  $h_0$  masses is plotted in Fig. 6.11. The relative change of the  $\tilde{\chi}_2^0$  mass with respect to  $M_{U(1)}$  is the largest, going up to 0.5% for a 25% change of the squark mass parameter. The effect on the LSP mass is about half of this, although still relevant as the ILC is expected to measure the masses to the permille-level. All these dependencies are visible assuming all the other parameters are fixed, which would be the ideal scenario, but the plot nevertheless proves that **SPheno3.3.9beta3** contains the relevant loop corrections which explain the sensitivity of the fit results on the first and second generation squark mass parameter. It is less surprising that the third generation squark masses are constrained as the Higgs mass is sensitive to these due to the large Yukawa couplings in the third generation.

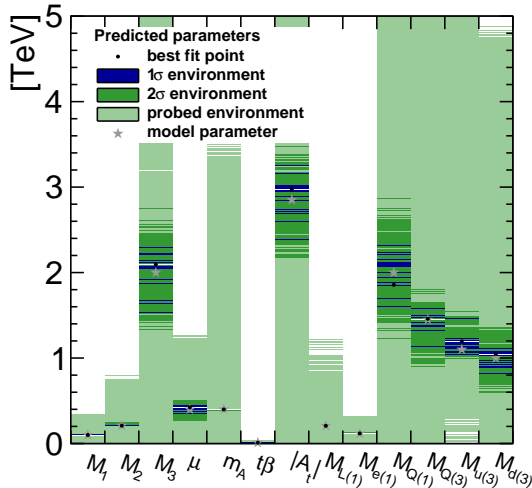


Figure 6.9: Predicted parameters from a 13-parameter fit to STC10' SUSY + Higgs observables with the expected precisions. Length of fit  $4 \times 10^6$  points.  $\tan\beta$  is plotted as if it was in GeV.

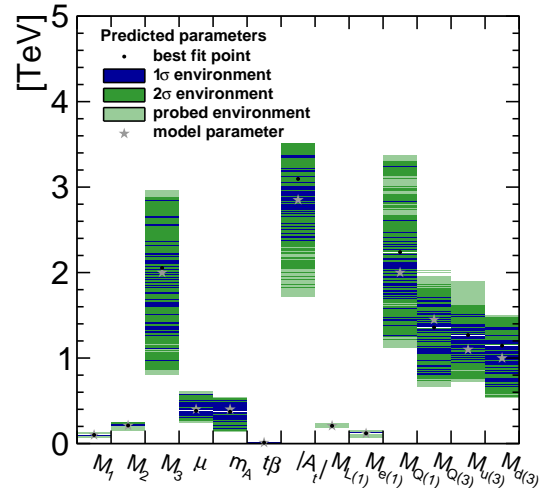


Figure 6.10: Predicted parameters from a 13-parameter fit to STC10' All SUSY observables. Length of fit  $10^6$  points.  $\tan\beta$  is plotted as if it was in GeV.

The  $2\sigma$  ranges are more than double the  $1\sigma$  ranges for all parameters except  $M_{U(3)}$  and  $A_t$ . In addition they are asymmetric, so it cannot be concluded that the fitted ranges are parabolic. This can be seen from Fig. 6.12 where the  $\Delta\chi^2 = \chi^2 - \chi_{min}^2$  distributions are plotted for  $M_1$ ,  $M_2$ ,  $\mu$ ,  $\tan\beta$ ,  $M_{L(1)}$  and  $M_{E(1)}$ . It can be seen that a longer Markov Chain would have been needed to find smooth distributions of  $\Delta\chi^2$  but it is computationally expensive to extend the Markov Chains. In terms of confidence in the  $1\sigma$  and  $2\sigma$  ranges being maximal, Fig. 6.9 shows that the fit did probe parameter

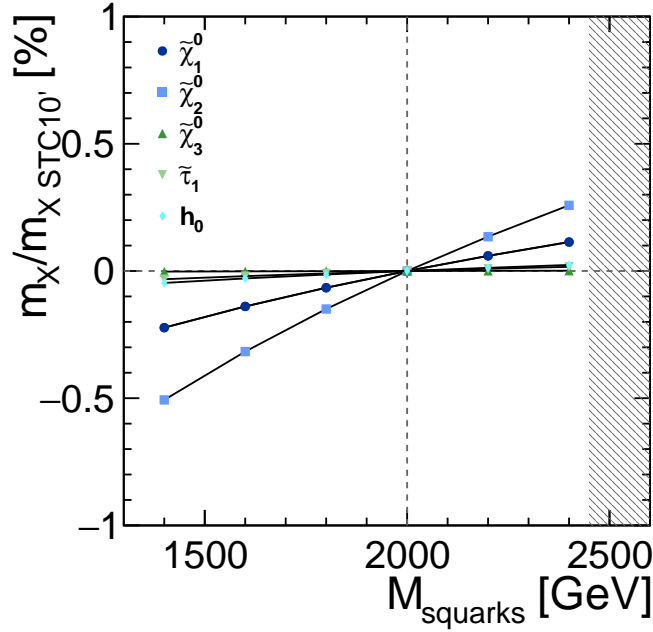


Figure 6.11: Dependence of sparticle and Higgs masses on  $M_{U(1)}$  according to SPheno3.3.9beta3 in the STC10' benchmark point. The grey area is not allowed by requiring sfermions to be non-tachyonic.

values far away from the best fit point. Thus, some confidence can be held in the fit not simply having got stuck in the minimum.

The fitted parameters can be compared with those from a fit which did not use the Higgs measurement inputs. The results are shown in Fig. 6.10 and listed in Tab. 6.17 for a  $10^6$ -point long fit. The best fit point again agrees with the benchmark parameter values. The  $\chi^2$  of the best fit point observables with respect to the model observables is 0.0627. Analogously to the case above where Higgs inputs are included, also here all the parameters are somewhat constrained, albeit with larger uncertainties.  $M_1$  is within a 3 GeV range with  $1\sigma$  CL, whereas  $M_{L(3)}$  and  $M_{E(3)}$  are within up to 8 GeV ranges at  $1\sigma$  CL. These ranges are four times as large as if the Higgs inputs are included. The determination of  $\mu$  is now only up to a 200 GeV range,  $m_A$  up to a 340 GeV range, and also  $M_2$  up to a 25 GeV range. It is proven that the Higgs mass and branching ratios are essential for maximising the constraints on the SUSY parameters especially for  $\mu$  and  $m_A$ . The coloured sector is again constrained somewhat, except that the gluino mass parameter  $M_3$  now is allowed within a 2 TeV range at  $1\sigma$  CL. If the ILC Higgs measurements are not available then direct constraints on the coloured sector masses from the LHC would be useful for the coloured sector parameter determination. All of the ranges should be interpreted as the most optimistic ranges from the point of view of the Markov Chains, as the length of the fit was limited to  $10^6$  points and the fit did not probe all of the possible parameter values especially for the coloured sector. On the other hand, the fit inputs do not take into account the final precision achievable in on 20-year timescale, so the fit results are conservative in this sense.

The scanning of the Markov Chain for  $\tan\beta$  and  $M_{L(3)}$  for the AllSUSY+h fit is plotted in Figs. 6.13 and 6.14. It can be seen that the Markov Chain shows a preference for

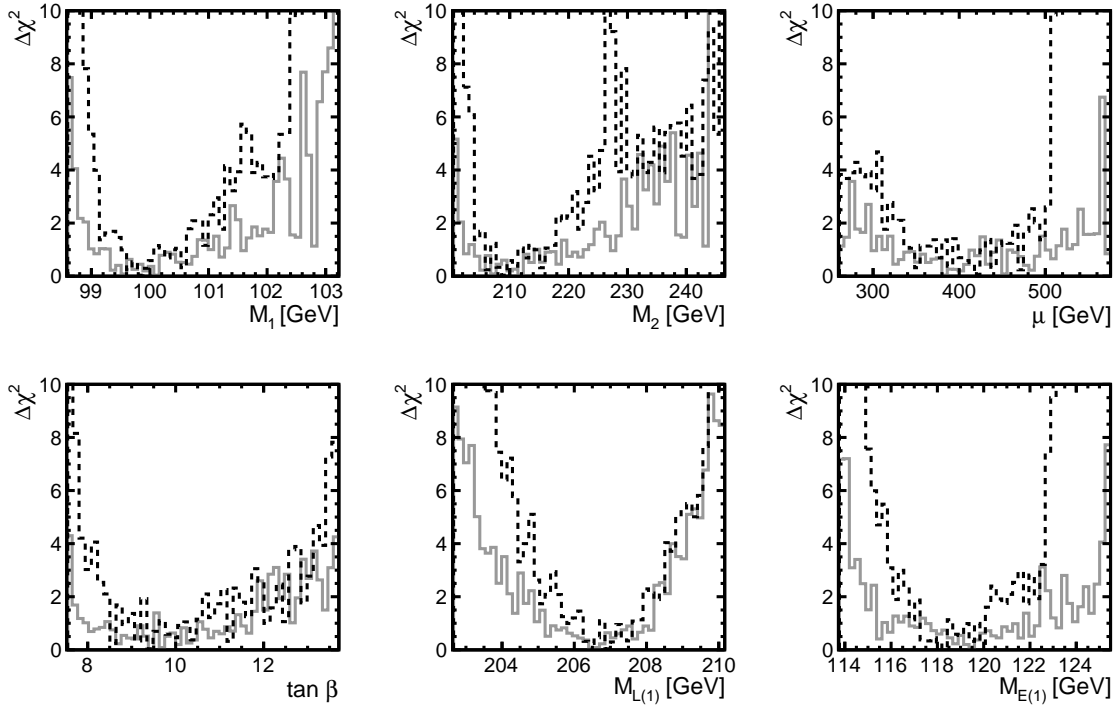


Figure 6.12: Parameter distributions in pMSSM-13 of fit STC10' to AllSUSY+h (dashed) using  $4 \times 10^6$  points and AllSUSY (solid) observables using  $10^6$  fit points.

parameter	STC10' true	best fit point	$1\sigma$	$2\sigma$
$M_1$	100	99.8	+0.79 -0.23	+2.35 -0.7
$M_2$	210	208.77	+6.54 -2.36	+33.68 -4.9
$\mu$	400	422.22	+49.7 -70.32	+83.99 -158.50
$\tan \beta$	10	9.41	+2.75 -0.9	+4.92 -1.45
$m_A$	400	398.7	+6.83 -4.87	+10.03 -15.16
$M_3$	2000	2096	+197 -565	+672 -779
$M_{L(1)}$	207	206.96	+0.58 -1.1	+1.73 -2.51
$M_{E(1)}$	118	118.25	+1.67 -0.9	+4.33 -2.35
$M_{Q(1)}$	2000	1856	+461 -265	+1114 -646
$M_{Q(3)}$	1450	1459	+129 -326	+351 -558
$M_{U(3)}$	1100	1196	+271 -160	+352 -200
$M_{D(3)}$	1000	1047	+78 -237	+319 -453
$A_{t=b=\tau}$	-2850	-2977	+604 -277	+806 -538
$\chi^2$	$9 \times 10^{-5}$	0.4345		

Table 6.16: STC10' pMSSM-13 fit results using AllSUSY+h inputs ( $4 \times 10^6$  points)

parameter	STC10' true	best fit point	$1\sigma$	$2\sigma$
$M_1$	100	100.12	+1.48 -1.08	+2.69 -1.36
$M_2$	210	211.44	+16.12 -9.29	+32.29 -10.21
$\mu$	400	382.58	+193.09 -81.73	+193.09 -119.64
$\tan\beta$	10	9.44	+2.29 -1.42	+4.15 -1.79
$m_A$	400	371.79	+139.01 -200.87	+150.09 -215.65
$M_3$	2000	2054	+804 -1090	+845 -1194
$M_{L(3)}$	207	206.54	+1.66 -1.35	+2.57 -3.08
$M_{E(3)}$	118	119.6	+3.65 -4.11	+5.29 -5.41
$M_{Q(1)}$	2000	2239	+1020 -995	+5.41 -5.29
$M_{Q(3)}$	1450	1358	+369 -557	+1085 -1038
$M_{U(3)}$	1100	1269	+249 -443	+512 -514
$M_{D(3)}$	1000	1145	+212 -540	+333 -586
$A_{t=b=\tau}$	-2850	-3096	+851 -428	+1271 -599
$\chi^2$	$9 \times 10^{-5}$	0.0627		

Table 6.17: STC10' pMSSM-13 fit results using AllSUSY inputs ( $10^6$  fit points).

the model value and values far from the model value are probed and disfavoured. If the Markov Chain was interpreted in the likelihood method, so that the intensity of probing corresponds to the high likelihood values of the parameter, then clearly the model value is recovered by the fit.

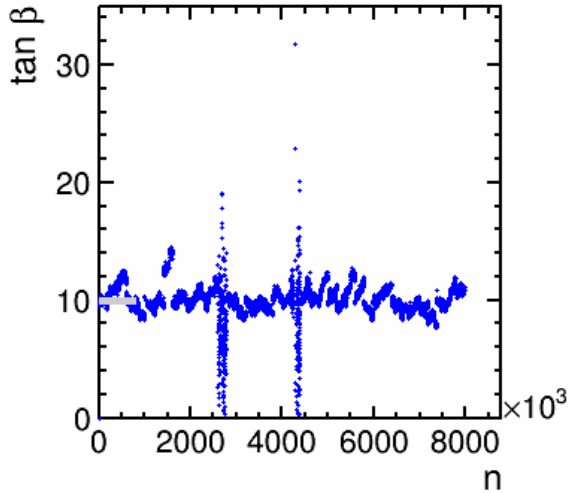


Figure 6.13: Depiction of the Markov Chain in the  $4 \times 10^6$  point pMSSM-13 fit to STC10' AllSUSY+h observables. Every 500th point is plotted and the  $x$ -axis labels refer only to those points.

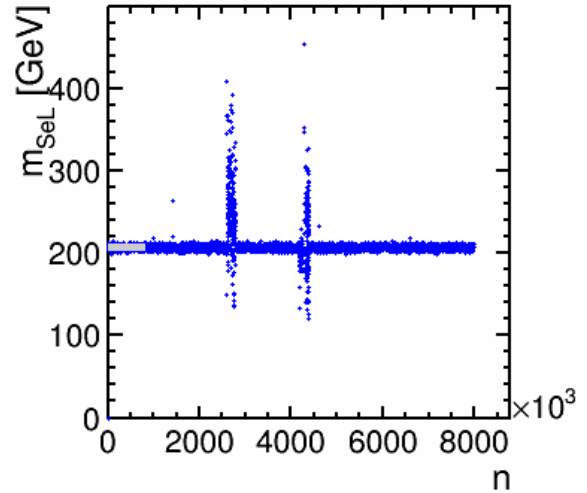


Figure 6.14: Depiction of the Markov Chain in the  $4 \times 10^6$  point pMSSM-13 fit to STC10' AllSUSY+h observables. Every 500th point is plotted and the  $x$ -axis labels refer only to those points.

It may be that some range which would be allowed due to correlations with another parameters is not probed by the fit, although this argument is tested in Fig. 6.16 where the fit results are plotted together with theoretically allowed parameter ranges. The latter ranges were obtained by changing the STC10' model one parameter at a time to find the boundaries in which a spectrum can be calculated without tachyons. If a spectrum is to be found in the shaded areas in Fig. 6.16, then more than one parameter has to be changed simultaneously. The figure shows that the Markov Chain does probe and even find  $1\sigma$  allowed points in the regions where multiple parameters have to be modified at the same time.

It has to be recognised that  $4 \times 10^6$  points are not enough to obtain smooth  $\Delta\chi^2$  distributions on two-dimensional planes. This can be seen from Fig. 6.15, in which correlations of  $M_1$  with three other parameters are plotted. The contours show the 1-dimensional  $1\sigma$  range, i.e.  $\Delta\chi^2 < 1$  and the 2-dimensional  $2\sigma$  range corresponding to  $\Delta\chi^2 < 5.99$ . The ranges are set to contain the parameter values where the deviation of  $\chi^2$  from the fit minimum is less than 10. The plot range is divided into  $25 \times 25$  bins. It can be seen that the correlation contours are not smooth over the whole range, thus indicating that the fit length is not long enough. The conclusion is that the parameter ranges and the derived predictions for the observables should be interpreted as the optimistic scenario for the assumed ILC observable data set which does not correspond to the full expected data set.

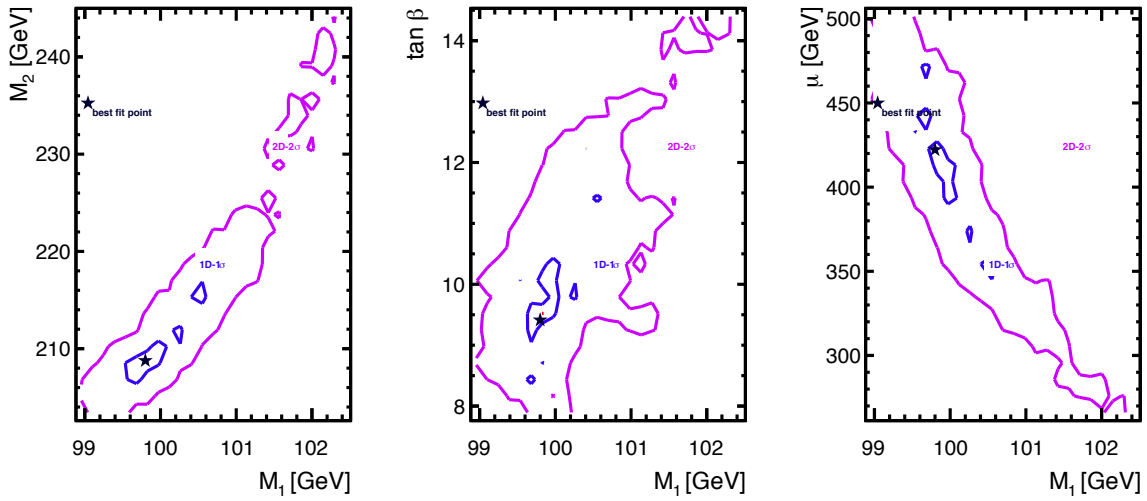


Figure 6.15: Some parameter correlations in the  $4 \times 10^6$  point pMSSM-13 fit to STC10' AllSUSY+h observables.

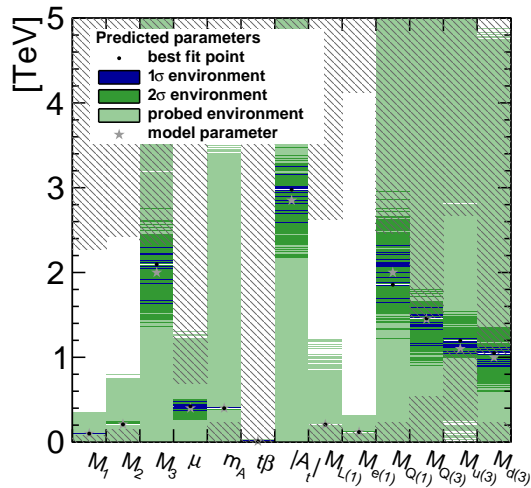


Figure 6.16: Predicted parameters from a 13-parameter fit to STC10' SUSY + Higgs observables (AllSUSY+h) with the expected precisions. The grey areas indicate where some fermions turn tachyonic according to `SPheno3.3.9beta3` if the STC10' parameters are modified from the model values parameter by parameter.

## Mass predictions

The predicted masses of unobserved sparticles are plotted in Fig. 6.17 for the All-SUSY+h STC10' fit of pMSSM-13. As can be seen from the figure, the best fit masses are close to the model masses. Predictions for all of the unobserved sparticles can be made. In more detail, the  $1\sigma$  and  $2\sigma$  uncertainties for all the predictions are listed in Tab. 6.18. The higgsino masses are predicted with 10-16% at  $1\sigma$  uncertainty and twice that at  $2\sigma$  uncertainty. The heavy Higgs masses are predicted within 3% uncertainty, which is due to the remarkable precision of the ILC Higgs measurements.

As the coloured sector affects the observables only at loop-level, it was not expected that strong predictions can be made for the squarks and the gluino. It turns out that the observables are sensitive, as discussed in Ch. 2 and above. The squark masses can be restricted to a 700 GeV range or less for the third generation. The gluino mass is also predicted with this uncertainty. At  $2\sigma$  CL the ranges expand to 0.6-1.7 TeV.

These mass predictions from ILC SUSY and Higgs measurements can be compared to ones without the Higgs measurements. These mass predictions are plotted in Fig. 6.10, from which it can be seen that the  $1\sigma$  confidence intervals are expanded compared to the previous case. Nevertheless, the ranges are still somewhat constrained by the fit.

The extended Higgs sector is less well predicted if the Higgs inputs are not used. The  $1\sigma$  range covers 350 GeV as can be read from Tab. 6.18. Both higgsinos and heavy Higgses are now predicted with similar precisions of 250-350 GeV at  $1\sigma$  CL. The  $2\sigma$  ranges are not much larger than the  $1\sigma$  ranges.

The coloured sector particles have allowed ranges of 1-2 TeV compared with about less than half that if the Higgs inputs are used in the fit. It appears that the Higgs inputs have to be considered simultaneously in order to exploit ILC SUSY measurements fully.

## Importance of permille-level SUSY mass measurements at ILC

It was studied whether the expected precisions for the SUSY masses from ILC are needed, and whether five times the size of the uncertainty on the masses would be enough, or whether a factor two better measurements would help. In both cases, the ILC H20 Higgs observables were used to test the importance of the SUSY measurement quality. The results of All SUSY5x+h (corresponding to  $\mathcal{L} = 2 \times 20 \text{ fb}^{-1}$ ) and All SUSY0.5x+h (corresponding to  $\mathcal{L} = 2 \times 2000 \text{ fb}^{-1}$ ) fits can be compared by looking at Figs. 6.19 and 6.20. It is clearly seen from these figures, which plot the parameter confidence intervals from  $10^6$  point long fits, that the permille-level precision measurements at the ILC are crucial for constraining the coloured sector parameters. Additionally, the parameters which are related to the sleptons or gauginos at tree-level are sensitive to the size of the uncertainty from the ILC mass measurements. Especially for  $M_1$ ,  $M_2$ ,  $\mu$ ,  $\tan\beta$ ,  $M_{L(1)}$  and  $M_{E(1)}$  whose  $\Delta\chi^2$  distributions are plotted in Fig. 6.21, the ranges are greatly reduced as the SUSY mass inputs get better.

A detailed listing of the predicted parameter ranges is in Tab. 6.19. It cannot be stressed enough that the high-precision measurements from the ILC are key to SUSY

prediction	STC10' All SUSY+h			STC10' All SUSY		
	best fit	1 $\sigma$	2 $\sigma$	best fit	1 $\sigma$	2 $\sigma$
$m_{\tilde{\chi}_3^0}$	-433	+49 -70	+82 -157	-394	+191 -83	+191 -119
$m_{\tilde{\chi}_4^0}$	447	+47 -64	+78 -122	411	+181 -66	+181 -85
$m_{\tilde{\chi}_2^\pm}$	448	+47 -64	+78 -123	412	+181 -67	+181 -86
$m_{H^0}$	399	+11 -9	+11 -19	373	+137 -203	+157 -223
$m_{A^0}$	400	+10 -10	+10 -20	372	+138 -202	+158 -212
$m_{H^\pm}$	408	+12 -8	+12 -18	382	+138 -192	+148 -212
$m_{\tilde{u}_L}$	1883	+457 -263	+1087 -673	2264	+996 -964	+1056 -1014
$m_{\tilde{u}_R}$	1880	+460 -260	+1080 -670	2261	+999 -961	+1049 -1011
$m_{\tilde{t}_1}$	1085	+245 -215	+335 -305	1102	+268 -632	+308 -842
$m_{\tilde{t}_2}$	1517	+143 -307	+333 -387	1461	+309 -371	+449 -401
$m_{\tilde{b}_1}$	1047	+83 -247	+333 -607	1154	+186 -784	+236 -944
$m_{\tilde{b}_2}$	1443	+127 -353	+357 -423	1341	+389 -761	+539 -831
$m_{\tilde{g}}$	2091	+179 -441	+699 -651	2113	+667 -993	+697 -1113

Table 6.18: STC10' fitted masses, pMSSM-13 fit with AllSUSY+h observables,  $4 \times 10^6$  points, and the same for a fit without Higgs observables using  $10^6$  points.

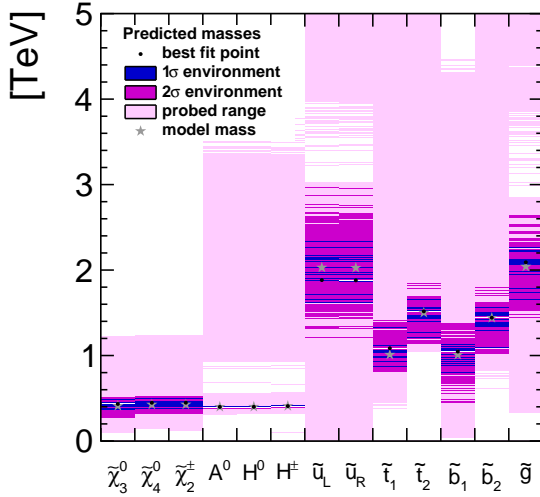


Figure 6.17: Predicted masses from a 13-parameter fit with  $4 \times 10^6$  points to STC10' SUSY + Higgs observables (All-SUSY+h) with the expected precisions.

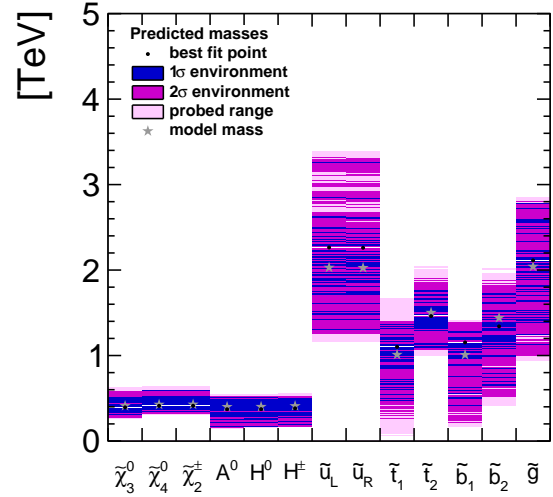


Figure 6.18: Predicted masses from a 13-parameter fit with  $10^6$  points to STC10' SUSY observables.

parameter determination, and this would not be simply achieved by observing excesses at the LHC with large uncertainties on the masses and the assignment of SUSY particles to decay chains.

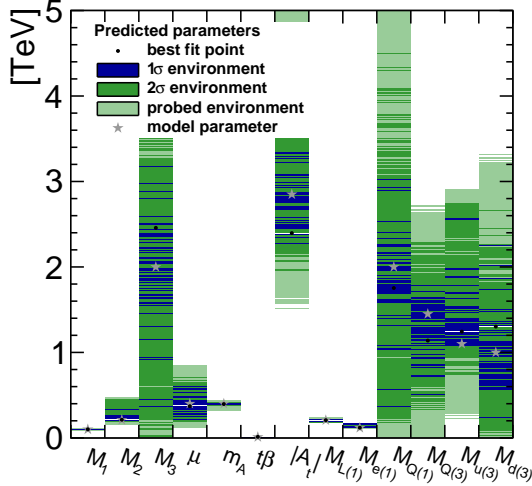


Figure 6.19: Predicted parameters from a 13-parameter fit with  $10^6$  points to STC10' All 5xSUSY+h observables.  $\tan \beta$  is plotted as if it was in GeV.

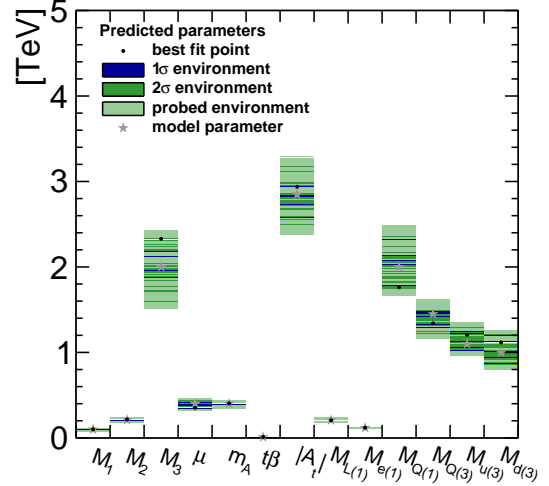


Figure 6.20: Predicted parameters from a 13-parameter fit with  $10^6$  points to STC10' AllSUSY05x +h observables.  $\tan \beta$  is plotted as if it was in GeV.

## Mass predictions

The quality of the mass predictions from SUSY parameter fits depends on the input measurements and their uncertainties. As we have just discussed, the parameter ranges are more strongly constrained as the ILC measurements get more accurate. The same is true for the mass predictions as can be seen from comparing Figs. 6.22 and 6.23. If the ILC SUSY mass measurements are five times worse than expected (or the data set is smaller), then the higgsino and heavy Higgs masses can be constrained but the coloured sector predictions are much weaker. The details are written out in Tab. 6.19. The higgsino mass predictions are now with 300-400 GeV ranges at  $1\sigma$  confidence compared to 120 GeV ranges with the expected SUSY inputs discussed above. The heavy Higgs mass predictions worsen only by 50% but this is due to the Higgs inputs being assumed to be the same as above. The coloured sector predictions are now with 1.4-2 TeV ranges, which is more than twice the uncertainty if the ILC SUSY measurements are as expected.

Improving the ILC SUSY measurements by a factor two, corresponding to the full  $\sqrt{s} = 500$  GeV data set in the H20 operating scenario, gives further benefits especially in the coloured sector. In this case, the higgsino masses are predicted to be within a 100 GeV  $1\sigma$  range while the heavy Higgs ranges remain the same, around 20 GeV - see Tab. 6.19. The  $2\sigma$  ranges on the other hand are now the same as the  $1\sigma$  ranges which could be an indication that more fit points would be needed to scan the boundaries properly. The coloured sector masses are now constrained to within 200-600 GeV, and similarly the  $2\sigma$  ranges are nearly the same as the  $1\sigma$  ranges.

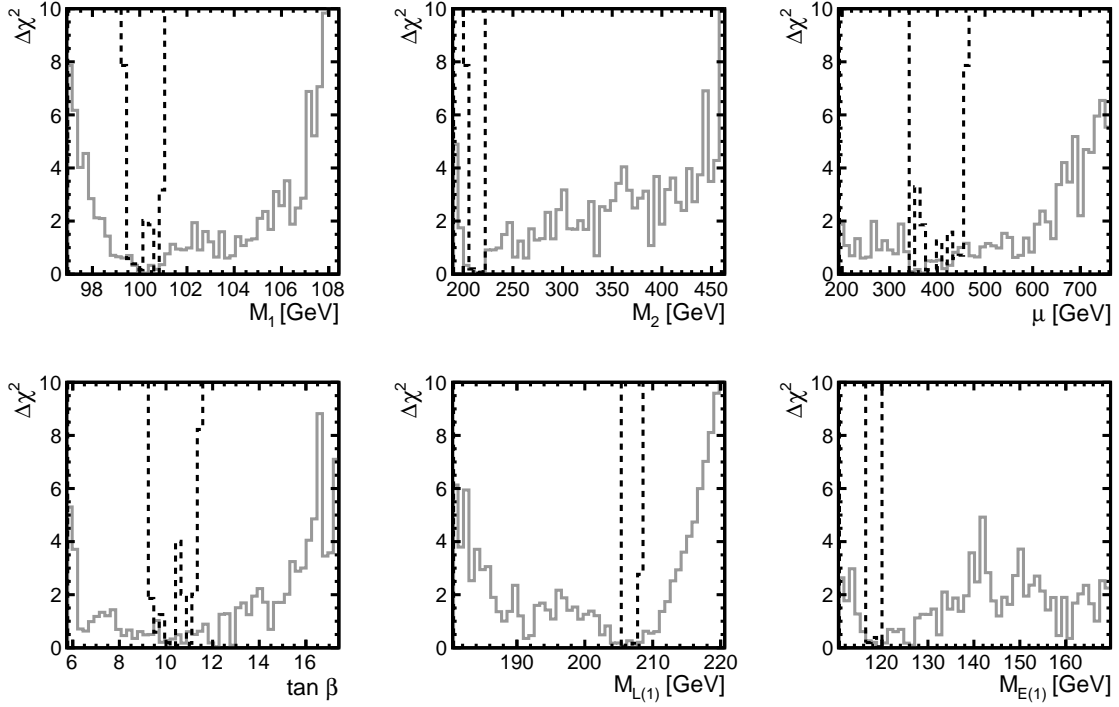


Figure 6.21: Parameter distributions in pMSSM-13 fit to STC10' AllSUSY5x+h (solid) and AllSUSY0.5x+h (dashed) observables. Length of fit  $10^6$  points.

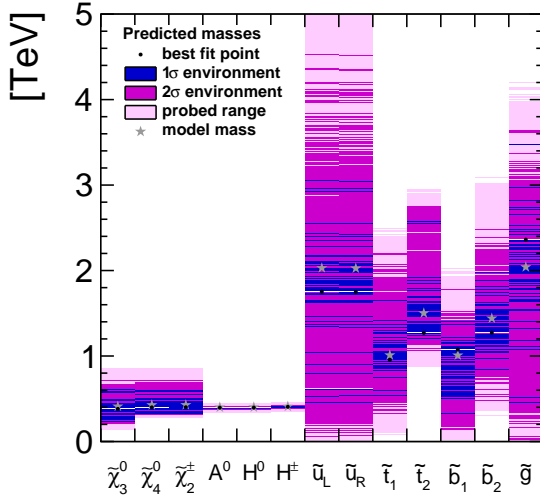


Figure 6.22: Predicted masses from a 13-parameter fit to STC10' All SUSY5x+h observables with the expected precisions. Length of fit  $10^6$  points.

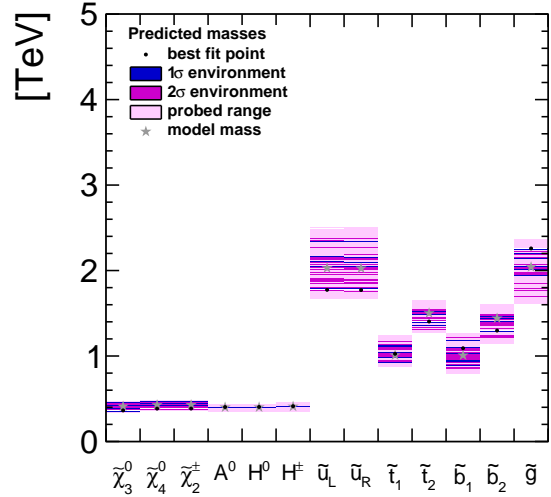


Figure 6.23: Predicted masses from a 13-parameter fit to STC10' All SUSY0.5x+h observables. Length of fit  $10^6$  points.

prediction	STC10' All SUSY5x+h			STC10' All SUSY05x+h		
	best fit	$1\sigma$	$2\sigma$	best fit	$1\sigma$	$2\sigma$
$m_{\tilde{\chi}_3^0}$	-382	+226 -151	+331 -170	-363	+97 -4	+97 -9
$m_{\tilde{\chi}_4^0}$	400	+215 -76	+318 -81	384	+89 -4	+89 -8
$m_{\tilde{\chi}_2^\pm}$	401	+215 -77	+318 -82	385	+89 -4	+89 -8
$m_{H_0}$	397	+13 -17	+23 -27	404	+6 -14	+6 -14
$m_{A_0}$	396	+14 -16	+24 -26	403	+7 -13	+8 -13
$m_{H^\pm}$	406	+14 -16	+24 -26	413	+7 -13	+7 -13
$m_{\tilde{u}_L}$	1753	+1307 -1353	+2777 -1703	1774	+576 -4	+606 -14
$m_{\tilde{u}_R}$	1750	+1300 -1351	+2770 -1680	1771	+579 -1	+609 -21
$m_{\tilde{t}_1}$	955	+705 -425	+1315 -635	1026	+104 -106	+154 -106
$m_{\tilde{t}_2}$	1270	+1310 -70	+1490 -210	1404	+126 -54	+146 -94
$m_{\tilde{b}_1}$	1076	+334 -756	+704 -936	1091	+99 -211	+129 -241
$m_{\tilde{b}_2}$	1273	+927 -433	+1417 -793	1298	+172 -18	+192 -88
$m_{\tilde{g}}$	2362	+1118 -1912	+1278 -2342	2259	+1 -319	+11 -569

Table 6.19: STC10' fitted masses in the pMSSM-13 fit with AllSUSY5x+h and AllSUSY05x+h observables. Fit length is  $10^6$  points for both.

It is quite clear that aiming for the highest possible precision for the ILC measurements brings benefits for the parameter and mass predictions from the SUSY parameter fits. As the measurements get more accurate statistically, then the systematic uncertainties begin to influence the results. Here only statistical uncertainties were considered. In addition, theoretical uncertainties gain significance as the measurements get more accurate. It can be expected that if SUSY particles were observed, then significant effort would be targeted at improving the theoretical calculations to match the experimental precisions.

### pMSSM-13 fit to fewer SUSY ILC observables

This subsection contains the results from using only some of the sleptons as fit inputs. This could occur for example if the centre-of-mass energy is lower than 500 GeV. A realistic case of  $\sqrt{s} = 250$  GeV for the ILC is considered here, which means that only  $\tilde{\chi}_1^0$ ,  $\tilde{\tau}_1$ ,  $\tilde{e}_R$  and  $\tilde{\mu}_R$  would be discovered.

The fit inputs are the “Min SUSY+h” inputs from Tab. 6.12, using the same precisions as for the other fits with  $\sqrt{s} = 500$  GeV observations for simplicity. In reality, the LSP measurement would rely more on the  $e^+e^- \rightarrow \tilde{\chi}_1^0\tilde{\chi}_1^0\gamma$  measurement, and  $\tilde{\tau}_1$  mass measurement would be more challenging due to  $\gamma\gamma$  backgrounds [170]. Threshold scans would be key to optimising the measurement precisions.

The fitted model is pMSSM-13 and the data consists of  $10^6$  Markov Chain points combined from 10 separate fits.

### Parameters and correlations

The fitted parameters are plotted in Fig. 6.24. All parameters are predicted correctly within the  $1\sigma$  uncertainty. Comparing this to the fit with all the SUSY observables and Higgs, Fig. 6.9 shows that the determined ranges for all parameters are larger for the present case with fewer SUSY observables. It is most strongly seen in the ranges for  $M_2$  and  $\mu$  but also for the slepton mass parameters. On the other hand, it is remarkable that predictions can be made with this smaller set of observables.

In more detail,  $M_1$  is predicted two times less accurately than in the fit with all the observables, and the  $M_2$   $1\sigma$  range is now more than 140 GeV wide. The  $\mu$  and  $\tan\beta$  ranges are similar to the fit with all the observables. The right-handed slepton mass  $M_{E(1)}$  is predicted with a similar precision as before, which makes sense as the right-handed sleptons are assumed to be observed with the same accuracy as before. The left-handed slepton mass  $M_{L(1)}$  on the other hand gets a 70 GeV  $1\sigma$  range whereas with the full SUSY observable set, the range was less than 2 GeV. The trilinear coupling precision remains similar to before. The precisions on the coloured parameters are worsened too, which makes sense as the sensitive mass of  $\tilde{\chi}_2^0$  (as plotted in Fig. 6.11) is not available in the MinSUSY observable set.

### Mass predictions

The fitted masses are plotted in Fig. 6.25. The best fit point agrees with the model values within  $1\sigma$  confidence. For the particles which would be accessible at  $\sqrt{s} = 500$  GeV but which were not used as fit inputs, predictions can be made: the best fit point masses agree with the model masses within  $1\sigma$ , which for the  $\tilde{\chi}_2^0$  and  $\tilde{\chi}_1^\pm$  is

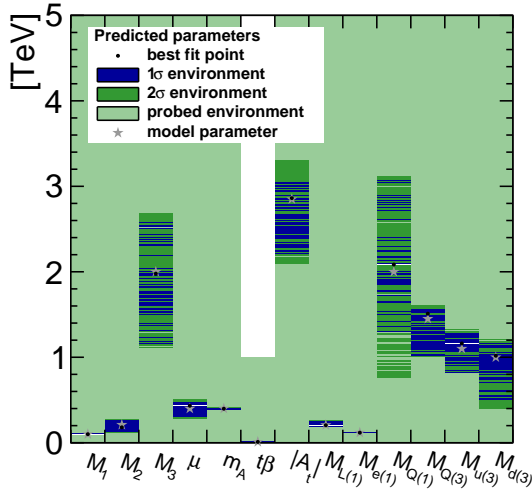


Figure 6.24: Predicted parameters from a 13-parameter fit to STC10' MinSUSY+h observables with the expected precisions. Length of fit  $10^6$  points.  $\tan \beta$  is plotted as if it was in GeV.

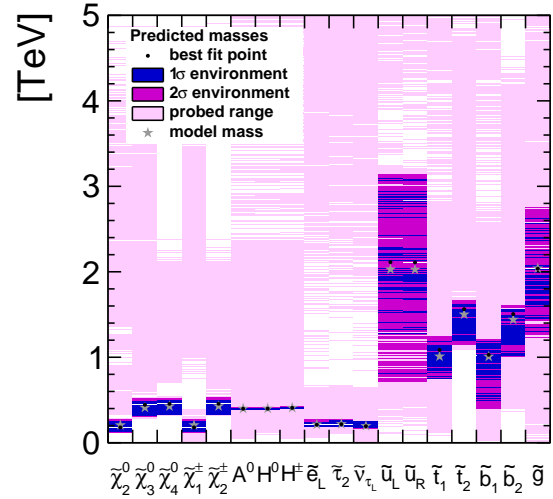


Figure 6.25: Predicted masses from a 13-parameter fit to STC10' MinSUSY+h observables. Length of fit  $10^6$  points.

about 30% and about 10-12% for the  $\tilde{e}_L$ ,  $\tilde{\tau}_2$  and  $\tilde{\nu}_\tau$  masses. For the heavier sparticles, the uncertainties are broadly speaking twice as large as in the pMSSM-13 fit with AllSUSY+h observables. Thus, while some predictions can be made using the  $\sqrt{s} = 250$  GeV data set, the comparison to the  $\sqrt{s} = 500$  GeV results gives direct motivation to operate the ILC with the highest feasible centre-of-mass energy. It is self-evident that discovering as many SUSY particles as possible is beneficial in restricting the pMSSM parameter space.

### STC10' pMSSM-13 with additional cross section inputs

This section discusses the results of a fit, whose inputs include the cross section measurements listed in Tab. 6.11 as well as the expected SUSY mass measurements with or without Higgs mass and branching fraction measurements from Tab. 6.12. It is interesting to find out whether cross section measurements help to constrain the fit of pMSSM-13 parameters.

#### Parameters

The fitted parameters are plotted in Fig. 6.26 for the case that Higgs measurements are included in the inputs. Comparing this to Fig. 6.9 it is clear that the SUSY cross section measurements bring further constraints to the SUSY parameters. Quantitatively, the determined parameters are detailed in Tab. 6.20. Comparing with the case without cross section measurements in Tab. 6.16, significant gains can be made by including cross sections in the fits. For  $M_1$  and  $M_2$  the gain is a factor four in precision. Even more importantly,  $\tan \beta$  can now be constrained to a range of 0.7 compared to 2.8 without cross section inputs. Similarly the  $\mu$  parameter prediction improves. The

difference is lesser for the slepton mass parameters, which makes sense as their mixing has only one free parameter to be constrained in any case. Visually the comparison is plotted in Fig. 6.28, from which it is undoubtedly visible that the cross section measurements reduce the asymmetry of the determined confidence intervals and reduce their size significantly.

If the Higgs measurements are not included but the SUSY cross section measurements are, then the parameters are determined according to Fig. 6.27. In this case the results are comparable to the case with SUSY masses and Higgs measurements included. As discussed above, the benefits of including the Higgs measurements can be most seen in the heavy Higgs sector and the coloured sector. This self-evident from comparing Fig. 6.26 with Higgs and SUSY cross section inputs and Fig. 6.27 with SUSY cross section inputs and no Higgs inputs.

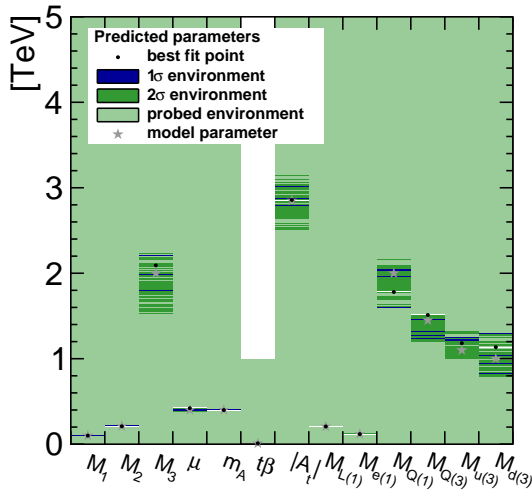


Figure 6.26: Predicted parameters from a 13-parameter fit to STC10'. All SUSY+xs+h observables with the expected precisions, i.e. including the cross section measurements. Length of fit  $10^6$  points.  $\tan \beta$  is plotted as if it was in GeV.

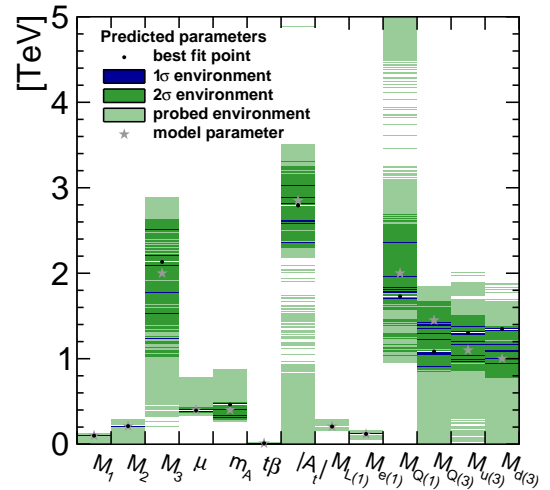


Figure 6.27: Predicted parameters from a 13-parameter fit to STC10'. All SUSY+xs observables, i.e. including the cross section measurements but not the Higgs measurements. Length of fit  $10^6$  points.  $\tan \beta$  is plotted as if it was in GeV.

## Masses

The predictions for the masses of unobserved sparticles improve if the SUSY cross section measurements are included in the fit. As can be seen from Fig. 6.29, all masses are narrowly constrained. The detailed mass predictions are written out in Tab. 6.21 for both cases when Higgs inputs are included and when they are not included. Overall, higgsino masses can be predicted about five times more accurately than if the SUSY cross section inputs are not used. There is also improvement in the coloured sector predictions, although there the difference is smaller. The cross section measurements help to make the best use of any data set.

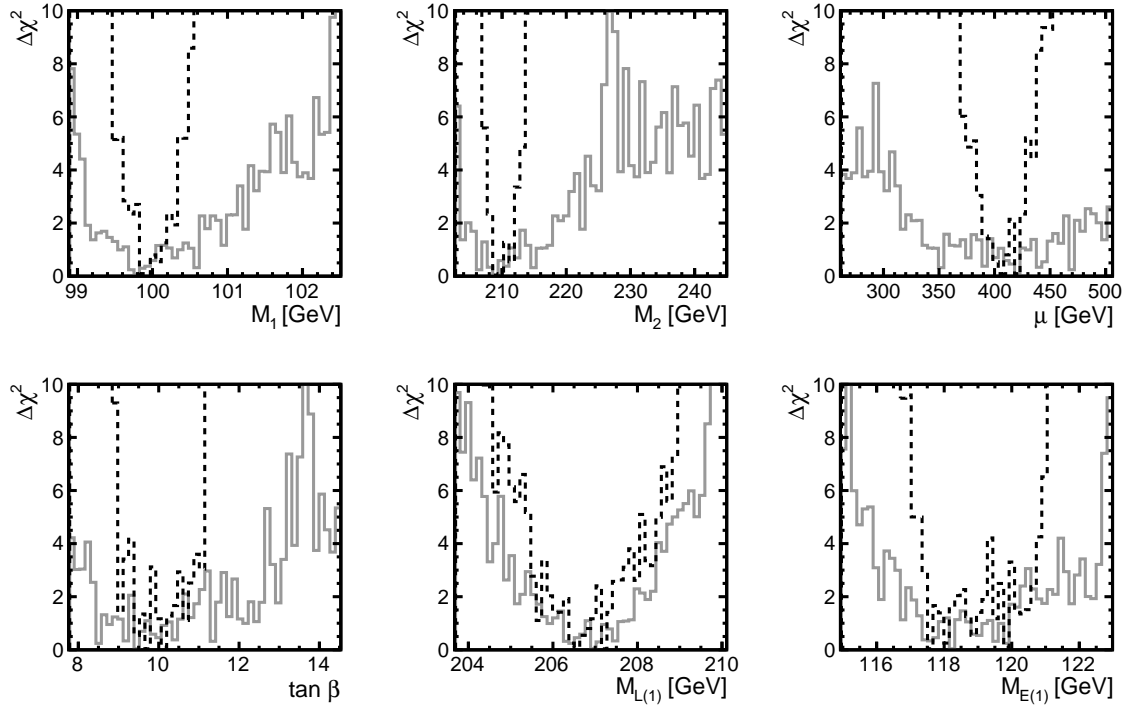


Figure 6.28: Parameter distributions in pMSSM-13 of fit STC10' to All SUSY+h (solid) with  $4 \times 10^6$  points and AllSUSY+xs+h (dashed) observables using  $10^6$  points.

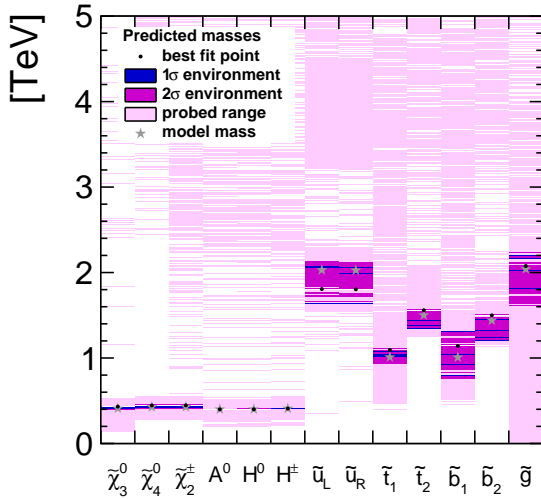


Figure 6.29: Predicted masses from a 13-parameter fit to STC10' All SUSY+xs+h observables with the expected precisions. Length of fit  $10^6$  points.

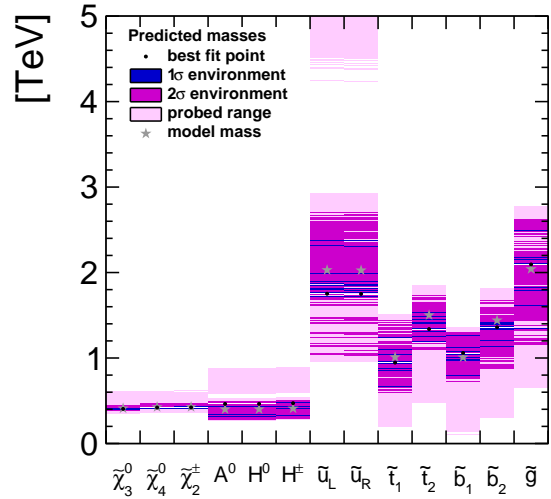


Figure 6.30: Predicted parameters from a 13-parameter fit to STC10' All SUSY+xs+h observables. Length of fit  $10^6$  points.

parameter	STC10' true	best fit point	$1\sigma$	$2\sigma$
$M_1$	100	99.93	+0.15 -0.08	+0.35 -0.30
$M_2$	210	209.14	+1.97 -0.05	+3.14 -1.10
$\mu$	400	420.49	+0.27 -21.24	+6.64 -35.59
$\tan\beta$	10	9.79	+0.34 -0.35	+1.26 -0.72
$m_A$	400	399.05	+1.96 -2.94	+10.67 -7.29
$M_3$	2000	2092	+118.12 -304.50	+141 -566
$M_{L(3)}$	207	207.22	+0.01 -0.75	+1.14 -1.74
$M_{E(3)}$	118	117.65	+2.25 -0.01	+3.09 -0.22
$M_{Q(1)}$	2000	1780	+272 -182	+389 -182
$M_{Q(3)}$	1450	1511	+3 -282	+3 -306
$M_{U(3)}$	1100	1181	+65 -71	+140 -180
$M_{D(3)}$	1000	1135	+165 -310	+343 -165
$A_{t=b=\tau}$	-2850	-2858	+87 -165	+346 -287
$\chi^2$	$9 \times 10^{-5}$	2.1746		

Table 6.20: STC10' pMSSM-13 fit results using All SUSY+xs+h inputs, , i.e. including the cross section measurements (fit length  $10^6$  fit points).

prediction	STC10' All SUSY+xs+h			STC10' All SUSY+xs		
	best fit	$1\sigma$	$2\sigma$	best fit	$1\sigma$	$2\sigma$
$m_{\tilde{\chi}_3^0}$	-432	+0 -22	+5 -37	-404	+11 -10	+43 -17
$m_{\tilde{\chi}_4^0}$	446	+0 -20	+5 -34	421	+9 -10	+40 -17
$m_{\tilde{\chi}_2^\pm}$	447	+0 -20	+5 -34	422	+9 -10	+40 -16
$m_{H_0}$	400	+10 -10	+10 -10	464	+16 -154	+36 -184
$m_{A_0}$	399	+11 -9	+21 -9	463	+17 -153	+37 -183
$m_{H^\pm}$	409	+11 -9	+11 -9	471	+18 -152	+38 -182
$m_{\tilde{u}_L}$	1806	+274 -176	+394 -176	1752	+628 -32	+958 -712
$m_{\tilde{u}_R}$	1804	+266 -174	+396 -174	1750	+630 -30	+960 -720
$m_{\tilde{t}_1}$	1094	+6 -84	+26 -164	946	+304 -286	+494 -356
$m_{\tilde{t}_2}$	1559	+1 -219	+11 -219	1339	+201 -149	+401 -239
$m_{\tilde{b}_1}$	1141	+179 -351	+179 -381	1059	+211 -269	+251 -339
$m_{\tilde{b}_2}$	1500	+0 -300	+20 -300	1359	+229 -229	+321 -489
$m_{\tilde{g}}$	2076	+134 -266	+164 -466	2095	+405 -755	+535 -945

Table 6.21: STC10' fitted masses, pMSSM-13 fit with All SUSY+xs+h and All SUSY+xs observables, i.e. including the cross section measurements with and without Higgs measurements. Length of fit  $10^6$  points for both.

### 6.6.3 STC10' relic density predictions

In all the fits, the dark matter relic density for each calculated point was saved. The  $\Delta\chi^2$  distribution of the dark matter relic density can be studied to check whether the fit returns the model relic density. To do this, the  $\Delta\chi^2$  distributions were plotted, the  $2\sigma$  range extracted. Then the mean of the  $2\sigma$  range was calculated to be the mean and half of the size of the  $2\sigma$  width was taken to be the  $1\sigma$  width. Then a Gaussian was plotted with this mean and uncertainty with the  $x$ -axis normalised to the model relic density. This is emulating what would happen if many toy fits were performed with smeared experimental observables and the distribution of  $\chi^2_{min}$  for each fit was plotted.

The results are plotted in Fig. 6.31 for three fits: STC10' with SUSY masses only, one with Higgs measurements added and one with Higgs measurements and SUSY cross sections added. As long as the Higgs measurements are included, the relic density is predicted precisely around the model value with about 4% uncertainty if SUSY cross sections are not included or 1.9% if SUSY cross sections are included.

If the SUSY cross section inputs are used alongside with the SUSY mass and Higgs measurements from the ILC, then the prediction of the relic density is more accurate than in the case without the SUSY cross sections. A similar relationship was found for the SUSY mass predictions above, so this argument further enhances the case for including SUSY cross section measurements in the SUSY parameter fits.

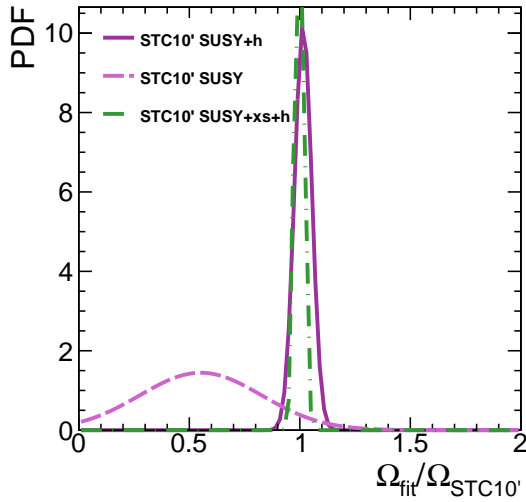


Figure 6.31: Comparison of determined relic densities from the STC10' All-SUSY+h, AllSUSY and AllSUSY+xs+h.

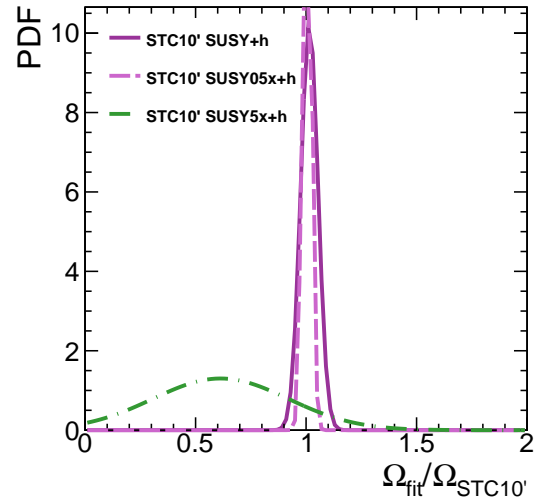


Figure 6.32: Comparison of determined relic densities from the STC10' All-SUSY+h with expected precisions, 0.5x precisions and 5x precisions.

If the Higgs measurements are not included, then low values of  $\Omega$  are allowed. In this case the uncertainty on  $\Omega$  is roughly 28% which does not correspond the 68% confidence interval as the underlying  $\Delta\chi^2$  distribution is not parabolic unlike in the other fits. The low  $\Omega$  values are allowed because low values of  $m_A$  are not excluded by the ILC SUSY measurements. If  $m_A$  is low, then this enhances the LSP annihilation

into  $b\bar{b}$  via the Higgs funnel. It should be noted that if  $m_A$  gets too low, then negative sfermion mass squared values appear, so  $\tan\beta$  has to be lowered simultaneously.

To recover the correct relic density value if ILC Higgs measurements are not available, LHC exclusions could be invoked. If  $m_A$  is required to be higher than 260 GeV so the Higgs funnel is eliminated, then the correct relic density is recovered:  $\Omega_{\text{fit}}/\Omega_{\text{STC10}'} = 1.01 \pm 0.08$ . The key result is that Higgs sector input is needed to get the correct relic density.

A comparison highlighting the importance of the precision SUSY measurements at ILC is plotted in Fig. 6.32. In this figure, the relic density predictions are plotted for All SUSY+h, All SUSY05x+h and All SUSY5x+h fits. It can be seen that if the SUSY measurements are five times worse than expected, then low values of  $\Omega$  are again allowed. The uncertainty in that case is 31% however the true  $\Delta\chi^2$  distribution does not correspond to a parabola.

The worsening of the relic density prediction in the case of less accurate SUSY mass measurements has a few sources. One is if  $M_3$  is very low, which is allowed due to the less accurate SUSY measurements, then the light gluino affects the relic density significantly. These allowed points can be excluded by invoking the LHC lower limit on the gluino mass.

Another source of low allowed relic density values is light squark masses, which again influence the relic density, but can be avoided with LHC limits. At least one point in the fit was allowed due to parameters with 590 GeV first and second generation squarks, light  $\mu \sim 220$  GeV and a heavy gluino with  $m_{\tilde{g}} = 2.7$  TeV. These together caused the  $\tilde{\chi}_2^0$  decays according to `SPheno3.3.9beta3` to change from mostly  $\tilde{\tau}_1\tau$  to virtual squark-quark pairs, which then enhances the dark matter annihilation dramatically. Therefore, all the calculators for observables should be checked for correct behaviour in extreme scenarios. This particular point would have been removed by LHC exclusions on squark masses but the statement about checking the observable calculators is valid in any case.

If the SUSY mass measurements are made twice as accurately as expected, then the uncertainty on the relic density is halved, 1.8%. Thus there is a clear argument for aiming for the highest possible precision of the ILC SUSY mass measurements.

#### 6.6.4 pMSSM-4 fit to STC10' observables

STC10' SUSY masses and Higgs mass and branching fractions were used as input to a fit of pMSSM-4, i.e. only  $M_1$ ,  $M_2$ ,  $\mu$  and  $\tan\beta$ . The purpose was to check what importance the sfermion sector parameters have on the electroweakino sector determination.  $10^6$  points were calculated.

The resulting parameter distributions are plotted in Fig. 6.33 with respect to the equivalent distributions from the pMSSM-13 fit. The best fit points fall exactly on the model values. The shape of the  $\Delta\chi^2$  distributions is parabolic, with the uncertainties written out in Tab. 6.22. The uncertainties are reduced by a factor 5-10 compared to the equivalent pMSSM-13 fit results in Tab. 6.16. This is the reflecting amount

of freedom induced on the parameters from the sfermion sector,  $M_3$  and  $A_t$  into the pMSSM-13 fits.

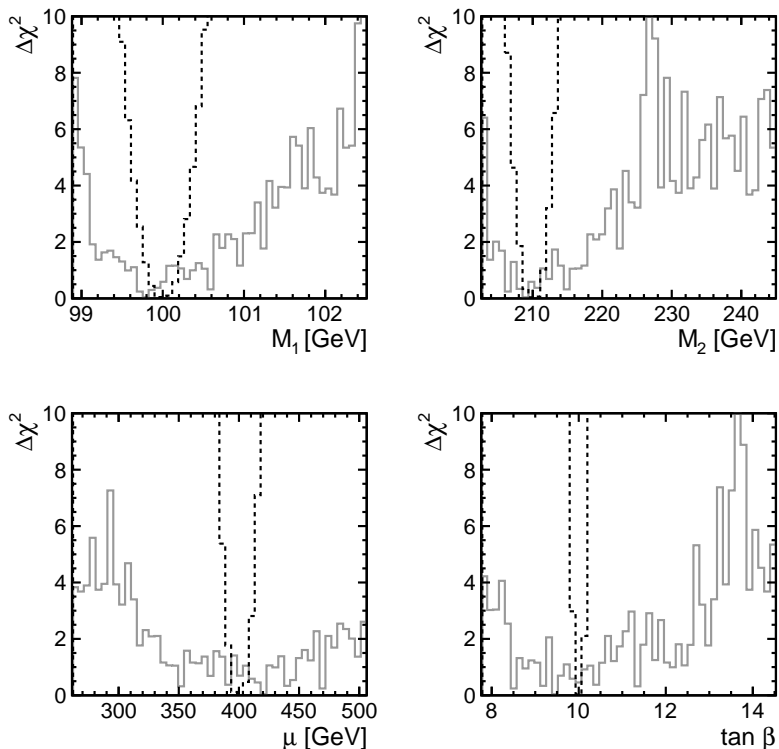


Figure 6.33: Predicted parameters from a 4-parameter fit to STC10' AllSUSY+h observables with the expected precisions. Length of fit  $10^6$  points.

parameter	STC10' true	best fit point	$1\sigma$	$2\sigma$
$M_1$	100	100.00	+0.16 -0.16	+0.32 -0.31
$M_2$	210	209.97	+1.15 -1.10	+2.24 -2.13
$\mu$	400	400.10	+4.83 -5.1	+9.79 -10.07
$\tan\beta$	10	10.00	+0.04 -0.04	+0.09 -0.09
$\chi^2$	$9 \times 10^{-5}$	0.0024		

Table 6.22: STC10' pMSSM-4 fit results using AllSUSY+h inputs ( $10^6$  fit points).

Masses are similarly restricted in this case. The higgsino masses are predicted correctly with a 4.5-5.0 GeV uncertainty at  $1\sigma$  confidence, or 9.5-10 GeV uncertainty at  $2\sigma$  confidence. This is around a factor 5 better than in the corresponding pMSSM-13 in Tab. 6.18.

The relic density is predicted correctly with a 1.6% uncertainty at  $1\sigma$  or 3% at  $2\sigma$  confidence.

### Effect of fixed parameters

It is interesting to check what effect the fixed parameters have on the fitted four parameters above. For this purpose, the pMSSM-13 fit results were searched to find a point with a squark mass above 2.7 TeV, away from the model point 2 TeV, and with a  $\Delta\chi^2 < 4$  to be within the  $2\sigma$  allowed region. A point like this was found with  $M_1 = 99$ ,  $M_2 = 206$ ,  $\mu = 449$ ,  $\tan\beta = 9.95$ ,  $m_A = 384$ ,  $M_3 = 2759$ ,  $M_{L(1)} = 206$ ,  $M_{E(1)} = 121$ ,  $M_{Q(1)} = 2959$ ,  $M_{Q(3)} = 1309$ ,  $M_{U(3)} = 1392$ ,  $M_{D(3)} = 731$ , and  $A_t = -2667$ , giving a  $\chi^2 = 2.3$  with AllSUSY+h inputs. These parameters were taken as fixed values for the fit except the fitted parameters  $M_1$ ,  $M_2$ ,  $\mu$  and  $\tan\beta$  were input with the model value as the central value, or some value within  $\pm 10\%$ . Then fits were run using the AllSUSY+h inputs, amounting to a total of  $10^6$  fit points from 10 separate fits.

The results are plotted in Fig. 6.34. The best fit point has a  $\chi^2 = 1.1$ , which is lower than the  $\chi^2$  of the originally found point in the pMSSM-13. It can be seen that the central values of  $M_1$ ,  $M_2$ ,  $\mu$  and  $\tan\beta$  are shifted to lower values by 1-2% except for  $\mu$  which is increased by more than 12%. The uncertainties remain the same. This tells us that these parameters are not independent of the fixed parameters, but the overall picture of the electroweakino-sector parameter remains the same. It would be an interesting next step to perform the same fits but fitting also the slepton parameters and  $m_A$  which are well-determined in the pMSSM-13 fit. However, this pMSSM-4 fit will be useful later for comparing with the higgsino scenario where no sfermions are observed. Another idea for a further study would be to fix the nine parameters to the best fit values found by the pMSSM-13 fit and fit the four electroweakino-sector parameters.

The shifted parameter values affect the best fit masses and relic density. The higgsino masses are increased to 460-470 GeV and the heavy higgses lowered to 384-393 GeV. The coloured sparticles are shifted corresponding to the changes in the values of the fixed parameters, e.g. the best fit of the first and second generation squark mass is now 3 TeV instead of 2 TeV corresponding to the increase in the fixed value of  $M_{Q(1)}$ .

The relic density  $\Omega_{\text{fit}}/\Omega_{\text{STC10}'} = 0.999 \pm 0.016$  if the fixed parameters take the model values and  $\Omega_{\text{fit}}/\Omega_{\text{STC10}'} = 0.973 \pm 0.015$  if the parameters are fixed to the above non-true values. Thus the uncertainty remains the same but the central value is decreased by 2.6%.

### 6.6.5 pMSSM-13 fits to STC10'- $\Omega_{75}$ and STC10'- $\Omega_{50}$

While it may be that the LSP saturates the relic density, it is not ruled out that could be some other type of dark matter simultaneously. Therefore, we will go through the results of pMSSM-13 fits to STC10'- $\Omega_{75}$  and STC10'- $\Omega_{50}$ . The same relative precisions for the SUSY mass observables have been assumed as for STC10', see Tab. 6.12 again. Both sets of results originate from a fit with one million Markov Chain points composed of 10 different fits.

#### Parameters

All parameters were fitted to the expected SUSY mass and Higgs measurements ‘‘All SUSY+h’’ in STC10'- $\Omega_{75}$ . The best fit parameters and their  $1\sigma$  uncertainties are listed

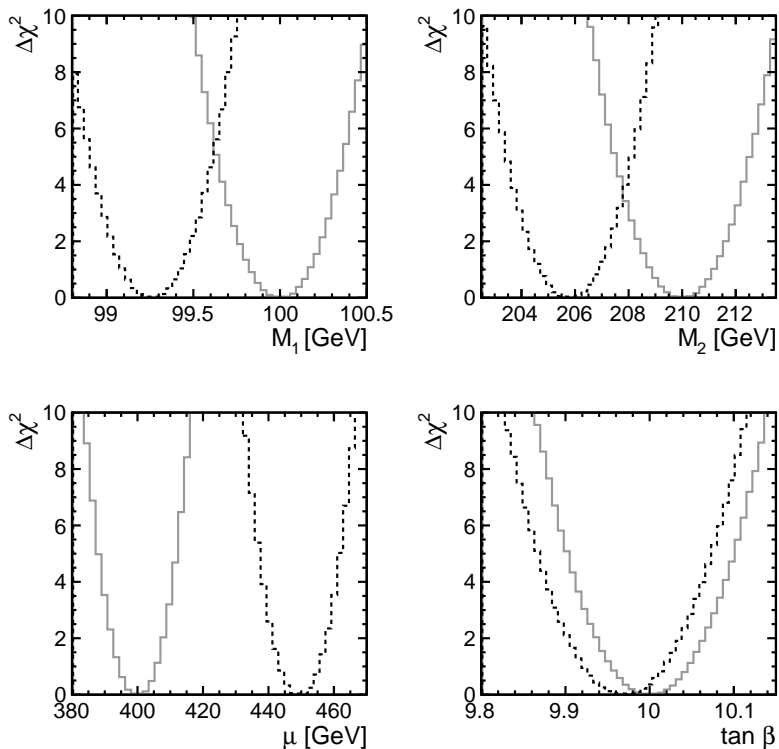


Figure 6.34: Comparison of fitted parameters in pMSSM-4 fits with fixed parameters to true (solid line) and non-true (dashed line) values.

in Tab. 6.23 and plotted in Fig. 6.35. All parameters can be constrained, and the best fit points agree with the model values within  $2\sigma$ . The uncertainties are comparable to the STC10' fit results.

The same fits were performed for the STC10'- $\Omega_{50}$  benchmark as well. The fitted parameters are listed in Tab. 6.24 and plotted in Fig. 6.36. The results are very similar to the results of the STC10'- $\Omega_{75}$  fit. It appears that changing the trilinear coupling between STC10'- $\Omega_{75}$  and STC10'- $\Omega_{50}$  does not significantly influence the fit results. The two benchmarks are compared directly in Fig. 6.37. Essentially no difference can be seen in the  $\Delta\chi^2$  distributions of  $M_1$ ,  $M_2$ ,  $\tan\beta$  and  $\mu$  parameters. As long as the ILC SUSY measurements i.e. the fit inputs are the same in the two benchmarks then no major difference can be seen in the fitted parameter ranges.

### Mass predictions

The predicted SUSY masses in the STC10'- $\Omega_{75}$  fit are plotted in Fig. 6.38. The predictions follow the same pattern as in STC10'. The best fit masses agree with the model masses within the  $2\sigma$  confidence intervals. All masses are well constrained, as can be read from Tab. 6.25. The predictions have similar precisions as in the corresponding STC10' fit.

The predicted masses in the STC10'- $\Omega_{50}$  fit are shown in Fig. 6.39, which are similar to the STC10'- $\Omega_{75}$  and STC10' fit results. This is to be expected as the benchmarks do not differ much and the same relative precisions were assumed for the ILC fit inputs.

parameter	STC10'- $\Omega_{75}$ true	best fit point	$1\sigma$	$2\sigma$
$M_1$	100	99.61	+0.85 -0.01	+1.12 -0.22
$M_2$	210	206.19	+7.77 -0.09	+12.58 -1.05
$\mu$	400	488.07	+1.71 -122	+17.21 -159
$\tan\beta$	10	8.79	+1.51 -0	+2.20 -0.30
$m_A$	400	398.6	+4.89 -0.21	+11.44 -4.83
$M_3$	2000	1516	+769 -8.5	+882 -39.2
$M_{L(1)}$	207	206.92	+0.74 -0.17	+1.66 -1.57
$M_{E(1)}$	110	111.05	+0.06 -3.02	+0.46 -3.77
$M_{Q(1)}$	2000	1490	+733 -8.52	+964 -191
$M_{Q(3)}$	1450	1323	+446 -0.47	+461 -206
$M_{U(3)}$	1100	1114	+248 -148	+248 -360
$M_{D(3)}$	1000	873	+211 -3.25	+285 -263
$A_{t=b=\tau}$	-2300	-2330	+87 -306	+309 -335
$\chi^2$	$1 \times 10^{-4}$	0.4561		

Table 6.23: STC10'- $\Omega_{75}$  pMSSM-13 fitted parameters using AllSUSY+h inputs ( $10^6$  points).

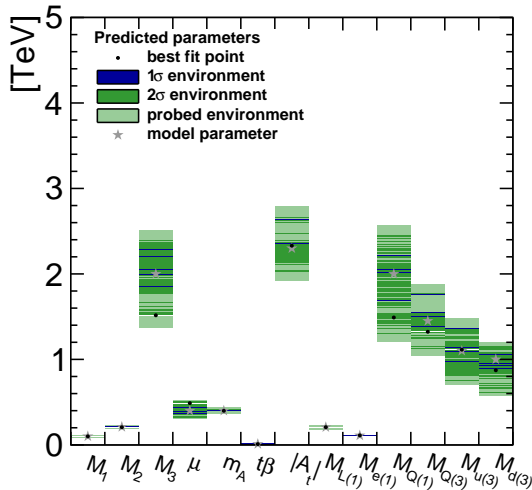


Figure 6.35: Predicted parameters from a 13-parameter fit to STC10'- $\Omega_{75}$  SUSY + Higgs observables with the expected precisions. Length of fit  $10^6$  points.  $\tan\beta$  is plotted as if it was in GeV.

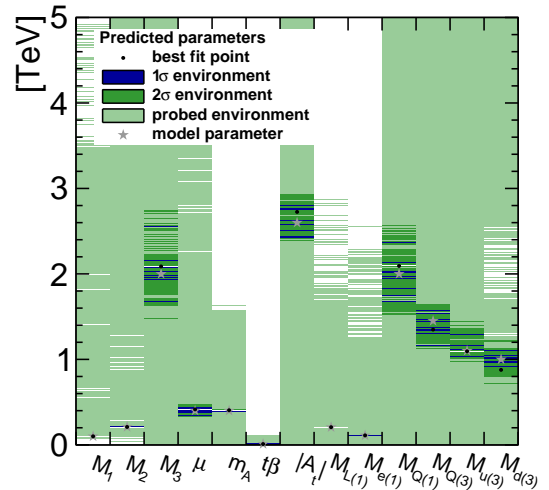


Figure 6.36: Predicted parameters from a 13-parameter fit to STC10'- $\Omega_{50}$  All SUSY + Higgs observables. Length of fit  $10^6$  points. The wide coverage of the probed region seems accidental.  $\tan\beta$  is plotted as if it was in GeV.

parameter	STC10'- $\Omega_{50}$ true	best fit point	$1\sigma$	$2\sigma$
$M_1$	100	99.85	+1.03 -0.21	+1.03 -0.56
$M_2$	210	209.49	+7.89 -1.98	+9.97 -4.58
$\mu$	400	415.11	+37.43 -74.78	+64.23 -81.48
$\tan\beta$	10	9.43	+1.89 -0.55	+2.02 -0.96
$m_A$	400	404.77	+0.24 -8.03	+6.15 -14.53
$M_3$	2000	2088	+467 -422	+661 -617
$M_{L(1)}$	207	206.72	+0.89 -0.78	+1.89 -2.11
$M_{E(1)}$	110	110.72	+1.42 -1.56	+3.54 -2.22
$M_{Q(1)}$	2000	2093	+276 -422	+473 -574
$M_{Q(3)}$	1450	1349	+228 -191	+299 -230
$M_{U(3)}$	1100	1095	+252 -56	+351 -125
$M_{D(3)}$	1000	877	+235 -6	+350 -165
$A_{t=b=\tau}$	-2600	-2725	+299 -82	+329 -213
$\chi^2$	$8 \times 10^{-4}$	0.5893		

Table 6.24: STC10'- $\Omega_{50}$  pMSSM-13 fitted parameters using AllSUSY+h inputs ( $10^6$  fit points).

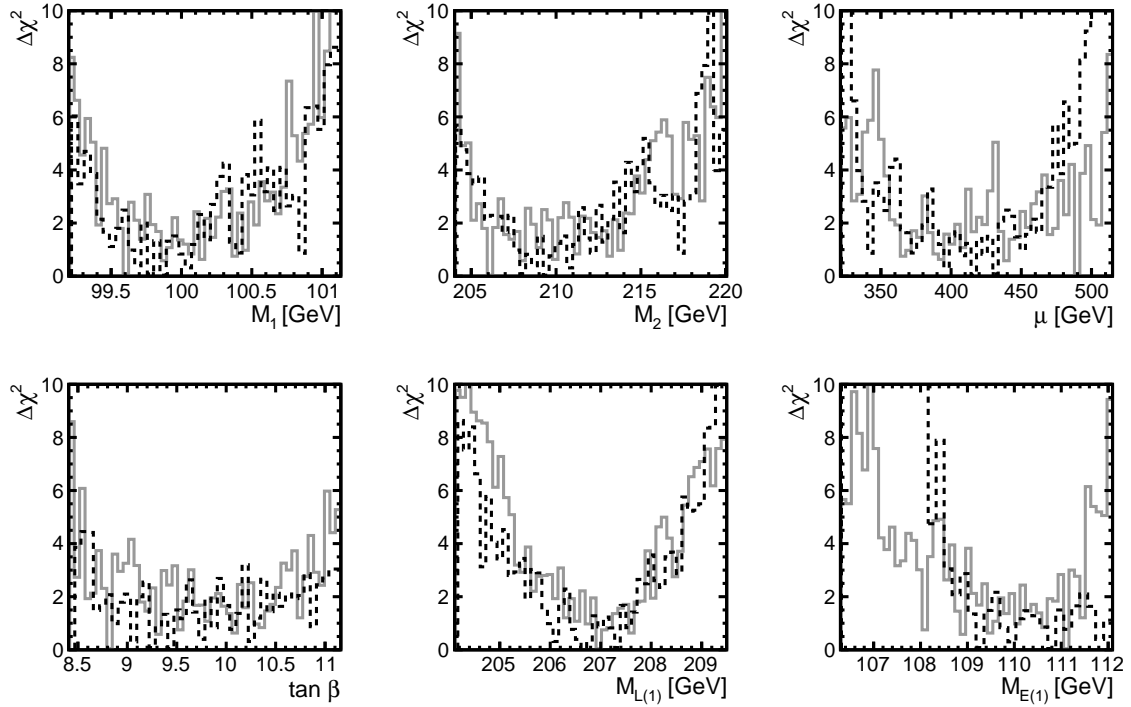


Figure 6.37: Parameter distributions in pMSSM-13 of fit STC10'- $\Omega_{75}$  to AllSUSY+h (solid) and STC10'- $\Omega_{50}$  AllSUSY+h (dashed) observables using  $10^6$  fit points for both.

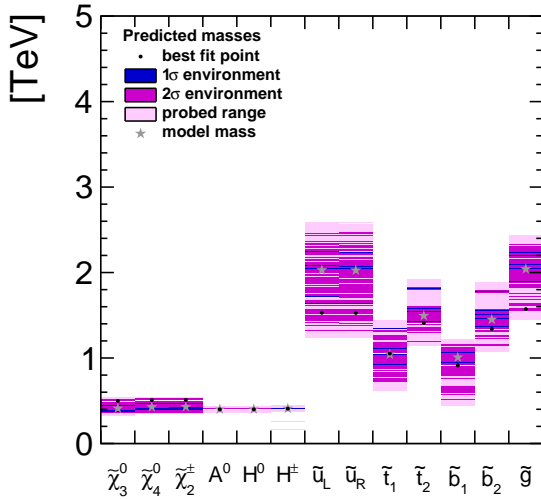


Figure 6.38: Predicted masses from a 13-parameter fit to STC10'- $\Omega_{75}$  SUSY + Higgs observables with the expected precisions. Length of fit  $10^6$  points.

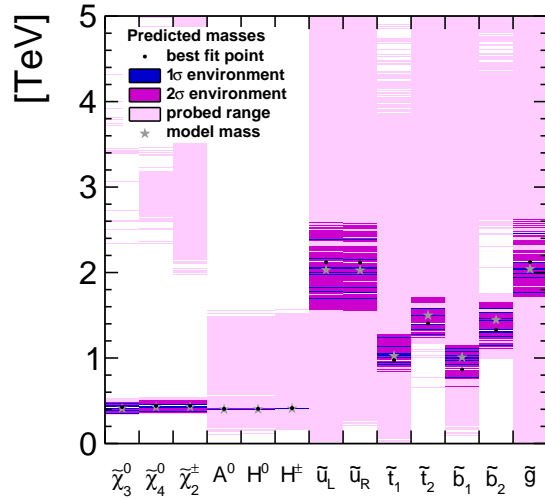


Figure 6.39: Predicted masses from a 13-parameter fit to STC10'- $\Omega_{50}$  All SUSY observables. Length of fit  $10^6$  points.

prediction	STC10'- $\Omega 75$ All SUSY+h			STC10'- $\Omega 50$ All SUSY+h		
	best fit	$1\sigma$	$2\sigma$	best fit	$1\sigma$	$2\sigma$
$m_{\tilde{\chi}_3^0}$	-498	$^{+0}_{-119}$	$^{+16}_{-157}$	-425	$^{+39}_{-74}$	$^{+64}_{-81}$
$m_{\tilde{\chi}_4^0}$	508	$^{+0}_{-110}$	$^{+16}_{-142}$	440	$^{+36}_{-66}$	$^{+61}_{-72}$
$m_{\tilde{\chi}_2^\pm}$	509	$^{+0}_{-110}$	$^{+16}_{-142}$	441	$^{+36}_{-66}$	$^{+61}_{-72}$
$m_{H_0}$	400	$^{+10}_{-10}$	$^{+20}_{-10}$	406	$^{+4}_{-16}$	$^{+14}_{-16}$
$m_{A_0}$	399	$^{+11}_{-9}$	$^{+21}_{-9}$	405	$^{+5}_{-15}$	$^{+15}_{-15}$
$m_{H^\pm}$	408	$^{+12}_{-8}$	$^{+12}_{-9}$	414	$^{+6}_{-14}$	$^{+6}_{-14}$
$m_{\tilde{u}_L}$	1530	$^{+720}_{-10}$	$^{+950}_{-210}$	2120	$^{+270}_{-430}$	$^{+470}_{-560}$
$m_{\tilde{u}_R}$	1527	$^{+713}_{-7}$	$^{+953}_{-207}$	2117	$^{+273}_{-427}$	$^{+463}_{-568}$
$m_{\tilde{t}_1}$	1052	$^{+298}_{-132}$	$^{+298}_{-372}$	975	$^{+275}_{-55}$	$^{+305}_{-135}$
$m_{\tilde{t}_2}$	1408	$^{+412}_{-8}$	$^{+422}_{-218}$	1405	$^{+245}_{-135}$	$^{+305}_{-165}$
$m_{\tilde{b}_1}$	913	$^{+157}_{-23}$	$^{+257}_{-403}$	865	$^{+255}_{-95}$	$^{+285}_{-205}$
$m_{\tilde{b}_2}$	1340	$^{+440}_{-10}$	$^{+460}_{-200}$	1330	$^{+260}_{-190}$	$^{+330}_{-220}$
$m_{\tilde{g}}$	1572	$^{+668}_{-2}$	$^{+758}_{-22}$	2123	$^{+337}_{-363}$	$^{+507}_{-553}$

Table 6.25: STC10'- $\Omega 75$  and STC10'- $\Omega 50$  fitted masses, pMSSM-13 fit with All-SUSY+h observables, fit length  $10^6$  points for both.

### Dark matter relic density

These benchmarks are interesting for the dark matter predictions as the coannihilation mechanism is more efficient in STC10'- $\Omega_{75}$  and STC10'- $\Omega_{50}$  compared to STC10'. The comparison of the fitted relic density in the different pMSSM-13 fits is shown in Fig. 6.40. In the fits with All SUSY+h inputs the relic density mean agrees with the model value  $\Omega_{model}$  within 1%. The  $1\sigma$  uncertainty for  $\Omega/\Omega_{model}$  in STC10'- $\Omega_{75}$  and STC10'- $\Omega_{50}$  fits is 3.4%, whereas for STC10' it was 3.9%. The small difference could be due to the STC10' fit being four times longer than the other two fits. Nevertheless, it is promising that the relic density determination does not depend on the actual amount of relic density filled by the LSP. This means that it is likely that, as long as there are slepton and gaugino measurements from the ILC which are accurate enough, then the relic density is determined correctly in stau coannihilation scenarios. The fourth line in Fig. 6.40 corresponds to a STC10'-LH150 fit discussed in the following subsection.

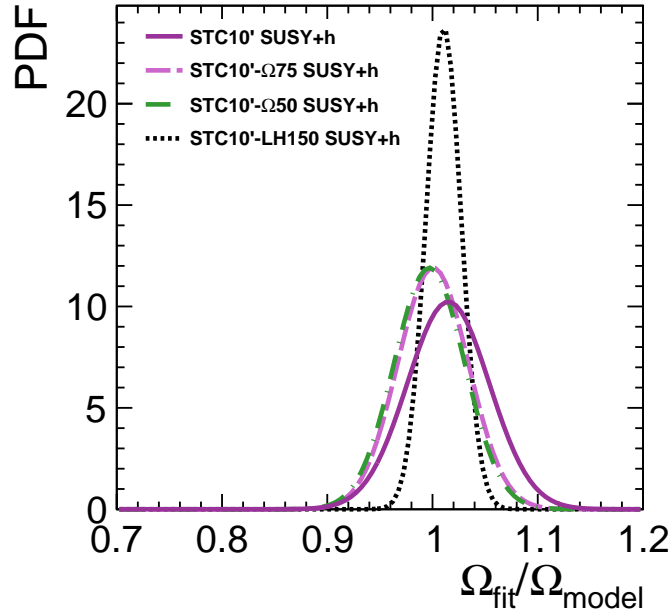


Figure 6.40: Comparison of determined relic densities from the STC10', STC10'- $\Omega_{75}$ , STC10'- $\Omega_{50}$  and STC10'-LH150 fits with AllSUSY+h inputs. The  $x$ -axis is scaled so that the  $\Omega_{fit}$  is divided by the model relic density of the assumed observables. This enables comparing the precisions of the predictions directly from the widths of the Gaussians.

### 6.6.6 pMSSM-14 fits to STC10'-LH150

This subsection shows fit results for the STC10'-LH150 benchmark which escapes current LHC limits on  $\tilde{e}_L$  and  $\tilde{\mu}_L$ . The difference in the model is that there is a fourteenth parameter, as explained in Sec. 6.2, which is fitted along with the other 13 pMSSM parameters. The fit was performed for one million Markov Chain points.

## Parameters

The full set of SUSY mass measurements and Higgs measurements (All SUSY+h) was input, and pMSSM-14 parameters were fitted. The fitted parameters, best fit values and their uncertainties are listed in Tab. 6.26. All parameters are fitted correctly within the  $1\sigma$  uncertainties, with a small  $\chi_{min}^2 = 0.6$ . Broadly speaking, the results are similar to the STC10' results. Some of the parameters are plotted in comparison with the equivalent STC10' fit results in Fig. 6.43, from which essentially no difference can be found for  $M_1$ ,  $M_2$ ,  $\tan\beta$  and  $\mu$  parameters. In the coloured sector the quark parameters appear to be more constrained as is depicted in Fig. 6.41. This may be an artefact from 14 parameters having been probed with the same number of Markov Chain points as in the 13 parameter case. In general all parameters are well constrained as in the other benchmarks.

The slepton parameters  $M_{L(1)}$  and  $M_{E(1)}$  are determined with similar precisions as the  $M_{L(1)}$  and  $M_{E(1)}$  in the other benchmarks despite the fact that in STC10'-LH150  $M_{L(1)}$  is split into  $M_{L(1)} = M_{L(2)}$  and  $M_{L(3)}$ .  $M_{L(3)}$  is determined with a 4.2 GeV range, which is worse than for the other two slepton parameters but is reasonable as the  $\tilde{\tau}_2$  mass measurement is worse than the  $\tilde{e}_L$  and  $\tilde{e}_R$  mass measurements.

## Masses

All unobserved SUSY particle masses are constrained by the fit as in the pMSSM-13 fits above. The predicted masses from the STC10'-LH150 fit including SUSY and Higgs measurements from ILC are plotted in Fig. 6.42. The overall pattern remains the same as in the fits for the other benchmarks. Higgsino masses are predicted with 70 GeV ranges at  $1\sigma$  confidence, while the heavy Higgses are predicted with 20 GeV ranges. The coloured sector is constrained too. Comparing more closely to the equivalent STC10' fit, the  $2\sigma$  confidence intervals of the higgsinos are smaller in STC10'-LH150 but the difference could easily be caused by the limitation of the Markov Chain. Otherwise the ranges are similar. This is reasonable because the extra parameter in STC10'-LH150 gives freedom for the slepton sector which is assumed to be measured very precisely.

## Dark Matter

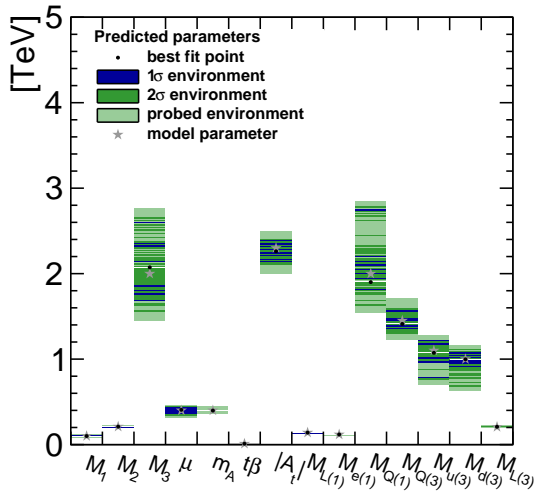
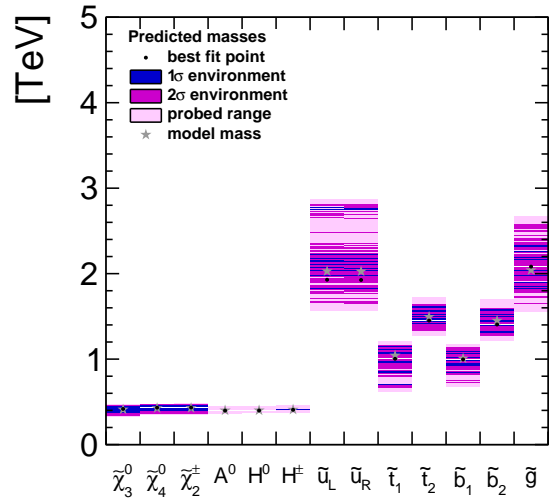
The relic density can be predicted by the fit in STC10'-LH150 like in the other benchmarks. This can be seen from Fig. 6.40 that the most precise prediction for the relic density can be made in the STC10'-LH150 benchmark. The relic density uncertainty is about half of the uncertainties in the other benchmarks, 1.7%. This is reasonable as  $\tilde{e}_L$  and  $\tilde{\mu}_L$  are lighter in STC10'-LH150 than in the other scenarios, leading to a stronger dependence of the relic density on the fit inputs.

### 6.6.7 Comparison to direct and indirect DM detection experiments

The fits give predictions for the astrophysical observables: Tab. 6.28 lists the fitted direct and indirect detection cross sections  $\sigma^{SI}$  and  $\langle\sigma v\rangle$  in the pMSSM-13 fits. In all benchmarks, if SUSY masses and Higgs observables are used as fit inputs, then both the direct and indirect detection cross sections are predicted correctly within

parameter	STC10'-LH150 true	best fit point	$1\sigma$	$2\sigma$
$M_1$	100	99.96	+0.49 -0.44	+1.04 -0.44
$M_2$	210	210.06	+4.03 -2.46	+8.85 -3.96
$\mu$	400	406.43	+26.5 -45.95	+35.09 -75.42
$\tan\beta$	10	10.12	+0.56 -0.81	+1.72 -0.96
$m_A$	400	398.03	+7.15 -4.41	+9.91 -7.43
$M_3$	2000	2074	+533 -401	+592 -531
$M_{L(1)}$	140	140.04	+0.50 -0.70	+1.61 -1.63
$M_{L(3)}$	207	208.54	+0.05 -3.68	+1.58 -4.66
$M_{E(1)}$	118	118.34	+0.45 -1.68	+0.96 -2.06
$M_{Q(1)}$	2000	1901	+852 -93	+889 -289
$M_{Q(3)}$	1450	1412	+164 -60	+182 -108
$M_{U(3)}$	1100	1074	+138 -295	+158 -315
$M_{D(3)}$	1000	998	+78 -181	+117 -316
$A_{t=b=\tau}$	-2300	-2264	+123 -127	+155 -143
$\chi^2$	$6 \times 10^{-6}$	0.5893		

Table 6.26: STC10'-LH150 pMSSM-13 fit results using AllSUSY+h inputs


 Figure 6.41: Predicted parameters from a 13-parameter fit to STC10'-LH150 SUSY + Higgs observables with the expected precisions. Length of fit  $10^6$  points.  $\tan\beta$  is plotted as if it was in GeV.

 Figure 6.42: Predicted masses from a 13-parameter fit to STC10'-LH150 All SUSY+h observables. Length of fit  $10^6$  points.

prediction	STC10'-LH150 All SUSY+h		
	best fit	$1\sigma$	$2\sigma$
$m_{\tilde{\chi}_3^0}$	-416.9	+26.1 -44.9	+35.1 -74.9
$m_{\tilde{\chi}_4^0}$	432.2	+23.8 -40.2	+32.2 -65.2
$m_{\tilde{\chi}_2^\pm}$	433.1	+24.9 -40.1	+32.9 -66.1
$m_{H_0}$	398.8	+11.2 -8.8	+11.2 -8.8
$m_{A_0}$	398.0	+12.0 -8.0	+12.0 -8.0
$m_{H^\pm}$	407.2	+12.8 -7.2	+12.8 -7.2
$m_{\tilde{u}_L}$	1929	+851 -109	+881 -289
$m_{\tilde{u}_R}$	1926	+844 -106	+884 -286
$m_{\tilde{t}_1}$	1004	+156 -304	+166 -344
$m_{\tilde{t}_2}$	1451	+169 -91	+189 -121
$m_{\tilde{b}_1}$	997	+103 -157	+143 -277
$m_{\tilde{b}_2}$	1405	+185 -95	+195 -135
$m_{\tilde{g}}$	2085	+458 -312	+498 -442

Table 6.27: STC10'-LH150 fitted masses, pMSSM-13 fit with AllSUSY+h observables, fit length  $10^6$  Markov Chain points.

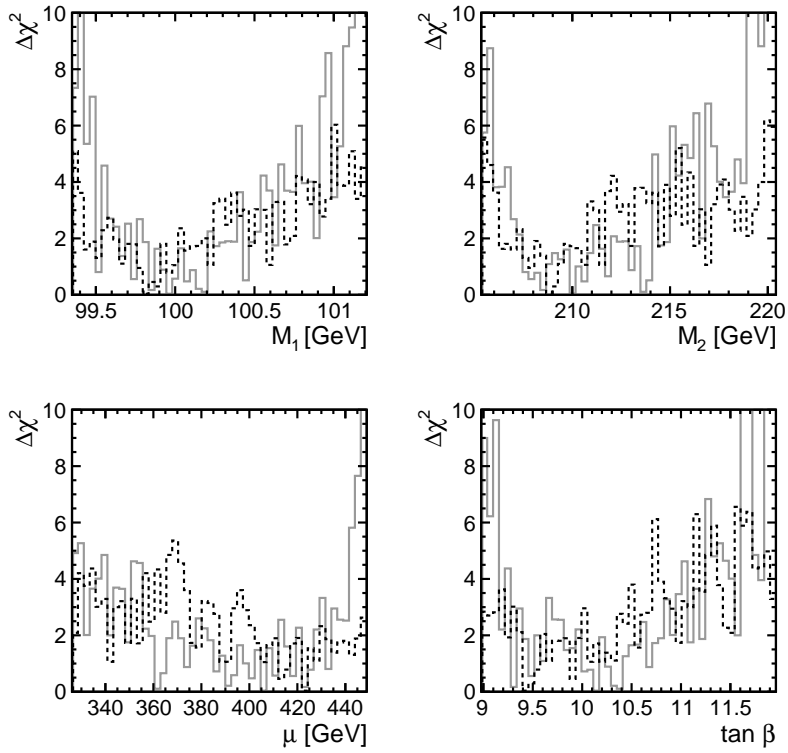


Figure 6.43: Distributions of the  $\Delta\chi^2$  in the fit of pMSSM-13 parameters to AllSUSY+h observables in STC10'- $\Omega_{75}$  (solid) and AllSUSY+h observables in STC10' (dashed) using  $10^6$  fit points for both.

the  $1\sigma$  uncertainty. The uncertainties are not symmetric around the best fit point though.

If only SUSY masses are used, as in the STC10' AllSUSY fit, then the best fit cross sections are still near the model values but the  $1\sigma$  ranges reach an order of magnitude higher for the indirect detection cross section and the direct detection cross section. This is in correlation with the allowed low values of the relic density in this fit, as discussed in Sec. 6.6.3. If the condition is imposed that  $m_A > 260$  GeV as in the relic density case then the indirect detection cross section  $1\sigma$  confidence interval is reduced to  $[1.051, 3.616] \times 10^{-27} \text{ cm}^3\text{s}^{-1}$  and the direct detection cross section to  $[0.727, 16.593] \times 10^{-9} \text{ pb}$ .

After the  $m_A$  cut, some points remain in the  $2\sigma$  range of the direct detection cross section with a size  $> 400 * 10^{-9} \text{ pb}$ . The points with the largest direct detection cross section have  $M_{Q(3)} < M_{U(3)}$  so that  $\tilde{t}_1$  is left-chiral rather than right-chiral as in the benchmark. Requiring the correct hierarchy along with the  $m_A$  requirement reduces the  $2\sigma$  upper bound on the direct detection cross section to  $45 \times 10^{-9} \text{ pb}$ . It could not be concluded what causes these larger values, so it has to be concluded that they are simply allowed by the fit. Nevertheless, it is remarkable that these cross sections can be somewhat predicted. Being able to predict the astrophysical observables means that the direct and indirect detection experiments can check whether their results agree with the collider predictions, maximally utilising the complementarity of the collider and the astrophysics experiments.

	STC10'	STC10'	STC10'- $\Omega_{75}$	STC10'- $\Omega_{50}$	STC10'-LH150
observable	AllSUSY+h	AllSUSY	AllSUSY+h	AllSUSY+h	AllSUSY+h
$\langle\sigma v\rangle[10^{-27} \text{ cm}^3\text{s}^{-1}]$ model	2.101	2.101	1.764	2.11	1.532
$\langle\sigma v\rangle[10^{-27} \text{ cm}^3\text{s}^{-1}]$ best fit	$2.371^{+0.525}_{-0.900}$	[1.051, 22.281]	$2.546^{+0.0}_{-1.055}$	$2.319^{+0.428}_{-0.969}$	$1.542^{+0.199}_{-0.329}$
$\sigma^{SI}[10^{-9} \text{ pb}]$ model	2.238	2.238	2.273	2.243	2.278
$\sigma^{SI}[10^{-9} \text{ pb}]$ best fit	$1.847^{+1.923}_{-0.530}$	[0.727, 26.303]	$1.229^{+1.663}_{-0.0}$	$1.906^{+2.078}_{-0.445}$	$2.226^{+0.950}_{-0.392}$

Table 6.28: Best fit astrophysics observables from pMSSM-13 fits to different benchmark models. The quoted uncertainties are for  $1\sigma$  CL. The results for the fit to STC10' AllSUSY observables are quoted after applying the cut  $m_A > 260$  GeV.

### 6.6.8 Effect of $Sign(\mu)$

The sign of the higgsino mass parameter  $\mu$  is positive in the STC10' benchmarks. If it is inverted, then the masses and cross sections change. The comparison of masses in STC10' with positive and negative  $Sign(\mu)$  benchmarks is in Tab. 6.29 as calculated with `SPheno3.3.9beta3`. The LSP mass is 2.3 GeV larger if  $Sign(\mu)$  is negative rather than positive. The mass of  $\tilde{\tau}_1$  also increases by 12.2 GeV and  $\tilde{\chi}_2^0$  and  $\tilde{\chi}_1^\pm$  masses are increased by 8 GeV. Using the expected ILC precisions on the SUSY mass measurements, the  $\chi^2$  between STC10' with positive and negative  $Sign(\mu)$  is 5400. The mass of the light Higgs is increased by 76 MeV according to `SPheno3.3.9beta3` thus adding to the  $\chi^2$ .

The branching fractions of  $\tilde{\chi}_1^\pm$  and  $\tilde{\chi}_2^0$  also change. Decays of  $\tilde{\chi}_1^\pm \rightarrow \tilde{\tau}_1 \nu_\tau$  decrease from a 72.4% branching fraction to 8.9%. Instead, the rate of decays to sneutrinos is increased. Similarly,  $\tilde{\chi}_2^0$  decays mainly to sneutrinos if  $\text{Sign}(\mu)$  is negative, as opposed to mainly to  $\tilde{\tau}_1 \tau$  when  $\text{Sign}(\mu)$  is positive. Furthermore, the production cross section for  $\tilde{\chi}_2^0 \tilde{\chi}_1^0$  is modified by 5% which together with the change in branching fractions would amount to an observable difference. Similarly, the production cross sections for  $\tilde{e}_R \tilde{e}_R$  and  $\tilde{\tau}_1 \tilde{\tau}_1$  are modified by 2.6% and 1.4% respectively, leading to an observable difference in the overall  $\sigma \times BR$  of the studied channels.

With a combination of mass and cross section measurements, it should be possible to conclude that  $\text{Sign}(\mu)$  should be positive if STC10' phenomenology is observed. It was not possible to test this by fitting the SUSY parameters with  $\text{Sign}(\mu) = -1$  to STC10' observables as the `Fittino1` code for fitting pMSSM did not include this option at the time of writing.

observable	STC10'	STC10'
	with $\text{Sign}(\mu) = +1$	with $\text{Sign}(\mu) = -1$
$m_{\tilde{\chi}_1^0}$	95.93	98.24
$m_{\tilde{\tau}_1}$	107.36	119.58
$m_{\tilde{\chi}_2^0}$	206.23	214.14
$m_{\tilde{\chi}_1^\pm}$	206.13	214.48
$m_{\tilde{\tau}_2}$	219.49	211.13
$m_{\tilde{e}_L}$	214.08	214.17
$m_{\tilde{e}_R}$	130.09	130.13
$m_{\tilde{\mu}_L}$	214.09	214.2
$m_{\tilde{\mu}_R}$	130.07	130.10
$m_{\tilde{\nu}_\tau}$	196.7	196.04
$m_{\tilde{\nu}_e}, m_{\tilde{\nu}_\mu}$	199.4	199.51
$m_{\tilde{t}_1}$	1010	1015
$m_{\tilde{b}_1}$	1008	1008
$m_{\tilde{g}}$	2041	2041

Table 6.29: Light sparticle masses in STC10' with positive and negative  $\text{Sign}(\mu)$  from `SPheno3.3.9beta3`.

## 6.7 From the weak scale to the GUT scale

The pMSSM parameters were fitted at the 1 TeV energy scale. As the parameter values are governed by the RGEs introduced in Ch. 2, it is possible to evolve the fitted

parameters to higher energy scales. In high-scale models, some of the parameters unify, famously the gauge sector masses. It is interesting to check what behaviour the fitted parameters show.

The model STC10' parameter running is shown in Figs. 6.44 for the gaugino masses, 6.45 for sfermion masses and 6.46 for the Higgs mass-squared parameters respectively.  $M_1$  and  $M_2$  unify and  $M_3$  is too large to unify at the same scale. Down-type third generation mass parameter and left-handed slepton mass parameters are not well-behaved at high energies. Additionally, the down-type Higgs mass parameter is staying just above zero except while going negative at low and high energies. As the model was designed as a pMSSM model, the parameters need not behave well at high energies as long as this does not imply problems for the fit. If this kind of running parameter situation was discovered, then more new physics than SUSY would have to exist below the GUT scale.

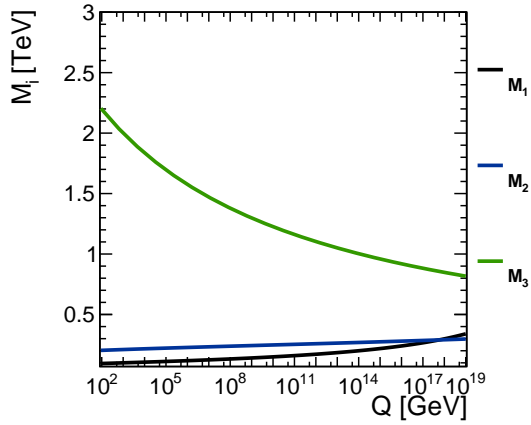


Figure 6.44: STC10' model running of the gaugino mass parameters  $M_i$ .

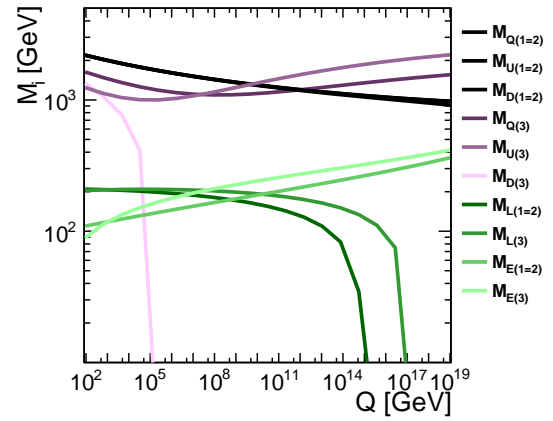


Figure 6.45: STC10' model running of the sfermion mass parameters.

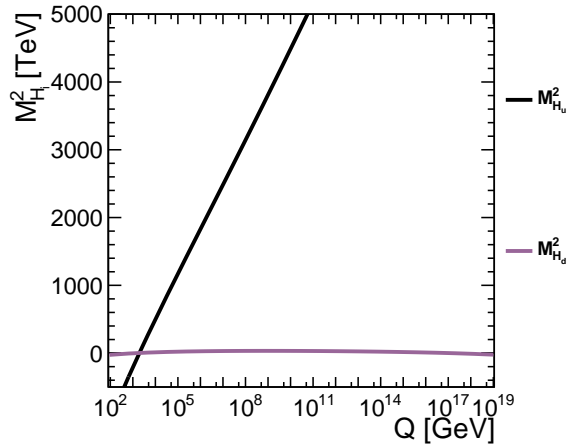


Figure 6.46: STC10' model Higgs squared-mass running.

First the method to study the RGE evolution is discussed. Then the results from the pMSSM-13 fit to STC10' AllSUSY+h observables and pMSSM-14 fit to STC10'-LH150

AllSUSY+h observables are shown.

### 6.7.1 Method

The parameter running is calculated with `SPheno3.3.9beta3` [206]. A Les Houches input file is given with the parameter values at 1 TeV and `SPheno` computes the running values up to  $10^{19}$  GeV. The input values are defined as follows: a value for each parameter is drawn randomly from a Gaussian distribution with the fitted value as the mean and the uncertainty from the fit (despite not all distributions being truly Gaussian). Then for each parameter set the running is calculated with 21 values equidistant between 91 GeV and  $10^{19}$  GeV. This set of values is saved. It is necessary to vary all parameters at once as the RGE equations are coupled.

This drawing and running is repeated  $5 \times 10^4$  times, leading to a toy distribution for each parameter at each of the 21 energy scales. It should be noted that not all  $5 \times 10^4$  points lead to an acceptable (non-tachyonic) SUSY spectrum. Those points are excluded from the distributions. The distributions are used to extract the mean and uncertainty for each parameter at each energy scale. These are then plotted and coloured bands are drawn to indicate the  $1\sigma$  confidence ranges for each parameter. This method considers the worst case scenario where all of the SUSY parameters are uncorrelated.

### 6.7.2 Results

The fitted parameters from a fit of pMSSM-13 to all SUSY STC10' masses with expected precisions and Higgs mass and branching fractions were listed in Tab. 6.16 in Sec. 6.6.2. These results were used to calculate the running of the parameters.

The running of the gaugino mass parameters is plotted in Fig. 6.47. What is seen is that the bino and wino mass parameters  $M_1$  and  $M_2$  unify at about  $10^{16}$  as would be expected from the design of the STC10' benchmark -  $M_1 : M_2 = 100 : 210 \sim 1 : 2$  as in GUT unified mSUGRA models. It is clear to see that  $M_3$  does not unify with  $M_1$  and  $M_2$ . This is as expected from the design of the benchmark point where the famous relation  $M_1 : M_2 : M_3 = 1 : 2 : 4$  [75] is not satisfied for  $M_3$ . What is remarkable is that this information could be extracted from SUSY mass and Higgs measurements at the ILC by fitting the pMSSM parameters.

The sfermion mass parameters have their RGE evolution too, and for the same fit the result is plotted in Fig. 6.48. It can be seen that  $M_{D(3)}$ ,  $M_{E(3)}$  and  $M_{E(1)}$  crash to negative values leading to similar effects as in the model point. There  $M_{L(1,3)}$  were unstable. In any case it is not clear from this plot whether any of the parameters unify with each other. What can be concluded is that there would be motivation for experimentally testing physics at the very high scales of 100 TeV.

Finally, the Higgs mass squared parameters  $M_{H_u}^2$  and  $M_{H_d}^2$  are plotted in Fig. 6.49 in the linear scale. It can be seen that the up-type parameter  $M_{H_u}^2$  runs to high values from its small 1 TeV value and  $M_{H_d}^2$  remains at low or even negative values at all energies.

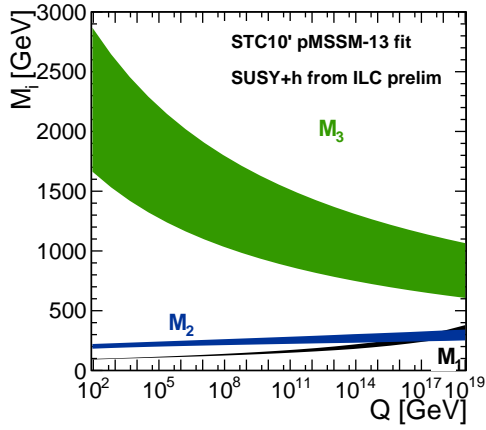


Figure 6.47: The running of gaugino mass parameters based on the pMSSM-13 fit to STC10' AllSUSY+h observables.

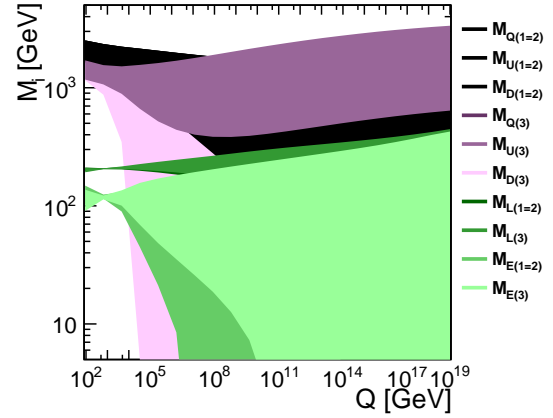


Figure 6.48: Running of sfermion mass parameters based on the pMSSM-13 fit to STC10' AllSUSY+h observables.

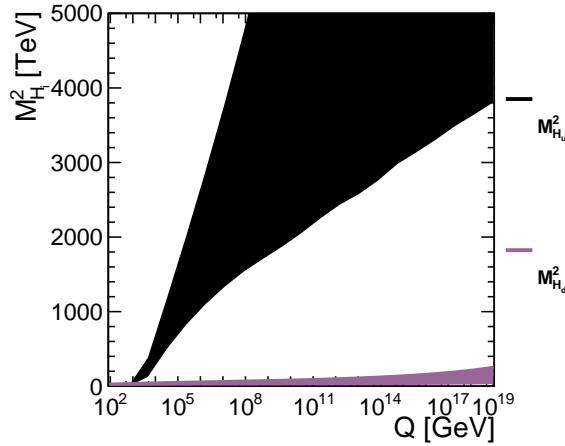


Figure 6.49: Running of Higgs mass-squared parameters based on a pMSSM-13 fit to STC10' AllSUSY+h observables.

As a comparison, the running of the parameters in the STC10'-LH150 benchmark are shown in Figs. 6.50, 6.51 and 6.52. The same discoveries for  $M_i$  were made, namely that  $M_1$  and  $M_2$  unify but  $M_3$  does not. The sfermion masses and Higgs mass-squared parameters show similar behaviour as above.

It is clear that this kind of predictions for the running parameters rely on precise SUSY measurements from the ILC. Any theoretical uncertainties are currently ignored. It is reasonable to expect that if such SUSY discoveries were once made, there would be a great effort from the phenomenology community to reduce these theoretical uncertainties to the minimum.

One irreducible uncertainty is the assumption that there is no new physics between the SUSY scale and the Planck scale. The observation of a running group evolution as in the case above would indicate that this assumption is false.

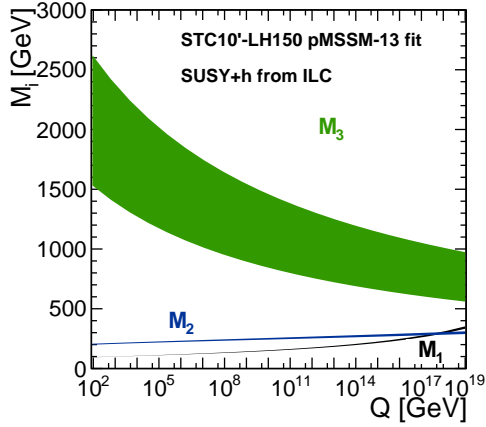


Figure 6.50: Running of gaugino mass parameters based on a pMSSM-14 fit to STC10'-LH150 AllSUSY+h observables.

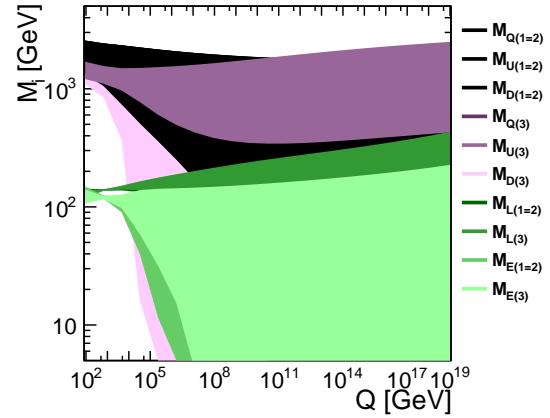


Figure 6.51: Running of sfermion mass parameters based on a pMSSM-14 fit to STC10'-LH150 AllSUSY+h observables.

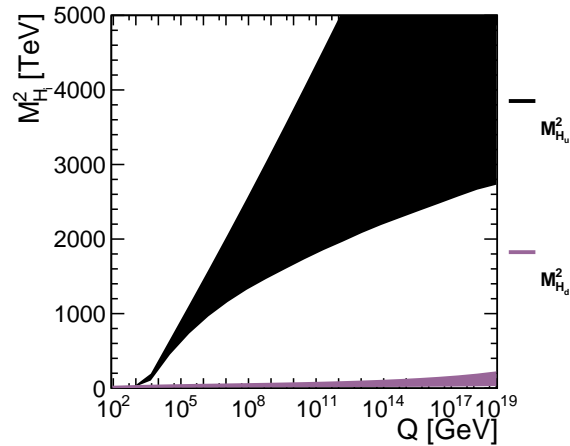


Figure 6.52: Running of Higgs mass-squared parameters based on a pMSSM-14 fit to STC10'-LH150 AllSUSY+h observables.

## 6.8 Outlook

It has been shown that precision SUSY and Higgs measurements at the ILC would greatly reduce the available SUSY parameter space and enable strong predictions for the heavier sparticle masses and relic density. It would be interesting to find out what effect the possible LHC observations would have on the SUSY parameter determination: The STC8 and STC10 points were designed to cause a signal at the LHC or HL-LHC, as discussed above and in [170]. The measurement on  $\tilde{b}_1$  would allow constraining the coloured sector further.

Additional suggestions have been made to include limits from flavour physics experiments and electroweak precision measurements into the parameter fits. The flavour constraints, such as the rate of  $b \rightarrow s\gamma$ , would contribute to restricting the squark masses and electroweakino and gluino masses, which influence the decay rate via loop corrections [75].  $B_s \rightarrow \mu^+\mu^-$  and  $B_d \rightarrow \tau^+\tau^-$  are sensitive to  $\tan\beta$  and  $m_A$  [75] which, in the STC models, would be well-restricted by the ILC SUSY and Higgs measurements alone. It could be tested whether the  $B$  decays inputs restrict  $m_A$  and  $\tan\beta$  further.

Electroweak precision measurements could restrict the parameter space even further. For example, the  $Z$  and  $W$  masses are corrected dominantly by the scalar top and bottom loops [176]. Another example is the top quark mass which receives corrections from stop-gluino and sbottom-chargino loops [254]. Therefore, including electroweak precision observables should bring additional constraints to the parameters. It would be worthwhile to include the corrections despite the increase in the required computing time.



# Chapter 7

## Light higgsino scenario

### 7.1 Motivation

Naturalness has been used as a guiding principle when arguing for the existence of weak-scale supersymmetry. As briefly discussed in Ch. 2, the Higgs mass receives arbitrarily large corrections to its mass from the Standard Model fermions and bosons, unless some new physics effects cancel these. The largest Standard Model contribution to the Higgs mass arises from the top quark loop, displayed in Fig. 7.1 where  $f$  would stand for the top quark. The size of the correction is

$$\Delta m_H^2 = -\frac{|\lambda_t|^2}{8\pi^2} \Lambda_{\text{UV}}^2 + \dots \quad (7.1)$$

where  $\Lambda_{\text{UV}}$  is the UV-cutoff scale where new physics is expected to appear. This would mean an enormous correction as we expect  $\lambda_t \sim \mathcal{O}(1)$ .

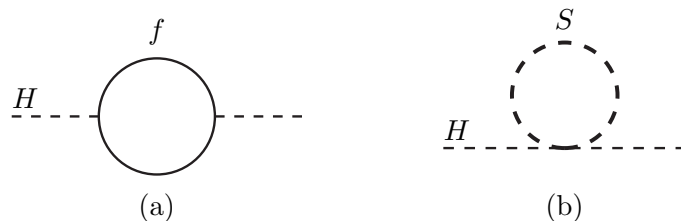


Figure 7.1: Figure from [31].

The divergence of the Higgs mass can be removed by introducing a scalar SUSY particle  $\tilde{t}$  at some mass scale  $m_{\tilde{t}}$  with coupling  $\lambda_{\tilde{t}}$  to the Higgs. The scalar top would then induce the second diagram in Fig. 7.1 which gives rise to a correction

$$\Delta m_H^2 = \frac{\lambda_{\tilde{t}}}{16\pi^2} \left[ \Lambda_{\text{UV}}^2 - 2m_{\tilde{t}}^2 \ln(\Lambda_{\text{UV}}/m_{\tilde{t}}) + \dots \right] \quad (7.2)$$

Therefore, if  $m_{\tilde{t}}$  is not too large, then the negative top loop contribution is balanced by the positive scalar top loop contribution.

As the top loop gives the largest contribution to the Higgs mass, traditional quantifications of fine-tuning in SUSY are based on it. One quantity is the Barbieri-Giudice

measure of fine-tuning on  $m_Z^2$  induced by parameter  $p_i$  [255–257], which is defined as

$$\Delta_{BG}(p_i) \equiv \left| \frac{p_i}{m_Z^2} \frac{\partial m_Z^2}{\partial p_i} \right|. \quad (7.3)$$

The value of interest is the maximum value  $\Delta_{BG} \equiv \max_i(\Delta_{BG}(p_i))$ . This fine-tuning measure gives a preference for coloured sector masses of order less than 1 TeV. However, the problem with this definition is that it neglects the interdependence of the pMSSM parameters in a more complete, perhaps realistic model with GUT motivation, see e.g. [258].

The Barbieri-Giudice fine-tuning measure is not the only possible way to quantify fine-tuning, as is argued e.g. in [256]. A heavy coloured sector is allowed in the alternative definition of fine-tuning based on the requirement that the  $Z$ -mass should be obtained without large cancellations. As familiar from Ch. 2, the scalar potential minimisation condition gives

$$\frac{m_Z^2}{2} = \frac{M_{H_d}^2 + \Sigma_d^d - (M_{H_u}^2 + \Sigma_u^u) \tan^2 \beta}{\tan^2 \beta - 1} - \mu^2, \quad (7.4)$$

where  $m_{H_u}^2$  and  $m_{H_d}^2$  are soft SUSY breaking Lagrangian terms,  $\mu$  is the higgsino mass parameter and  $\tan \beta$  is the ratio of the Higgs VEVs.  $\Sigma_u^u$  and  $\Sigma_d^d$  denote radiative corrections. The electroweak fine-tuning measure  $\Delta_{EW}$  is then defined by

$$\Delta_{EW} \equiv \max_i \left( \frac{2|C_i|}{m_Z^2} \right). \quad (7.5)$$

with the  $C_i$  being the individual terms in Eq. 7.4 listed below for clarity:

$$\begin{aligned} C_{H_d} &= M_{H_d}^2 / (\tan^2 \beta - 1), \\ C_{H_u} &= -M_{H_u}^2 \tan^2 \beta / (\tan^2 \beta - 1), \\ C_\mu &= -\mu^2, \\ C_{\Sigma_u^u(k)} &= -\Sigma_u^u(k) \tan^2 \beta / (\tan^2 \beta - 1), \\ C_{\Sigma_d^d(k)} &= -\Sigma_d^d(k) / (\tan^2 \beta - 1). \end{aligned} \quad (7.6)$$

The index  $k$  refers to all the loop contributions.

If  $\Delta_{EW} \sim 10 - 30$ , then  $M_Z$  is not fine-tuned [257]. From the requirement on  $\Delta_{EW}$  we see that  $\mu$  should be  $\mathcal{O} = 100 - 300$  GeV and  $-M_{H_u}^2 \sim M_Z^2/2$ , which can be obtained by the radiative running of  $M_{H_u}^2$  to small values. Additionally, scalar top loop contributions  $\Sigma_u^u$  should be less than 300 GeV, implying  $m_{\tilde{t}_1} = 1 - 2$  TeV,  $m_{\tilde{t}_2} = 2 - 4$  TeV with a large  $A_t$  [257]. These conditions can be satisfied by the NUHM2 models with  $M_{H_u}^2$ ,  $M_{H_d}^2$ ,  $M_0$ ,  $M_{1/2}$ ,  $A_0$  and  $\tan \beta$  as free parameters.

The implications of small electroweak fine-tuning on the collider phenomenology are depicted in Fig. 7.2 for NUHM2 models. It can be seen that large areas of the low fine-tuning region are excluded by LEP but that there is room for natural SUSY in the  $\mu < 300$  GeV,  $M_{1/2} < 1.3$  TeV range. In this case,  $M_1$  and  $M_2$  are much larger than  $\mu$  so the lightest neutralinos and chargino are higgsino-like. In this case the  $\mu$  parameter is the main contributor to the higgsino masses, as can be seen from the equations for higgsino masses at tree-level,

$$m_{\tilde{\chi}_1^0, \tilde{\chi}_2^0} = \eta_{1,2} \left( |\mu| \mp \frac{m^2}{2} (1 \pm \sin 2\beta \text{Sign}(\mu)) \times \left( \frac{\sin^2 \theta_W}{M_1} + \frac{\cos^2 \theta_W}{M_2} \right) \right) + \mathcal{O}(1/M_{1,2}^2) + \dots, \quad (7.7)$$

$$M_{\tilde{\chi}^\pm} = |\mu| - \sin 2\beta \text{Sign}(\mu) \cos^2 \theta_W \frac{m_Z^2}{M_2} + \mathcal{O}(1/M_{1,2}^2), \quad (7.8)$$

where the SUSY parameters are labelled as usual, and  $\eta_{1,2}$  are the signs of the higgsino mass eigenvalues [169]. Thus,  $\mu$  being small implies higgsino masses should be light,  $\mathcal{O}(100 - 300)$  GeV. It is important to emphasise that the reach of the ILC with  $\sqrt{s} = 500$  GeV covers almost the entire region of  $\Delta_{EW} < 30$ . This is the key motivation for studying light higgsinos at the ILC and in this thesis.

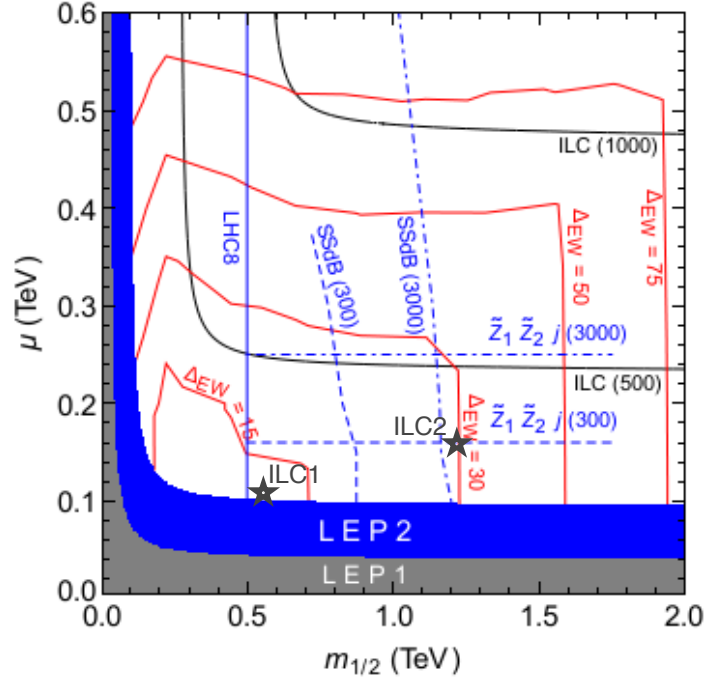


Figure 7.2: The size of the electroweak fine-tuning measure on the  $\mu$ - $M_{1/2}$ -plane in NUHM2 models. Figure from [259], with two benchmarks discussed in this chapter, ILC1 and ILC2, marked on it.

To understand why the LHC is not sufficient to cover the natural SUSY parameter space despite the low energy scale of natural SUSY, attention should be drawn to Fig. 7.3. In this plot, the tree-level masses of the higgsino-like LSP and light chargino are plotted. Each point represents some combination of the parameters  $M_1$ ,  $M_2$ ,  $\mu$  and  $\tan \beta$  that leads to light higgsinos. Most of the points lie in the mass-degenerate range, where the difference between the higgsino masses is less than 20 GeV. As discussed in Ch. 2, the LHC prospects for detecting these kinds of particles are weak until a large data set of  $300 \text{ fb}^{-1}$  or  $3000 \text{ fb}^{-1}$  has been gathered. The search with most sensitivity for higgsinos is the  $\tilde{\chi}_1^0 \tilde{\chi}_2^0 + \text{jet}$  channel [259]. Another useful channel is the same-sign di-boson search channel. The projections for LHC sensitivity are also plotted in Fig. 7.2 based on theoretical assumptions - see Ref. [259] and references therein for details. Most of the area covered by the ILC  $\sqrt{s} = 500$  GeV machine would be covered by the full  $3000 \text{ fb}^{-1}$  data set of HL-LHC [259]. For the very low mass differences, the higgsino decay signal would correspond to a totally invisible final state. This region could be covered with a monojet search with only a  $2\sigma$  confidence via the  $3000 \text{ fb}^{-1}$  HL-LHC data set [261].

There is one fundamental difference, however, between the higgsino measurements at the LHC and the ILC. At ILC, there is less ambiguity to assigning the decay products

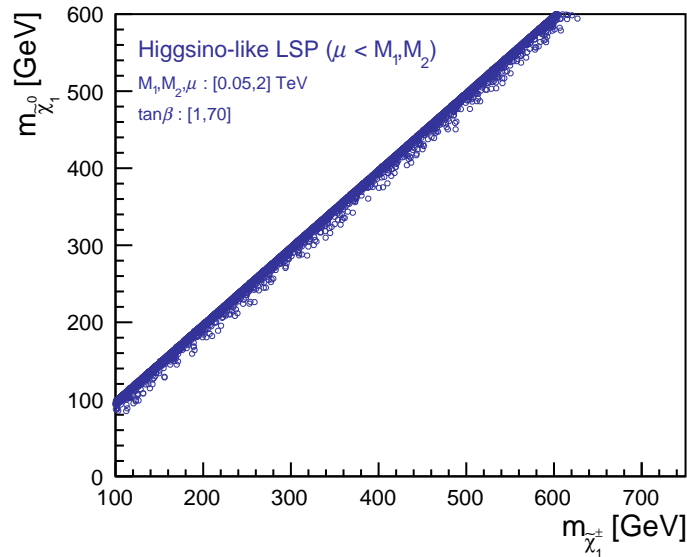


Figure 7.3: At tree-level, most scenarios with a higgsino-like LSP have a very small  $\tilde{\chi}_1^\pm - \tilde{\chi}_1^0$  mass difference [260].

to the parent particle than at the LHC. Additionally, the LHC prospects are restricted to merely measuring an excess with some uncertainty about the actual masses. The ILC on the other hand can measure the masses accurately, as we will discuss later, and has the undoubted advantage of the possibility for threshold scans to further confirm that the spin and coupling of the new particles correspond to higgsinos in SUSY. This kind of model-independent information is difficult to extract at the LHC due to the unknown initial energy and flavour.

A caveat is of course that the existence of higgsinos demands the existence of altogether four neutralinos and two charginos. It is a valid question to ask would higgsinos not be ruled out or indirectly discovered via measuring the gauginos. Indeed, gaugino searches do restrict the parameter space for higgsinos but it should be possible to tune the masses of those gauginos to escape any current searches. Additionally, the complicated decay chains of these heavier SUSY particles make detection at the LHC harder.

Some studies have shown that the toughest competition for the ILC with respect to higgsinos are in fact direct dark matter detection experiments [112]. In Ref. [112], current and future direct and indirect detection prospects are compared to the natural SUSY parameter space. In Fig. 7.4 the exclusion limits on the spin-independent WIMP-nucleon scattering cross sections are plotted vs. the LSP mass. The exclusion limits have been scaled by the factor of relic density saturated by the LSP. This is especially important for higgsino-like LSPs as these provide e.g. only 5% of the relic density (as in the benchmark ILC1, ILC2 and nGMM1 discussed in this chapter). The same figure also contains highlighted regions which have high naturalness and low fine-tuning, after points with gluino mass less than 2 TeV have been excluded. The remaining region lies almost entirely in the projected exclusion range of XENON 1T [262]. On the other hand, the interpretation of direct detection experiment results relies on theoretical assumptions on e.g. the shape of the WIMP velocity distribu-

tion [263], meaning that the ILC would still be useful for checking whether higgsinos exist.

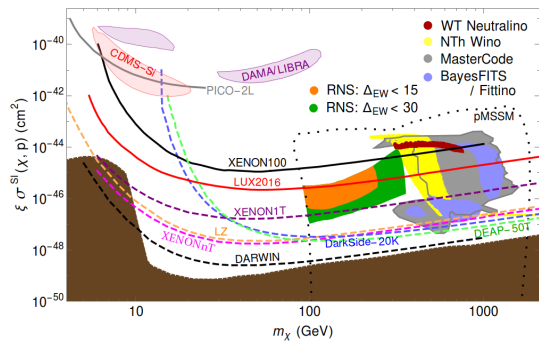


Figure 7.4: Exclusion limits for direct detection (WIMP spin-independent nucleon scattering cross section times the fraction of Planck relic density satisfied by the LSP) vs. LSP mass. Figure from [112].

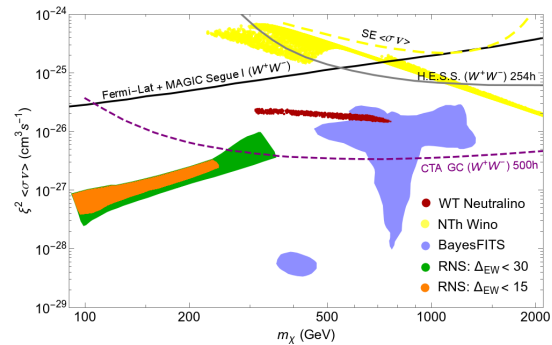


Figure 7.5: Exclusion limits for indirect WIMP detection (WIMP annihilation cross section times the square of the fraction of Planck relic density satisfied by LSP) vs. LSP mass. Figure from [112].

The indirect detection experiments, i.e. the gamma ray observatories, do not probe the natural SUSY space yet or in the foreseeable future as can be seen from Fig. 7.5 [112].

We have picked three benchmarks which avoided LHC exclusion limits in 2012, two of them still do at the time of writing. Collaborators [264] have performed a simulation study of these three higgsino benchmarks using the ILD detector concept (version ILD\_o1\_v05) [182] and the corresponding Mokka [265] simulation and Marlin [266] reconstruction tools. The masses of the three higgsinos can be measured very accurately from the kinematic endpoint, and the cross section times branching fraction can be found by a cut-and-count method.

Using these measurements, SUSY parameters were fitted and the SUSY parameter running was investigated. The benchmarks, simulation results, parameter fits and running investigations all are explained in the sections below. Answers are given to the questions what information can be extracted from the SUSY measurements, what is the significance of the Higgs measurements, do the results depend on the higgsino mass difference, and what conclusions can be reached about the high-scale behaviour of the SUSY model. First, though, the study will be put in historical context by discussing the previous studies on higgsinos at the ILC.

### 7.1.1 Previous study of very degenerate higgsinos at ILC

There is a pre-existing study on light higgsinos presented in Ref. [169]. In this paper, two light higgsino benchmarks were investigated. There the masses of the higgsinos differ by 1.6 GeV and 0.77 GeV, which is a smaller amount than in the benchmarks that will be studied in this chapter. These models are natural and can arise from hybrid gauge-gravity mediation models. Because of the small mass difference,  $\tilde{\chi}_2^0$  decays via a photon or hadrons, and  $\tilde{\chi}_1^\pm$  decays into one charged pion and some more pions. There is a large background from  $\gamma\gamma$  to two-fermion Standard Model interactions, which

needs to be suppressed by requiring one initial state radiation photon. Thus the signal channels studied were  $e^+e^- \rightarrow \gamma\tilde{\chi}^+\tilde{\chi}^- \rightarrow \tilde{\chi}_1^0\tilde{\chi}_1^0\pi^+(\pi^+)\mu\nu_\mu(e\nu_e)$  and  $e^+e^- \rightarrow \tilde{\chi}_1^0\tilde{\chi}_1^0\gamma$ . Via measuring the pion and photon energy, and with the knowledge of the centre-of-mass energy, the kinematic threshold of the reduced centre-of-mass energy of the chargino production can be fitted. After calibrating the detector performance, the chargino mass can be measured with 0.9-1.2% uncertainty with  $500 \text{ fb}^{-1}$  with  $\mathcal{P}(e^-, e^+) = (-80\%, +30\%)$  in a fast simulation with SGV [240]. The effect of  $\gamma\gamma$  backgrounds was not considered. The  $\tilde{\chi}_2^0$  mass can be measured with a similar technique with 1.0-1.9% uncertainty. Tightening the cuts a little further, the remaining parameter, the LSP mass, may be measured from the pion energy in the chargino-pair rest frame. The mass difference is measured with 5-17% accuracy. The polarised cross sections can be measured with 2-5% precision.

The measurements allow fitting the electroweakino sector parameters  $\mu$ ,  $M_1$ ,  $M_2$  and  $\tan\beta$  at tree-level by minimising a  $\chi^2$  between the observables and the tree-level theoretical observables with MINUIT [267]. The difference between the tree-level theoretical masses and the one-loop masses used in the simulation were taken into account. The result is that  $\tan\beta$  is not constrained much,  $M_1$  and  $M_2$  are bounded from below, and  $\mu$  is constrained to a 3 GeV range. The missing part in this study was to consider the one-loop corrected masses properly and to consider a larger set of parameters than simply the ones relevant at tree-level, as it may be that those provide additional freedom which relaxes the constraints on  $\mu$ ,  $M_1$  and  $M_2$ . Additionally, ILC Higgs measurements were not used to constrain the fit.

### 7.1.2 Previous study on running of SUSY parameters

If SUSY parameters are determined at the weak scale, it is possible to plug the results in the renormalisation group equations (see Sec. 2.4) and obtain the same parameters at high scale. These kinds of tests have not been done before for a benchmark with light higgsinos. However, this has been done for a stau coannihilation benchmark (SPS1a [238]) in Ref. [268]. The above in Ch. 6 contains more up-to-date results. In this benchmark all SUSY particles would be accessible at a linear collider and LHC. All the relevant SUSY parameters can be extracted at the weak scale, and run up to the GUT scale to find that the gaugino mass parameters  $M_i$  unify, as do the sfermion and Higgs sector parameters amongst themselves, as would be expected in a mSUGRA model like SPS1a.

## 7.2 Higgsino benchmarks

The study in this chapter is based on three benchmarks with light higgsinos with less than 20 GeV mass differences. The benchmarks are called ILC1, ILC2 and nGMM1 (for natural generalised mirage mediation 1). ILC1 and ILC2 were introduced in [257]. These benchmarks are based on a non-universal Higgs mass model type two, NUHM2, with the Higgs sector decoupled from the sfermions. This model is motivated by supergravity as CMSSM is, but the experimental exclusion limits on sfermions demand separate parameters to allow for light higgsinos. The six parameters are listed in

Tab. 7.1. ILC1 has a  $\mu$ -parameter of 115 GeV and  $M_{1/2}$  at 568.3 GeV, while ILC2 has  $\mu = 150$  GeV and  $M_{1/2} = 1200$  GeV. The sfermion parameter  $M_0$  is 7 TeV and 5 TeV respectively, and the universal trilinear coupling is large at -11 TeV and -8 TeV respectively. It should be noted, that for ILC1 the trilinear coupling is 1 TeV smaller than in the reference paper and the top mass is 100 GeV smaller. These modifications were necessary to get a spectrum from `SPheno3.3.9beta` without negative sfermion mass squared errors.

The third benchmark, nGMM1, defined in Ref. [89] is motivated by mirage unification of the gaugino masses. Mirage unification means that gaugino masses unify at intermediate energy scales while the gauge coupling unification remains at  $10^{16}$  GeV, and this can be caused by some versions of string theory [89]. The model is defined by 7 parameters listed in Tab. 7.2. For the details of the parameters, see Ch. 2.

As we will be fitting a pMSSM model later, it is important to know what pMSSM parameters these ILC1 and ILC2 NUHM2 model parameters correspond to. This was done by computing the running of the parameters with `SPheno-3.3.9beta` and setting the program to output the soft SUSY breaking parameters at 1 TeV. These were then taken as the pMSSM model parameters, as listed in Tab. 7.3.

parameter	scale	ILC1	ILC2
$M_0$	GUT	7025.0	5000
$M_{1/2}$	GUT	568.3	1200
$A_0$	GUT	-10426.6	-8000
$\tan \beta$	weak	10	15
$\mu$	weak	115	150
$m_A$	weak	1000	1000
$m_t$	pole	173.1	173.2

Table 7.1: Parameters of ILC1 and ILC2 NUHM2 models [257]. Note that the original ILC1 benchmark [257] had  $A_0 = -11426.6$  and  $m_t = 173.2$  GeV. All parameters except  $\tan \beta$  are in units of GeV.

For nGMM1, a similar trick was performed. However, in this case as `SPheno3.3.9beta` did not contain a mirage calculator, the soft SUSY breaking parameters were extracted from `Isasugra` at  $\sqrt{m_{\tilde{\tau}_1} m_{\tilde{\tau}_2}} = 2.3$  TeV. These were input to `SPheno` and running was calculated to get the parameters at the energy scale 1 TeV. The resulting pMSSM parameters are listed in Tab. 7.3.

For the simplicity of the fits, the pMSSM parameter set had to be reduced to 10 parameters, so that the remaining parameters are  $M_1, M_2, M_3, \mu, \tan \beta, m_A, A_t = A_b = A_\tau, M_{Q(3)}, M_{U(3)}$  and a common parameter for the rest of the sfermions denoted by  $M_{L(3)} = M_{U(1,2)} = M_{D(1,2,3)} = M_{L(1,2)} = M_{E(1,2,3)}$ . The the justification is the same as for the pMSSM-19 model except that with no evidence of light sfermions there is no need to separate the left-handed and right-handed cases except for the stops. This is also justifiable top-to-down as in the NUHM2 the right-handed sfermion masses do

parameter	scale	nGMM1
$\alpha$	GUT	4
$M_{3/2}$	GUT	75000 GeV
$\tan \beta$	weak	10
$a_3$	–	+3
$c_M$	GUT	6.9
$c_{H_u}$	GUT	11.3
$c_{H_d}$	GUT	1.15
$m_t$	<i>pole</i>	173.2 GeV

Table 7.2: Parameters of nGMM1 [89].  $c_{H_u}$  was modified from 11.77 in the paper to 11.3 as this value in `SPheno3.3.9beta` reproduces the same physical spectrum as `Isajet` in the paper.

parameter	scale	ILC1	ILC2	nGMM1
$M_1$	1 TeV	250.0	520.3	1493.1
$M_2$	1 TeV	463.4	957.2	1719.9
$M_3$	1 TeV	1268.4	2607.2	2645.8
$m_A$	1 TeV	1000	1000	2000
$\tan \beta$	1 TeV	10.0	15.0	10.0
$\mu$	1 TeV	115.0	150.0	150.0
$A_t$	1 TeV	−4400.7	−4713.7	−4857.1
$M_{Q(3)}$	1 TeV	4821.0	3757.2	3701.1
$M_{U(3)}$	1 TeV	1665.8	1394.9	1381.2
$M_{L(3)}$	1 TeV	7145.1	5146.0	5114.9
$m_t$	<i>pole</i>	173.1	173.2	173.2

Table 7.3: pMSSM-10 parameters of the three higgsino models considered in this chapter. All parameters except  $\tan \beta$  are in units of GeV. The top mass is listed for convenience.

not differ much from the left-handed sfermion masses. The pMSSM-10 parameters of ILC1 and ILC2 are listed in Tab. 7.3.

The essence of all three benchmarks is that they contain light higgsinos which would be accessible at the ILC  $\sqrt{s} = 500$  GeV. The masses of the higgsinos in all three benchmarks are shown in Tab. 7.4, as calculated with `SPheno3.3.9beta` using the pMSSM-10 definition of the three benchmarks. ILC1 has the largest mass differences, 22.7 GeV and 11.2 GeV for the  $\tilde{\chi}_2^0 - \tilde{\chi}_1^0$  and  $\tilde{\chi}_1^\pm - \tilde{\chi}_1^0$  mass differences respectively. For ILC2 the corresponding mass differences are 10.9 GeV and 5.5 GeV and for nGMM1 they are 5.3 GeV and 2.4 GeV. The higgsinos in ILC1 are about 110 GeV, being accessible at  $\sqrt{s} = 250$  GeV ILC, while the higgsinos in ILC2 and nGMM1 are slightly heavier than 150 GeV, requiring at least  $\sqrt{s} \sim 320$  GeV to be produced. All of the sparticle masses are listed in Tab. 7.4 for all three benchmarks. In addition, the spectra are plotted in Figures 7.6 to 7.11.

It is important to note that the mass spectra calculated with `SPheno3.3.9beta` from the pMSSM-10 ILC1 and ILC2 definitions differs from the NUHM2 ILC1 and ILC2 definitions by a few GeV. This effect has many potential causes, starting with the difference that in the NUHM2 models,  $\tan\beta$  and  $\mu$  are defined at  $Q = 100$  GeV as opposed to  $Q = 1$  TeV in the pMSSM-10 version. Also, the trilinear couplings of  $b$  and  $\tau$  are larger in the NUHM2 version than in the pMSSM-10 version where they are set equal to  $A_t$ . Furthermore, the sfermion soft mass parameters are not exactly equal to each other in the NUHM2 as is imposed in the pMSSM-10. The effect of the differences in the model observables is removed in the fits; When fitting each of these models, the observables are assumed to be exactly as they are in the benchmark model. This is necessary in order to be able to analyse whether the fit finds the model parameter values. If SUSY measurements were actually made, then it would be of ultimate importance to ensure that the calculator agrees with itself in these two setups, so that it would really be possible to check whether the observations match the NUHM2 model.

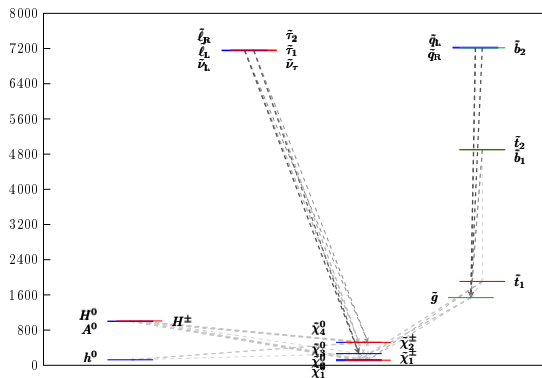


Figure 7.6: Mass spectrum of ILC1 MSSM version in GeV.

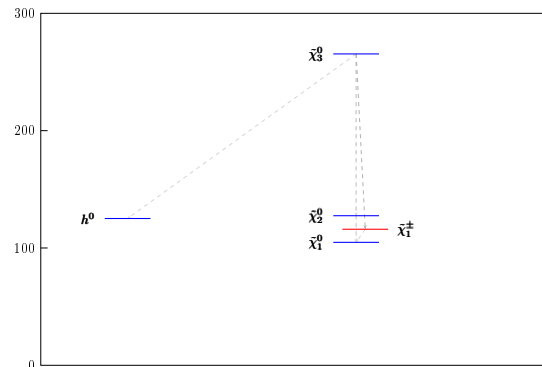


Figure 7.7: Zoom of mass spectrum of ILC1 MSSM version in GeV.

In fact, due to the LHC search for higgsinos, ILC1 is ruled out as the ILC1 higgsino mass difference is now probed by the CMS search for two soft leptons [269], see also Ch. 2. Another reason already ruling ILC1 out is its relatively light gluino mass of

parameter	ILC1MSSM	ILC2MSSM	nGMM1MSSM
$m_{\tilde{\chi}_1^0}$	104.806	151.534	154.936
$m_{\tilde{\chi}_2^0}$	-127.494	-162.423	-160.217
$m_{\tilde{\chi}_1^\pm}$	115.965	157.023	157.381
$m_{\tilde{\chi}_3^0}$	265.4	534.6	1522
$m_{\tilde{\chi}_4^0}$	521.4	1026	1809
$m_{\tilde{\chi}_2^\pm}$	521.2	1026	1808
$m_{\tilde{\tau}_1}$	7155	5153	5118
$m_{\tilde{\tau}_2}$	7165	5161	5126
$m_{\tilde{e}_L}$	7154	5152	5117
$m_{\tilde{e}_R}$	7163	5157	5124
$m_{\tilde{\mu}_L}$	7154	5152	5116
$m_{\tilde{\mu}_R}$	7163	5157	5126
$m_{\tilde{\nu}_\tau}$	7155	5153	5116
$m_{\tilde{\nu}_e}, m_{\tilde{\nu}_\mu}$	7153	5151	5116
$m_{\tilde{t}_1}$	1906	1535	1519
$m_{\tilde{t}_2}$	4903	3782	3719
$m_{\tilde{b}_1}$	4899	3774	3710
$m_{\tilde{b}_2}$	7216	5154	5120
$m_{\tilde{g}}$	1539	2846	2881
$m_h$	125.116	127.027	126.19

Table 7.4: Masses in the pMSSM model versions from SPheno-3.3.9b in GeV. Higgs mass from FeynHiggs2.10.4

parameter	ILC1 NUHM2	ILC2 NUHM2
$m_{\tilde{\chi}_1^0}$	105.88	154.48
$m_{\tilde{\chi}_2^0}$	-128.90	-165.40
$m_{\tilde{\chi}_1^\pm}$	117.18	160.00
$m_{\tilde{\chi}_3^0}$	265.22	534.69
$m_{\tilde{\chi}_4^0}$	520.47	1027.9
$m_{\tilde{\chi}_2^\pm}$	520.56	1027.8
$m_{\tilde{\tau}_1}$	6643	463.89
$m_{\tilde{\tau}_2}$	7120	5083
$m_{\tilde{e}_L}$	7159	5155
$m_{\tilde{e}_R}$	6727	4793
$m_{\tilde{\mu}_L}$	7159	5154
$m_{\tilde{\mu}_R}$	6726	4793
$m_{\tilde{\nu}_\tau}$	7119	5083
$m_{\tilde{\nu}_e}, m_{\tilde{\nu}_\mu}$	7159	5154
$m_{\tilde{t}_1}$	1926	1540
$m_{\tilde{t}_2}$	4906	3793
$m_{\tilde{b}_1}$	4902	3785
$m_{\tilde{b}_2}$	6876	5189
$m_{\tilde{g}}$	1523	2854
$m_h$	124.79	126.76

Table 7.5: Masses in the NUHM2 model versions from SPheno-3.3.9beta in GeV. Higgs mass from FeynHiggs2.10.4.

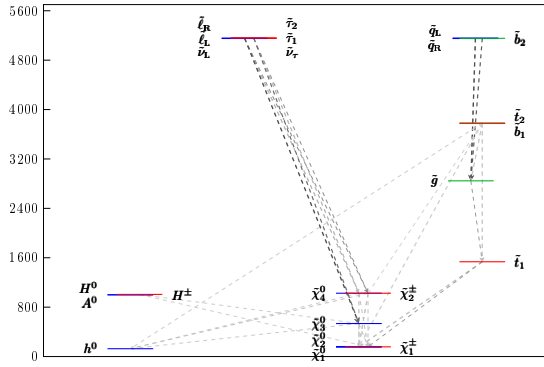


Figure 7.8: Mass spectrum of ILC2 MSSM version in GeV.

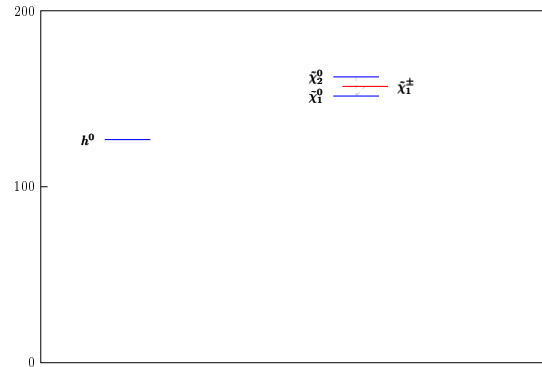


Figure 7.9: Zoom of mass spectrum of ILC2 MSSM version in GeV.

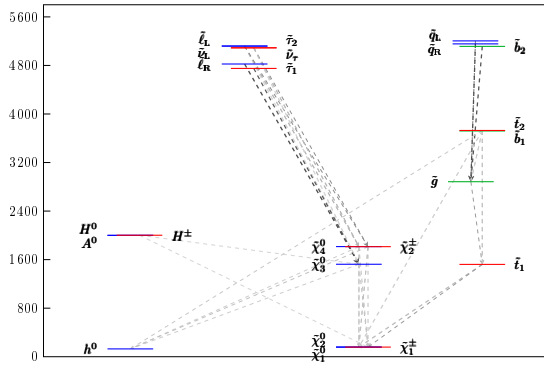


Figure 7.10: Mass spectrum of nGMM1 MSSM version in GeV.

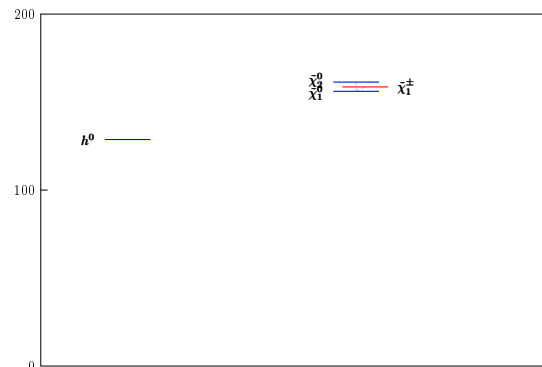


Figure 7.11: Zoom of mass spectrum of nGMM1 MSSM version in GeV.

1.5 TeV [270,271] due to the unified gaugino mass parameter in ILC1. If the gaugino mass unification condition was relaxed, then the gluino mass limit could be avoided without changing the higgsino phenomenology. All other masses except the gaugino masses are in the multi-TeV regime.

Higgsinos are produced at the ILC via the  $s$ -channel exchange of a  $Z$ -boson as depicted in Fig. 7.12. In principle,  $t$ -channel production would be possible if it was not suppressed by the heavy masses of the selectron and sneutrino. The cross sections for pair-production of higgsinos and gauginos are plotted in Fig. 7.13. It can be seen that the higgsino cross sections are of the order of a few hundred femtobarns at  $\sqrt{s} = 500$  GeV. This gives plentiful data to be studied. If the centre-of-mass energy was increased, then more channels would open up for sparticle production.

The higgsinos decay via a virtual  $Z$ -boson or  $W$ -boson, and the  $Z$  and  $W$  further decay approximately as in the Standard Model, as can be seen from Tab. 7.6. Only in nGMM1 the decay into taus is phase-space suppressed. It should be noted that there is also the very rare channel of  $\tilde{\chi}_2^0 \rightarrow \tilde{\chi}_1^0 \gamma$  which would be potentially an interesting channel as the higgsino mass difference gets below a few GeV.

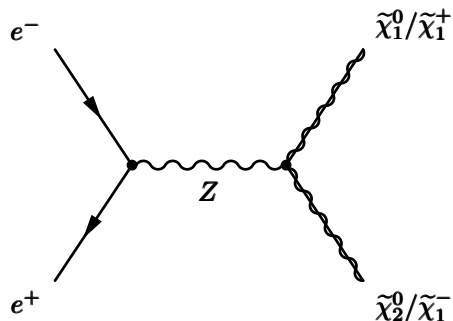
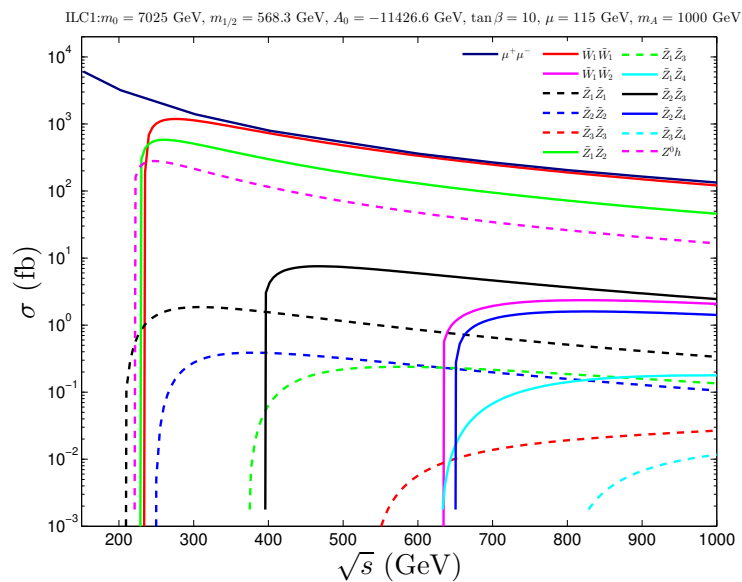


Figure 7.12: Higgsino pair production at the ILC proceeds in the s-channel.

Figure 7.13: ILC1 gaugino production cross sections in  $e^+e^-$  collisions [257].

BR [%]	ILC1MSSM	ILC2MSSM	nGMM1MSSM
$\tilde{\chi}_2^0 \rightarrow \tilde{\chi}_1^0 \gamma$	0.26	1.42	6.18
$\tilde{\chi}_2^0 \rightarrow \tilde{\chi}_1^0 q \bar{q}'$	61.4	58.8	53.9
$\tilde{\chi}_2^0 \rightarrow \tilde{\chi}_1^0 e^+ e^-$	3.29	3.70	3.79
$\tilde{\chi}_2^0 \rightarrow \tilde{\chi}_1^0 \mu^+ \mu^-$	3.29	3.70	3.78
$\tilde{\chi}_2^0 \rightarrow \tilde{\chi}_1^0 \tau^+ \tau^-$	3.17	3.15	1.41
$\tilde{\chi}_2^0 \rightarrow \tilde{\chi}_1^0 \nu \bar{\nu}$	19.7	22.2	22.7
$\tilde{\chi}_2^0 \rightarrow \tilde{\chi}_1^\pm f \bar{f}'$	8.89	7.04	5.39
$\tilde{\chi}_1^\pm \rightarrow \tilde{\chi}_1^0 q \bar{q}'$	66.8	67.1	64.9
$\tilde{\chi}_1^\pm \rightarrow \tilde{\chi}_1^0 e \nu_e$	11.5	12.6	17.2
$\tilde{\chi}_1^\pm \rightarrow \tilde{\chi}_1^0 \mu \nu_\mu$	11.5	12.6	17.1
$\tilde{\chi}_1^\pm \rightarrow \tilde{\chi}_1^0 \tau \nu_\tau$	10.2	7.65	0.85

Table 7.6: Branching fractions of neutralinos in the pMSSM versions of the higgsino models. All values are from `SPheno3.3.9b`. The sum of hadronic decays  $\tilde{\chi}_2^0 \rightarrow \tilde{\chi}_1^0 = 61.4\%$  for ILC1, 58.8% for ILC2, 53.9% for nGMM1.

This analysis concentrated on the leptonic decay of  $\tilde{\chi}_2^0$  due to the cleanness of this channel. For the  $\tilde{\chi}^\pm$  production, there are two chargino decays: one is required to decay leptonically in order to provide a tag, and another one hadronically in order to make the measurements and to keep the rate high. These cross-section times branching fractions are listed in Tab. 7.7, showing that all of these channels have rates of about 10-100 fb for the polarisations  $\mathcal{P}(\pm 80\%, \mp 30\%)$  and ILC centre-of-mass energies 500 GeV, 250 GeV and 350 GeV. The exception are ILC2 and nGMM1 whose higgsinos are not produced at  $\sqrt{s} = 250$  GeV.

The gauginos are not accessible at the ILC  $\sqrt{s} = 500$  GeV except for  $\tilde{\chi}_3^0$  in ILC1. This however, is only accessible in associated production with one of the higgsinos. While the cross section for  $\tilde{\chi}_3^0 \tilde{\chi}_1^0$  production is too small, the rate of  $\tilde{\chi}_3^0 \tilde{\chi}_2^0$  is slightly larger at around 10 fb. The complication is that  $\tilde{\chi}_3^0$  decays mainly via a chargino, making the analysis complicated. A careful study would be needed to see whether a measurement of  $\tilde{\chi}_3^0$  mass would be possible [272].

The light Higgs mass in each of the three benchmarks is listed in Tab. 7.4 as calculated by `FeynHiggs2.10.4` [207]. The masses are near the observed 125 GeV value, and these values are assumed as the fit input values. The Higgs branching fractions in these models are not much changed from the expected Standard-Model-like Higgs of the same mass. This can be seen from Fig. 7.14 where the branching fractions of the SUSY light Higgs are plotted with respect to the Standard-Model-like Higgs. It can be seen, that with ILC precisions on the Higgs branching fractions (scaled from the Higgs coupling fit), no deviation from the Standard Model can be seen. Additionally, the absolute branching fractions are listed in Tab. 7.8 for later convenience. They

	$\sigma \times \text{BR}$ [fb]	ILC1	ILC2	nGMM1
$\sqrt{s} = 500$ GeV $\mathcal{P} = (-80\%, 30\%)$	$\tilde{\chi}_1^0 \tilde{\chi}_2^0 \rightarrow \tilde{\chi}_1^0 \tilde{\chi}_1^0 e^+ e^-$	10.88	11.58	12.04
	$\tilde{\chi}_1^0 \tilde{\chi}_2^0 \rightarrow \tilde{\chi}_1^0 \tilde{\chi}_1^0 \mu^+ \mu^-$	10.88	11.58	12.01
	$\tilde{\chi}_1^+ \tilde{\chi}_1^- \rightarrow \tilde{\chi}_1^0 \tilde{\chi}_1^0 e \nu_e q \bar{q}'$	87.71	83.61	109.57
	$\tilde{\chi}_1^+ \tilde{\chi}_1^- \rightarrow \tilde{\chi}_1^0 \tilde{\chi}_1^0 \mu \nu_\mu q \bar{q}'$	87.67	83.45	108.56
$\sqrt{s} = 500$ GeV $\mathcal{P} = (80\%, -30\%)$	$\tilde{\chi}_1^0 \tilde{\chi}_2^0 \rightarrow \tilde{\chi}_1^0 \tilde{\chi}_1^0 e^+ e^-$	7.72	8.22	8.53
	$\tilde{\chi}_1^0 \tilde{\chi}_2^0 \rightarrow \tilde{\chi}_1^0 \tilde{\chi}_1^0 \mu^+ \mu^-$	7.72	8.22	8.51
	$\tilde{\chi}_1^+ \tilde{\chi}_1^- \rightarrow \tilde{\chi}_1^0 \tilde{\chi}_1^0 e \nu_e q \bar{q}'$	20.20	20.43	27.05
	$\tilde{\chi}_1^+ \tilde{\chi}_1^- \rightarrow \tilde{\chi}_1^0 \tilde{\chi}_1^0 \mu \nu_\mu q \bar{q}'$	20.19	20.39	26.80
$\sqrt{s} = 250$ GeV $\mathcal{P} = (-80\%, 30\%)$	$\tilde{\chi}_1^0 \tilde{\chi}_2^0 \rightarrow \tilde{\chi}_1^0 \tilde{\chi}_1^0 e^+ e^-$	21.45	—	—
	$\tilde{\chi}_1^0 \tilde{\chi}_2^0 \rightarrow \tilde{\chi}_1^0 \tilde{\chi}_1^0 \mu^+ \mu^-$	21.45	—	—
	$\tilde{\chi}_1^+ \tilde{\chi}_1^- \rightarrow \tilde{\chi}_1^0 \tilde{\chi}_1^0 e \nu_e q \bar{q}'$	152.26	—	—
	$\tilde{\chi}_1^+ \tilde{\chi}_1^- \rightarrow \tilde{\chi}_1^0 \tilde{\chi}_1^0 \mu \nu_\mu q \bar{q}'$	152.20	—	—
$\sqrt{s} = 250$ GeV $\mathcal{P} = (80\%, -30\%)$	$\tilde{\chi}_1^0 \tilde{\chi}_2^0 \rightarrow \tilde{\chi}_1^0 \tilde{\chi}_1^0 e^+ e^-$	14.95	—	—
	$\tilde{\chi}_1^0 \tilde{\chi}_2^0 \rightarrow \tilde{\chi}_1^0 \tilde{\chi}_1^0 \mu^+ \mu^-$	14.85	—	—
	$\tilde{\chi}_1^+ \tilde{\chi}_1^- \rightarrow \tilde{\chi}_1^0 \tilde{\chi}_1^0 e \nu_e q \bar{q}'$	29.87	—	—
	$\tilde{\chi}_1^+ \tilde{\chi}_1^- \rightarrow \tilde{\chi}_1^0 \tilde{\chi}_1^0 \mu \nu_\mu q \bar{q}'$	29.87	—	—
$\sqrt{s} = 350$ GeV $\mathcal{P} = (-80\%, 30\%)$	$\tilde{\chi}_1^0 \tilde{\chi}_2^0 \rightarrow \tilde{\chi}_1^0 \tilde{\chi}_1^0 e^+ e^-$	20.27	14.10	14.43
	$\tilde{\chi}_1^0 \tilde{\chi}_2^0 \rightarrow \tilde{\chi}_1^0 \tilde{\chi}_1^0 \mu^+ \mu^-$	20.27	14.10	14.40
	$\tilde{\chi}_1^+ \tilde{\chi}_1^- \rightarrow \tilde{\chi}_1^0 \tilde{\chi}_1^0 e \nu_e q \bar{q}'$	155.76	96.60	125.39
	$\tilde{\chi}_1^+ \tilde{\chi}_1^- \rightarrow \tilde{\chi}_1^0 \tilde{\chi}_1^0 \mu \nu_\mu q \bar{q}'$	155.69	96.42	124.23
$\sqrt{s} = 350$ GeV $\mathcal{P} = (80\%, -30\%)$	$\tilde{\chi}_1^0 \tilde{\chi}_2^0 \rightarrow \tilde{\chi}_1^0 \tilde{\chi}_1^0 e^+ e^-$	14.25	9.92	10.13
	$\tilde{\chi}_1^0 \tilde{\chi}_2^0 \rightarrow \tilde{\chi}_1^0 \tilde{\chi}_1^0 \mu^+ \mu^-$	14.25	9.91	10.11
	$\tilde{\chi}_1^+ \tilde{\chi}_1^- \rightarrow \tilde{\chi}_1^0 \tilde{\chi}_1^0 e \nu_e q \bar{q}'$	33.98	22.42	29.41
	$\tilde{\chi}_1^+ \tilde{\chi}_1^- \rightarrow \tilde{\chi}_1^0 \tilde{\chi}_1^0 \mu \nu_\mu q \bar{q}'$	33.97	22.37	29.14

Table 7.7: Cross sections times branching fractions at  $\sqrt{s} = 500, 250,$  and  $350$  GeV,  $\mathcal{P}(e^-, e^+) = (\pm 80\%, \mp 30\%)$ .

are listed for both the pMSSM-10 versions of the benchmarks as well as the NUHM2 version for ILC1 and ILC2, as these values are slightly different from each other.

BR [%]	ILC1 MSSM	ILC2 MSSM	nGMM1 MSSM	ILC1 NUHM2	ILC2 NUHM2
$h \rightarrow ZZ$	2.74	3.21	3.06	2.66	3.14
$h \rightarrow WW$	22.6	25.5	24.7	22.1	25.1
$h \rightarrow b\bar{b}$	57.8	55.0	55.5	58.3	55.4
$h \rightarrow gg$	7.07	6.84	7.09	7.10	6.88
$h \rightarrow \gamma\gamma$	0.235	0.229	0.234	0.235	0.229
$h \rightarrow \tau\tau$	6.64	6.34	6.40	6.69	6.38
$h \rightarrow c\bar{c}$	2.76	2.63	2.75	2.79	2.65

Table 7.8: Branching fractions the light Higgs in the pMSSM and NUHM2 versions of the higgsino models. All values are from `FeynHiggs2.10.4`.

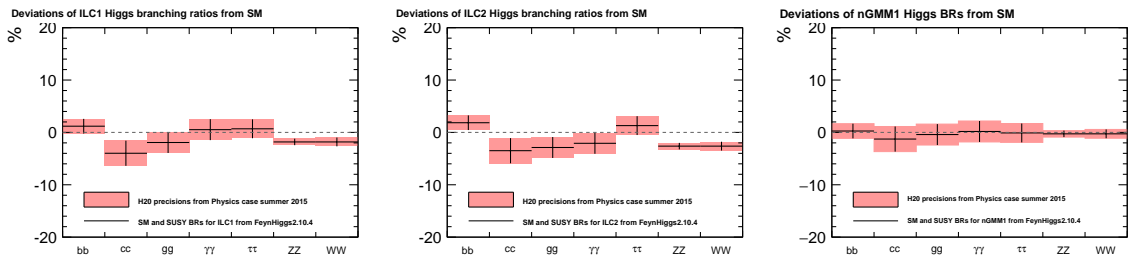


Figure 7.14: Deviations of the branching fractions of the SUSY light Higgs from the Standard Model expectations in ILC1, ILC2 and nGMM1.

The dark matter properties of higgsino models were discussed above in Sec. 7.1. Dark matter is not a motivation for higgsinos. Instead, higgsinos only provide 2.8%-5.4% of the observed dark matter, as calculated with `MicrOMEGAs2.4.5` [239] and listed in Tab. 7.9. As per design of the models, the direct detection cross section lies in the LUX excluded range (see Tab. 7.9 and Fig. 7.4). It will be checked later, whether these properties can be inferred from the ILC higgsino measurements.

Before proceeding to discuss SUSY parameter fits, the prospects for higgsino measurements at the ILC are discussed.

### 7.3 Expected measurements from ILD

The prospects for measuring higgsinos of ILC1, ILC2 and nGMM1 were investigated. Collaborators [264] performed a simulation study of the benchmarks with the aim of measuring the mass of the higgsinos and some of the cross sections. Events were generated with `Whizard 1.95` [273]. A detailed detector simulation was executed with `Mokka` [265] and `Marlin` [266]. The simulated samples correspond to  $\sqrt{s} = 500$  GeV operation with an integrated luminosity  $\mathcal{L} = 500 \text{ fb}^{-1}$  for polarisations  $\mathcal{P}(e^-, e^+) = (-80\%, +30\%)$  and  $\mathcal{P}(e^-, e^+) = (+80\%, -30\%)$ . The channels that were analysed

observable	ILC1	ILC2	nGMM1
$\Omega h^2$	0.0064934	0.00429965	0.00335279
$\Omega/\Omega_{\text{Planck}}$	5.4%	3.6%	2.8%
$\langle\sigma v\rangle[10^{-27} \text{ cm}^3\text{s}^{-1}]$	259.3	316.9	328.5
$\xi^2\text{af\_svind}[cm^3s^{-1} \times 10^{-27}]$	0.760	0.408	0.257
$\sigma^{SI}[10^{-9} \text{ pb}]$	15.36	3.439	0.5974
$\xi\text{af\_direct}[10^{-45}cm^2]$	0.83	0.12	0.017

Table 7.9: Relic density from `MicrOMEGAs` and `Astrofit`, and direct and indirect detection cross sections from `Astrofit` in the pMSSM versions of ILC1, ILC2 and nGMM1. The cross sections have been scaled with  $\xi$  and  $\xi^2$  to be able to compare these numbers with the exclusion curves in Figs. 7.4 and 7.5.  $\Omega_{\text{Planck}}$  is 0.1199 [28].

are the leptonic decay of  $\tilde{\chi}_2^0$ ,  $e^+e^- \rightarrow \tilde{\chi}_1^0\tilde{\chi}_2^0 \rightarrow \tilde{\chi}_1^0\tilde{\chi}_1^0e^+e^- (\mu^+\mu^-)$ , and the hadronic decay of  $\tilde{\chi}_1^\pm$ ,  $e^+e^- \rightarrow \tilde{\chi}_1^\pm\tilde{\chi}_1^\pm \rightarrow \tilde{\chi}_1^0q\bar{q}'\tilde{\chi}_1^0e\nu_e (\mu\nu_\mu)$ . The di-lepton decay is unique to the neutralino pair production, so while the decay channel is rarer than the hadronic decay, the di-lepton channel enables separating the neutralinos from charginos. In the chargino pair-production, the lepton is used as a tag, while the hadronic part enables the kinematic reconstruction of the chargino as there is no invisible contribution from the SM to the hadronic decay. In both cases there is missing energy from the LSP, and for the chargino decay there is also missing energy from the neutrino. The cuts were optimised to maintain the position and shape of the kinematic endpoints of the invariant mass distribution of the decay products and the energy distribution of the same. A brief account of the analysis method follows.

### 7.3.1 Event selection

The mass measurement proceeds by first selecting the events.

#### Neutralino cut strategy

The backgrounds to the neutralino process in the  $\mathcal{P}(e^-, e^+) = (-80\%, 30\%)$  data set are two-fermion processes with hadronic or leptonic content, four-fermion processes with leptonic, hadronic or semi-leptonic content,  $\gamma\gamma \rightarrow$  two or four fermions, and  $\gamma e \rightarrow$  three fermions. Of these, the hardest ones to remove are the four fermions to leptons process,  $\gamma\gamma \rightarrow$  two fermions and the SUSY background from charginos.

First a pair of isolated muons or electrons is required, as these are the final visible products in the desired channel. In all benchmarks in the neutralino process, the visible energy should total less than 80 GeV, which is slightly above the maximal energy of the  $Z$  in the considered models, and the missing energy in the event should be in excess of 300 GeV as this would be taken away by the LSP. The size of the missing angle is required to be  $|\cos\theta| < 0.98$  to ensure that the missing energy does not come from SM particles going down the beam pipe - the LSPs themselves are unlikely to be pointing in the direction of the beam pipe. There should be no hits in the BeamCAL,

and there should be exactly two tracks with transverse momentum greater than 2 GeV to separate from  $\gamma\gamma$  backgrounds. The leptons should not be coplanar, whereas the SM background would be expected to be more coplanar. For the di-lepton energy, a final cut depending on the benchmark is applied on the mass of the di-lepton system. Otherwise the cuts are the same for all benchmarks.

### Chargino cut strategy

The main backgrounds to the chargino process are the same as for the neutralino channels. In this case the hardest ones to remove are the leptonic four-fermion process and the neutralino background from  $\tilde{\chi}_2^0\tilde{\chi}_1^0$ .

The cuts for charginos are the following. There should be exactly one isolated lepton corresponding to the tag lepton and no BeamCAL hits. The lepton transverse momentum should exceed 5 GeV in order to remove  $\gamma\gamma$  backgrounds. As the second chargino should decay into quarks, the number of tracks in the events should be four or more to reduce  $\gamma e \rightarrow$  three fermions processes and taus. The total missing energy should exceed 400 GeV as this should correspond to the energy taken away by the LSP. Notice that this is larger than required for the neutralino process, as in the chargino decay into a lepton, there is also a neutrino causing more energy to go amiss. The missing  $|\cos\theta| < 0.99$  to ensure that the missing energy is truly invisible rather than SM particles going down the beam pipe, the visible energy should be less than 80 GeV. The jets must be detected in and the jets should not be coplanar.

## 7.3.2 Mass measurement

### Kinematics

After the event selection, the di-jet (or di-lepton) invariant mass distribution and energy distribution is plotted. These both depend on the masses of the SUSY particles in the process. The di-jet invariant mass and total energy distributions are used to fit the kinematic endpoints of the signal spectra. The endpoint is found by a toy Monte Carlo study on solving the crossing point of a background fit and a straight falling line fit of the signal. This gives one measurement of the energy edge and one measurement of the mass edge for each channel and polarisation.

The resulting 16 measurements are used to extract the underlying three masses,  $m_{\tilde{\chi}_1^0}$ ,  $m_{\tilde{\chi}_2^0}$  and  $m_{\tilde{\chi}_1^\pm}$ . The kinematics governing the edge values is as follows. The maximum of invariant mass of the di-electron system gives the mass splitting  $\Delta M = m_2 - m_1$  of masses  $m_2$  and  $m_1$ . Then the maximum of the di-electron energy gives the masses since the initial state is known. After imposing energy conservation, momentum conservation and the condition that the SUSY particles are on-shell, the equation for the maximum di-lepton/di-jet energy in the laboratory frame is

$$E_{\text{di-lepton max}} = \frac{1}{2}\gamma(1 + \beta)\Delta M \left(1 + \frac{m_1}{m_2}\right) \quad (7.9)$$

where

$$\beta = \frac{p}{\sqrt{p^2 + m_2^2}}, \quad (7.10)$$

$$\gamma = \frac{1}{\sqrt{1 - \beta^2}}, \quad (7.11)$$

and the maximum momentum of the di-lepton system

$$p = \sqrt{s}/2 \times \sqrt{1 - 2\left(\left(\frac{m_1}{\sqrt{s}}\right)^2 + \left(\frac{m_2}{\sqrt{s}}\right)^2\right) + \left(\left(\frac{m_2}{\sqrt{s}}\right)^2 - \left(\frac{m_1}{\sqrt{s}}\right)^2\right)^2}. \quad (7.12)$$

In these equations, the SM boson mass has been set to zero as it can be proven that this maximises the energy of the di-lepton system in the laboratory frame.

A  $\chi^2$  is constructed as

$$\chi^2 = \sum_i \left( \frac{E_{max}(m_1, m_2) - E_{max}^{obs}}{\sigma(E_{max}^{obs})} \right)^2, \quad (7.13)$$

where  $E_{max}(m_1, m_2)$  is the maximum energy if the SUSY particle masses are  $m_1$  and  $m_2$ ,  $E_{max}^{obs}$  is the maximum observed energy of the di-lepton/di-jet system and  $\sigma(E_{max}^{obs})$  is its experimental uncertainty. The index  $i$  sums over all the 16 measurements, note that  $m_2$  and  $m_1$  are not the same for all of them but rather  $m_2$  can be the  $\tilde{\chi}_2^0$  mass or the  $\tilde{\chi}_1^\pm$  mass. The  $\chi^2$  is then minimised by MINUIT [267] with the masses as free parameters. The output are the three SUSY masses with their respective uncertainties and correlations.

## Results

Examples of the event distributions are plotted in Figs. 7.15 and 7.16 for the  $\tilde{\chi}_2^0 \tilde{\chi}_1^0 \rightarrow e^+ e^- \tilde{\chi}_1^0 \tilde{\chi}_1^0$  and  $\tilde{\chi}_1^\pm \tilde{\chi}_1^\pm \rightarrow q\bar{q}' \mu\nu_\mu \tilde{\chi}_1^0 \tilde{\chi}_1^0$  respectively. It can be seen that the purity of the chargino sample is very high. There is some Standard Model background remaining for the neutralino process.

For the ILC2 processes for example, precisions of about 2% can be obtained for the neutralino edges, and precisions of around 5% for the chargino edges. The chargino measurements are skewed by jet energy resolution and shifted due to incorrect reconstruction of neutral components of the jets. The results are quoted here for the  $500 \text{ fb}^{-1}$  data set for the two oppositely handed beam polarisation combinations  $\mathcal{P}(\pm 80\%, \mp 30\%)$ . Detector calibration factors of around 10-20% are applied to correct the central values of the measurements. The mass results are listed in Tab. 7.10. The mass measurement precision is about 0.8% for ILC1. For ILC2 measurements gain a 1.3% uncertainty and for nGMM1 a 1.7% uncertainty.

It is crucial to note that the simulation study was done with the SUSY mass spectra given by *Isasugra* for the three benchmarks. These masses are a little bit different to the *SPheno* masses as can be seen by comparing Tab. 7.10 with Tab. 7.11. The main difference is that the mass hierarchy of  $\tilde{\chi}_1^\pm$  and  $\tilde{\chi}_2^0$  is inverted. However, the branching fraction of  $\tilde{\chi}_2^0$  into  $\tilde{\chi}_1^\pm$  is very small according to *SPheno*, so it is reasonable to assume that the inverted mass hierarchy does not modify the results. The mass differences change too, and they could be assumed to make a difference to the achievable measurement precisions. In the lack of a proper study on this, for the SUSY parameter fits presented in this chapter, it was assumed that the same precisions can be achieved for the *SPheno* definition of the benchmarks as was achieved in the simulation study for the *Isasugra* definition. The assumed precision on the higgsino mass is

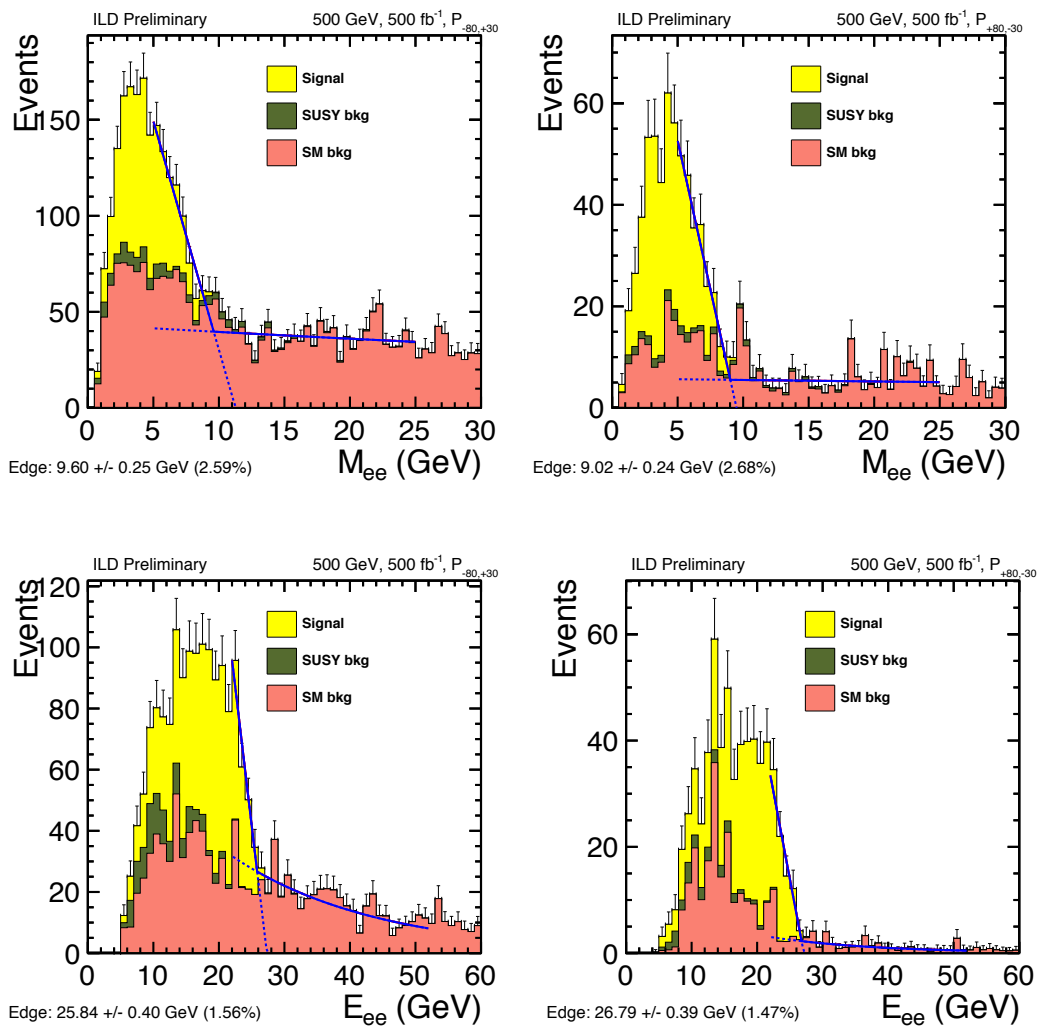


Figure 7.15: Measurements of neutralinos in ILC2 via the di-electron invariant mass and energy in two polarisation configurations.

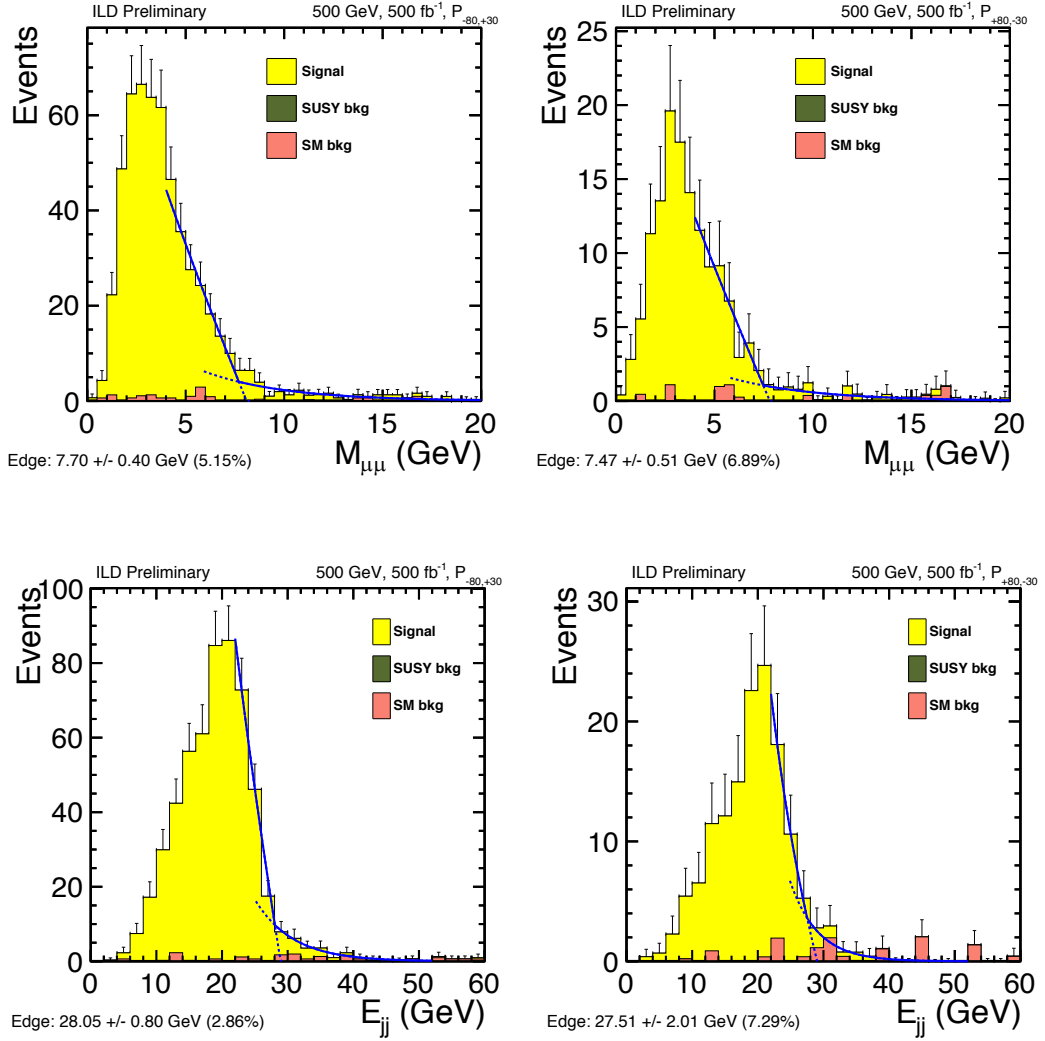


Figure 7.16: Measurements of charginos in ILC2 invariant mass and energy of the di-jet system in the  $\mu$ -tagged channel for two polarisation configurations.

model	particle	model mass [GeV]	obs. [GeV]	$\pm$	$1\sigma$ [GeV]	$1\sigma$ [%]
ILC1	$\tilde{\chi}_1^0$	102.7	102.6	$\pm$	0.85	0.828
	$\tilde{\chi}_2^0$	124.0	123.7	$\pm$	0.99	0.800
	$\tilde{\chi}_1^\pm$	117.3	117.2	$\pm$	0.95	0.811
ILC2	$\tilde{\chi}_1^0$	148.1	148.2	$\pm$	1.9	1.282
	$\tilde{\chi}_2^0$	157.8	157.9	$\pm$	2.1	1.330
	$\tilde{\chi}_1^\pm$	158.3	158.5	$\pm$	2.1	1.325
nGMM1	$\tilde{\chi}_1^0$	151.4	151.0	$\pm$	2.6	1.722
	$\tilde{\chi}_2^0$	155.8	155.3	$\pm$	2.7	1.739
	$\tilde{\chi}_1^\pm$	158.7	158.4	$\pm$	2.7	1.705

Table 7.10: Higgsino mass measurement results from simulation after calibrating the central values. The model mass values correspond to the *Isasugra* values. Obs. stands for the observed mass as given by the simulation after calibrating for detector effects. Data set  $\sqrt{s} = 500$  GeV,  $\mathcal{L} = 500$  fb $^{-1}$  and  $\mathcal{P}(\pm 80\%, \mp 30\%)$ .

the simulated precision scaled to the H20 or I20 data set for  $\sqrt{s} = 500$  GeV (see Ch. 3 for the definitions of H20 and I20), meaning the  $\mathcal{L} = 1600$  fb $^{-1}$  for both polarisations  $\mathcal{P}(\pm 80\%, \mp 30\%)$ . It was assumed that the polarisations contribute equally to the mass measurements.

### 7.3.3 SUSY cross section measurements

In addition to the mass measurements, simulated cross section times branching fraction measurements have been made. These were extracted from the event distributions used for the mass measurements above. This has the advantage of not having to redesign cuts to optimise efficiency instead of the edge position. The disadvantage is that the uncertainty will be larger in this case as a large proportion of the rate has been cut away in favour of a clean mass edge.

Using the mass distributions for neutralinos, the same background fit was made as for the invariant mass measurements. Then the events were counted for the neutralinos in a mass window. The mass window was optimised to give the largest significance  $S/\sqrt{S+B}$  where  $S$  ( $B$ ) stands for the number of signal (background) events in the window. This gives the neutralino cross section. For the chargino cross section measurement, all events were used including the background and no optimisation of the selected window was done.

The results of the cross section measurements are listed in Tabs. 7.12, 7.13 and 7.14. The first number column contains the precisions from the simulation study at  $\sqrt{s} = 500$  GeV,  $\mathcal{L} = 500$  fb $^{-1}$ . We have scaled these numbers to other data set sizes and centre-of-mass energies assuming that the uncertainty scales with the number of signal events. This is correct for  $\sqrt{s} = 500$  GeV as the background scales similarly to the

<b>ILC1</b>	model mass [GeV]	precision	H20 precision
$m_{\tilde{\chi}_1^0}$	104.8	0.828%	0.463%
$m_{\tilde{\chi}_2^0}$	127.5	0.800%	0.447%
$m_{\tilde{\chi}_1^\pm}$	116.0	0.811%	0.453%
<b>ILC2</b>	model mass [GeV]	precision	I20 precision
$m_{\tilde{\chi}_1^0}$	151.3	1.282%	0.717%
$m_{\tilde{\chi}_2^0}$	162.4	1.330%	0.743%
$m_{\tilde{\chi}_1^\pm}$	157.0	1.325%	0.741%
<b>nGMM1</b>	model mass [GeV]	precision	I20 precision
$m_{\tilde{\chi}_1^0}$	154.9	1.722%	0.963%
$m_{\tilde{\chi}_2^0}$	160.2	1.739%	0.972%
$m_{\tilde{\chi}_1^\pm}$	157.4	1.705%	0.953%

Table 7.11: ILC1, ILC2 and nGMM1 MSSM model masses from `SPheno3.3.9beta`. Experimental mass precision combined from 500 GeV  $500^{-1}$  fb for both  $\mathcal{P}(\pm 0.8, \mp 0.3)$ . It is assumed that the same precision is valid for these masses and mass differences as the simulation shows for the `Isajet` masses. Last column: precision scaled to  $1600 \text{ fb}^{-1}$  for both polarisations at  $\sqrt{s} = 500 \text{ GeV}$ , ignoring the data sets with other centre-of-mass energies in H20 and I20 operating scenarios.

signal. For  $\sqrt{s} = 250$  GeV and  $\sqrt{s} = 350$  GeV this assumption is optimistic as the low-energetic backgrounds should increase for lower centre-of-mass energies. In any case, the scalings of the ILC1  $\sigma \times$  BR measurements to the H20 operating scenario are listed in Tab. 7.12. The relevant operating scenario in the case that the higgsinos are not accessible at  $\sqrt{s} = 250$  GeV is I20, and thus the ILC2 and nGMM1  $\sigma \times$  BR measurements have been scaled to that scenario. The uncertainties can be read from Tabs. 7.13 and 7.14 for ILC2 and nGMM1 respectively. For ILC1 the uncertainties are  $\sim 1$ -3% percent except for the small data set at  $\sqrt{s} = 350$  GeV. For ILC2 and nGMM1 the precisions are worse,  $\sim 3$ -6% even for the large data set at  $\sqrt{s} = 500$  GeV. These values refer to statistical uncertainties - systematic uncertainties are neglected.

ILC1 $\Delta(\sigma \times BR)[\%]$	$\sqrt{s} = 500$ GeV	$\sqrt{s} = 500$ GeV	$\sqrt{s} = 250$ GeV	$\sqrt{s} = 350$ GeV
	$\mathcal{L} = 500 \text{ fb}^{-1}$	$\mathcal{L} = 1600 \text{ fb}^{-1}$	$\mathcal{L} = 1350 \text{ fb}^{-1}$	$\mathcal{L} = 135 \text{ fb}^{-1}$
$LR \sigma(\tilde{\chi}_2^0 \tilde{\chi}_1^0 \rightarrow \tilde{\chi}_1^0 \tilde{\chi}_1^0 ee)$	3.80	2.12	1.65	5.36
$LR \sigma(\tilde{\chi}_2^0 \tilde{\chi}_1^0 \rightarrow \tilde{\chi}_1^0 \tilde{\chi}_1^0 \mu\mu)$	3.42	1.91	1.48	4.82
$LR \sigma(\tilde{\chi}_1^+ \tilde{\chi}_1^- \rightarrow \tilde{\chi}_1^0 \tilde{\chi}_1^0 qqe\nu_e)$	2.59	1.45	1.20	3.74
$LR \sigma(\tilde{\chi}_1^+ \tilde{\chi}_1^- \rightarrow \tilde{\chi}_1^0 \tilde{\chi}_1^0 qq\nu\mu)$	2.27	1.27	1.05	3.28
$\Delta(\sigma \times BR)[\%]$	$\mathcal{L} = 500 \text{ fb}^{-1}$	$\mathcal{L} = 1600 \text{ fb}^{-1}$	$\mathcal{L} = 450 \text{ fb}^{-1}$	$\mathcal{L} = 45 \text{ fb}^{-1}$
$RL \sigma(\tilde{\chi}_2^0 \tilde{\chi}_1^0 \rightarrow \tilde{\chi}_1^0 \tilde{\chi}_1^0 ee)$	3.38	1.89	2.56	8.29
$RL \sigma(\tilde{\chi}_2^0 \tilde{\chi}_1^0 \rightarrow \tilde{\chi}_1^0 \tilde{\chi}_1^0 \mu\mu)$	3.33	1.86	2.52	8.17
$RL \sigma(\tilde{\chi}_1^+ \tilde{\chi}_1^- \rightarrow \tilde{\chi}_1^0 \tilde{\chi}_1^0 qqe\nu_e)$	4.94	2.76	4.28	12.70
$RL \sigma(\tilde{\chi}_1^+ \tilde{\chi}_1^- \rightarrow \tilde{\chi}_1^0 \tilde{\chi}_1^0 qq\nu\mu)$	4.30	2.40	3.73	11.05

Table 7.12: ILC1: Simulation results for experimental precisions. Scaled precisions for the various centre of mass energies and the two polarisations. LR refers to the beam polarisation  $\mathcal{P} = (-80\%, +30\%)$  and RL refers to  $\mathcal{P} = (+80\%, -30\%)$ .

### 7.3.4 Higgs measurements

The prospects for measuring the properties of the light Higgs at the ILC have been studied extensively, as discussed in Ch. 3. The Higgs properties in ILC1, ILC2 and nGMM1 do not deviate much from the Standard Model expectations for which the ILD simulation studies have been performed and recapped in Ch. 3. Thus, it is reasonable to assume that the same relative uncertainties can be achieved in the higgsino benchmarks as have been achieved in the Standard Model studies. Tab. 7.15 contains a summary of the uncertainties on light Higgs measurements as discussed in Ch. 3 in more detail. These will be used as fit input uncertainties in the following sections.

### 7.3.5 Expected measurements from LHC

In ILC1 the LHC would have discovered the gluino and measure its mass to a 11% uncertainty [259] with  $\tilde{g} \rightarrow t\bar{t}\tilde{\chi}_i^0$  and  $\tilde{g} \rightarrow tb\tilde{\chi}_i^\pm$  with the HL-LHC data set. These are difficult cascade decays but strong enough to stand out above background.

<b>ILC2</b> $\Delta(\sigma \times BR)[\%]$	$\sqrt{s} = 500$ GeV	$\sqrt{s} = 500$ GeV	$\sqrt{s} = 250$ GeV	$\sqrt{s} = 350$ GeV
	$\mathcal{L} = 500$ fb $^{-1}$	$\mathcal{L} = 1600$ fb $^{-1}$	$\mathcal{L} = 337.5$ fb $^{-1}$	$\mathcal{L} = 1147.5$ fb $^{-1}$
$LR \sigma(\tilde{\chi}_2^0 \tilde{\chi}_1^0 \rightarrow \tilde{\chi}_1^0 \tilde{\chi}_1^0 ee)$	5.52	3.09	–	3.30
$LR \sigma(\tilde{\chi}_2^0 \tilde{\chi}_1^0 \rightarrow \tilde{\chi}_1^0 \tilde{\chi}_1^0 \mu\mu)$	5.04	2.82	–	3.01
$LR \sigma(\tilde{\chi}_1^+ \tilde{\chi}_1^- \rightarrow \tilde{\chi}_1^0 \tilde{\chi}_1^0 qqe\nu_e)$	5.17	2.89	–	3.17
$LR \sigma(\tilde{\chi}_1^+ \tilde{\chi}_1^- \rightarrow \tilde{\chi}_1^0 \tilde{\chi}_1^0 qq\mu\nu_\mu)$	4.39	2.45	–	2.70
$\Delta(\sigma \times BR)[\%]$	$\mathcal{L} = 500$ fb $^{-1}$	$\mathcal{L} = 1600$ fb $^{-1}$	$\mathcal{L} = 112.5$ fb $^{-1}$	$\mathcal{L} = 382.5$ fb $^{-1}$
$RL \sigma(\tilde{\chi}_2^0 \tilde{\chi}_1^0 \rightarrow \tilde{\chi}_1^0 \tilde{\chi}_1^0 ee)$	6.54	3.66	–	3.93
$RL \sigma(\tilde{\chi}_2^0 \tilde{\chi}_1^0 \rightarrow \tilde{\chi}_1^0 \tilde{\chi}_1^0 \mu\mu)$	6.50	3.63	–	3.91
$RL \sigma(\tilde{\chi}_1^+ \tilde{\chi}_1^- \rightarrow \tilde{\chi}_1^0 \tilde{\chi}_1^0 qqe\nu_e)$	10.30	5.76	–	6.49
$RL \sigma(\tilde{\chi}_1^+ \tilde{\chi}_1^- \rightarrow \tilde{\chi}_1^0 \tilde{\chi}_1^0 qq\mu\nu_\mu)$	8.84	4.94	–	5.57

Table 7.13: ILC2: Simulation results for experimental precisions. Scaled precisions for the various centre of mass energies and the two polarisations. LR refers to the beam polarisation  $\mathcal{P} = (-80\%, +30\%)$  and RL refers to  $\mathcal{P} = (+80\%, -30\%)$ .

<b>nGMM1</b> $\Delta(\sigma \times BR)[\%]$	$\sqrt{s} = 500$ GeV	$\sqrt{s} = 500$ GeV	$\sqrt{s} = 250$ GeV	$\sqrt{s} = 350$ GeV
	$\mathcal{L} = 500$ fb $^{-1}$	$\mathcal{L} = 1600$ fb $^{-1}$	$\mathcal{L} = 337.5$ fb $^{-1}$	$\mathcal{L} = 1147.5$ fb $^{-1}$
$LR \sigma(\tilde{\chi}_2^0 \tilde{\chi}_1^0 \rightarrow \tilde{\chi}_1^0 \tilde{\chi}_1^0 ee)$	6.81	3.81	–	4.11
$LR \sigma(\tilde{\chi}_2^0 \tilde{\chi}_1^0 \rightarrow \tilde{\chi}_1^0 \tilde{\chi}_1^0 \mu\mu)$	6.21	3.47	–	3.74
$LR \sigma(\tilde{\chi}_1^+ \tilde{\chi}_1^- \rightarrow \tilde{\chi}_1^0 \tilde{\chi}_1^0 qqe\nu_e)$	6.20	3.47	–	3.83
$LR \sigma(\tilde{\chi}_1^+ \tilde{\chi}_1^- \rightarrow \tilde{\chi}_1^0 \tilde{\chi}_1^0 qq\mu\nu_\mu)$	4.99	2.79	–	3.08
$\Delta(\sigma \times BR)[\%]$	$\mathcal{L} = 500$ fb $^{-1}$	$\mathcal{L} = 1600$ fb $^{-1}$	$\mathcal{L} = 112.5$ fb $^{-1}$	$\mathcal{L} = 382.5$ fb $^{-1}$
$RL \sigma(\tilde{\chi}_2^0 \tilde{\chi}_1^0 \rightarrow \tilde{\chi}_1^0 \tilde{\chi}_1^0 ee)$	5.88	3.29	–	3.56
$RL \sigma(\tilde{\chi}_2^0 \tilde{\chi}_1^0 \rightarrow \tilde{\chi}_1^0 \tilde{\chi}_1^0 \mu\mu)$	5.55	3.10	–	3.36
$RL \sigma(\tilde{\chi}_1^+ \tilde{\chi}_1^- \rightarrow \tilde{\chi}_1^0 \tilde{\chi}_1^0 qqe\nu_e)$	11.70	6.54	–	7.41
$RL \sigma(\tilde{\chi}_1^+ \tilde{\chi}_1^- \rightarrow \tilde{\chi}_1^0 \tilde{\chi}_1^0 qq\mu\nu_\mu)$	9.90	5.53	–	6.27

Table 7.14: nGMM1: Simulation results on experimental precisions. Scaled precisions for the various centre of mass energies and the two polarisations. LR refers to the beam polarisation  $\mathcal{P} = (-80\%, +30\%)$  and RL refers to  $\mathcal{P} = (+80\%, -30\%)$ .

coupling	H20 $\Delta g$	H20 $\Delta \text{BR}$
$g(hZZ)$	0.31%	0.62%
$g(hWW)$	0.42%	0.84%
$g(hb\bar{b})$	0.7%	1.4%
$g(hgg)$	1.0%	2.0%
$g(h\gamma\gamma)$	1.0%	2.0%
$g(h\tau\tau)$	0.9%	1.8%
$g(hc\bar{c})$	1.2%	2.4%
$m_h$	15 MeV	

Table 7.15: Model independent Higgs coupling uncertainties for the full luminosity scenario H20 which has  $4000 \text{ fb}^{-1}$  at  $\sqrt{s} = 500 \text{ GeV}$ ,  $2000 \text{ fb}^{-1}$  at  $\sqrt{s} = 250 \text{ GeV}$ , and  $200 \text{ fb}^{-1}$  at  $\sqrt{s} = 350 \text{ GeV}$ . The 500 GeV data set consists of 40% with +-, 40% with -+, 10% with - and 10% with ++ beam polarisations. The coupling uncertainties are from Ref. [155]. The coupling uncertainties have been scaled by two to obtain the branching fraction uncertainty. For more details see Ch. 3.

## 7.4 Parameter fits

The idea is to find which SUSY parameters can be determined from the measurements of higgsinos at the ILC. Again, `Fittino` [201] is used for this purpose. A summary of the fitting setup, the fitted models and fit inputs follows.

### 7.4.1 Fitting setup

The fitting setup is essentially the same as in Ch. 6. `Fittino1` [201] is used as the fitting code. SUSY particle spectrum, cross sections and branching ratios were obtained with `SPheno3.3.9beta` [206, 213], Higgs sector observables with `FeynHiggs2.10.4` [207]. Dark matter relic density was calculated with `MicrOMEGAs 2.4.5` [239] and the direct and indirect dark matter detection cross sections with `Astrofit` [208]. Recaps of the calculation methods in these codes can be found in Ch. 4.

The fits were started from near the true model point. The fits are composed of 10 separate fits of 100 000 Markov Chain points each. Each chain is started so that two of the parameters are  $\pm 10\%$  off from the true value and the rest within 1%. It would not be possible to find the starting values for all the parameters with tree-level estimates from the measurements of  $\tilde{\chi}_1^0$ ,  $\tilde{\chi}_2^0$  and  $\tilde{\chi}_1^\pm$ . Only the neutralino-sector parameters  $M_1$ ,  $M_2$ ,  $\tan\beta$  and  $\mu$  could be determined, at least up to a two-fold degeneracy [246, 274]. Here it is assumed that tree-level estimates would bring the starting values of those parameters close to the true values. It is known from the non-observation of other SUSY particles at the ILC and LHC that parameters related to these particles must be large. It is assumed that the fit will probe the other parameters as far away from the

true point as necessary. This claim can be checked by fixing the other parameters to true values or non-true values and checking whether the determined neutralino-sector parameters differ in the two cases.

### 7.4.2 Fitted models

If higgsinos were observed and no fermionic SUSY particles were detected at the LHC or ILC, then it would be clear that CMSSM is not the correct model. We have fitted CMSSM to the higgsino models to check how bad the minimum  $\chi^2$  value would be in this case. The parameters are  $\tan\beta$ ,  $A_0$ ,  $M_0$  and  $M_{1/2}$ . Sign  $\mu$  is set positive. Similarly as the heavy Higgses are not found at the same scale as the higgsinos, then NUHM1 would be unlikely, and we check the minimum  $\chi^2$  in this case too. The parameters are  $\tan\beta$ ,  $A_0$ ,  $M_0$  and  $M_{1/2}$  and  $M_{H_0}^2$ .

It could be possible that the higgsinos originate from an NUHM2 model, so this possibility is investigated here. The parameters fitted in this case are  $\tan\beta$ ,  $\mu$ ,  $m_A$ ,  $M_0$ ,  $M_{1/2}$  and  $A_0$ . It would seem reasonable that if all sfermions are heavy that they might have the same mass parameter, and this assumption is good enough for describing the data. It is noteworthy that instead of the usual GUT-scale  $M_{H_u}^2$  and  $M_{H_d}^2$  parameters, we fit the weak-scale  $m_A$  and  $\mu$ . This is because the  $M_{H_d}^2$  has to be brought to negative values near the electroweak scale, and the running has to be quite fine-tuned for this as discussed above. Therefore, it is more stable to fit the weak-scale Higgs sector  $\mu$  and  $m_A$ . A new version of `SPheno` (version 3.3.9beta and later) has been created for this purpose [275].

The bulk of the chapter focuses on pMSSM fits. The parameters can be reduced a little further compared to the STC fits, as the experiment does not suggest that the sfermion parameters have to be split up. Therefore we fit a 10-parameter model with  $M_1$ ,  $M_2$ ,  $M_3$ ,  $\mu$ ,  $\tan\beta$ ,  $m_A$ ,  $M_Q(3)$ ,  $M_U(3)$ , a common sfermion mass  $M_{L(3)} = M_Q(1, 2) = M_U(1, 2) = M_D(1, 2) = M_L(1, 2) = M_E(1, 2, 3)$  and a common trilinear coupling  $A_t = A_b = A_{\tau}$ . This is the pMSSM-10 model. All of these parameters are defined at the 1 TeV scale.

Sometimes, a subsection of the pMSSM-10 model is fitted. There, only  $M_1$ ,  $M_2$ ,  $\mu$  and  $\tan\beta$  are allowed to vary. This model is labelled as pMSSM-4.

### 7.4.3 Fit inputs

The fit inputs are the higgsino measurements discussed in the previous sections: the masses of  $\tilde{\chi}_1^0$ ,  $\tilde{\chi}_2^0$  and  $\tilde{\chi}_1^\pm$ , as well as the cross section times branching fractions of certain higgsino decay channels for all three operating centre-of-mass energies,  $\sqrt{s} = 250, 350$  and  $500$  GeV. The inputs are all scaled to the most relevant ILC operating scenario. Those are H20 for ILC1 and I20 for ILC2 and nGMM1, as the ILC1 higgsinos are accessible at  $\sqrt{s} = 250$  GeV but the ILC2 and nGMM1 higgsinos only at  $\sqrt{s} = 320$  GeV. Only the ILC machine with  $\sqrt{s} = 500$  GeV is considered here, as the LHC has closed the phase-space for higgsinos with masses accessible at  $\sqrt{s} = 250$  GeV and mass differences like in ILC1 (as discussed in Sec. 7.1 and Ch. 2).

All the central input values are assumed to correspond to the true model values, so perfect detector calibration in this sense is assumed. All of the used mass measurements can be found in Tabs. 7.11. The cross section times branching fraction uncertainties are listed in Tab. 7.12 for ILC1, Tab. 7.13 for ILC2 and Tab.7.14 for nGMM1. Additionally, Higgs mass and branching fraction measurements are used. The Higgs branching fractions are assumed to be measured exactly according to Tab. 7.8 with the H20 uncertainties listed in Tab. 7.15. It should be a reasonable assumption that the H20 precisions for the Higgs can be reached with I20 operation, so H20 precisions are used for fit of all three benchmarks.

Some of the fits contain the assumption of the LHC gluino measurement from the LHC from Sec. 7.3.5. This will be highlighted when relevant.

For the case of nGMM1, it appeared that the higgsino mass difference measurements may be useful as in Ref. [169]. One nGMM1 fit has the LSP mass and the mass differences to the heavier higgsinos as input.

Next, the results of the GUT scale fits are described, starting with NUHM2 fits. Weak scale fit results follow in the next section.

## 7.5 GUT scale fit results

First, results from fitting NUHM2 to ILC1 and ILC2 observables are described. Then the possibilities are discussed for verifying that CMSSM and NUHM1 are not the underlying models.

### 7.5.1 Results of fitting NUHM2 to ILC1 observables

The six parameters of NUHM2 were fitted to the observables in ILC1. The total number of Markov Chain points was a million. The minimum  $\chi^2 = 0.0011$ , which corresponds to a very small goodness-of-fit value  $\chi^2/n.d.f. = 0.0011/19 = 0.00006$  for the 25 observables and 6 parameters. The fitted parameters are plotted in Fig. 7.17, so that the plots are limited to the parameter ranges where  $\chi^2 - \chi_{min}^2 < 10$ . It can be seen that the resulting  $\Delta\chi^2$  distributions of  $M_{1/2}$ ,  $M_0$  and  $m_A$  show parabolic behaviour, while the  $\mu$  and  $A_0$  have low values allowed in the  $2\sigma$  range, despite the distribution around the best fit point resembling a parabola. The  $\Delta\chi^2$  distribution of  $\tan\beta$  is slowly rising as  $\tan\beta$  increases. The lower limit on  $\tan\beta$  comes from the Higgs measurements. The  $1\sigma$  and  $2\sigma$  confidence intervals for all parameters are listed in Tab.7.16. The best fit point corresponds to the benchmark point within 10%, and the  $1\sigma$  intervals contains the model parameters.  $M_{1/2}$  is predicted with a 4% uncertainty while  $\mu$  and  $\tan\beta$  get a 12% and 49% uncertainty respectively. Only  $M_0$  and  $A_0$  are only slightly restricted. The Higgs observables are expected to have the same effect as in Ch. 6, namely helping to restrict in particular  $\tan\beta$  and  $m_A$ .

Translating these results into sparticle masses, it can be seen from Fig. 7.18 that the gaugino masses are very well predicted to be accessible at ILC with  $\sqrt{s} = 1$  TeV. The  $1\sigma$  confidence interval for  $\tilde{\chi}_3^0$  is around 16 GeV, while the  $1\sigma$  confidence interval for  $\tilde{\chi}_4^0$

and  $\tilde{\chi}_2^\pm$  is 26 GeV, corresponding to uncertainties of about 3%. The heavy Higgses are constrained to 900 – 1140 GeV at  $1\sigma$  and gluino to 1460 – 1560 GeV at  $1\sigma$  (note that the gluino mass was not included in the fit inputs). The rest of the coloured sector is found to be heavier than 4 TeV, apart from  $\tilde{t}_1$ , which could potentially lie in the reach of LHC with the  $2\sigma$  confidence interval reaching down to 1.6 TeV.

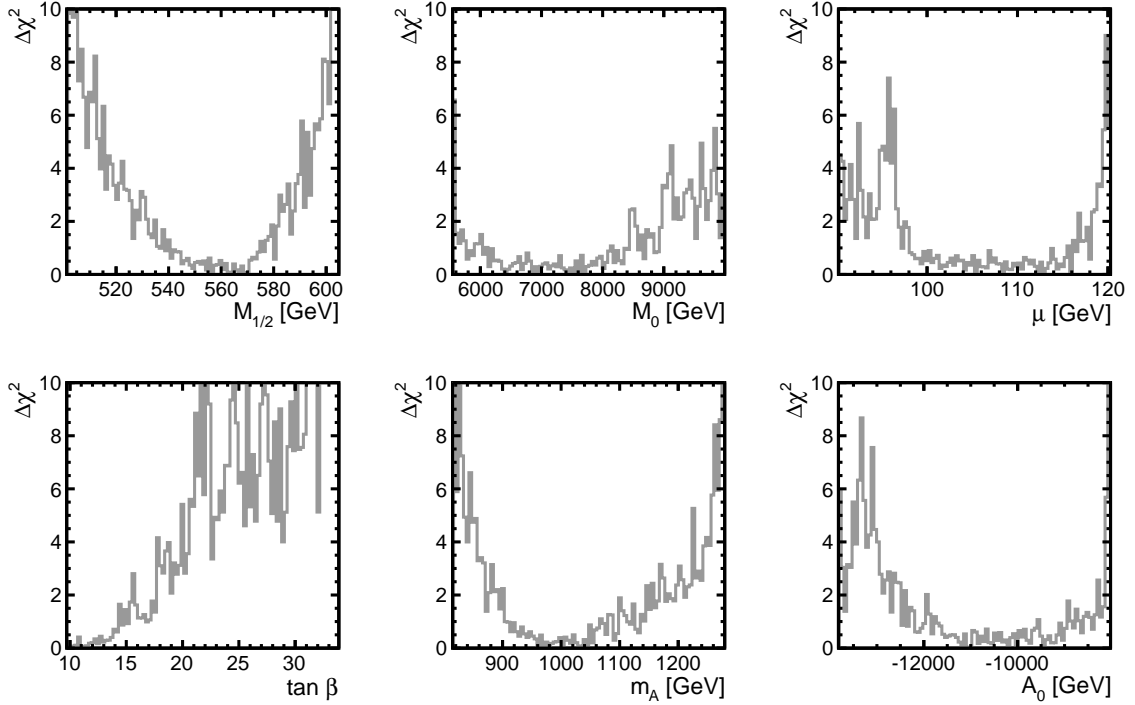


Figure 7.17: Fitted NUHM2 parameters to ILC1 observables.

### 7.5.2 Results of fitting NUHM2 to ILC2 observables

The results from fitting NUHM2 to ILC2 observables are qualitatively similar to the results from fitting NUHM2 to ILC1 observables. The  $\chi^2$  of the best fit point is 0.02848, which corresponds to a goodness-of-fit measure  $\chi^2/n.d.f. = 0.02848/19 = 0.00150$  for the 25 observables and 6 parameters. The parameter distributions are plotted in Fig. 7.19 which shows that  $M_{1/2}$  and  $m_A$  distributions are parabolic while all other distributions are flat over a wide parameter range. Compared to ILC1 results, the fitted parameter ranges in Tab. 7.17 are wider. In this case  $M_{1/2}$  has a 9% uncertainty and  $\tan\beta$  has a  $1\sigma$  interval of 20. On the other hand, the precision on  $\mu$  improves to 3%.

The fitted masses are plotted in 7.20. The allowed ranges are wider than in the ILC1 case, which can be explained by the worse experimental precisions of the higgsino measurements in ILC2 compared to ILC1. The gaugino masses and Higgs masses are predicted. The  $\tilde{\chi}_3^0$  mass is predicted within a 60 GeV  $1\sigma$  interval, and  $\tilde{\chi}_4^0$  and  $\tilde{\chi}_2^\pm$  with a 21 GeV range at  $1\sigma$  confidence. It would be clear from the predicted ranges, that only  $\tilde{\chi}_3^0$  could be produced at ILC with  $\sqrt{s} = 1$  TeV. For the heaviest neutralino and chargino, a larger centre-of-mass energy would be required, as would be for the heavy

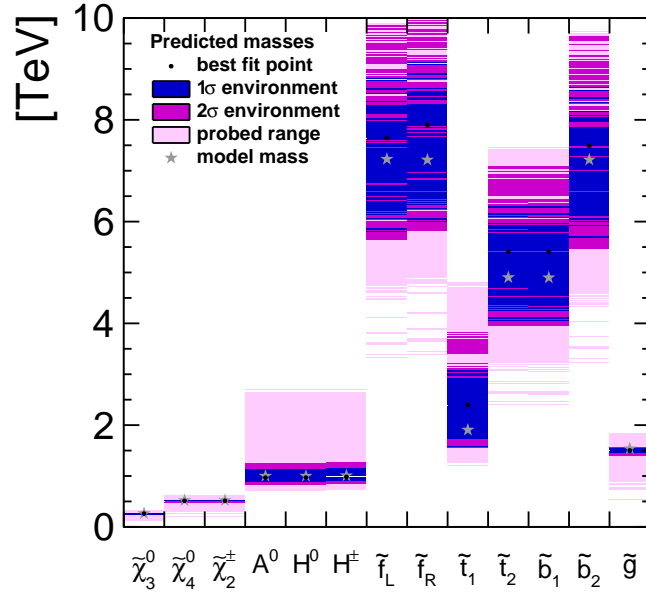


Figure 7.18: Predicted mass ranges for all the unobserved sparticles from the NUHM2 fit to ILC1 observables.

parameter	ILC1 NUHM2 true	best fit point	$1\sigma$ CL	$2\sigma$ CL
$M_{1/2}$	568.3	556.7	+24.3 -20.3	+37.7 -43.1
$\mu$	115.0	105.3	+12.8 -8.2	+14.0 -14.5
$\tan\beta$	10.0	11.4	+5.6 -1.6	+11.4 -1.6
$m_A$	1000	968	+167 -65	+288 -130
$M_0$	7025	7685	+1243 -1917	+2311 -2095
$A_0$	-10427	-11064	+2695 -1422	+2927 -2698
$\chi^2$	0.0013	0.0011		

Table 7.16: Fitted parameters in the fit of NUHM2 parameters to ILC1 observables in the H20 scenario. The length of the fit was  $10^6$  points. Note that the  $\chi^2$  value of the model point is increased from 0 by the rounding errors of the observables in the inputs.

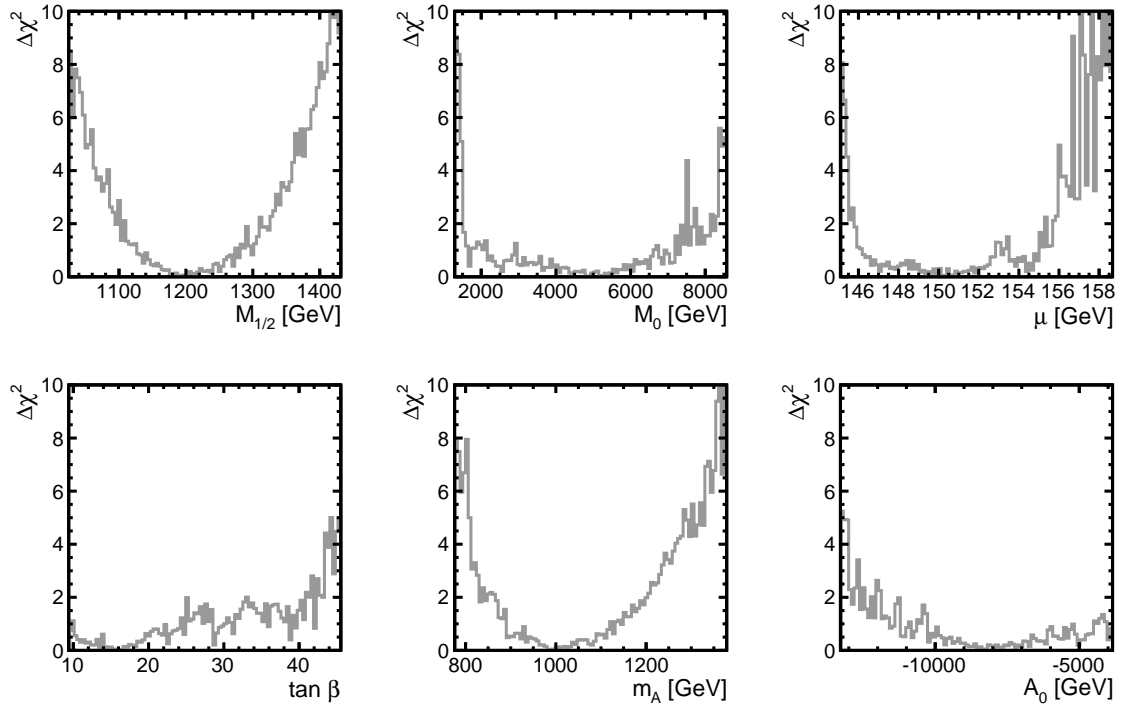


Figure 7.19: NUHM2 parameters fitted to ILC2 observables including SUSY and Higgs measurements from ILC I20 operation. Length of fit  $10^6$  points.

Higgses, which are predicted to have masses contained in the interval 880 – 1160 GeV. The coloured sector is predicted to be heavy above 2 TeV. The exception is  $\tilde{t}_1$ , whose mass would be allowed to be as low as 800 GeV with  $1\sigma$  confidence. This indicates that including LHC exclusion limits would help in this case to exclude more of the parameter space. The gluino mass should be contained in 2720 – 2980 GeV. Again, it should be noted that the gluino mass measurement was not included in the fit inputs.

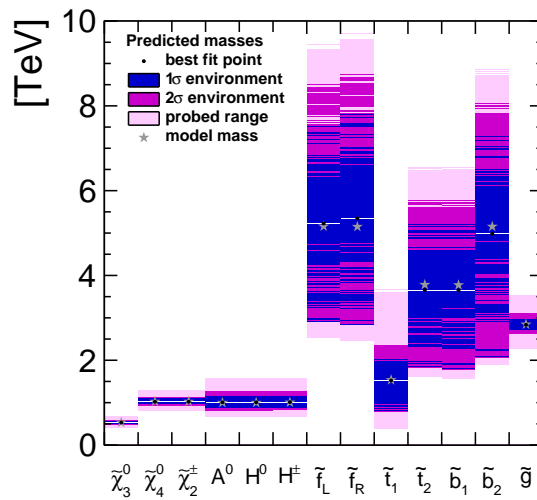


Figure 7.20: Predicted mass ranges for all the unobserved sparticles from the NUHM2 fit to ILC2 observables.

parameter	ILC2 NUHM2 true	best fit point	$1\sigma$ CL	$2\sigma$ CL
$M_{1/2}$	1200	1194	+107 -68	+164 -129
$\mu$	150.0	150.7	+4.3 -4.5	+7.2 -5.2
$\tan\beta$	15.0	16.0	+26.2 -6.6	+28.8 -6.6
$m_A$	1000	1008	+141 -118	+256 -196
$M_0$	5000	4788	+2546 -3137	+3566 -3283
$A_0$	-8000	-7663	+3817 -3926	+3817 -5342
$\chi^2$	0.0007	0.02848		

Table 7.17: Best fit point and confidence intervals of the NUHM2 parameters fitted to ILC2 SUSY and Higgs measurements in the I20 operating scenario.  $10^6$  points in the Markov Chain.

### 7.5.3 Results of fitting NUHM2 to nGMM1 observables

Despite nGMM1 not being defined as an NUHM2 but rather as a mirage unification model, it is interesting to check the results of fitting NUHM2 parameters to nGMM1 observables. A fit was performed with the nGMM1 higgsino and Higgs measurements as fit inputs, and all six parameters of NUHM2 were fitted.  $10^6$  Markov Chain points were calculated, divided into 10 fits of  $10^5$  points each. All of the fits were started with the NUHM2 parameters of ILC2 with a initial 1% uncertainty.

The result is that the best fit point has a  $\chi^2$  of 0.233 which means that the observables are in very good agreement with this NUHM2 point. It is noteworthy that the differences between the observables in ILC2 and nGMM1 benchmarks are only a few GeV for the higgsino masses (cf. Tabs. 7.4 and 7.5) and less than a percent for the Higgs branching fractions (cf. Tab. 7.8). With the comparatively large experimental uncertainties in the nGMM1 benchmark scenario, it is reasonable that an NUHM2 model fits the observations well.

The best fit values and confidence intervals for the parameters are listed in Tab. 7.18 and plotted in Fig. 7.21. The sizes of the confidence intervals are broadly similar to those obtained in the ILC2 NUHM2 fit Tab. 7.17, although the lower bound on  $M_0$  and upper bound on the size of  $A_0$  is stronger.

Predictions are made for the unobserved SUSY masses in Fig. 7.22. It is clear from the plot that the predicted best fit masses disagree with the model masses more than they do in the NUHM2 fits to ILC1 and ILC2 observables. Especially the  $\tilde{\chi}_3^0$  mass prediction lies far from the model mass: A discrepancy of 300 GeV is found between the model mass and the upper bound of the  $2\sigma$  confidence level for the fitted mass. Therefore, it would be likely that a lower limit on the  $\tilde{\chi}_3^0$  mass which would cover some of the predicted range around 1 TeV would increase the minimum  $\chi^2$  of the fit, leading to a larger disagreement between the observables and the NUHM2 model. Similarly if  $\tilde{\chi}_3^0$  or any other heavier particles were observed, this would help to distinguish that the underlying SUSY model is not NUHM2.

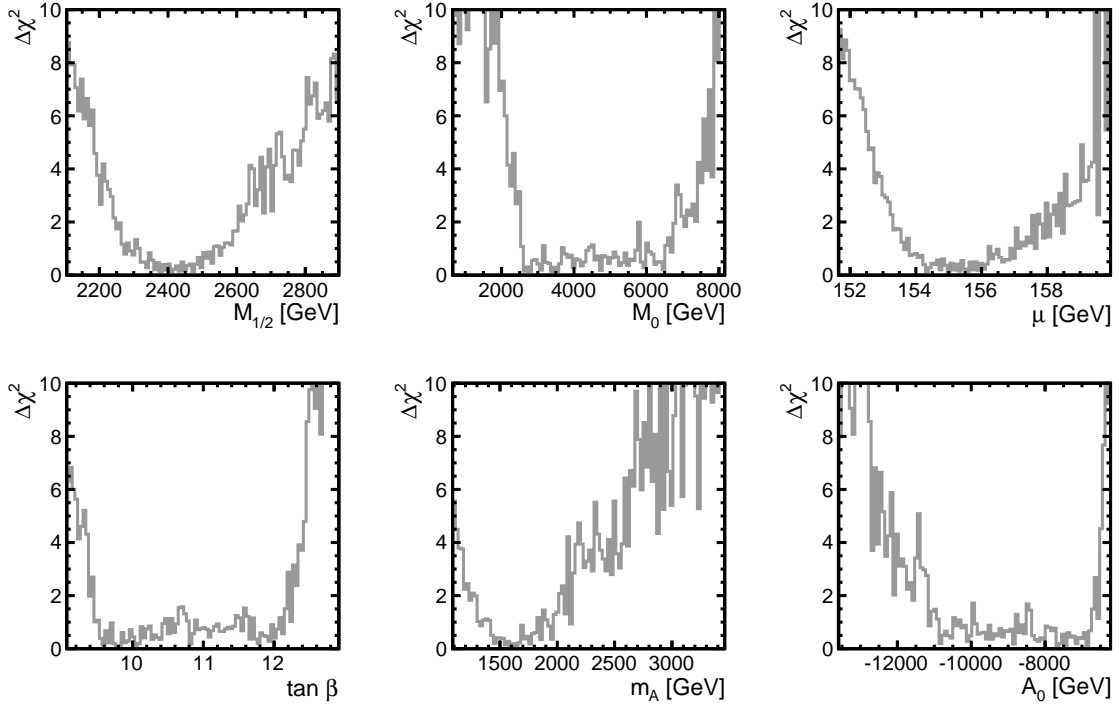


Figure 7.21: NUHM2 parameters fitted to nGMM1 observables including SUSY and Higgs measurements from ILC I20 operation. The length of the fit is  $10^6$  points.

parameter	best fit point	$1\sigma$ CL	$2\sigma$ CL
$M_{1/2}$	2407	+150 -135	+356 -215
$\mu$	155.6	+1.5 -1.9	+4.0 -2.9
$\tan \beta$	10.0	+2.1 -0.5	+2.4 -0.7
$m_A$	1603	+528 -279	+1026 -469
$M_0$	3422	+3309 -820	+4435 -1196
$A_0$	-7409	+666 -3756	+887 -5304
$\chi^2$	0.233		

Table 7.18: Best fit point and confidence intervals of the NUHM2 parameters fitted to nGMM1 SUSY and Higgs measurements in the I20 operating scenario.  $10^6$  points in the Markov Chain.

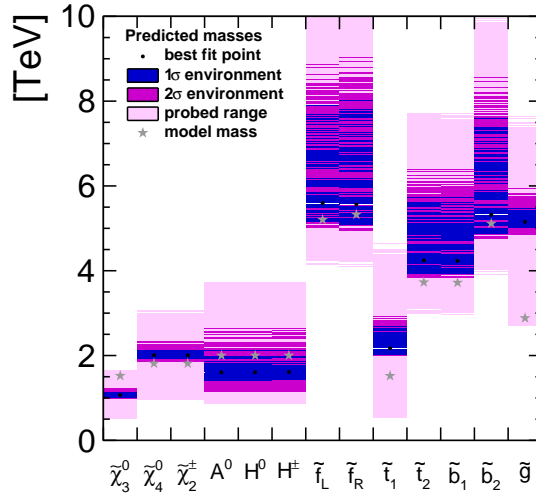


Figure 7.22: Predicted mass ranges for all the unobserved sparticles from the NUHM2 fit to nGMM1 observables.

#### 7.5.4 CMSSM and NUHM1 fits

The constrained models CMSSM and NUHM1 were fitted to both ILC1 and ILC2 observables. In this case  $10^6$  Markov Chain points were computed. The best fit points are minimum  $\chi^2$  are listed in Tab. 7.19. In all four cases, the minimum  $\chi^2$  found is of the order of  $10^5$ , leading to goodness-of-fit values of  $5 - 10 \times 10^3$ . This tells us that it is extremely unlikely that the observables originate from a CMSSM or NUHM1 model. The minimum  $\chi^2$  points of the fits have a low  $M_{1/2}$  around 130-160 GeV which is excluded by LHC searches for the gluino [126, 251].

In the ILC1 CMSSM fit, the  $\chi_{min}^2$  has the largest contribution from the  $\tilde{\chi}_2^0$  mass measurement ( $434^2$ ) and the  $\tilde{\chi}_1^0$  mass measurement ( $94^2$ ). The cross section measurements contribute from  $3^2$  up to  $93^2$ . The  $\chi^2$  deviation of the Higgs mass from the observation is only  $9^2$ . This is not to say that the Higgs measurements would not be important. The same is true for the best fit point of ILC1 NUHM1 fit.

In the ILC2 CMSSM, the Higgs mass contributes more to the  $\chi_{min}^2$  than in the ILC1 CMSSM fit,  $59^2$ . The neutralino masses agree slightly better with the best fit neutralino masses, but still give the largest contributions with  $71^2$  and  $268^2$  for  $\tilde{\chi}_1^0$  and  $\tilde{\chi}_2^0$  respectively. The maximal contribution from the cross section measurements is now  $45^2$ . It should be remembered that the SUSY measurement precisions are worse in the ILC2 benchmark than in the ILC1 benchmark, leading to smaller SUSY contributions to the overall  $\chi^2$ . The NUHM1 best fit point is similar in terms of the contributions from the Higgs and the SUSY cross sections. However, in this fit the  $\tilde{\chi}_1^0$  mass measurement contributes  $518^2$ ,  $\tilde{\chi}_2^0$  mass measurement  $1278^2$  and  $\tilde{\chi}_1^\pm$  mass measurement  $1006^2$  to the  $\chi^2$ . The ILC2 NUHM1 is the only one of the four fits where this is the case.

Fig. 7.23 shows the particle spectrum of the best fit point in the CMSSM fit to ILC1 observables as an example. It can be seen that the gluino mass is well below 1 TeV

best fit points				
parameter	ILC1 CMSSM	ILC2 CMSSM	ILC1 NUHM1	ILC2 NUHM1
$M_{1/2}$ [ GeV ]	128.8	155.9	136.9	159.9
$M_0$ [ GeV ]	3585	5631	1796	4264
$A_0$ [ GeV ]	-6873	-10873	-4396	-10086
$\tan \beta$	13.7	16.2	16.2	14.8
$M_{H_0}^0$ [ GeV ]	–	–	47659	56553
$\chi^2_{min}$	238046	93155	235014	85174
$\chi^2/d.o.f$	11336	4436	11751	4259

Table 7.19: Best fit points in CMSSM and NUHM1 fits of ILC1 and ILC2 observables, including SUSY and Higgs measurements in the H20 operation for ILC1 and I20 operation for ILC2. All four fits contain  $10^6$  Markov Chain points. The number of observables in each fit was 25. CMSSM has 4 parameters and NUHM1 has 5 parameters.

in the already excluded range. It can be concluded in both scenarios ILC1 and ILC2 that CMSSM and NUHM1 would be excluded as underlying models.

## 7.6 Weak scale fit results

The following subsections cover the results of various pMSSM-10 and pMSSM-4 fits to the ILC1, ILC2 and nGMM1 observables.

### 7.6.1 ILC1 pMSSM-10 fit

In this section, pMSSM-10 fit results to ILC1 observables are discussed. The best fit point agrees with the benchmark parameters within the  $1\sigma$  uncertainties of the parameters. The parameter space is large and this is reflected in the ragged parameter distributions in Fig. 7.24.  $M_1$  and  $M_2$  show parabola-like shapes. If  $\mu$  and  $\tan \beta$  are increased then the  $\Delta\chi^2$  value increases slowly, while low values of the parameters are sharply constrained. The  $1\sigma$  and  $2\sigma$  ranges are listed in Tab. 7.20. All the  $1\sigma$  ranges contain the model values. The extracted  $1\sigma$  uncertainty for  $M_1$  is 6.2%, for  $M_2$  5.2%, for  $\mu$  9.4% and for  $\tan \beta$  91%, considering the larger of the asymmetric uncertainties as only the  $M_2$  uncertainty is symmetric. Fig. 7.25 shows all the parameter ranges in a visual format. It is noteworthy that the allowed  $1\sigma$  parameter ranges contain  $M_3$  values down to 300 GeV and sfermion mass parameter values down to 900 GeV for the  $M_{U(3)}$  parameter. On the other hand, none of the distributions have allowed values all the way up to 10 TeV, which is the border of the scanning range in *Fittino*.

Correlation plots are not presented as the length of the Markov Chain was not enough

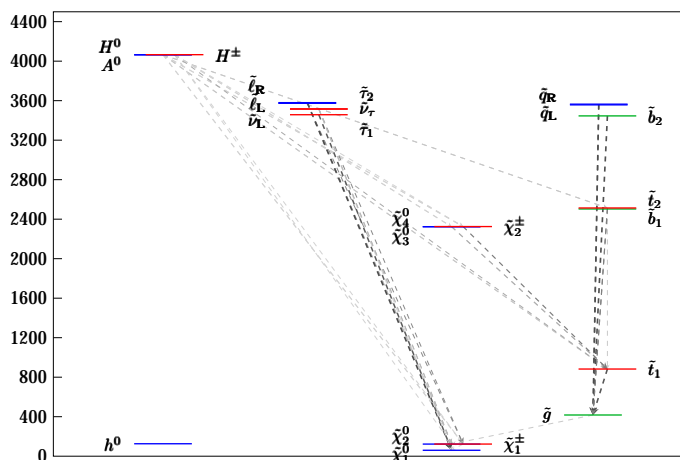


Figure 7.23: Mass spectrum of the best fit point in the 1-million point CMSSM fit to ILC1 observables.

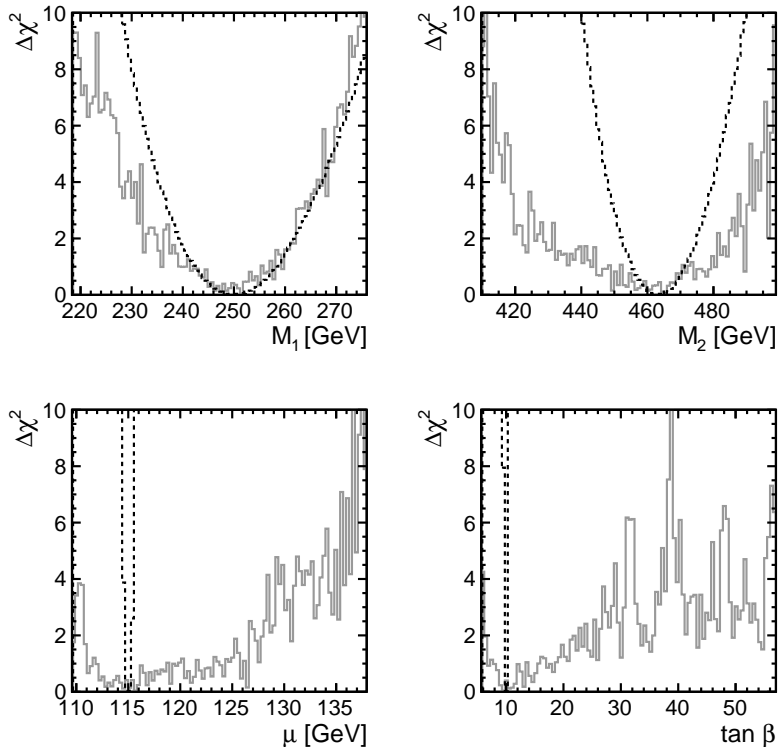


Figure 7.24: ILC1 fitted parabolae for  $M_1$ ,  $M_2$  and  $\mu$  and  $\tan \beta$  in pMSSM-4 fit (dashed black line) and pMSSM-10 fit (solid grey line)

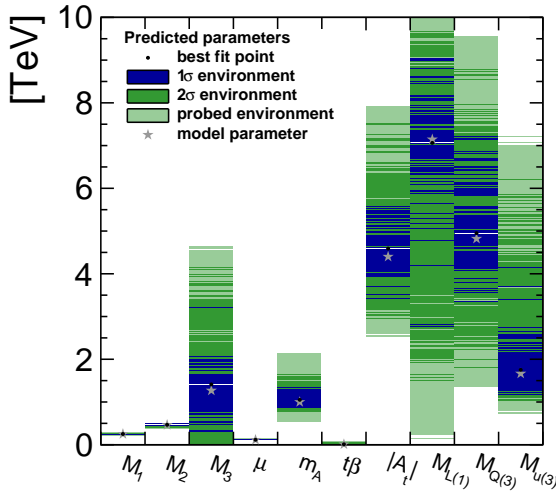


Figure 7.25: Fitted parameters in the pMSSM-10 fit to ILC1 observables. Here  $\tan\beta$  is plotted as if it was in GeV.

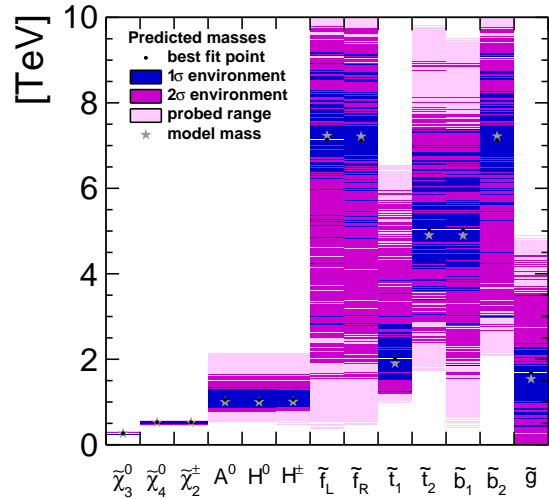


Figure 7.26: Fitted masses in the pMSSM-10 fit to ILC1 observables.

to obtain smooth correlation contours. The extent of the Markov Chain probing is shown in Figs. 7.27 and 7.28 for  $M_1$  and  $\tan\beta$  respectively. It can be seen that  $M_1$  is stable throughout the fits but  $\tan\beta$  does not converge. It is promising that the fit has probed a wide range of values for  $\tan\beta$  as this increases the confidence in the Markov Chain covering all necessary parameter ranges.

The predicted masses are plotted in Fig. 7.26. Gaugino masses are again perfectly constrained to within about 5-6% of the model value. Heavy Higgs masses are predicted with a 500 GeV total range for the  $1\sigma$  CL. The coloured sector is not well constrained, and masses of below 2 TeV are allowed for  $\tilde{t}_1$  and  $\tilde{b}_1$  with  $1\sigma$  confidence and for first and second generation sfermions at  $2\sigma$  confidence. These first and second generation sfermions are excluded by the squark search - see Ch. 2 for more details. Crucially, the gluino mass range goes all the way down to 0 TeV at  $2\sigma$  confidence. Clearly including LHC exclusion limits would be helpful for reducing the allowed parameter space. The same is also true for the sfermions - the fit allows already excluded values of sfermion masses at  $2\sigma$  CL.

### 7.6.2 Effect of including gluino mass measurement on ILC1 pMSSM-10 fit

Another pMSSM-10 fit was performed to ILC1 observables including the should-have-been measured gluino mass with 11% uncertainty from the LHC. The fitted parameter plots in Fig. 7.29 show the same pattern as the fit without the gluino observation in Fig. 7.24. Only now  $M_3$  is determined (not plotted in Fig. 7.24). All the fitted parameters are plotted in Fig. 7.30 and the ranges are listed in Tab. 7.22. The best fit point agrees with the model parameters within  $1\sigma$ , and the  $1\sigma$  parameter ranges are similar to the results if the gluino mass is not included in the fit observables. Only

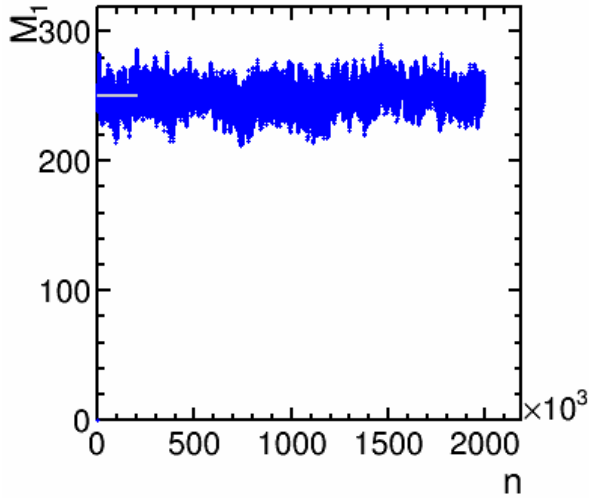


Figure 7.27: The probing of  $M_1$  in the pMSSM-10 fit to ILC1 observables.  $M_1$  is in units of GeV and the grey line indicates the model value.

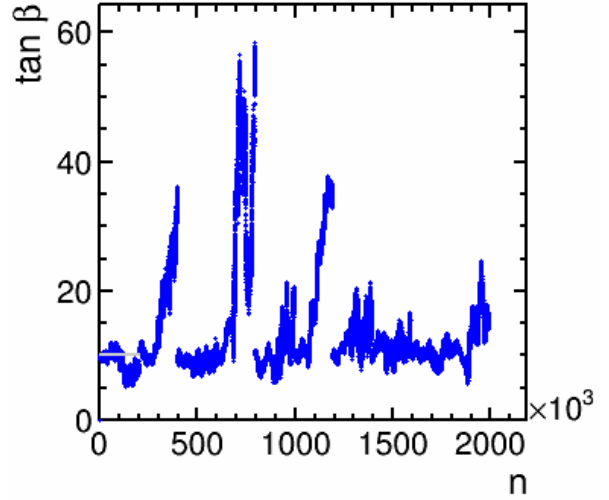


Figure 7.28: The probing of  $\tan \beta$  in the pMSSM-10 fit to ILC1 observables. The grey line indicates the model value.

parameter	ILC1 pMSSM true	pMSSM-4			pMSSM-10		
		best fit point	$1\sigma$ CL	$2\sigma$ CL	best fit point	$1\sigma$ CL	$2\sigma$ CL
$M_1$	250	250.2	+8.2 -7.7	+17.1 -15.1	251.3	+8.6 -15.7	+17.2 -23.7
$M_2$	463	463.3	+8.0 -8.1	+16.2 -14.9	465.8	+24.2 -23.0	+31.4 -49.8
$\mu$	115.0	115.0	+0.2 -0.2	+0.3 -0.3	115.7	+10.9 -4.7	+20.3 -6.1
$\tan \beta$	10.0	10.0	+0.1 -0.1	+0.2 -0.2	9.7	+8.8 -3.0	+45.3 -3.5
$m_A$	1000				1050	+310 -180	+607 -296
$M_3$	1270				1412	+1791 -1104	+1411 -2843
$M_{L(3)}$	7150				7063	+2029 -4311	+2645 -5632
$M_{U(3)}$	1670				1751	+2414 -628	+4498 -740
$M_{Q(3)}$	4820				4951	+2324 -3226	+3858 -3226
$A_{t=b=\tau}$	-4400				-4591	+1371 -973	+1647 -2949
$\chi^2$		0.0011			0.1360		

Table 7.20: Fitted parameters in the ILC1 pMSSM-4 and pMSSM-10 fits, with a fit length of one million points. All units in GeV except for  $\tan \beta$  and  $\chi^2$ .

prediction	ILC1 All SUSY+h		
	best fit	1 $\sigma$ CL	2 $\sigma$ CL
$m_{\tilde{\chi}_3^0}$	267	+8 -16	+16 -26
$m_{\tilde{\chi}_4^0}$	524	+20 -26	+26 -55
$m_{\tilde{\chi}_2^\pm}$	524	+19 -26	+25 -55
$m_{H_0}$	1050	+310 -190	+610 -290
$m_{A_0}$	1050	+310 -190	+610 -290
$m_{H^\pm}$	1056	+304 -176	+604 -276
$m_{\tilde{u}_L}$	7143	+2037 -4343	+2657 -5603
$m_{\tilde{u}_R}$	7117	+2023 -4337	+2643 -5577
$m_{\tilde{t}_1}$	2003	+1857 -763	+3957 -803
$m_{\tilde{t}_2}$	5033	+2347 -1993	+3947 -2653
$m_{\tilde{b}_1}$	5028	+2352 -3188	+3912 -3488
$m_{\tilde{b}_2}$	7130	+2030 -4310	+2650 -4470
$m_{\tilde{g}}$	1693	+1807 -1273	+2827 -1693

Table 7.21: Fitted masses in the pMSSM-10 fit to ILC1 AllSUSY+h observables. The fit length was  $10^6$  points.

the gluino mass parameter  $M_3$  is now determined with a 12% uncertainty as opposed to being allowed to be massless in the fit without the gluino mass observation. No other obvious effects are found from including the gluino mass observation in the fit inputs.

The predicted masses are shown in Fig. 7.31. The best fit masses agree with the model masses within the  $1\sigma$  uncertainty. The results are similar to the case without the gluino mass observation, only the  $\tilde{u}_{R,L}$  and  $\tilde{b}_2$   $1\sigma$  lower bounds are increased by 1 TeV.

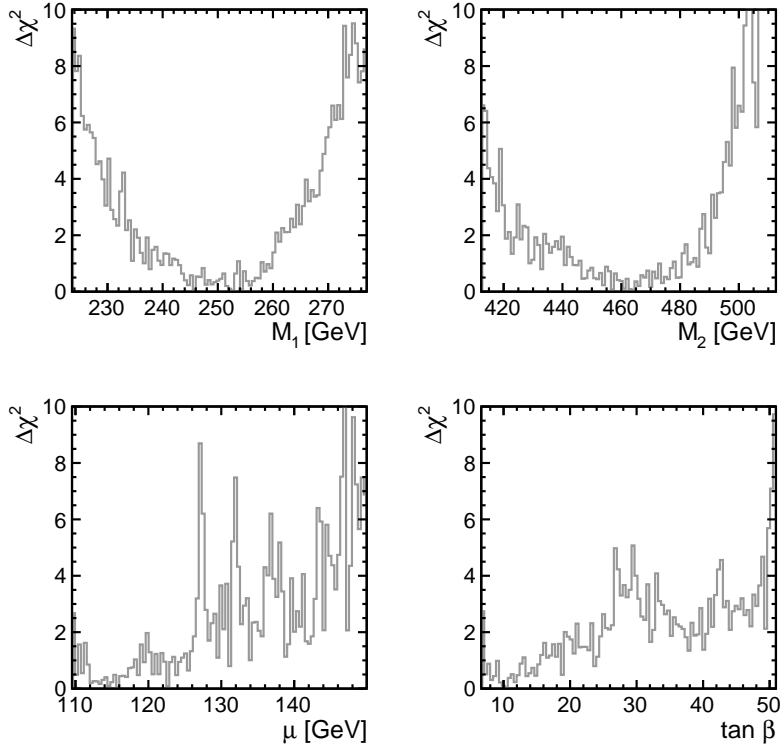


Figure 7.29: Fitted parabolae for some of the parameters in the pMSSM-10 fit with ILC1 measurements and gluino observation included in the fit inputs.

### 7.6.3 ILC1 pMSSM-4 fit

The higgsino properties are determined at tree-level by  $M_1$ ,  $M_2$ ,  $\mu$  and  $\tan\beta$  only. In this section, the importance of the loop corrections are investigated by performing a 4-parameter fit of the pMSSM. The fitted parameters are the aforementioned four parameters, which were found in the pMSSM-10 fit to be strongly constrained. Here, the pMSSM-4 model was fitted to ILC1 so that the fixed parameters take the true model values.

The fitted parameters are plotted in Fig. 7.24: The resulting distributions are very smooth compared to the the pMSSM-10 fit results. This is because the parameter space is small and the fitted parameters very restricted by the observables. All four parameters are determined accurately as can be read from Tab. 7.20. The best fit

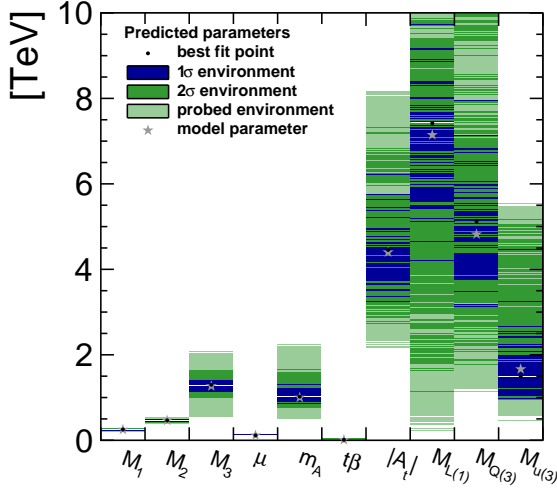


Figure 7.30: Fitted parameters in pMSSM-10 fit to ILC1 measurements including the gluino observation. Here  $\tan\beta$  is plotted as if it was in GeV.

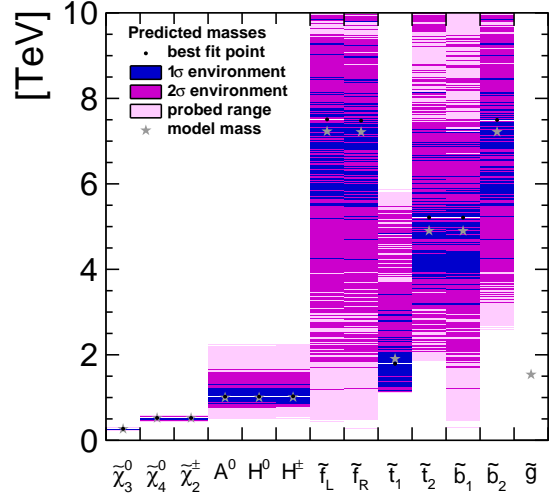


Figure 7.31: Fitted masses in pMSSM-10 fit to ILC1 measurements including the gluino observation.

parameter	ILC1 pMSSM true	best fit point	$1\sigma$ CL	$2\sigma$ CL
$M_1$	250.0	252.9	+7.0 -15.4	+15.6 -24.0
$M_2$	463.0	463.8	+22.8 -31.4	+30.8 -47.4
$\mu$	115.0	115.7	+15.7 -5.7	+31.9 -6.1
$\tan\beta$	10.0	10.5	+13.4 -3.5	+39.1 -3.9
$m_A$	1000	1021	+296 -183	+628 -263
$M_3$	1270	1298	+117 -150	+337 -322
$M_{L(3)}$	7150	7421	+2380 -3267	+2562 -6276
$M_{U(3)}$	1670	1491	+3004 -556	+3690 -556
$M_{Q(3)}$	4820	5124	+2842 -2057	+4869 -3493
$A_{t=b=\tau}$	-4400	-4452	+1210 -1793	+1770 -2913
$\chi^2$	0.00062	0.1360		

Table 7.22: Fitted parameters in the pMSSM-10 fit to ILC1 measurements including the gluino mass measurement. The fit length was one million points.

prediction	ILC1 All SUSY+h+g		
	best fit	1 $\sigma$ CL	2 $\sigma$ CL
$m_{\tilde{\chi}_3^0}$	268	+7 -16	+15 -24
$m_{\tilde{\chi}_4^0}$	523	+18 -33	+27 -50
$m_{\tilde{\chi}_2^\pm}$	522	+18 -33	+27 -49
$m_{H_0}$	1022	+298 -182	+638 -262
$m_{A_0}$	1022	+298 -182	+638 -262
$m_{H^\pm}$	1029	+291 -189	+631 -249
$m_{\tilde{u}_L}$	7508	+2352 -3268	+2452 -6328
$m_{\tilde{u}_R}$	7480	+2340 -3260	+2500 -6280
$m_{\tilde{t}_1}$	1790	+3070 -630	+3690 -650
$m_{\tilde{t}_2}$	5213	+2927 -2053	+4787 -3153
$m_{\tilde{b}_1}$	5210	+2070 -2050	+4270 -4010
$m_{\tilde{b}_2}$	7495	+2365 -3255	+2505 -4275

Table 7.23: ILC fitted masses, pMSSM-10 fit with AllSUSY+h observables and gluino mass,  $1 \times 10^6$  points

values correspond perfectly to the ILC1 model values. The uncertainties of the parameters range from 1.0% for  $\tan\beta$  up to 3.3% for  $M_1$ . The  $2\sigma$  ranges are approximately two times the  $1\sigma$  ranges, as was already visually observed from the parameter distributions.

The fitted masses are plotted in Fig. 7.33. The gaugino masses are determined correctly to a 1.6-3% precision. All other masses correspond precisely to the model masses.

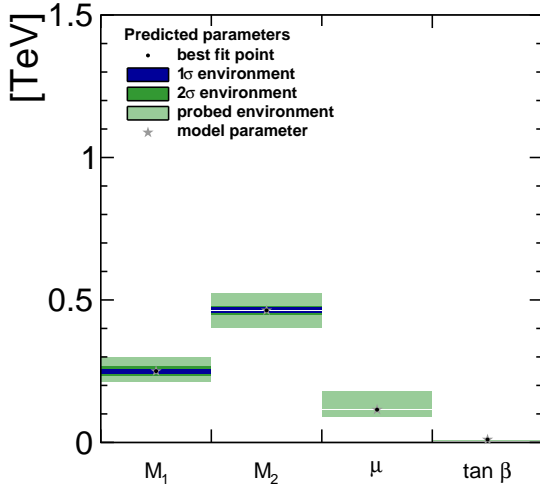


Figure 7.32: Fitted parameters in the pMSSM-4 to ILC1 observables. Here  $\tan\beta$  is plotted as if it was in GeV.

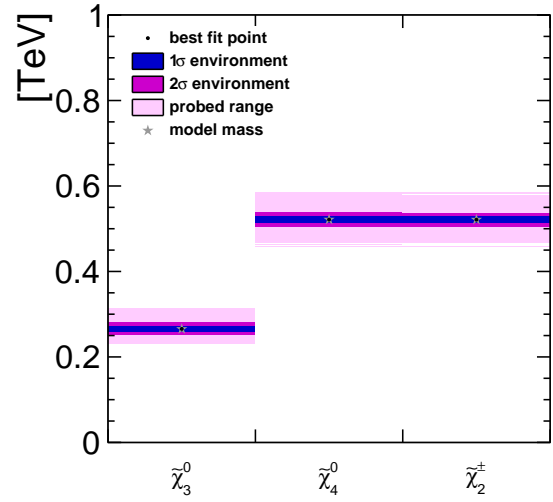


Figure 7.33: Fitted gaugino masses in the pMSSM-4 fit to ILC1 observables.

### The effect of the fixed parameters in the pMSSM-4 fit

To check the significance of the fixed parameters in the pMSSM-4 fit to ILC1 observables, the other six parameters were fixed to values which are not the model parameters. These values were obtained by searching the pMSSM-10 fit results for points within the  $2\sigma$  range from the fit minimum. To try to find extremal points, the sfermion mass parameter  $M_{L(1)}$  and stop mass parameter  $M_{Q(3)}$  were both required to be below 3 TeV. In total 1583 points in the Markov Chain satisfied these criteria.

One such point was picked with  $\chi^2 = 3.6$ ,  $M_1 = 243.51$ ,  $M_2 = 469.35$ ,  $\mu = 111.36$ ,  $\tan\beta = 10.68$ ,  $m_A = 1437.98$ ,  $M_3 = 440.00$ ,  $M_{L(1)} = 2735.49$ ,  $M_{Q(3)} = 2711.12$ ,  $M_{U(3)} = 1960.45$  and  $A_t = -3309.10$ . If the parameters  $M_1$ ,  $M_2$ ,  $\mu$  and  $\tan\beta$  are set to the ILC1 model values and the other parameters remain as they are, then the  $\chi^2$  with respect to the ILC1 model observables is  $\chi^2 = 1608$ .

A pMSSM-4 fit was conducted but with the six fixed parameters as above. Again,  $10^6$  Markov Chain points were computed. The resulting  $\chi^2_{min} = 1.4$  which is very good, although worse than 0.0011 in the other pMSSM-4 fit. The  $\Delta\chi^2$  distributions are shown in Fig. 7.34 in comparison to the fit results when the six fixed parameters take the ILC1 model values. The uncertainties for all four parameters are very similar in both fits. It can be seen that the best fit  $M_1$  is nearly the same in both cases.  $M_2$  and  $\tan\beta$  are shifted to higher values, 14 GeV and 0.78 respectively. These amount to a  $2\sigma$  and  $8\sigma$  discrepancies with respect to the pMSSM-4 results in Tab. 7.20. On the

other hand  $\mu$  is reduced with respect to the pMSSM-4 fit with model fixed parameters by 4 GeV, causing a  $20\sigma$  disagreement between the two fits. The general scale of each of the parameters is clear, though. Thus it can be concluded that the fixed parameters do influence the central value of the four fitted parameters, and a simple 4-parameter fit is not enough if the fixed parameters are fixed ad hoc and not by observations.

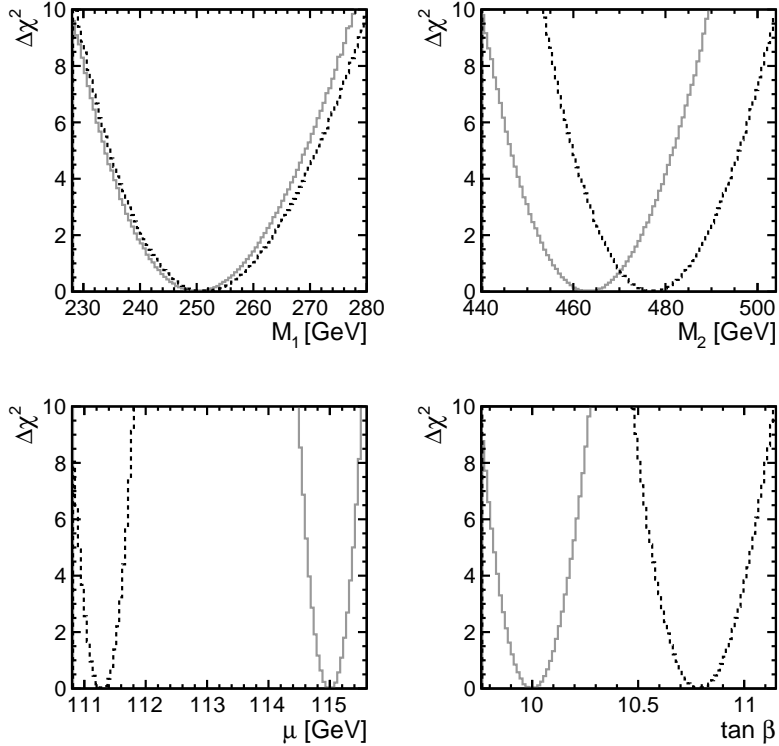


Figure 7.34: ILC1 fitted parabolae for  $M_1$ ,  $M_2$  and  $\mu$  and  $\tan\beta$  in pMSSM-4 fit with non-true values for the fixed parameters (dashed black line) and pMSSM-4 fit (solid grey line).

The best fit gaugino masses are nearly the same in the two pMSSM-4 fits irrespective of the fixed parameters. Their difference is only 2.5 GeV for  $\tilde{\chi}_3^0$  and 0.8 GeV for  $\tilde{\chi}_4^0$  and  $\tilde{\chi}_2^\pm$ . The two sets of best fit masses agree within the  $1\sigma$  uncertainties.

#### 7.6.4 ILC2 pMSSM-10 fit

Here pMSSM-10 parameters were fitted to ILC2 observables. The best fit point has a small  $\chi^2 = 0.1627$ , and the best fit parameters agree with the model parameters within the  $1\sigma$  uncertainties of the fitted parameters. The resulting parameter distributions for some of the parameters are plotted in Fig. 7.35. It can be seen that, like for ILC1,  $M_1$  and  $M_2$  distributions resemble parabolas and  $\mu$  and  $\tan\beta$  have rising slopes at high values and a steep cutoff at low values. This is qualitatively the same behaviour of the parameters as in the ILC1 pMSSM-10 fit.

The precise  $1\sigma$  and  $2\sigma$  confidence intervals can be read out from Tab. 7.24. In this fit, the fitted ranges are not parabolic. In fact, for all parameters, the  $2\sigma$  range is less than twice the  $1\sigma$  range.

The  $1\sigma$  uncertainty on  $M_1$  is 18.2%, 15.5% on  $M_2$ , 16.0% on  $\mu$  and 17.0% on  $m_A$ . The upper bound on  $\tan\beta$  is as high as 53, thus it does not make sense to quote a percentage uncertainty. All of these uncertainties are worse than in the ILC1 pMSSM-10 fit, as is expected because the fit inputs are less accurate. It is interesting to note that the coloured sector is poorly constrained by the higgsino observables. In particular, values of  $M_3$  and the sfermion mass parameters are allowed to be 1 TeV or even below at  $1\sigma$  confidence. This is not surprising as the higgsinos couple weakly to coloured particles. The only possible dependence then comes from the Higgs sector. It is clear that including current and future LHC exclusion limits on the coloured particles would constrain the fit further.

Looking at Fig. 7.37 for the predicted masses, the same pattern is observed as for ILC1. The precise predictions are listed in Tab. 7.25. The gaugino masses are predicted with an 8-14% uncertainty and the heavy Higgses with a 360 GeV range. The coloured masses are poorly constrained by the ILC measurements, motivating the inclusion of LHC limits in future studies.

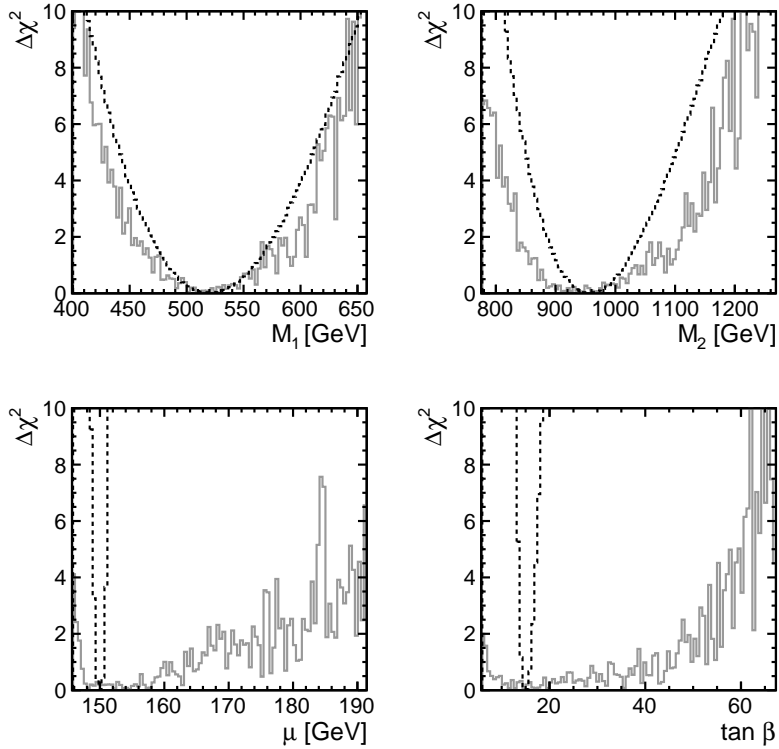


Figure 7.35: ILC2 parameter distributions for  $M_1$ ,  $M_2$  and  $\mu$  and  $\tan\beta$  in pMSSM-4 fit (black dashed line) and pMSSM-10 fit (grey solid line).

### 7.6.5 ILC2 pMSSM-4 fit

As for ILC1, it was investigated whether the poorly constrained coloured sector parameters and  $m_A$  influence the fitted  $M_1$ ,  $M_2$ ,  $\mu$  and  $\tan\beta$  uncertainties. For this purpose a pMSSM-4 model with  $M_1$ ,  $M_2$ ,  $\mu$  and  $\tan\beta$  as the free parameters was fitted to the ILC2 observables. The fixed parameters take the model values.

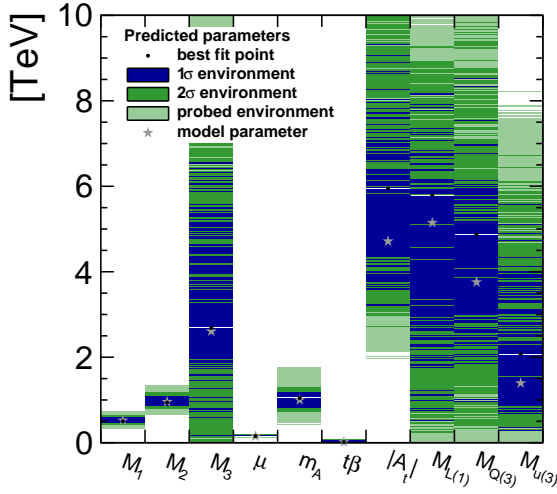


Figure 7.36: Fitted parameters of ILC2 observables in pMSSM-10 fit. Here  $\tan \beta$  is plotted as if it was in GeV.

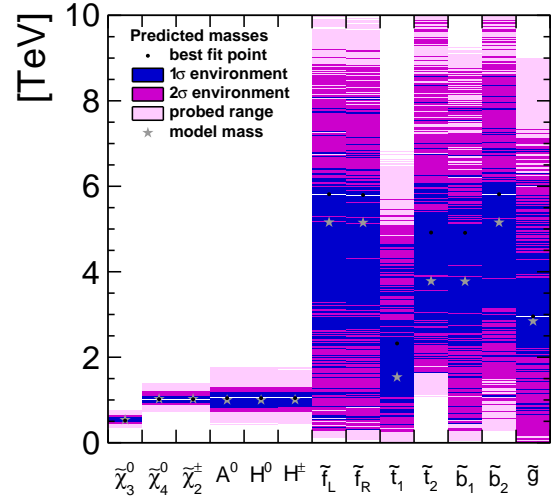


Figure 7.37: Fitted masses in pMSSM-10 fit of ILC2 observables.

parameter	ILC2 pMSSM true	pMSSM-4			pMSSM-10		
		best fit point	1 $\sigma$ CL	2 $\sigma$ CL	best fit point	1 $\sigma$ CL	2 $\sigma$ CL
$M_1$	520.3	520.7	+38.6 -37.6	+79.1 -71.0	502.1	+91.3 -32.9	+130.1 -71.7
$M_2$	957.2	959.42	+55.4 -53.1	+124.1 -100.1	941.0	+145.4 -71.7	+229.2 -130.9
$\mu$	150.0	150.0	+0.4 -0.4	+0.7 -0.8	154.4	+24.7 -7.3	+36.6 -8.2
$\tan \beta$	15.0	15.0	+0.7 -0.6	+1.7 -1.2	14.8	+38.4 -7.8	+48.2 -9.0
$m_A$	1000				1043	+135 -203	+240 -325
$M_3$	2607				2684	+4990 -2585	+5670 -2682
$M_{L(3)}$	5146				5797	+2402 -5359	+3511 -5544
$M_{U(3)}$	1395				2073	+3518 -1805	+4716 -1805
$M_{Q(3)}$	3757				4871	+3680 -3933	+5030 -4608
$A_t$	-4714				-5948	+2734 -3387	+3250 -4050
$\chi^2$		0.0026			0.1627		

Table 7.24: ILC2 fit 1m points, pMSSM-4 and pMSSM-10 fits. All units in GeV except for  $\tan \beta$  and  $\chi^2$ .

prediction	ILC2 All SUSY+h		
	best fit	$1\sigma$	$2\sigma$
$m_{\tilde{\chi}_3^0}$	518	+72 -34	+110 -74
$m_{\tilde{\chi}_4^0}$	1018	+82 -76	+190 -134
$m_{\tilde{\chi}_2^\pm}$	1018	+82 -76	+190 -134
$m_{H_0}$	1043	+137 -223	+257 -323
$m_{A_0}$	1043	+137 -223	+257 -323
$m_{H^\pm}$	1045	+135 -205	+255 -325
$m_{\tilde{u}_L}$	5814	+2286 -5474	+3406 -5534
$m_{\tilde{u}_R}$	5795	+2285 -5495	+3385 -5495
$m_{\tilde{t}_1}$	2322	+2318 -1902	+3378 -2062
$m_{\tilde{t}_2}$	4917	+3663 -3277	+4983 -3317
$m_{\tilde{b}_1}$	4911	+3189 -4471	+3869 -4631
$m_{\tilde{b}_2}$	5814	+2766 -4734	+4086 -5254
$m_{\tilde{g}}$	2955	+3925 -2735	+4445 -2935

Table 7.25: ILC2 fitted masses, pMSSM-10 fit with AllSUSY+h observables,  $1 \times 10^6$  points

The best fit point agrees perfectly with the model point, with the best fit  $\chi^2 = 0.0026$ . The fitted parameter distributions are plotted in Fig. 7.35 as  $\Delta\chi^2$  distributions and in Fig. 7.38 showing the uncertainty ranges. The difference to the pMSSM-10 fit results is striking as was in ILC1. The extracted parameters and uncertainties are listed in Tab. 7.24, from which it can be seen that the uncertainties are symmetric and the distributions almost parabolic in that the  $2\sigma$  range is about twice the  $1\sigma$  range. The uncertainties are reduced with respect to the pMSSM-10 especially for  $\mu$  and  $\tan\beta$ , so it can be concluded that the fixed parameters influence the determination of those parameters the most.  $M_1$  and  $M_2$  get contributions from the fixed parameters too, as their uncertainties are smaller in the pMSSM-4 fit than in the pMSSM-10 fit.

As can be seen from Fig. 7.39, the gaugino masses are predicted but with larger uncertainties than in the corresponding fit with ILC1 observables. The uncertainty is 7% for  $\tilde{\chi}_3^0$  mass and 5% for  $\tilde{\chi}_4^0$  and  $\tilde{\chi}_2^\pm$  masses (3% and 2% in ILC1). This can be explained by the worse experimental precisions for the fit inputs in the ILC2 scenario.

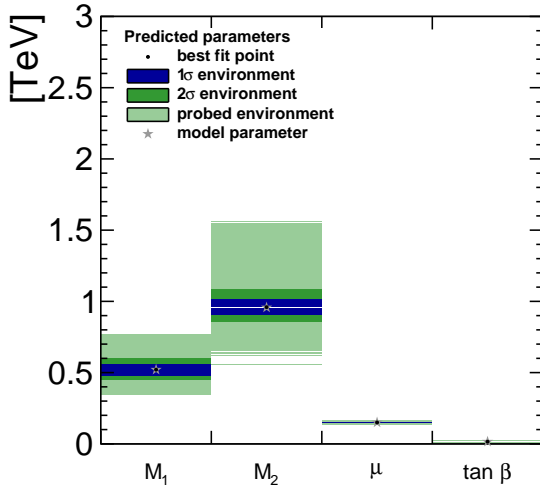


Figure 7.38: Fitted parameters in the pMSSM-4 to ILC2 observables. Here  $\tan\beta$  is plotted as if it was in GeV.

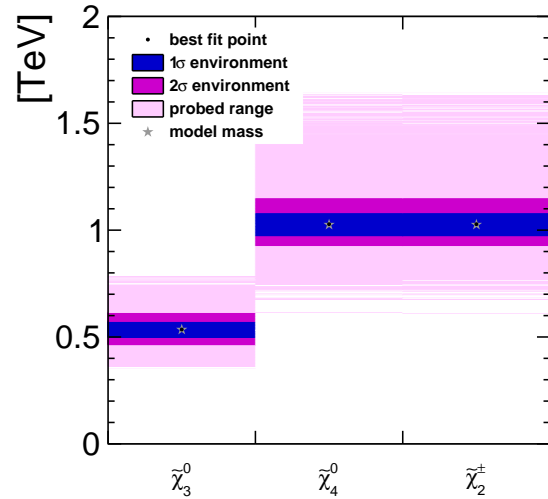


Figure 7.39: Fitted gaugino masses in the pMSSM-4 fit to ILC2 observables.

### 7.6.6 nGMM1 pMSSM-10 fit

Fitting pMSSM-10 parameters to nGMM1 observables gives significantly different results compared to the fits to ILC1 and ILC2 observables. This can be seen from Fig. 7.35 where these parameters are plotted. The shape of the distribution for  $M_1$  is not parabolic anymore but the  $2\sigma$  range extends far from the model value up to 4.2 TeV, see also Tab. 7.26. The range for  $M_2$  is more moderate with an uncertainty of 26% for the  $1\sigma$  confidence interval. The key, though, is that the centre of the  $1\sigma$  interval for  $M_1$  is 640 GeV higher than the same for  $M_2$ , although the model difference is 230 GeV in the opposite direction. This has a significant impact on the results as we will discuss shortly.

Like in ILC1 and ILC2 fits, the other parameters are not determined accurately in the pMSSM-10 nGMM1 fit. It is worth pointing out that again, low values of  $M_3$  and other coloured sector parameters are allowed. LHC exclusions would be useful for constraining the fit further.

The determined mass ranges are in shown Fig. 7.47. These are a lot wider for the gauginos and heavy Higgses than in the ILC1 and ILC2 cases. The central values of the gaugino mass predictions are around 1.4 TeV for  $\tilde{\chi}_3^0$  and 1.9 TeV for  $\tilde{\chi}_4^0$  and  $\tilde{\chi}_2^\pm$ . This means that a high centre-of-mass energy of about 2 TeV would be required to produce the gauginos in associated production with one of the higgsinos.

It should be highlighted that  $m_A$  in this model is 2 TeV, so that the Higgs observables are closer to Standard Model expectations, which may worsen the precision on the heavy Higgs sector in addition to the less accurate higgsino measurements in nGMM1 compared to ILC1 and ILC2.

The coloured sector masses are allowed to be as low as a few hundred GeV at 1 $\sigma$  confidence. LHC exclusions seem to be crucial if the higgsino mass difference gets smaller. It is tested in the next section whether using the mass difference measurements instead of the mass measurements for higgsinos would help to obtain stronger fit constraints.

parameter	nGMM1	pMSSM-4			pMSSM-10		
		pMSSM true best fit point	1 $\sigma$ CL	2 $\sigma$ CL	best fit point	1 $\sigma$ CL	2 $\sigma$ CL
$M_1$	1493	1501	+173 -149	+411 -280	1386	+2386 -145	+2830 -282
$M_2$	1720	1711	+220 -158	+530 -279	1768	+254 -451	+717 -549
$\mu$	150.0	150.0	+0.4 -0.4	+0.9 -0.9	154.2	+7.4 -8.7	+12.9 -8.3
$\tan \beta$	10.0	10.0	+0.5 -0.3	+1.2 -0.6	8.3	+41.9 -1.3	+44.6 -1.9
$m_A$	2000				2655	+6493 -1449	+11492 -1596
$M_3$	2646				3173	+4229 -3168	+5347 -3168
$M_{L(3)}$	5115				4781	+3589 -4077	+4630 -4456
$M_{U(3)}$	1381				1774	+2384 -1086	+4826 -1214
$M_{Q(3)}$	3701				4011	+3254 -3535	+3982 -3697
$A_t$	-4857				-6766	+3698 -509	+4012 -1702
$\chi^2$		0.0138			0.0927		

Table 7.26: Fitted parameters in nGMM1 pMSSM-4 and pMSSM-10 fit using 1m. points. All units in GeV except for  $\tan \beta$  and  $\chi^2$ .

While in all the pMSSM-10 fits here smooth correlation curves cannot be extracted, it is worth highlighting the correlation of  $M_1$  and  $M_2$  in the two cases with mass difference observables vs. mass observables in the nGMM1 fits. Comparing Figs. 7.40 and 7.41 it is clear that the correlation of  $M_1$  and  $M_2$  is reduced in the fit with mass difference observables with respect to the fit with masses.

prediction	nGMM1 All SUSY+h		
	best fit	$1\sigma$	$2\sigma$
$m_{\tilde{\chi}_3^0}$	1412	+454 -134	+640 -260
$m_{\tilde{\chi}_4^0}$	1854	+1920 -264	+2364 -336
$m_{\tilde{\chi}_2^\pm}$	1853	+229 -443	+601 -557
$m_{H_0}$	2655	+6365 -1355	+7125 -1555
$m_{A_0}$	2655	+6365 -1355	+7125 -1555
$m_{H^\pm}$	2656	+6364 -1336	+7124 -1556
$m_{\tilde{u}_L}$	4762	+3698 -4282	+4718 -4582
$m_{\tilde{u}_R}$	4754	+3666 -4294	+4706 -4594
$m_{\tilde{t}_1}$	1951	+1549 -1411	+3889 -1471
$m_{\tilde{t}_2}$	4029	+3120 -2160	+3900 -2520
$m_{\tilde{b}_1}$	4008	+2852 -3448	+3712 -3748
$m_{\tilde{b}_2}$	4763	+3697 -3703	+4717 -4263
$m_{\tilde{g}}$	3361	+3259 -3261	+4559 -3361

Table 7.27: nGMM1 fitted masses, pMSSM-10 fit with AllSUSY+h observables,  $10^6$  Markov Chain points.

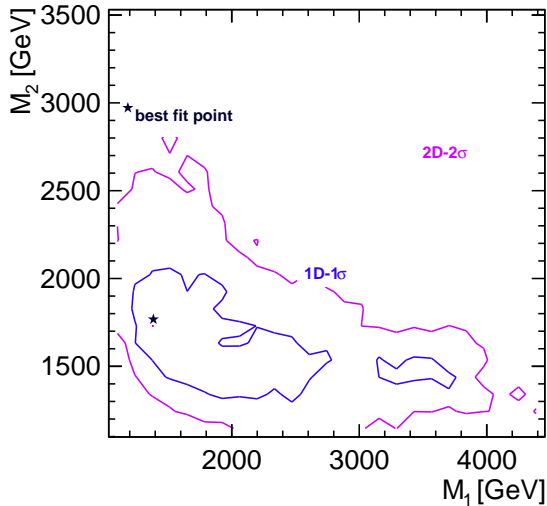


Figure 7.40: The correlation of  $M_1$  and  $M_2$  in the pMSSM-10 fit to nGMM1 observables.

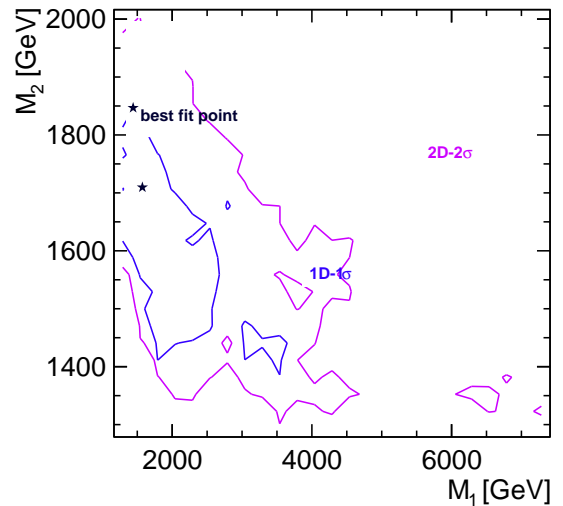


Figure 7.41: The correlation of  $M_1$  and  $M_2$  in the pMSSM-10 fit to nGMM1 observables with higgsino mass differences instead of masses.

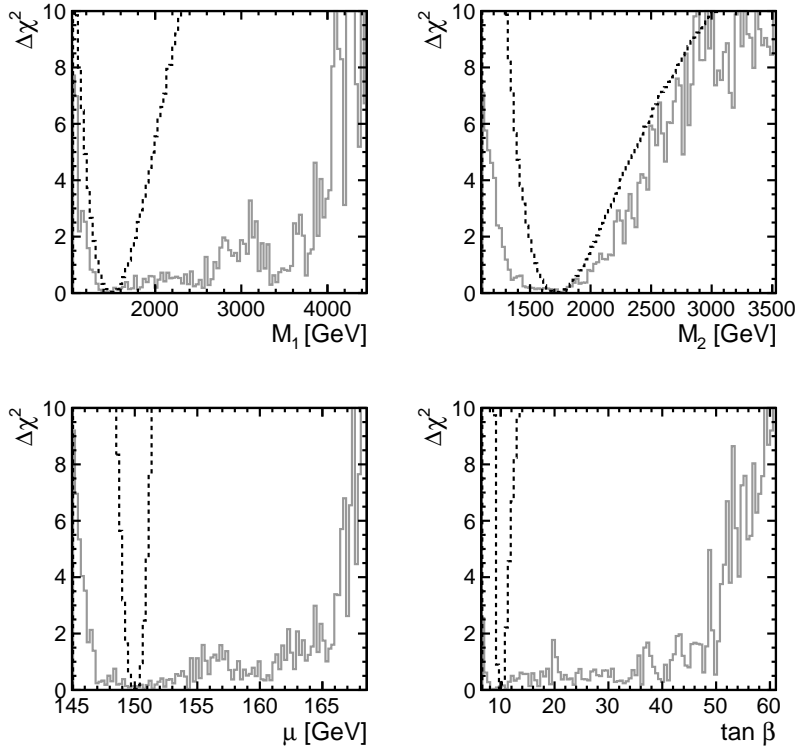


Figure 7.42: nGMM1 fitted parabolae for  $M_1$ ,  $M_2$  and  $\mu$  and  $\tan\beta$  in pMSSM-4 fit (black dashed line) and pMSSM-10 fit (grey solid line).

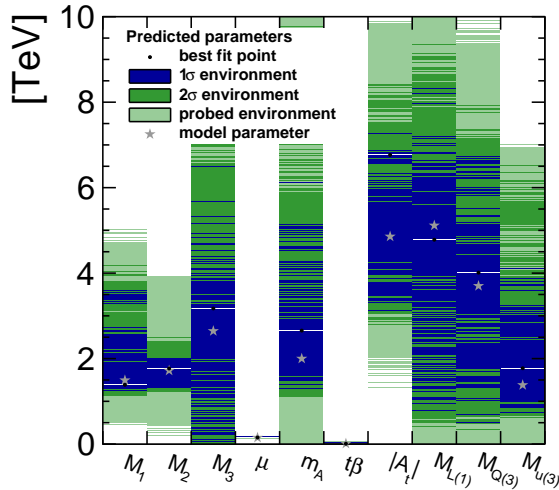


Figure 7.43: Fitted parameters in pMSSM-10 fit to nGMM1 observables. Here  $\tan\beta$  is plotted as if it was in GeV.

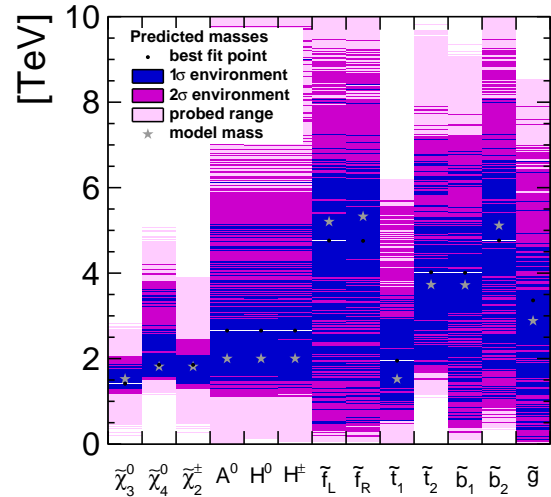


Figure 7.44: Fitted masses in pMSSM-10 fit to nGMM1 observables.

## 7.6.7 nGMM1 pMSSM-10 fit with mass difference measurements

It was found in the previous section that the allowed range for  $M_1$  is rather wide in the 10-parameter fit of nGMM1. It was suggested in Ref. [169] that mass difference measurements can be useful for parameter fits if the higgsinos have masses within 2 GeV of each other. Therefore, a fit was conducted, where instead of  $\tilde{\chi}_2^0$  and  $\tilde{\chi}_1^\pm$  masses, the mass differences  $|m_{\tilde{\chi}_2^0} - m_{\tilde{\chi}_1^0}|$  and  $m_{\tilde{\chi}_1^\pm} - m_{\tilde{\chi}_1^0}$  were input.

The uncertainties of  $m_{\tilde{\chi}_1^0}$ ,  $|m_{\tilde{\chi}_2^0} - m_{\tilde{\chi}_1^0}|$  and  $m_{\tilde{\chi}_1^\pm} - m_{\tilde{\chi}_1^0}$  were obtained via the same method as the results in Sec. 7.3.2, but with these observables as the free parameters in the minimisation of the  $\chi^2$  of the maximum energy of the di-lepton or di-jet system.

The uncertainties of  $m_{\tilde{\chi}_1^0}$ ,  $|m_{\tilde{\chi}_2^0} - m_{\tilde{\chi}_1^0}|$  and  $m_{\tilde{\chi}_1^\pm} - m_{\tilde{\chi}_1^0}$  are as follows for the  $500 \text{ fb}^{-1}$  data set: 1.72% for  $m_{\tilde{\chi}_1^0}$ , 2.08% for  $|m_{\tilde{\chi}_2^0} - m_{\tilde{\chi}_1^0}|$  and 2.47% for  $m_{\tilde{\chi}_1^\pm} - m_{\tilde{\chi}_1^0}$ . The correlations are not 100% anymore as they were if the masses were the parameters. However, the correlations are ignored in both cases.

The obtained precisions were scaled to the I20 scenario, leading to the inputs in Tab 7.28. It should be noted that the model values for the mass differences are those from **SPheno3.3.9beta** even though the detector simulation was performed for the slightly larger mass differences in the **Isasugra** spectrum.

observable	nGMM1 model value [GeV]	I20 uncertainty [GeV]
$m_{\tilde{\chi}_1^0}$	154.936	1.49
$ m_{\tilde{\chi}_2^0} - m_{\tilde{\chi}_1^0} $	5.280	0.073
$m_{\tilde{\chi}_1^\pm} - m_{\tilde{\chi}_1^0}$	2.445	0.028

Table 7.28: The mass observables in the nGMM1 fit with mass differences as fit inputs, along with the usual cross section inputs and Higgs mass and branching fraction inputs. The model values are from **SPheno3.3.9beta**.

The fitted parameter distributions are plotted in Fig. 7.45 as  $\Delta\chi^2$  distributions. It is striking that  $M_2$  is determined much more accurately in the case with mass differences as observables compared to if the masses are given individually. The parameters are plotted Fig. 7.46 as confidence intervals. There is not much difference in the determination of the other parameters in the two fits. As before, the best fit point agrees with the model point within  $1\sigma$ , as can be read from Tab. 7.29. Simply from the better determination of  $M_2$ , it would be useful to use the mass differences as observables, confirming the recommendation from Ref. [169]. Another reason is that the correlations between the mass difference observables are smaller than in the pure mass observables. In the former case, it is more justified to neglect the correlations of the observables as is done in the fits.

The fitted masses are shown in Fig. 7.47. The allowed gaugino mass ranges are slightly reduced with respect to the case with masses as inputs: for example the  $\tilde{\chi}_3^0$  mass range is 430 instead of 590 GeV, which is self-evident as this is the wino in the model. A

similar but smaller effect is found for the heaviest neutralino and chargino. It does appear beneficial from the point of view of the mass predictions to use the higgsino mass differences as fit inputs.

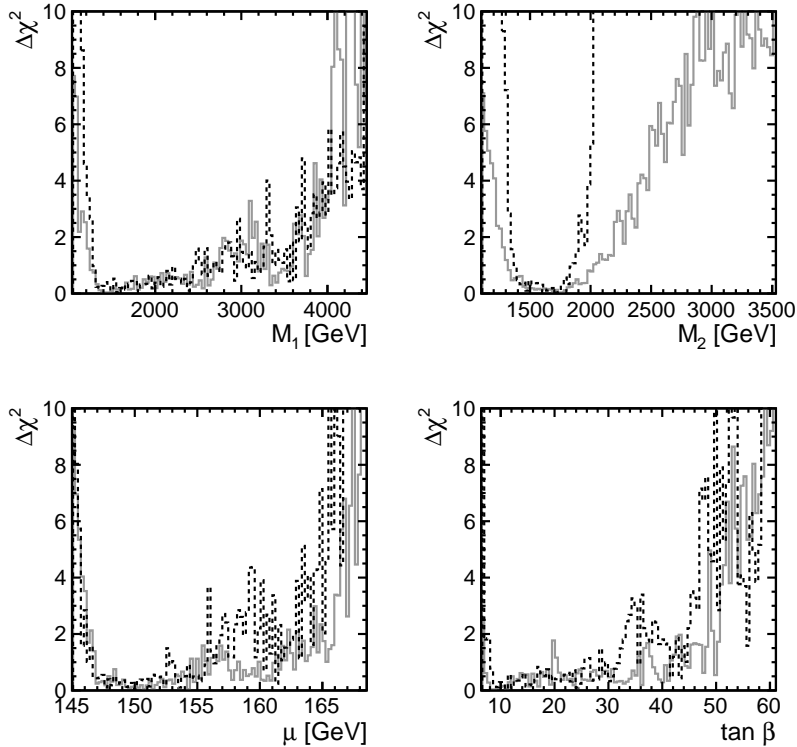


Figure 7.45: nGMM1mssm I20 fitted parabolae for some of the parameters in the 10-parameter fit with mass differences (black, dashed) and the same fit with masses as observables (grey, solid).

### 7.6.8 nGMM1 pMSSM-4 fit

Fitting pMSSM-4 parameters to nGMM1 observables gives similar results as the previously discussed 4-parameter fits with ILC1 and ILC2 observables. The fitted parameters are plotted in Fig. 7.42, from which it can be seen that the parabolas are slightly slanted for higher parameter values. The best fit point agrees with the model parameters within  $1\sigma$ . The uncertainties extracted from these confidence intervals are 11.5% for  $M_1$ , 12.9% for  $M_2$ , 0.3% for  $\mu$  and 4.9% for  $\tan\beta$ . The precisions of  $\mu$  and  $\tan\beta$  are similar to ILC2 results and the precisions of  $M_1$  and  $M_2$  are up to twice the same uncertainties for ILC2. The parameters are visualised in Fig. 7.48 for convenience.

The unobserved sparticle masses are predicted correctly, as the fixed parameters are set to model nGMM1 values. The gaugino masses are predicted to be in the  $1.5 - 2 \text{ TeV}$  range with an 9-10% uncertainty as plotted in Fig. 7.49. These fit results are in agreement with the prediction from the pMSSM-10 fit that a high  $e^+e^-$  centre-of-mass energy of about 2 TeV would be required to produce the unobserved gauginos in associated production with one of the light higgsinos.

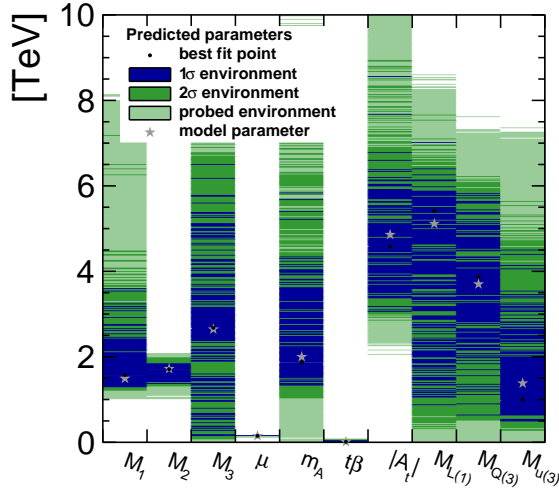


Figure 7.46: Fitted parameters in pMSSM-10 fit to nGMM1 observables with mass differences. Here  $\tan \beta$  is plotted as if it was in GeV.

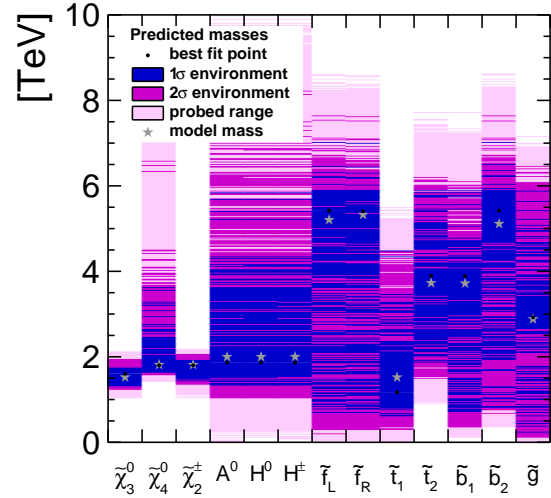


Figure 7.47: Fitted masses in pMSSM-10 fit to nGMM1 observables with mass differences.

parameter	nGMM1 pMSSM true	best fit point	$1\sigma$ CL	$2\sigma$ CL
$M_1$	1493	1573	+2091 -282	+5650 -344
$M_2$	1720	1710	+137 -313	+277 -394
$\mu$	150.0	149.9	+11.5 -3.4	+15.3 -4.2
$\tan \beta$	10.0	11.2	+32.5 -3.4	+63.9 -4.2
$m_A$	2000	1868	+4018 -567	+6423 -867
$M_3$	2646	2677	+3892 -2541	+4550 -2614
$M_{L(3)}$	5115	5412	+1629 -4581	+2319 -5118
$M_{U(3)}$	1381	996	+3540 -500	+4686 -741
$M_{Q(3)}$	3701	3874	+1983 -3245	+2356 -3370
$A_t$	-4857	-4582	+1558 -4006	+1750 -4390
$\chi^2$	0.00041	0.0668		

Table 7.29: Fitted parameters in the pMSSM-10 fit to nGMM1 observables including mass differences instead of masses.

prediction	nGMM1 All SUSY mass diff+h		
	best fit	1 $\sigma$ CL	2 $\sigma$ CL
$m_{\tilde{\chi}_3^0}$	1603	+149 -283	+347 -349
$m_{\tilde{\chi}_4^0}$	1802	+1834 -146	+2710 -218
$m_{\tilde{\chi}_2^\pm}$	1801	+137 -349	+275 -433
$m_{H_0}$	1868	+3992 -528	+6372 -828
$m_{A_0}$	1868	+3992 -528	+6372 -828
$m_{H^\pm}$	1863	+3997 -523	+6377 -823
$m_{\tilde{u}_L}$	5421	+1619 -4721	+2239 -5221
$m_{\tilde{u}_R}$	5408	+1612 -4708	+2232 -5108
$m_{\tilde{t}_1}$	1168	+3332 -548	+3332 -868
$m_{\tilde{t}_2}$	3894	+2026 -2014	+2326 -2394
$m_{\tilde{b}_1}$	3888	+2032 -3168	+2232 -3528
$m_{\tilde{b}_2}$	5419	+1621 -4599	+2241 -4739
$m_{\tilde{g}}$	2924	+2976 -2684	+3556 -2804

Table 7.30: nGMM1 fitted masses in the pMSSM-10 fit with the higgsino mass differences replacing the  $\tilde{\chi}_2^0$  and  $\tilde{\chi}_1^\pm$  masses as observables. The fit length was  $10^6$  points.

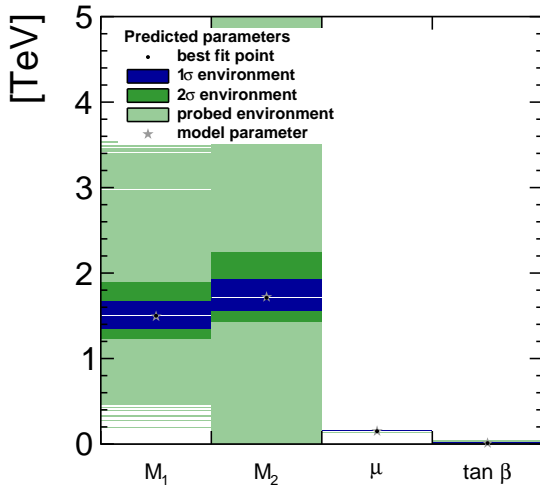


Figure 7.48: Fitted parameter confidence ranges for nGMM1 pMSSM-4 parameters. Here  $\tan\beta$  is plotted as if it was in GeV.

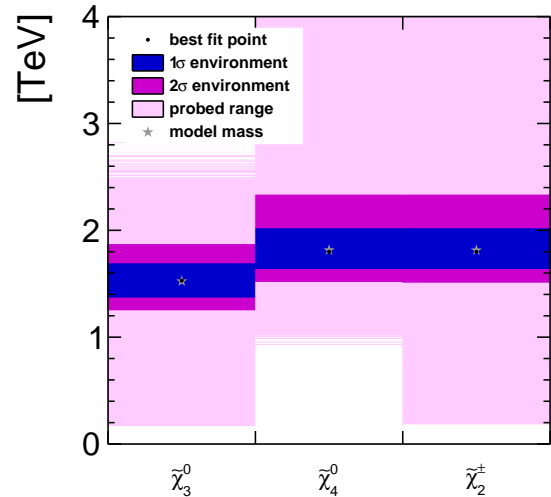


Figure 7.49: Fitted masses in pMSSM-4 fit to nGMM1 observables.

### 7.6.9 Effect of fit input precisions

Direct comparisons were not presented here for results from parameter fits to the same benchmark observables but with differing experimental precisions. However, some guidance on the importance of the input precisions can be gained by comparing the presented results to those in Ref. [276]. Those results are based on the same benchmark scenarios as the results in this chapter but they are based on more optimistic estimates of the SUSY measurement precisions. It turned out that after considering all effects, the measurement precisions are  $\sim 0.45\%$  rather than  $0.20\%$  for ILC1 higgsino masses in the H20 scenario. Another difference between the two sets of results is that the Markov Chain was only  $10^5$  points long, so a direct comparison is not possible due to the additional uncertainty caused by the limited Markov Chain.

Nevertheless, making the simplistic comparison of the ILC1 pMSSM-10 fit results in this thesis and in Ref. [276] shows that the better ILC measurements would benefit the SUSY parameter determination. The bino and wino mass parameters  $M_1$  and  $M_2$  are determined with  $1 - 2\%$  in Ref. [276], while here the precisions are  $5-6\%$ . Of the observables for example the gaugino masses are predicted with a  $2\%$  uncertainty with the optimistic higgsino measurement precisions, while the results here indicate a  $5-6\%$  uncertainty. This correlation between the measurement precisions and the fit results is in accordance with the conclusion in Ch. 6 on the importance of the precision of the SUSY fit inputs in stau coannihilation models. Thus, it is crucial to aim for the highest possible experimental precision on the properties of accessible SUSY particles in order to utilise the predictive power of the parameter fits to the full extent.

### 7.6.10 Dark matter in higgsino fits

In all of the previously discussed pMSSM fits, the relic density was calculated for each probed SUSY parameter point. The cosmologically observed relic density was not used to constrain the fit, so it is interesting to see whether the fits predict the higgsino benchmark relic density correctly. As discussed above, the ILC1, ILC2 and nGMM1 benchmarks the model relic density is only  $3-5\%$  of the observed relic density. The fitted relic density is scaled by the model relic density in order to be able to compare the different benchmarks directly.

The fitted and scaled relic density is plotted and  $2\sigma$  confidence interval is extracted. Then the centre of the  $2\sigma$  confidence level is calculated and used as the mean. The width of the  $2\sigma$  range is divided by two to obtain the  $1\sigma$  width assuming the  $\Delta\chi^2$  distribution is parabolic. The distributions are more flat than parabolic so this procedure gives a conservative estimate of the  $1\sigma$  width. Then a Gaussian is plotted.

The relic density distribution from each fit is plotted in Fig. 7.50. It can be read from this figure, that under some conditions, the relic density is predicted correctly and accurately by the fit. These conditions are that either only pMSSM-4 is fitted and the other six parameters are fixed to model values, or gluino mass is required to be greater than  $200$  GeV. For example in the ILC1 fit, the number of points within the  $2\sigma$  range from the fit minimum and with gluino mass less than  $200$  GeV is  $7676$ . In the pMSSM-10 fits the low allowed gluino values come with a low relic density, and

therefore a wide range of relic densities is allowed if the cut is not applied, as can be seen from the figure.

Quantitatively, the results are similar for all benchmarks as can easily be seen from Fig. 7.50. In the pMSSM-10 fits, excluding the points with gluino mass less than 200 GeV, the relic density is predicted correctly within 2% of the model value for all the benchmarks. The relative uncertainty of the relic density prediction in these fits is 4.1% for ILC1, 3.5% for ILC2 and 2.0% for nGMM1.

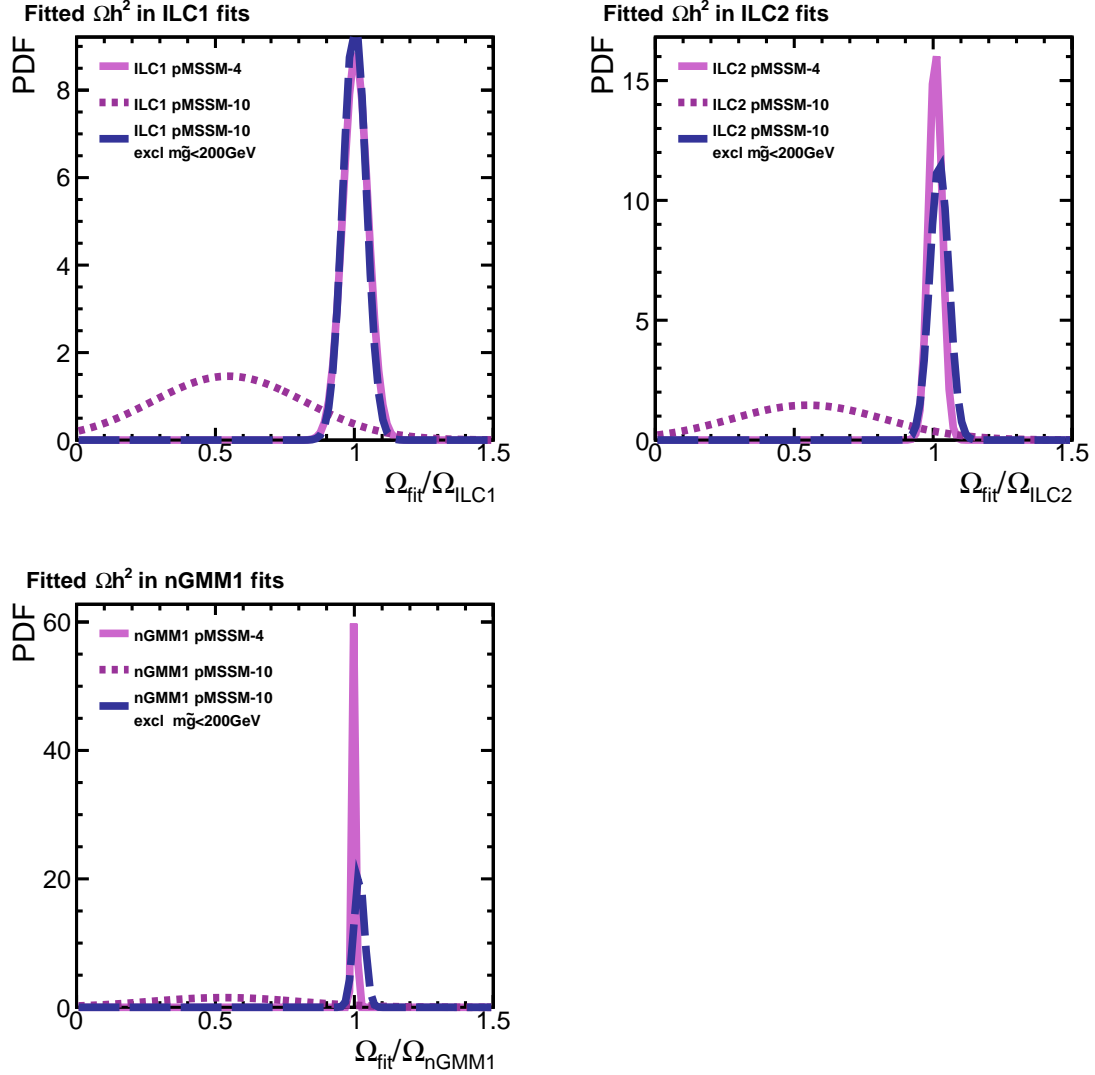


Figure 7.50: Fitted relic densities in pMSSM fits to ILC1, ILC2 and nGMM1 observables.

In the pMSSM-10 fits to ILC1, ILC2 and nGMM1 observables, predictions for the direct and indirect detection cross sections can be made. The results are listed in Tab. 7.31 along with the benchmark values. It can be seen that the predictions agree with the benchmark values within the  $1\sigma$  uncertainty of the best fit cross section. The uncertainties in each case are small, except for the indirect detection cross section  $\langle\sigma v\rangle$  in the ILC2 and nGMM1 fits, where the upper bound is extended. However, this is not important as the order of magnitude for each of the predicted values is correct.

observable	ILC1	ILC2	nGMM1
$\sigma^{SI}$ model [ $10^{-9}$ pb]	259.3	316.9	328.5
$\sigma^{SI}$ best fit [ $10^{-9}$ pb]	$260.7_{-6.9}^{+4.1}$	$317.0_{-2.1}^{+2.1}$	$328.5_{-0.9}^{+1.5}$
$\langle\sigma v\rangle$ model [ $10^{-27}$ cm <sup>3</sup> s <sup>-1</sup> ]	15.36	3.439	0.597
$\langle\sigma v\rangle$ best fit [ $10^{-27}$ cm <sup>3</sup> s <sup>-1</sup> ]	$15.01_{-0.88}^{+1.52}$	$3.501_{0.523}^{+5.741}$	$0.621_{-0.165}^{+0.994}$

Table 7.31: Relic density from **MicrOMEGAs** and **Astrofit**, and direct and indirect detection cross sections from **Astrofit** in the pMSSM-10 fits to ILC1, ILC2 and nGMM1 observables (without the gluino mass observation).  $\Omega_{\text{Planck}}$  is 0.1199 [28].

Thus, the ILC measurements would be accurate enough for guiding what the direct and indirect detection prospects of the observed SUSY particles would or should be.

## 7.7 Testing gaugino mass unification

The pMSSM parameters fitted in the previous sections were fitted at the 1 TeV energy scale. The scale dependence of the parameters is governed by the Renormalisation Group Equations, which were discussed in Sec. 2.4. Thus the fitted parameters can be evolved to higher energy scales in order to check whether they unify.

### 7.7.1 Method

The running parameters are calculated with **SPheno3.3.9beta** in the same way as in Sec. 6.7. The results of the fitted parameters are used to generate distributions of each of the 10 running parameters at 1 TeV scale. These distributions are sampled randomly  $10^4$  times. The used distributions for ILC1 and ILC2 are Gaussians for  $M_1$  and  $M_2$  and from a uniform distribution for  $M_3$  corresponding to the  $1\sigma$  range for the determined parameter from the corresponding pMSSM-10 fit. For nGMM1 the  $M_1$  and  $M_3$  distributions are uniform and  $M_2$  a Gaussian. Then a Les Houches file is generated for each of these toy points and **SPheno** is executed.

The running parameters are extracted from the **SPheno** output files for 21 different energy scales from 91 GeV to  $10^{19}$  GeV. A distribution of each running parameter for each of these energy scales is plotted and the standard deviation is extracted for the width. Then the running parameters are plotted, with coloured bands highlighting the found confidence intervals.

The unification scale is found by fitting a line to the running parameters. The fitted range is  $10^{10}$  GeV to  $10^{18}$  GeV. The crossing point of the line is found and the energy scale and  $M_1 = M_2 = M_{1/2}$  is plotted. Then Gaussians can be fitted to these distributions to see whether there is indeed unification of  $M_1$  and  $M_2$  or not.

Using the extracted  $M_{1/2}$  and unification scale combinations, Les Houches files are created based on an NUHM2 model. Parameters other than  $M_{1/2}$  take the model

values, even though these are not extracted from the parameter fit. Then the running of  $M_3$  and the gluino mass are calculated. This allows to see whether predictions for  $M_3(Q = 1 \text{ TeV})$  and the gluino mass can be made.

### 7.7.2 ILC1 running

The running of the gaugino mass parameters in the ILC1 pMSSM-10 fit is plotted in Fig. 7.51. It can be seen that  $M_1$  and  $M_2$  cross near  $10^{16}$  GeV. The uncertainty band for  $M_3$  is so wide that it is not possible to say whether all three parameters unify at the same energy scale.

The extracted  $M_1$  and  $M_2$  unification scales are plotted in Fig. 7.51 from which it can be seen that the distributions follow a Gaussian. The gaugino mass unification scale is found to be  $3.8 \times 10^{16}$  GeV with a 68% confidence range of  $[3.0 \times 10^{15}, 4.9 \times 10^{17}]$  GeV as can be read from Fig. 7.53. The same figure shows that the unified mass parameter is found to be  $583 \pm 40$  GeV, correspond to the model value. This gives the expectation that the observed higgsinos may be inherited from a GUT scale SUSY model assuming that there is no further new physics up to the GUT scale.

If it is assumed that the unification is due to an NUHM2 model, and true model parameter values are assumed for parameters other than  $M_{1/2}$ , then  $M_3$  can be extrapolated down to find a value of  $M_3$  at 1 TeV. Simultaneously a prediction for the gluino mass is obtained:  $m_{\tilde{g}} = 1467 \pm 80$  GeV and  $M_3(Q = 1 \text{ TeV}) = 1216 \pm 76$  GeV, which agree with the model values.

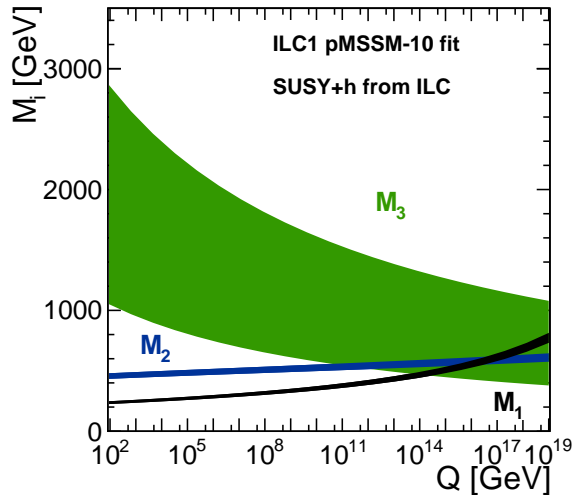


Figure 7.51: The scale-dependence of the gaugino mass parameters based on the pMSSM-10 fit to ILC1 observables. The gluino observation is not assumed in the fit. The bands correspond to one standard deviation.

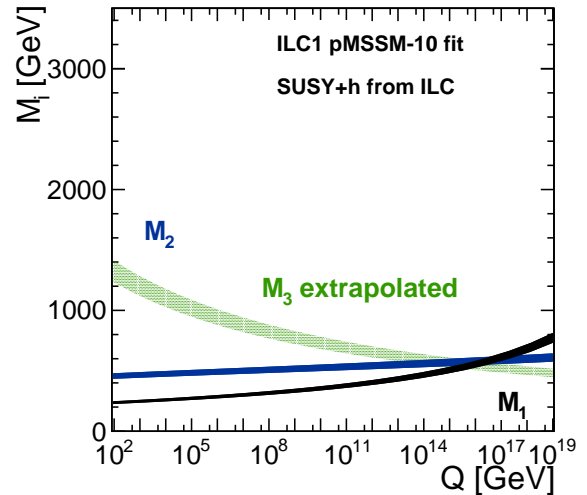


Figure 7.52: The  $M_i$  based on the pMSSM-10 fit to ILC1 observables.  $M_3$  was extrapolated down assuming the unification of all three  $M_i$ .

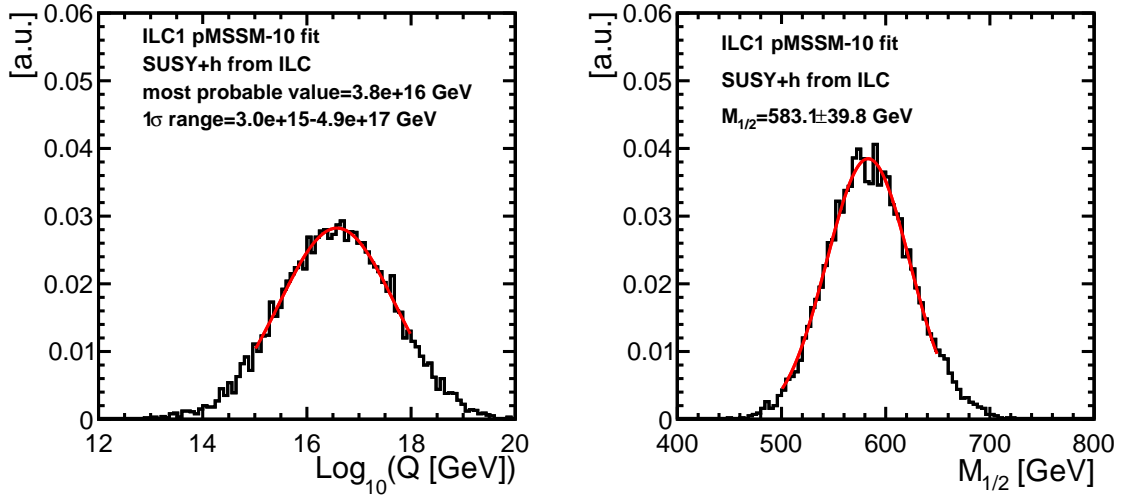


Figure 7.53: The extracted unification scale  $Q$  and  $M_{1/2}$  from the running parameters  $M_1$  and  $M_2$ , which were obtained based on the fit results from the pMSSM-10 to ILC1 observables not including the gluino mass.

### 7.7.3 ILC2 running

The uncertainties of the gaugino mass parameters were larger in ILC2 than in ILC1. This is reflected in the running plot in Fig. 7.54, from which it is nevertheless possible to verify that  $M_1$  and  $M_2$  unify. The band for  $M_3$  is so wide that it could unify with  $M_1$  or  $M_2$  at almost any scale.

In the same way as above, the unification scale for  $M_1 = M_2$  is found to be Gaussian with a mean of  $1.5 \times 10^{16}$  GeV with a 68% confidence interval  $[5.4 \times 10^{13}, 4.4 \times 10^{18}]$  GeV - see Fig. 7.56. The unified value  $M_{1/2}$  is found to be Gaussian with  $M_{1/2} = 1220 \pm 170$  GeV, which corresponds to the model value. There would then be motivation for expecting the higgsinos to originate from a GUT model.

If  $M_3$  is assumed to unify with  $M_1$  and  $M_2$ , and a NUHM2 model is taken, then the extrapolated  $M_3$  at 1 TeV is  $M_3(Q = 1 \text{ TeV}) = 2616 \pm 582$  GeV and  $m_{\tilde{g}} = 2872 \pm 605$  GeV, which agree with the model values within  $1\sigma$ .

### 7.7.4 nGMM1 running

The running of the gaugino mass parameters in nGMM1 differs from the running of ILC1 and ILC2 parameters. There are two reasons. One is that the model is a mirage model, where the gaugino mass parameters unify at an intermediate energy scale. The second reason is that the determination of  $M_1$  and  $M_2$  is much less accurate in nGMM1 than in the other two benchmarks. Thus the resulting running plot in Fig. 7.57 it is harder to draw a conclusion on the possible unification of  $M_i$ .

The expectation from the benchmark is that  $M_i$  unify at  $10^7$  GeV but the extracted unification scale shows an increasing likelihood as the scale approaches zero. This can be seen from Fig. 7.58. It can be determined that unification at  $10^{16}$  GeV is

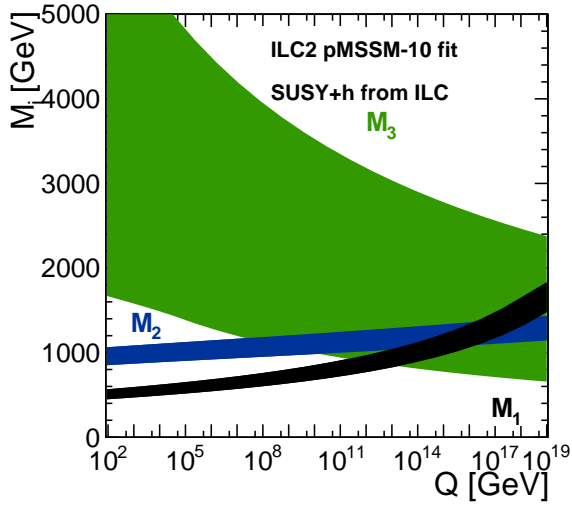


Figure 7.54: The extracted gaugino mass parameters in the pMSSM-10 fit to ILC2 observables not including the gluino mass. The bands correspond to one standard deviation.

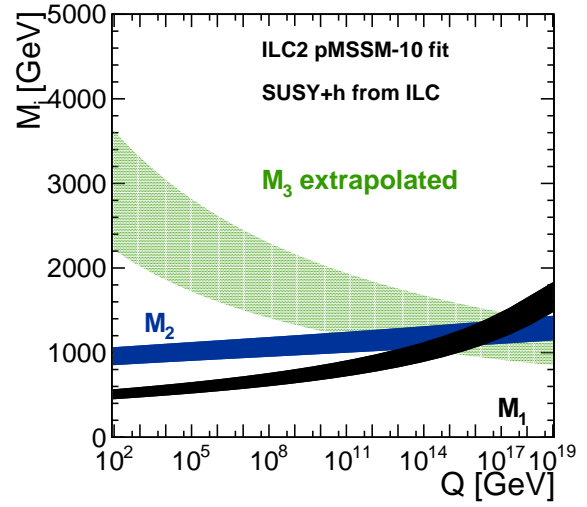


Figure 7.55: The  $M_i$  based on the pMSSM-10 fit to ILC2 observables.  $M_3$  was extrapolated down assuming the unification of  $M_1$  and  $M_2$ .

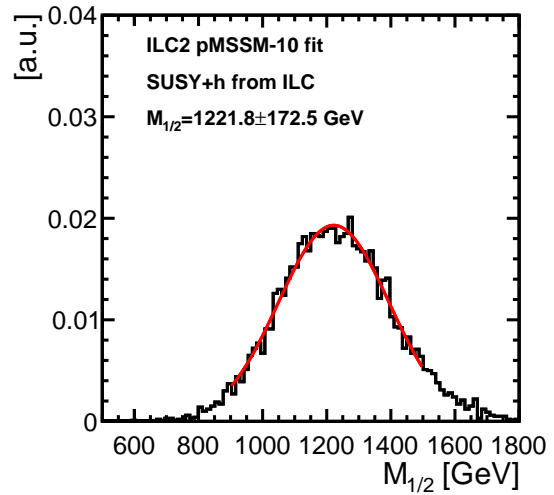
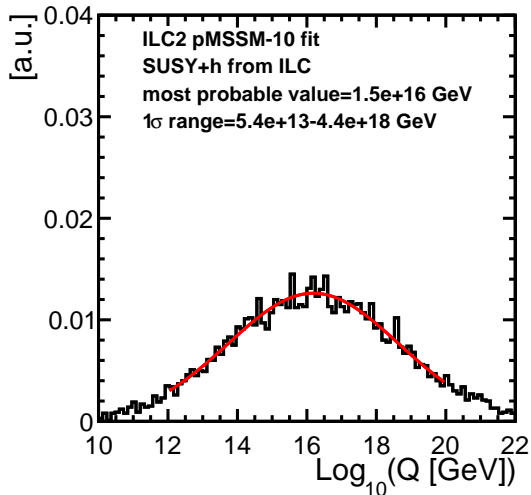


Figure 7.56: The extracted unification scale  $Q$  and  $M_{1/2}$  from the running parameters  $M_1$  and  $M_2$ , which were obtained based on the fit results from the pMSSM-10 to ILC2 observables.

excluded with 99.9% probability as only a fraction 1 : 1000 points were found where the determined unification scale is higher than  $10^{16}$  GeV. The most probable unified value of  $M_{1/2}$  is  $1600 \pm 450$  GeV. Due to the extracted gaugino mass unification scale not matching with the GUT scale, there would be great implications for SUSY model building. It is noteworthy that the pMSSM fit and the fit parameter evolution indicate that the underlying model does not have gaugino mass unification, even though the fit of NUHM2 parameters to the nGMM1 observables did not rule NUHM2 out as a possible model.

Sufficient measurement precision is required for the SUSY parameter fit inputs to enable a precise extraction of  $M_1$  and  $M_2$  at 1 TeV. In order to try to recover the correct  $10^7$  GeV gaugino mass unification scale, a few improvements could be made. First of all, in the above case, only the higgsino mass measurements and Higgs measurements were used. It was seen in the above sections that using higgsino mass differences instead of higgsino masses as observables would improve the determination of  $M_2$ , decreasing the uncertainty on the running  $M_2$  values. In addition, threshold scans could be used to attempt to improve the higgsino measurement precisions. Furthermore, LHC and flavour physics bounds, as well as electroweak precision measurements could be used as fit inputs, with the expectation that the precisions on the fitted parameters would increase.

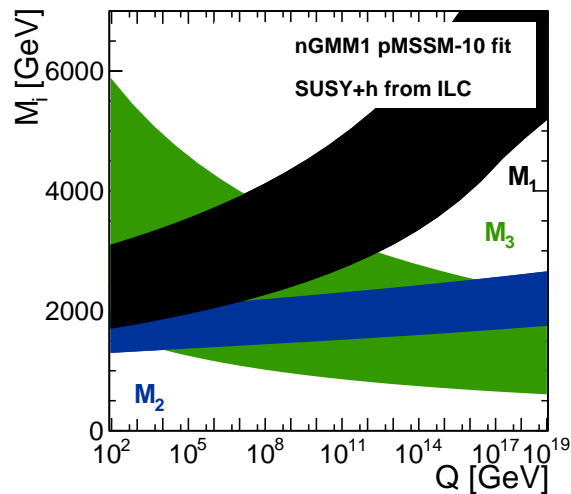


Figure 7.57: The extracted gaugino mass parameters in the pMSSM-10 fit to nGMM1 observables. The bands correspond to one standard deviation.

## 7.8 Outlook

There are great prospects for determining SUSY parameters in NUHM2 and pMSSM-10 based on ILC higgsino and Higgs observations. It is crucial that the precisions of the SUSY mass and cross section measurements are as accurate as possible. The importance increases as the higgsino mass difference decreases, and it was found beneficial to use the mass difference measurements instead of the mass measurements. Predictions

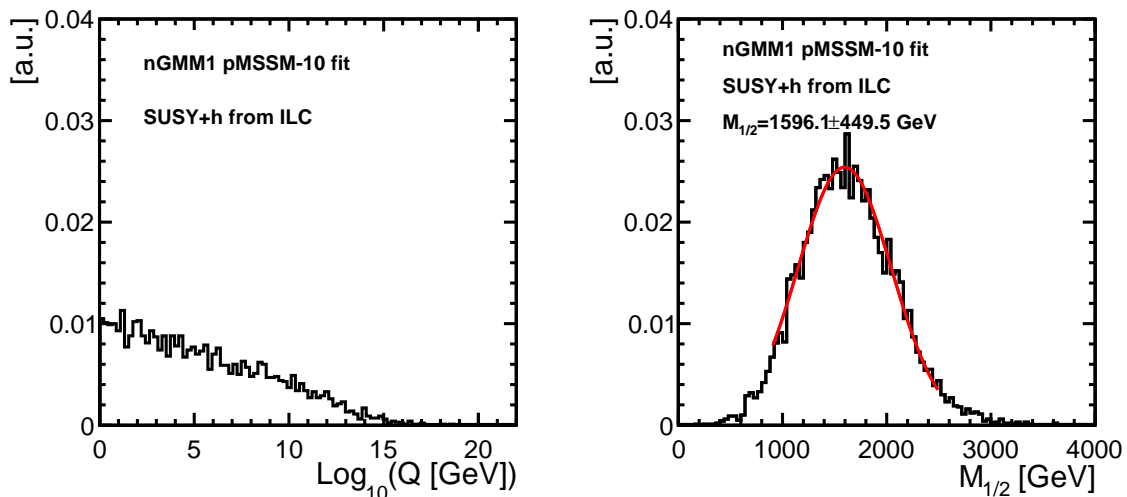


Figure 7.58: The extracted unification scale  $Q$  and  $M_{1/2}$  from the running parameters  $M_1$  and  $M_2$ , which were obtained based on the fit results from the pMSSM-10 to nGMM1 observables.

for heavy particle properties can be made. The dark matter properties of the LSP can be predicted correctly if the gluino exclusion from the LHC is taken into account. The renormalisation group evolution of the fitted gaugino mass parameters gives insight on the high-scale behaviour of the underlying model, both in the case that the SUSY observations originate from a model with gaugino mass unification at the GUT scale or at a lower scale.

As further work, it would be interesting to check explicitly what impact improving the higgsino measurements from the current expected precisions would have on the results of the SUSY parameter fits. In addition, it would be useful to verify what contribution the Higgs observables have on the SUSY parameter fits. In all cases, it would be important to ensure that the parameter space is explored to the full necessary extent.

Further constraints on the SUSY parameters could be gained and therefore improved predictions for the heavy, unobserved sparticles could be made by including limits from other kinds of experiments. For example, the gluino mass limit or measurement from the LHC or the HL-LHC would bring further constraints. Additionally, flavour observables and electroweak precision observables, such as the top quark mass could be used.



# Chapter 8

## Conclusion

If supersymmetric (SUSY) particles were to exist with masses accessible at a centre-of-mass energy of 500 GeV, then an  $e^+e^-$  collider like the International Linear Collider (ILC) could measure the mass and cross section times branching fractions of the SUSY particles with high precision. In this thesis, the results of hypothetical measurements of supersymmetric particles from the ILC were used as inputs for fitting the SUSY parameters of different kinds of GUT-scale and weak scale SUSY models. The fits were performed with `Fittino`, with the following questions in mind: Is the precision of the ILC SUSY measurement enough to determine the underlying SUSY model and its parameters? Which parameters can be determined? What predictions can be made about unobserved SUSY particles? Can the relic density be calculated based on the observations? What is the significance of precision Higgs measurements for the SUSY parameter determination? The latest theory predictions for the SUSY and Higgs observables were used in the fits.

Two types of scenario were considered in this thesis: stau coannihilation and light higgsino scenarios. The common theme between the two types of scenario is that they are challenging for the LHC to discover as the signal is present with lots of missing energy and only a small amount of visible energy. This leaves some corners of model space for the ILC to uncover. If such SUSY particles were discovered, then the ILC could be used to measure the particle masses and polarised cross sections with percent-level or better precision in the 20-year operating scheme.

In the stau coannihilation scenarios, all sleptons, sneutrinos and gauginos are assumed to be measured at the ILC with  $\sqrt{s} = 500$  GeV. With the assumed ILC observations, `Fittino` fits were performed on CMSSM, NUHM1 and NUHM2 parameters as well as a pMSSM-13 model. Four different benchmarks were considered: the physical spectrum of sparticles is similar but the relic density is different in three benchmarks. The fourth one was designed to avoid the LHC exclusion limits on left-handed sleptons. The fit inputs include all the SUSY mass measurements, some polarised cross section measurements and the ILC measurements on the Higgs mass and Higgs branching fractions. It was concluded that in these scenarios, GUT-type models would be excluded by the ILC measurements. In the pMSSM-13 fit, it was found that the permille-level precision on the SUSY particle observables and the Higgs observables is sufficient to constrain the full supersymmetric spectrum to some extent. Sensitivity can be seen to SUSY parameters which contribute to the observables at loop level, and predictions

for heavy, unobserved SUSY particles can be made. It was concluded that the precision measurements from the International Linear Detector are crucial, and that any changes in the experimental precisions are reflected on the quality of the parameter fit results. It was found that the dark matter relic density can only be predicted if the ILC Higgs measurements are used along with the SUSY measurements.

It was additionally found that the dark matter relic density can be calculated in the aforementioned stau coannihilation scenario with saturated relic density, from the SUSY masses alone if both the LSP and stau masses are known to the expected permille precision and their mixing factors to the optimistic 1% precision, and some percent-level measurements are made of the masses of other gauginos and sleptons. The prediction of the dark matter relic density has an uncertainty comparable to the current precision on the relic density from the Planck experiment. If the heavy Higgs sector is not measured, then the predicted value of the relic density is slightly reduced with respect to the model value, although leaving very little room for other types of dark matter than the LSP.

For the higgsino scenario, the study is motivated by arguments about the fine-tuning of the  $Z$ -boson mass. Naturalness leads to the conclusion that light higgsinos should exist below 300 GeV. In the three scenarios considered in this thesis, only three higgsinos are observable and the rest of the spectrum is heavy, apart from the gauginos which may be within the LHC reach with the HL-LHC data set. Three different scenarios were studied where the higgsinos have mass differences of 3-20 GeV. The benchmarks originate from GUT scale models: two benchmarks from NUHM2 and one from mirage unification.

The GUT models CMSSM, NUHM1 and NUHM2 were fitted to the three benchmarks. Additionally pMSSM-10 was fitted. The experimental inputs include the ILC higgsino mass measurements, polarised higgsino cross section times branching fraction measurements as well as the ILC Higgs mass and branching fraction inputs. The results of the fits show that permille-level precision is essential for the higgsino measurements in order to be able to constrain the SUSY parameters. In this case, predictions for the masses of unobserved heavy sparticles can be made, and the dark matter relic density can be predicted correctly as long as the LHC exclusion limit on the gluino mass is taken into account. It is especially important to have precise measurements of the higgsinos if the higgsino masses are close to each other. In this regime, it is found to be useful to replace the higgsino mass measurement inputs with mass difference inputs. The higgsino fit results show also that the dark matter content of the universe is not filled by the higgsinos as is designed in the model. If the higgsinos were observed then, via the SUSY parameter fits, it would be clear that other kinds of DM such as axions need to exist or assumptions about the standard cosmology used in the relic density calculator are not correct.

The fitted parameters in the higgsino model were evolved to the GUT scale via the renormalisation group running, assuming no other new physics exists between the SUSY scale and the GUT scale. The hypothesis of gaugino mass unification can be tested, provided that the parameters were determined accurately enough, which hinges on the accuracy of the experimental inputs.

Further work is required to ensure that the fit is probing the SUSY parameter space

---

sufficiently precisely. This will get easier as computing resources are expected to get larger and the parameter scanning methods will get more sophisticated, as is planned by the `Fittino` collaboration. If SUSY particles were discovered, then significant effort would be needed to obtain a consistent calculation of the SUSY particle properties from the SUSY parameters, and of the Higgs mass and branching fractions in SUSY, as there currently are discrepancies of a few GeV in the predictions from different calculators. Also, uncertainties induced by the renormalisation of the SUSY parameters should be taken into account and solved consistently between different benchmarks.

First and foremost, though, the focus should be on discovering or excluding supersymmetric particles, for which the ILC would be a magnificent machine. The work in this thesis shows that a significant amount of information could be extracted from SUSY measurements, provided that the particle masses and cross sections are measured with percent or sub-percent precision, as is currently expected in the 20-year operation scheme of the ILC. Fitting SUSY parameters to these measurements would provide information on the unobserved SUSY particles, which in turn would give guidance as to what collider experiments to build next. Furthermore, synergies between the collider and other dark matter experiments may be gained as the ILC measurements would, under certain circumstances, allow us to find the dark matter relic density of the lightest SUSY particle. Who can argue that the ILC should not be built?



# Appendix A

## Tree-level estimates of SUSY parameters

It is possible to estimate SUSY parameters from sparticle masses and chargino mixing angles [246, 274] using tree-level equations.

Below is a representation of the procedure implemented in `Fittino` [201]. The order of calculation is important as some equations depend on others. First,  $\tan \beta$ ,  $M_2$ ,  $|\mu|$ , and  $Sign(\mu)$ , are determined from chargino mixing angles  $\cos 2\phi_{R,L}$ ,  $\tilde{\chi}_1^\pm$ ,  $\tilde{\chi}_2^\pm$ , and  $W$ -boson masses following [268]:

$$\tan \beta = \left( \frac{1 + \Delta(\cos 2\phi_R - \cos 2\phi_L)}{1 - \Delta(\cos 2\phi_R - \cos 2\phi_L)} \right)^{\frac{1}{2}}, \quad (\text{A.1})$$

and

$$\mu = m_W(\Sigma + \Delta(\cos 2\phi_L + \cos 2\phi_R)), \quad (\text{A.2})$$

where

$$\Sigma = \frac{m_{\tilde{\chi}_2^\pm}^2 + m_{\tilde{\chi}_1^\pm}^2}{2m_W^2} - 1, \quad (\text{A.3})$$

and

$$\Delta = \frac{m_{\tilde{\chi}_2^\pm}^2 - m_{\tilde{\chi}_1^\pm}^2}{4m_W^2}. \quad (\text{A.4})$$

$M_2$  is given by

$$M_2 = m_W \sqrt{\Sigma - \Delta(\cos 2\phi_L - \cos 2\phi_R)}, \quad (\text{A.5})$$

after which  $Sign(\mu)$  can be calculated as

$$sign\mu = \frac{\left( m_{\tilde{\chi}_2^\pm}^2 - m_{\tilde{\chi}_1^\pm}^2 \right)^2 - M_2^2 - |\mu|^2 - 4m_W^2(M_2^2 + |\mu|^2) - 4m_W^4 \cos^2 2\beta}{8m_W^2 M_2 |\mu| \sin 2\beta}. \quad (\text{A.6})$$

Then  $M_1$  is calculated directly from the characteristic equation of the neutralino mass matrix squared  $M_1 = M_1(m_{\tilde{\chi}_1^0}, M_2, \mu, m_Z, \cos \beta, \sin \beta, \sin \theta_W)$  [277] i.e. `Fittino` uses

only the LSP mass to calculate a value for  $M_1$  even though it could use all the neutralino masses.

$M_3$  at tree level is simply given by the gluino mass,  $M_3 = m_{\tilde{g}}$ . The equations for the sfermion mass parameters depend on  $\tan\beta$ , the corresponding sfermion and fermion mass, and  $m_Z$  and  $\sin^2\theta_W$  [278]. All of the equations are listed below for completeness.

$$M_{\tilde{e}_L} = \sqrt{m_Z^2 \cos(2\beta) \left(\frac{1}{2} - \sin^2\theta_W\right) - m_e^2 + m_{\tilde{e}_L}^2}, \quad (\text{A.7})$$

$$M_{\tilde{e}_L} = \sqrt{m_Z^2 \cos(2\beta) \left(\frac{1}{2} - \sin^2\theta_W\right) - m_e^2 + m_{\tilde{e}_L}^2}, \quad (\text{A.8})$$

$$M_{\tilde{e}_R} = \sqrt{m_Z^2 \cos(2\beta) (-\sin^2\theta_W) - m_e^2 + m_{\tilde{e}_R}^2}, \quad (\text{A.9})$$

$$M_{\tilde{\mu}_L} = \sqrt{m_Z^2 \cos(2\beta) \left(\frac{1}{2} - \sin^2\theta_W\right) - m_{\mu}^2 + m_{\tilde{\mu}_L}^2}, \quad (\text{A.10})$$

$$M_{\tilde{\mu}_R} = \sqrt{m_Z^2 \cos(2\beta) (-\sin^2\theta_W) - m_{\mu}^2 + m_{\tilde{\mu}_R}^2}, \quad (\text{A.11})$$

$$M_{\tilde{\tau}_L} = \sqrt{m_Z^2 \cos(2\beta) \left(\frac{1}{2} - \sin^2\theta_W\right) - m_{\tau}^2 + m_{\tilde{\tau}_L}^2}, \quad (\text{A.12})$$

$$M_{\tilde{\tau}_R} = \sqrt{m_Z^2 \cos(2\beta) (-\sin^2\theta_W) - m_{\tau}^2 + m_{\tilde{\tau}_R}^2}, \quad (\text{A.13})$$

$$M_{\tilde{u}_L} = \sqrt{m_Z^2 \cos(2\beta) \left(\frac{1}{2} - \frac{2}{3} \sin^2\theta_W\right) + m_{\tilde{u}_L}^2}, \quad (\text{A.14})$$

$$M_{\tilde{c}_L} = \sqrt{m_Z^2 \cos(2\beta) \left(\frac{1}{2} - \frac{2}{3} \sin^2\theta_W\right) + m_{\tilde{c}_L}^2}, \quad (\text{A.15})$$

$$M_{\tilde{t}_L} = \sqrt{m_Z^2 \cos(2\beta) \left(\frac{1}{2} - \frac{2}{3} \sin^2\theta_W\right) - m_t^2 + m_{\tilde{t}_L}^2}, \quad (\text{A.16})$$

$$M_{\tilde{u}_R} = \sqrt{m_Z^2 \cos(2\beta) \left(-\frac{2}{3} \sin^2\theta_W\right) + m_{\tilde{u}_R}^2}, \quad (\text{A.17})$$

$$M_{\tilde{c}_R} = \sqrt{m_Z^2 \cos(2\beta) \left(-\frac{2}{3} \sin^2\theta_W\right) + m_{\tilde{c}_R}^2}, \quad (\text{A.18})$$

$$M_{\tilde{t}_R} = \sqrt{m_Z^2 \cos(2\beta) \left(-\frac{2}{3} \sin^2\theta_W\right) - m_t^2 + m_{\tilde{t}_R}^2}, \quad (\text{A.19})$$

---


$$M_{\tilde{d}_R} = \sqrt{m_Z^2 \cos(2\beta) \left(-\frac{1}{3} \sin^2 \theta_W\right) + m_{\tilde{d}_R}^2}, \quad (\text{A.20})$$

$$M_{\tilde{s}_R} = \sqrt{m_Z^2 \cos(2\beta) \left(-\frac{1}{3} \sin^2 \theta_W\right) + m_{\tilde{s}_R}^2}, \quad (\text{A.21})$$

$$M_{\tilde{b}_R} = \sqrt{m_Z^2 \cos(2\beta) \left(-\frac{1}{3} \sin^2 \theta_W\right) - m_b^2 + m_{\tilde{b}_2}^2}. \quad (\text{A.22})$$

The trilinear couplings are initialised roughly, e.g. for the top trilinear  $X_t = A_t - \mu/\tan\beta$  [278] setting  $A_t$  to zero. This leads to

$$X_\tau = \mu \tan \beta, \quad (\text{A.23})$$

$$X_t = \mu/\tan \beta, \quad (\text{A.24})$$

and

$$X_b = \mu \tan \beta. \quad (\text{A.25})$$



# Appendix B

## Example files

### B.1 Les Houches input file for SPheno with STC10' parameters

```
BLOCK MODSEL
  1  0 # General MSSM
  3  0 # MSSM particle content
 12  1.000000e+03 # Q_EWSB (fixed)
BLOCK SMINPUTS
  1  1.279340e+02 # 1/alpha_em(M_Z) (fixed)
  2  1.166390e-05 # G_F
  3  1.172000e-01 # alpha_s (fixed)
  4  9.118750e+01 # mZ (fixed)
  5  4.200000e+00 # mb(mb) (fixed)
  6  1.731000e+02 # mtop (fixed)
  7  1.777000e+00 # mtau (fixed)
 24  1.270000e+00 # mcharm (fixed)
BLOCK MINPAR
  3  1.000000e+01 # TanBeta
BLOCK EXTPAR
  0  1000. # Input scale for mSUGRA
  1  1.000000e+02 # M1
  2  2.100000e+02 # M2
  3  2.000000e+03 # M3
 11 -2.850000e+03 # Atop
 12 -2.850000e+03 # Abottom
 13 -2.850000e+03 # Atau
 23  4.000000e+02 # mu
 26  4.000000e+02 # mA
 31  2.070000e+02 # MSelectronL
 32  2.070000e+02 # MSmuL
 33  2.070000e+02 # MStauL
 34  1.180000e+02 # MSelectronR
```

```

35 1.180000e+02 # MSmuR
36 1.180000e+02 # MStauR
41 2.000000e+03 # MSupL
42 2.000000e+03 # MScharmL
43 1.450000e+03 # MStopL
44 2.000000e+03 # MSupR
45 2.000000e+03 # MScharmR
46 1.100000e+03 # MStopR
47 2.000000e+03 # MSdownR
48 2.000000e+03 # MSstrangerR
49 1.000000e+03 # MSbottomR
BLOCK SPHENOPINPUT
  1 0 # error level
  2 0 # if 1, then SPA conventions are used
11 1 # calculate branching ratios
12 1.00000000E-04 # write only branching ratios larger than this value
21 1 # calculate cross section
22 5.000000e+02 # cms energy in GeV
23 -8.000000e-01 # polarisation of incoming e- beam
24 -3.000000e-01 # polarisation of incoming e+ beam
25 1 # ISR is calculated
22 5.000000e+02 # cms energy in GeV
23 8.000000e-01 # polarisation of incoming e- beam
24 3.000000e-01 # polarisation of incoming e+ beam
25 1 # ISR is calculated
22 5.000000e+02 # cms energy in GeV
23 -8.000000e-01 # polarisation of incoming e- beam
24 3.000000e-01 # polarisation of incoming e+ beam
25 1 # ISR is calculated
22 5.000000e+02 # cms energy in GeV
23 8.000000e-01 # polarisation of incoming e- beam
24 -3.000000e-01 # polarisation of incoming e+ beam
25 1 # ISR is calculated
26 1.00000000E-05 # write only cross sections larger than this value [fb]
31 -1.00000000E+00 # m_GUT, if < 0 than it determined via g_1=g_2
32 0 # require strict unification g_1=g_2=g_3 if '1' is set
80 1 # SPheno Exit wit hnon-zero-value for sure!!

```

## B.2 SPheno output file for the STC10' benchmark

The text below contains only part of the whole SPheno file, as the whole file would be inconveniently long. These parts have been labelled as omitted. In addition, there are supplementary blocks at the end of this file from Fittino as it runs FeynHiggs and MicrOMEGAs. Line continuation is indicated with \.

```

# SUSY Les Houches Accord 2 - MSSM spectrum + Decays
# SPheno v3.3.9be

```

## B.2. SPHENO OUTPUT FILE FOR THE STC10' BENCHMARK

```
# W. Porod, Comput. Phys. Commun. 153 (2003) 275-315, hep-ph/0301101
# in case of problems send email to porod@physik.uni-wuerzburg.de
# Created: 18.08.2017, 15:45
Block SPINFO          # Program information
  1  SPheno          # spectrum calculator
  2  v3.3.9be       # version number
#
Block SPhenoINFO     # SPheno specific information
  1    2            # using 2-loop RGEs
  2    2            # using pole masses for boundary conditions at mZ
Block MODSEL        # Model selection
  1    0            # general MSSM
Block MINPAR        # Input parameters
  3    1.00000000E+01 # tanb at m_Z
  4    1.00000000E+00 # Sign(mu)
Block EXTPAR        # non-universal input parameters
  1    1.00000000E+02 # M_1
  2    2.10000000E+02 # M_2
  3    2.00000000E+03 # M_3
 11   -2.85000000E+03 # A_t
 12   -2.85000000E+03 # A_b
 13   -2.85000000E+03 # A_tau
 23    4.00000000E+02 # mu
 26    4.00000000E+02 # m_A, pole mass
 31    2.07000000E+02 # M^2_L11
 32    2.07000000E+02 # M^2_L22
 33    2.07000000E+02 # M^2_L33
 34    1.18000000E+02 # M^2_E11
 35    1.18000000E+02 # M^2_E22
 36    1.18000000E+02 # M^2_E33
 41    2.00000000E+03 # M^2_Q11
 42    2.00000000E+03 # M^2_Q22
 43    1.45000000E+03 # M^2_Q33
 44    2.00000000E+03 # M^2_U11
 45    2.00000000E+03 # M^2_U22
 46    1.10000000E+03 # M^2_U33
 47    2.00000000E+03 # M^2_D11
 48    2.00000000E+03 # M^2_D22
 49    1.00000000E+03 # M^2_D33
Block SMINPUTS     # SM parameters
  1    1.27934000E+02 # alpha_em^-1(MZ)^MSbar
  2    1.16639000E-05 # G_mu [GeV^-2]
  3    1.17200000E-01 # alpha_s(MZ)^MSbar
  4    9.11875000E+01 # m_Z(pole)
  5    4.20000000E+00 # m_b(m_b), MSbar
  6    1.73100000E+02 # m_t(pole)
  7    1.77700000E+00 # m_tau(pole)
  8    0.00000000E+00 # m_nu_3
```

APPENDIX B. EXAMPLE FILES

---

```

11      5.10998930E-04 # m_e(pole)
12      0.00000000E+00 # m_nu_1
13      1.05658372E-01 # m_muon(pole)
14      0.00000000E+00 # m_nu_2
21      5.00000000E-03 # m_d(2 GeV), MSbar
22      2.50000000E-03 # m_u(2 GeV), MSbar
23      9.50000000E-02 # m_s(2 GeV), MSbar
24      1.27000000E+00 # m_c(m_c), MSbar
Block gauge Q= 1.00000000E+03 # (SUSY scale)
  1      3.63213341E-01 # g'(Q)^DRbar
  2      6.44269135E-01 # g(Q)^DRbar
  3      1.04282850E+00 # g3(Q)^DRbar
Block Yu Q= 1.00000000E+03 # (SUSY scale)
  1  1      7.03863903E-06 # Y_u(Q)^DRbar
  2  2      3.57562848E-03 # Y_c(Q)^DRbar
  3  3      8.42103117E-01 # Y_t(Q)^DRbar
Block Yd Q= 1.00000000E+03 # (SUSY scale)
  1  1      1.40235134E-04 # Y_d(Q)^DRbar
  2  2      2.32052829E-03 # Y_s(Q)^DRbar
  3  3      1.26408872E-01 # Y_b(Q)^DRbar
Block Ye Q= 1.00000000E+03 # (SUSY scale)
  1  1      2.71449235E-05 # Y_e(Q)^DRbar
  2  2      5.61269241E-03 # Y_mu(Q)^DRbar
  3  3      8.95333498E-02 # Y_tau(Q)^DRbar
Block Au Q= 1.00000000E+03 # (SUSY scale)
  1  1      0.00000000E+00 # A_u(Q)^DRbar
  2  2      0.00000000E+00 # A_c(Q)^DRbar
  3  3     -2.85000000E+03 # A_t(Q)^DRbar
Block Ad Q= 1.00000000E+03 # (SUSY scale)
  1  1      0.00000000E+00 # A_d(Q)^DRbar
  2  2      0.00000000E+00 # A_s(Q)^DRbar
  3  3     -2.84999995E+03 # A_b(Q)^DRbar
Block Ae Q= 1.00000000E+03 # (SUSY scale)
  1  1      0.00000000E+00 # A_e(Q)^DRbar
  2  2      0.00000000E+00 # A_mu(Q)^DRbar
  3  3     -2.84999993E+03 # A_tau(Q)^DRbar
Block MSOFT Q= 1.00000000E+03 # soft SUSY breaking masses at Q
  1      1.00000000E+02 # M_1
  2      2.10000000E+02 # M_2
  3      2.00000000E+03 # M_3
21     -2.68470382E+03 # M^2_(H,d)
22     -2.09738479E+05 # M^2_(H,u)
31      2.07000000E+02 # M_(L,11)
32      2.07000000E+02 # M_(L,22)
33      2.07000000E+02 # M_(L,33)
34      1.18000000E+02 # M_(E,11)
35      1.18000000E+02 # M_(E,22)
36      1.18000000E+02 # M_(E,33)

```

B.2. SPHENO OUTPUT FILE FOR THE STC10' BENCHMARK

```

41  2.00000000E+03  # M_(Q,11)
42  2.00000000E+03  # M_(Q,22)
43  1.45000000E+03  # M_(Q,33)
44  2.00000000E+03  # M_(U,11)
45  2.00000000E+03  # M_(U,22)
46  1.10000000E+03  # M_(U,33)
47  2.00000000E+03  # M_(D,11)
48  2.00000000E+03  # M_(D,22)
49  1.00000000E+03  # M_(D,33)
Block MASS # Mass spectrum
#  PDG code      mass      particle
   6      1.73100000E+02 # m_t(pole)
  23      9.11875000E+01 # m_Z(pole)
  24      8.03242024E+01 # W+
  15      1.77700000E+00 # m_tau(pole)
  25      1.25592997E+02 # h0
  35      4.00872496E+02 # H0
  36      4.00000000E+02 # A0
  37      4.09633520E+02 # H+
1000001    2.03062492E+03 # ~d_L
2000001    2.02623215E+03 # ~d_R
1000002    2.02933637E+03 # ~u_L
2000002    2.02620090E+03 # ~u_R
1000003    2.03062521E+03 # ~s_L
2000003    2.02623179E+03 # ~s_R
1000004    2.02933651E+03 # ~c_L
2000004    2.02620088E+03 # ~c_R
1000005    1.00808653E+03 # ~b_1
2000005    1.44069976E+03 # ~b_2
1000006    1.01006640E+03 # ~t_1
2000006    1.50161752E+03 # ~t_2
1000011    2.14078448E+02 # ~e_L-
2000011    1.30093597E+02 # ~e_R-
1000012    1.99420898E+02 # ~nu_eL
1000013    2.14090418E+02 # ~mu_L-
2000013    1.30072664E+02 # ~mu_R-
1000014    1.99420735E+02 # ~nu_muL
1000015    1.07356130E+02 # ~tau_1-
2000015    2.19484660E+02 # ~tau_2-
1000016    1.96737810E+02 # ~nu_tauL
1000021    2.04100879E+03 # ~g
1000022    9.59263308E+01 # ~chi_10
1000023    2.06239214E+02 # ~chi_20
1000025    -4.10894450E+02 # ~chi_30
1000035    4.26505045E+02 # ~chi_40
1000024    2.06127286E+02 # ~chi_1+
1000037    4.27452401E+02 # ~chi_2+
# Higgs mixing

```

## APPENDIX B. EXAMPLE FILES

---

```

BLOCK ALPHA
      -1.16241019E-01 # Alpha
BLOCK HMIX Q= 0.10000000E+04
      1 4.00000000E+02 # MUE
      2 9.65985681E+00 # TB
      3 2.42675829E+02 # VEV
      4 2.55101832E+05 # MA02
Block stopmix # stop mixing matrix
  1 1 3.64843632E-01 # Re[R_st(1,1)]
  1 2 9.31068807E-01 # Re[R_st(1,2)]
  2 1 -9.31068807E-01 # Re[R_st(2,1)]
  2 2 3.64843632E-01 # Re[R_st(2,2)]
Block sbotmix # sbottom mixing matrix
  1 1 1.35314704E-02 # Re[R_sb(1,1)]
  1 2 9.99908445E-01 # Re[R_sb(1,2)]
  2 1 -9.99908445E-01 # Re[R_sb(2,1)]
  2 2 1.35314704E-02 # Re[R_sb(2,2)]
Block staumix # stau mixing matrix
  1 1 3.08292891E-01 # Re[R_sta(1,1)]
  1 2 9.51291487E-01 # Re[R_sta(1,2)]
  2 1 -9.51291487E-01 # Re[R_sta(2,1)]
  2 2 3.08292891E-01 # Re[R_sta(2,2)]
Block Nmix # neutralino mixing matrix
  1 1 -9.90852382E-01 # Re[N(1,1)]
  1 2 3.44217464E-02 # Re[N(1,2)]
  1 3 -1.23763398E-01 # Re[N(1,3)]
  1 4 4.13439328E-02 # Re[N(1,4)]
  2 1 -7.04806135E-02 # Re[N(2,1)]
  2 2 -9.54659638E-01 # Re[N(2,2)]
  2 3 2.50385962E-01 # Re[N(2,3)]
  2 4 -1.44790637E-01 # Re[N(2,4)]
  3 1 -5.47601280E-02 # Re[N(3,1)]
  3 2 7.93433296E-02 # Re[N(3,2)]
  3 3 6.97636658E-01 # Re[N(3,3)]
  3 4 7.09935954E-01 # Re[N(3,4)]
  4 1 -1.01219404E-01 # Re[N(4,1)]
  4 2 2.84859184E-01 # Re[N(4,2)]
  4 3 6.59767069E-01 # Re[N(4,3)]
  4 4 -6.87980590E-01 # Re[N(4,4)]
Block Umix # chargino mixing matrix
  1 1 -9.32665494E-01 # Re[U(1,1)]
  1 2 3.60742395E-01 # Re[U(1,2)]
  2 1 3.60742395E-01 # Re[U(2,1)]
  2 2 9.32665494E-01 # Re[U(2,2)]
Block Vmix # chargino mixing matrix
  1 1 -9.77739145E-01 # Re[V(1,1)]
  1 2 2.09824126E-01 # Re[V(1,2)]
  2 1 2.09824126E-01 # Re[V(2,1)]

```

B.2. SPHENO OUTPUT FILE FOR THE STC10' BENCHMARK

```

2 2 9.77739145E-01 # Re[V(2,2)]
#####
# start writing paramaters at Q= 9.11875000E+01
#####
Block gauge Q= 9.11875000E+01 # (SUSY scale)
1 3.55329918E-01 # g'(Q)^DRbar
2 6.39407666E-01 # g(Q)^DRbar
3 1.09642312E+00 # g3(Q)^DRbar
Block Yu Q= 9.11875000E+01 # (SUSY scale)
1 1 7.61758734E-06 # Y_u(Q)^DRbar
2 2 3.86973144E-03 # Y_c(Q)^DRbar
3 3 8.81323740E-01 # Y_t(Q)^DRbar
Block Yd Q= 9.11875000E+01 # (SUSY scale)
1 1 1.56768164E-04 # Y_d(Q)^DRbar
2 2 2.59410587E-03 # Y_s(Q)^DRbar
3 3 1.39653210E-01 # Y_b(Q)^DRbar
Block Ye Q= 9.11875000E+01 # (SUSY scale)
1 1 2.77892847E-05 # Y_e(Q)^DRbar
2 2 5.74591701E-03 # Y_mu(Q)^DRbar
3 3 9.16243032E-02 # Y_tau(Q)^DRbar
Block EXTPAR # non-universal input parameters
0 9.11875000E+01 # Q
25 1.00000000E+01 # tan(beta)
Block Au Q= 9.11875000E+01 # (SUSY scale)
1 1 -1.96445053E+02 # A_u(Q)^DRbar
2 2 -1.96444946E+02 # A_c(Q)^DRbar
3 3 -2.85905862E+03 # A_t(Q)^DRbar
Block Ad Q= 9.11875000E+01 # (SUSY scale)
1 1 -3.90652801E+02 # A_d(Q)^DRbar
2 2 -3.90652670E+02 # A_s(Q)^DRbar
3 3 -3.17458528E+03 # A_b(Q)^DRbar
Block Ae Q= 9.11875000E+01 # (SUSY scale)
1 1 -2.93378501E+00 # A_e(Q)^DRbar
2 2 -2.93378037E+00 # A_mu(Q)^DRbar
3 3 -2.85079552E+03 # A_tau(Q)^DRbar
Block MSOFT Q= 9.11875000E+01 # soft SUSY breaking masses at Q
1 9.44269080E+01 # M_1
2 2.03172981E+02 # M_2
3 2.20491053E+03 # M_3
21 -2.62801109E+04 # M^2_(H,d)
22 -1.01737257E+06 # M^2_(H,u)
31 2.09090476E+02 # M_(L,11)
32 2.09090387E+02 # M_(L,22)
33 2.04175451E+02 # M_(L,33)
34 1.09448776E+02 # M_(E,11)
35 1.09448429E+02 # M_(E,22)
36 8.88239935E+01 # M_(E,33)
41 2.19187287E+03 # M_(Q,11)

```

APPENDIX B. EXAMPLE FILES

---

```

42    2.19187174E+03 # M_(Q,22)
43    1.63305718E+03 # M_(Q,33)
44    2.19357125E+03 # M_(U,11)
45    2.19356973E+03 # M_(U,22)
46    1.24255375E+03 # M_(U,33)
47    2.19336877E+03 # M_(D,11)
48    2.19336803E+03 # M_(D,22)
49    1.34060598E+03 # M_(D,33)
Block Hmix Q= 9.11875000E+01 # Higgs mixing parameters
  1    3.94040025E+02 # mu
  2    1.00000000E+01 # tan[beta](Q)
  4    1.04743518E+06 # m^2_A(Q)
#####
# stop writing paramaters at Q= 9.11875000E+01
#####
# start writing paramaters at Q= 1.00000000E+03
#####
Block gauge Q= 1.00000000E+03 # (SUSY scale)
  1    3.63213341E-01 # g'(Q)^DRbar
  2    6.44269135E-01 # g(Q)^DRbar
  3    1.04282850E+00 # g3(Q)^DRbar
Block Yu Q= 1.00000000E+03 # (SUSY scale)
  1  1    7.03863903E-06 # Y_u(Q)^DRbar
  2  2    3.57562848E-03 # Y_c(Q)^DRbar
  3  3    8.42103117E-01 # Y_t(Q)^DRbar
Block Yd Q= 1.00000000E+03 # (SUSY scale)
  1  1    1.40235134E-04 # Y_d(Q)^DRbar
  2  2    2.32052829E-03 # Y_s(Q)^DRbar
  3  3    1.26408872E-01 # Y_b(Q)^DRbar
Block Ye Q= 1.00000000E+03 # (SUSY scale)
  1  1    2.71449235E-05 # Y_e(Q)^DRbar
  2  2    5.61269241E-03 # Y_mu(Q)^DRbar
  3  3    8.95333498E-02 # Y_tau(Q)^DRbar
Block EXTPAR # non-universal input parameters
  0    1.00000000E+03 # Q
 25    9.65985681E+00 # tan(beta)
Block Au Q= 1.00000000E+03 # (SUSY scale)
  1  1    0.00000000E+00 # A_u(Q)^DRbar
  2  2    0.00000000E+00 # A_c(Q)^DRbar
  3  3   -2.85000000E+03 # A_t(Q)^DRbar
Block Ad Q= 1.00000000E+03 # (SUSY scale)
  1  1    0.00000000E+00 # A_d(Q)^DRbar
  2  2    0.00000000E+00 # A_s(Q)^DRbar
  3  3   -2.84999995E+03 # A_b(Q)^DRbar
Block Ae Q= 1.00000000E+03 # (SUSY scale)
  1  1    0.00000000E+00 # A_e(Q)^DRbar
  2  2    0.00000000E+00 # A_mu(Q)^DRbar

```

B.2. SPHENO OUTPUT FILE FOR THE STC10' BENCHMARK

```

3 3 -2.84999993E+03 # A_tau(Q)^DRbar
Block MSOFT Q= 1.00000000E+03 # soft SUSY breaking masses at Q
  1 1.00000000E+02 # M_1
  2 2.10000000E+02 # M_2
  3 2.00000000E+03 # M_3
 21 -2.68470382E+03 # M^2_(H,d)
 22 -2.09738479E+05 # M^2_(H,u)
 31 2.07000000E+02 # M_(L,11)
 32 2.07000000E+02 # M_(L,22)
 33 2.07000000E+02 # M_(L,33)
 34 1.18000000E+02 # M_(E,11)
 35 1.18000000E+02 # M_(E,22)
 36 1.18000000E+02 # M_(E,33)
 41 2.00000000E+03 # M_(Q,11)
 42 2.00000000E+03 # M_(Q,22)
 43 1.45000000E+03 # M_(Q,33)
 44 2.00000000E+03 # M_(U,11)
 45 2.00000000E+03 # M_(U,22)
 46 1.10000000E+03 # M_(U,33)
 47 2.00000000E+03 # M_(D,11)
 48 2.00000000E+03 # M_(D,22)
 49 1.00000000E+03 # M_(D,33)
Block Hmix Q= 1.00000000E+03 # Higgs mixing parameters
  1 4.00000000E+02 # mu
  2 9.65985681E+00 # tan[beta](Q)
  4 2.55101832E+05 # m^2_A(Q)
#####
# stop writing paramaters at Q= 1.00000000E+03
#####
DECAY      23      2.49520000E+00 # Z
DECAY      24      2.08500000E+00 # W
DECAY  2000011      1.39587909E-01 # ~e^-_R
# BR      NDA      ID1      ID2
      1.00000000E+00      2      1000022      11 # BR(~e^-_R -> chi^0_1 e^-)
# BR      NDA      ID1      ID2      ID3
DECAY  1000011      1.67823101E-01 # ~e^-_L
# BR      NDA      ID1      ID2
      9.24373164E-01      2      1000022      11 # BR(~e^-_L -> chi^0_1 e^-)
      2.69205263E-02      2      1000023      11 # BR(~e^-_L -> chi^0_2 e^-)
      4.87002472E-02      2      -1000024      12 # BR(~e^-_L -> chi^-_1 nu_e)
# BR      NDA      ID1      ID2      ID3
DECAY  2000013      1.39444296E-01 # ~mu^-_R
# BR      NDA      ID1      ID2
      1.00000000E+00      2      1000022      13 # BR(~mu^-_R -> chi^0_1 mu^-)
# BR      NDA      ID1      ID2      ID3
DECAY  1000013      1.67957160E-01 # ~mu^-_L
# BR      NDA      ID1      ID2
      9.24234854E-01      2      1000022      13 # BR(~mu^-_L -> chi^0_1 mu^-)

```

APPENDIX B. EXAMPLE FILES

---

```

      2.69660286E-02      2      1000023      13 # BR(~mu^-_L -> chi^0_2 mu^-)
      4.87892371E-02      2     -1000024      14 # BR(~mu^-_L -> chi^-_1 nu_mu)
#    BR                    NDA      ID1      ID2      ID3
DECAY  1000015      2.14715110E-02 # ~tau^-_1
#    BR                    NDA      ID1      ID2
      1.00000000E+00      2      1000022      15 # BR(~tau^-_1 -> chi^0_1 tau^-)
DECAY  2000015      2.63991522E-01 # ~tau^-_2
#    BR                    NDA      ID1      ID2
      8.00909799E-01      2      1000022      15 # BR(~tau^-_2 -> chi^0_1 tau^-)
      3.97908008E-02      2      1000023      15 # BR(~tau^-_2 -> chi^0_2 tau^-)
      7.26686855E-02      2     -1000024      16 # BR(~tau^-_2 -> chi^-_1 nu_tau)
      8.65998548E-02      2      1000015      23 # BR(~tau^-_2 -> ~tau^-_1 Z)
#    BR                    NDA      ID1      ID2      ID3
DECAY  1000012      1.71068338E-01 # ~nu_e
#    BR                    NDA      ID1      ID2
      1.00000000E+00      2      1000022      12 # BR(~nu_e -> chi^0_1 nu_e)
#    BR                    NDA      ID1      ID2      ID3
DECAY  1000014      1.71068546E-01 # ~nu_mu
#    BR                    NDA      ID1      ID2
      9.99996983E-01      2      1000022      14 # BR(~nu_mu -> chi^0_1 nu_mu)
#    BR                    NDA      ID1      ID2      ID3
DECAY  1000016      1.78132045E-01 # ~nu_tau
#    BR                    NDA      ID1      ID2
      9.31824625E-01      2      1000022      16
      # BR(~nu_tau -> chi^0_1 nu_tau)
      6.81753751E-02      2      1000015      24
      # BR(~nu_tau -> ~tau^-_1 W^+)
DECAY  2000001      1.17512066E+00 # ~d_R
#    BR                    NDA      ID1      ID2
----
Omitted
----
DECAY  1000001      2.47341509E+01 # ~d_L
#    BR                    NDA      ID1      ID2
----
Omitted
----
DECAY  2000003      1.17736341E+00 # ~s_R
#    BR                    NDA      ID1      ID2
----
Omitted
----
DECAY  1000003      2.47329782E+01 # ~s_L
#    BR                    NDA      ID1      ID2
----
Omitted
----
DECAY  1000005      1.01106978E+00 # ~b_1

```

B.2. SPHENO OUTPUT FILE FOR THE STC10' BENCHMARK

```

#   BR                NDA      ID1      ID2
5.67446900E-01      2      1000022      5   # BR(~b_1 -> chi^0_1 b)
2.80352571E-02      2      1000023      5   # BR(~b_1 -> chi^0_2 b)
1.06741116E-01      2      1000025      5   # BR(~b_1 -> chi^0_3 b)
9.25058097E-02      2      1000035      5   # BR(~b_1 -> chi^0_4 b)
4.90103625E-02      2      -1000024      6   # BR(~b_1 -> chi^-_1 t)
1.56260554E-01      2      -1000037      6   # BR(~b_1 -> chi^-_2 t)
DECAY  2000005      6.61268575E+01  # ~b_2
#   BR                NDA      ID1      ID2
4.39678145E-03      2      1000022      5   # BR(~b_2 -> chi^0_1 b)
7.67337255E-02      2      1000023      5   # BR(~b_2 -> chi^0_2 b)
3.49344430E-03      2      1000025      5   # BR(~b_2 -> chi^0_3 b)
9.56548966E-03      2      1000035      5   # BR(~b_2 -> chi^0_4 b)
1.54891466E-01      2      -1000024      6   # BR(~b_2 -> chi^-_1 t)
2.65621146E-01      2      -1000037      6   # BR(~b_2 -> chi^-_2 t)
4.79333285E-01      2      1000006     -24  # BR(~b_2 -> ~t_1 W^-)
2.43915102E-04      2      1000006     -37  # BR(~b_2 -> ~t_1 H^-)
3.35696261E-04      2      1000005      23  # BR(~b_2 -> ~b_1 Z)
2.49747721E-03      2      1000005      36  # BR(~b_2 -> ~b_1 A^0)
4.39920148E-04      2      1000005      25  # BR(~b_2 -> ~b_1 h^0)
2.44765448E-03      2      1000005      35  # BR(~b_2 -> ~b_1 H^0)
DECAY  2000002      4.70037647E+00  # ~u_R
#   BR                NDA      ID1      ID2
---
Omitted
---
DECAY  1000002      2.48232852E+01  # ~u_L
#   BR                NDA      ID1      ID2
---
Omitted
---
DECAY  2000004      4.70185788E+00  # ~c_R
#   BR                NDA      ID1      ID2
---
Omitted
---
DECAY  1000004      2.48234209E+01  # ~c_L
#   BR                NDA      ID1      ID2
---
Omitted
---
DECAY  1000006      2.16488336E+01  # ~t_1
#   BR                NDA      ID1      ID2
9.25449380E-02      2      1000022      6   # BR(~t_1 -> chi^0_1 t)
1.25092766E-04      2      1000023      4   # BR(~t_1 -> chi^0_2 c)
5.97986588E-02      2      1000023      6   # BR(~t_1 -> chi^0_2 t)
2.51626693E-01      2      1000025      6   # BR(~t_1 -> chi^0_3 t)
1.40322814E-01      2      1000035      6   # BR(~t_1 -> chi^0_4 t)

```

APPENDIX B. EXAMPLE FILES

```

1.32778526E-01  2  1000024  5  # BR(~t_1 -> chi^+_1 b)
3.22795979E-01  2  1000037  5  # BR(~t_1 -> chi^+_2 b)
# BR          NDA      ID1      ID2      ID3
DECAY  2000006  6.74989543E+01  # ~t_2
# BR          NDA      ID1      ID2
6.01646819E-03  2  1000022  6  # BR(~t_2 -> chi^0_1 t)
6.05119458E-02  2  1000023  6  # BR(~t_2 -> chi^0_2 t)
1.18777764E-01  2  1000025  6  # BR(~t_2 -> chi^0_3 t)
1.57882640E-01  2  1000035  6  # BR(~t_2 -> chi^0_4 t)
1.16863308E-01  2  1000024  5  # BR(~t_2 -> chi^+_1 b)
7.24747232E-02  2  1000037  5  # BR(~t_2 -> chi^+_2 b)
8.09981345E-04  2  1000005  24  # BR(~t_2 -> ~b_1 W^+)
6.74638146E-03  2  1000005  37  # BR(~t_2 -> ~b_1 H^+)
2.94389667E-01  2  1000006  23  # BR(~t_2 -> ~t_1 Z)
2.38343467E-04  2  1000006  36  # BR(~t_2 -> ~t_1 A^0)
1.65254545E-01  2  1000006  25  # BR(~t_2 -> ~t_1 h^0)
DECAY  1000024  7.01543293E-02  # chi^+_1
# BR          NDA      ID1      ID2
1.08916099E-03  2  -2000013  14  # BR(chi^+_1 -> ~mu^+_R nu_mu)
7.23992621E-01  2  -1000015  16  # BR(chi^+_1 -> ~tau^+_1 nu_tau)
4.75206336E-02  2  1000012  -11  # BR(chi^+_1 -> ~nu_e e^+)
4.75225860E-02  2  1000014  -13  # BR(chi^+_1 -> ~nu_mu mu^+)
9.23658059E-02  2  1000016  -15  # BR(chi^+_1 -> ~nu_tau tau^+)
8.64594177E-02  2  1000022  24  # BR(chi^+_1 -> chi^0_1 W^+)
# BR          NDA      ID1      ID2      ID3
3.72169570E-04  3  1000022  -11  12  \
# BR(chi^+_1 -> chi^0_1 e^+ nu_e)
3.71991259E-04  3  1000022  -13  14  \
# BR(chi^+_1 -> chi^0_1 mu^+ nu_mu)
3.05551519E-04  3  1000022  -15  16  \
# BR(chi^+_1 -> chi^0_1 tau^+ nu_tau)
DECAY  1000037  2.85011706E+00  # chi^+_2
# BR          NDA      ID1      ID2
4.52294274E-02  2  -1000011  12  # BR(chi^+_2 -> ~e^+_L nu_e)
4.52453127E-02  2  -1000013  14  # BR(chi^+_2 -> ~mu^+_L nu_mu)
4.92851329E-02  2  -2000015  16  # BR(chi^+_2 -> ~tau^+_2 nu_tau)
1.66866410E-02  2  1000012  -11  # BR(chi^+_2 -> ~nu_e e^+)
1.67108601E-02  2  1000014  -13  # BR(chi^+_2 -> ~nu_mu mu^+)
2.31769256E-02  2  1000016  -15  # BR(chi^+_2 -> ~nu_tau tau^+)
7.61778141E-02  2  1000022  24  # BR(chi^+_2 -> chi^0_1 W^+)
2.84542569E-01  2  1000023  24  # BR(chi^+_2 -> chi^0_2 W^+)
2.52381172E-01  2  1000024  23  # BR(chi^+_2 -> chi^+_1 Z)
1.90242730E-01  2  1000024  25  # BR(chi^+_2 -> chi^+_1 h^0)
# BR          NDA      ID1      ID2      ID3
1.11344216E-04  3  1000022  -5  6  \
# BR(chi^+_2 -> chi^0_1 b_bar t)
DECAY  1000022  0.00000000E+00  # chi^0_1
DECAY  1000023  7.45965360E-02  # chi^0_2

```

B.2. SPHENO OUTPUT FILE FOR THE STC10' BENCHMARK

#	BR	NDA	ID1	ID2	
	1.30674065E-02	2	2000011	-11	# BR(chi <sup>0</sup> <sub>2</sub> -> $\tilde{e}^-_R e^+$ )
	1.30674065E-02	2	-2000011	11	# BR(chi <sup>0</sup> <sub>2</sub> -> $\tilde{e}^+_R e^-$ )
	1.36126165E-02	2	2000013	-13	# BR(chi <sup>0</sup> <sub>2</sub> -> $\tilde{\mu}^-_R \mu^+$ )
	1.36126165E-02	2	-2000013	13	# BR(chi <sup>0</sup> <sub>2</sub> -> $\tilde{\mu}^+_R \mu^-$ )
	3.86803674E-01	2	1000015	-15	# BR(chi <sup>0</sup> <sub>2</sub> -> $\tilde{\tau}^-_1 \tau^+$ )
	3.86803674E-01	2	-1000015	15	# BR(chi <sup>0</sup> <sub>2</sub> -> $\tilde{\tau}^+_1 \tau^-$ )
	2.02033221E-02	2	1000012	-12	# BR(chi <sup>0</sup> <sub>2</sub> -> $\tilde{\nu}_e \nu_{\bar{e}}$ )
	2.02033221E-02	2	-1000012	12	# BR(chi <sup>0</sup> <sub>2</sub> -> $\tilde{\nu}^*_e \nu_e$ )
	2.02042728E-02	2	1000014	-14	\
	# BR(chi <sup>0</sup> <sub>2</sub> -> $\tilde{\nu}_\mu \nu_{\bar{\mu}}$ )				
	2.02042728E-02	2	-1000014	14	# BR(chi <sup>0</sup> <sub>2</sub> -> $\tilde{\nu}^*_\mu \nu_\mu$ )
	3.87150670E-02	2	1000016	-16	\
	# BR(chi <sup>0</sup> <sub>2</sub> -> $\tilde{\nu}_\tau \nu_{\bar{\tau}}$ )				
	3.87150670E-02	2	-1000016	16	# BR(chi <sup>0</sup> <sub>2</sub> -> $\tilde{\nu}^*_\tau \nu_\tau$ )
	1.33590986E-02	2	1000022	23	# BR(chi <sup>0</sup> <sub>2</sub> -> chi <sup>0</sup> <sub>1</sub> Z)
#	BR	NDA	ID1	ID2	ID3
	5.16475079E-04	3	1000022	11	-11 \
	# BR(chi <sup>0</sup> <sub>2</sub> -> chi <sup>0</sup> <sub>1</sub> e <sup>-</sup> e <sup>+</sup> )				
	5.16146729E-04	3	1000022	13	-13 \
	# BR(chi <sup>0</sup> <sub>2</sub> -> chi <sup>0</sup> <sub>1</sub> $\mu^- \mu^+$ )				
	3.91257258E-04	3	1000022	15	-15 \
	# BR(chi <sup>0</sup> <sub>2</sub> -> chi <sup>0</sup> <sub>1</sub> $\tau^- \tau^+$ )				
DECAY	1000025	2.30998564E+00	# chi <sup>0</sup> <sub>3</sub>		
#	BR	NDA	ID1	ID2	
	1.13332598E-03	2	2000011	-11	# BR(chi <sup>0</sup> <sub>3</sub> -> $\tilde{e}^-_R e^+$ )
	1.13332598E-03	2	-2000011	11	# BR(chi <sup>0</sup> <sub>3</sub> -> $\tilde{e}^+_R e^-$ )
	4.57957975E-04	2	1000011	-11	# BR(chi <sup>0</sup> <sub>3</sub> -> $\tilde{e}^-_L e^+$ )
	4.57957975E-04	2	-1000011	11	# BR(chi <sup>0</sup> <sub>3</sub> -> $\tilde{e}^+_L e^-$ )
	1.14784692E-03	2	2000013	-13	# BR(chi <sup>0</sup> <sub>3</sub> -> $\tilde{\mu}^-_R \mu^+$ )
	1.14784692E-03	2	-2000013	13	# BR(chi <sup>0</sup> <sub>3</sub> -> $\tilde{\mu}^+_R \mu^-$ )
	4.77484651E-04	2	1000013	-13	# BR(chi <sup>0</sup> <sub>3</sub> -> $\tilde{\mu}^-_L \mu^+$ )
	4.77484651E-04	2	-1000013	13	# BR(chi <sup>0</sup> <sub>3</sub> -> $\tilde{\mu}^+_L \mu^-$ )
	4.34944518E-03	2	1000015	-15	# BR(chi <sup>0</sup> <sub>3</sub> -> $\tilde{\tau}^-_1 \tau^+$ )
	4.34944518E-03	2	-1000015	15	# BR(chi <sup>0</sup> <sub>3</sub> -> $\tilde{\tau}^+_1 \tau^-$ )
	5.71485549E-03	2	2000015	-15	# BR(chi <sup>0</sup> <sub>3</sub> -> $\tilde{\tau}^-_2 \tau^+$ )
	5.71485549E-03	2	-2000015	15	# BR(chi <sup>0</sup> <sub>3</sub> -> $\tilde{\tau}^+_2 \tau^-$ )
	2.60679055E-03	2	1000012	-12	# BR(chi <sup>0</sup> <sub>3</sub> -> $\tilde{\nu}_e \nu_{\bar{e}}$ )
	2.60679055E-03	2	-1000012	12	\
	# BR(chi <sup>0</sup> <sub>3</sub> -> $\tilde{\nu}^*_e \nu_e$ )				
	2.60679318E-03	2	1000014	-14	\
	# BR(chi <sup>0</sup> <sub>3</sub> -> $\tilde{\nu}_\mu \nu_{\bar{\mu}}$ )				
	2.60679318E-03	2	-1000014	14	\
	# BR(chi <sup>0</sup> <sub>3</sub> -> $\tilde{\nu}^*_\mu \nu_\mu$ )				
	2.64990417E-03	2	1000016	-16	\
	# BR(chi <sup>0</sup> <sub>3</sub> -> $\tilde{\nu}_\tau \nu_{\bar{\tau}}$ )				
	2.64990417E-03	2	-1000016	16	\
	# BR(chi <sup>0</sup> <sub>3</sub> -> $\tilde{\nu}^*_\tau \nu_\tau$ )				

APPENDIX B. EXAMPLE FILES

```

2.93833516E-01    2    1000024    -24    # BR(chi^0_3 -> chi^+_1 W^-)
2.93833516E-01    2   -1000024    24     # BR(chi^0_3 -> chi^-_1 W^+)
1.02104324E-01    2    1000022    23     # BR(chi^0_3 -> chi^0_1 Z)
2.34547790E-01    2    1000023    23     # BR(chi^0_3 -> chi^0_2 Z)
2.16277927E-02    2    1000022    25     # BR(chi^0_3 -> chi^0_1 h^0)
1.17052595E-02    2    1000023    25     # BR(chi^0_3 -> chi^0_2 h^0)
#    BR                NDA    ID1    ID2    ID3
DECAY  1000035    2.95882848E+00 # chi^0_4
#    BR                NDA    ID1    ID2
3.18832949E-03    2    2000011    -11    # BR(chi^0_4 -> ~e^-_R e^+)
3.18832949E-03    2   -2000011    11     # BR(chi^0_4 -> ~e^+_R e^-)
8.64117614E-03    2    1000011    -11    # BR(chi^0_4 -> ~e^-_L e^+)
8.64117614E-03    2   -1000011    11     # BR(chi^0_4 -> ~e^+_L e^-)
3.18791254E-03    2    2000013    -13    # BR(chi^0_4 -> ~mu^-_R mu^+)
3.18791254E-03    2   -2000013    13     # BR(chi^0_4 -> ~mu^+_R mu^-)
8.66236404E-03    2    1000013    -13    # BR(chi^0_4 -> ~mu^-_L mu^+)
8.66236404E-03    2   -1000013    13     # BR(chi^0_4 -> ~mu^+_L mu^-)
1.94811727E-03    2    1000015    -15    # BR(chi^0_4 -> ~tau^-_1 tau^+)
1.94811727E-03    2   -1000015    15     # BR(chi^0_4 -> ~tau^+_1 tau^-)
1.44901073E-02    2    2000015    -15    # BR(chi^0_4 -> ~tau^-_2 tau^+)
1.44901073E-02    2   -2000015    15     # BR(chi^0_4 -> ~tau^+_2 tau^-)
2.12416284E-02    2    1000012    -12    # BR(chi^0_4 -> ~nu_e nu_bar_e)
2.12416284E-02    2   -1000012    12     # BR(chi^0_4 -> ~nu^*_e nu_e)
2.12416479E-02    2    1000014    -14    \
# BR(chi^0_4 -> ~nu_mu nu_bar_mu)
2.12416479E-02    2   -1000014    14     \
# BR(chi^0_4 -> ~nu^*_mu nu_mu)
2.15605126E-02    2    1000016    -16    \
# BR(chi^0_4 -> ~nu_tau nu_bar_tau)
2.15605126E-02    2   -1000016    16     \
# BR(chi^0_4 -> ~nu^*_tau nu_tau)
2.61322657E-01    2    1000024    -24    # BR(chi^0_4 -> chi^+_1 W^-)
2.61322657E-01    2   -1000024    24     # BR(chi^0_4 -> chi^-_1 W^+)
2.19784714E-02    2    1000022    23     # BR(chi^0_4 -> chi^0_1 Z)
1.96570465E-02    2    1000023    23     # BR(chi^0_4 -> chi^0_2 Z)
6.75816830E-02    2    1000022    25     # BR(chi^0_4 -> chi^0_1 h^0)
1.59518862E-01    2    1000023    25     # BR(chi^0_4 -> chi^0_2 h^0)
#    BR                NDA    ID1    ID2    ID3
DECAY  1000021    6.88084283E+01 # ~g
#    BR                NDA    ID1    ID2
1.38081909E-04    2    1000006    -4     # BR(~g -> ~t_1 c_bar)
1.38081909E-04    2   -1000006    4      # BR(~g -> ~t^*_1 c)
1.54294012E-01    2    1000006    -6     # BR(~g -> ~t_1 t_bar)
1.54294012E-01    2   -1000006    6      # BR(~g -> ~t^*_1 t)
8.09155940E-02    2    2000006    -6     # BR(~g -> ~t_2 t_bar)
8.09155940E-02    2   -2000006    6      # BR(~g -> ~t^*_2 t)
1.83383983E-01    2    1000005    -5     # BR(~g -> ~b_1 b_bar)
1.83383983E-01    2   -1000005    5      # BR(~g -> ~b^*_1 b)

```

B.2. SPHENO OUTPUT FILE FOR THE STC10' BENCHMARK

```

8.07929292E-02    2    2000005    -5    # BR(~g -> ~b_2 b_bar)
8.07929292E-02    2    -2000005    5    # BR(~g -> ~b^*_2 b)
DECAY      25    4.95497824E-03    # Gamma(h0)
1.88480033E-03    2    22    22    # BR(h0 -> photon photon)
1.27128801E-03    2    22    23    # BR(h0 -> photon Z)
2.35500720E-02    2    23    23    # BR(h0 -> Z Z)
1.92284032E-01    2    -24    24    # BR(h0 -> W W)
5.45777951E-02    2    21    21    # BR(h0 -> gluon gluon)
5.53835212E-09    2    -11    11    # BR(h0 -> Electron electron)
2.46356238E-04    2    -13    13    # BR(h0 -> Muon muon)
7.11436740E-02    2    -15    15    # BR(h0 -> Tau tau)
1.17015361E-07    2    -2    2    # BR(h0 -> Up up)
2.29940767E-02    2    -4    4    # BR(h0 -> Charm charm)
6.48221937E-07    2    -1    1    # BR(h0 -> Down down)
2.34453509E-04    2    -3    3    # BR(h0 -> Strange strange)
6.31812681E-01    2    -5    5    # BR(h0 -> Bottom bottom)
DECAY      35    2.80201627E+00    # Gamma(HH)
---
Omitted
---
DECAY      36    3.17023448E+00    # Gamma(A0)
3.59987653E-06    2    22    22    # BR(A0 -> photon photon)
1.05464386E-05    2    22    23    # BR(A0 -> photon Z)
1.98333085E-04    2    21    21    # BR(A0 -> gluon gluon)
2.01765173E-09    2    -11    11    # BR(A0 -> Electron electron)
8.97801495E-05    2    -13    13    # BR(A0 -> Muon muon)
2.60289837E-02    2    -15    15    # BR(A0 -> Tau tau)
4.29157563E-12    2    -2    2    # BR(A0 -> Up up)
8.43911266E-07    2    -4    4    # BR(A0 -> Charm charm)
4.13189157E-02    2    -6    6    # BR(A0 -> Top top)
1.84709389E-07    2    -1    1    # BR(A0 -> Down down)
6.68146036E-05    2    -3    3    # BR(A0 -> Strange strange)
1.83952054E-01    2    -5    5    # BR(A0 -> Bottom bottom)
2.98568245E-02    2    -1000024    1000024    # BR(A0 -> Chargino1 chargino1)
4.74270790E-03    2    1000022    1000022    # BR(A0 -> neutralino1 neutralino1)
2.28477502E-02    2    1000022    1000023    # BR(A0 -> neutralino1 neutralino2)
1.21047951E-02    2    1000023    1000023    # BR(A0 -> neutralino2 neutralino2)
1.10277607E-03    2    23    25    # BR(A0 -> Z h0)
1.03900762E-35    2    25    25    # BR(A0 -> h0 h0)
5.45194340E-12    2    -1000011    2000011    # BR(A0 -> Selectron1 selectron2)
5.45194340E-12    2    -2000011    1000011    # BR(A0 -> Selectron2 selectron1)
2.33099400E-07    2    -1000013    2000013    # BR(A0 -> Smuon1 smuon2)
2.33099400E-07    2    -2000013    1000013    # BR(A0 -> Smuon2 smuon1)
3.38837311E-01    2    -1000015    2000015    # BR(A0 -> Stau1 stau2)
3.38837311E-01    2    -2000015    1000015    # BR(A0 -> Stau2 stau1)
DECAY      37    3.00838514E+00    # Gamma(Hp)
---
Omitted

```

APPENDIX B. EXAMPLE FILES

---

```

---
Block SPhenoCrossSections # cross sections
XS 11 -11 500.0 -0.80 -0.30 1 # e+ e- XS, Pe-, Pe+, including ISR
#      Sigma [fb]      NDA      ID1      ID2
    1.03574524E+02      2      2000011  -2000011 # ~e_R-      ~e_R+
    1.18627026E+01      2      2000011  -1000011 # ~e_R-      ~e_L+
    1.98276585E+02      2      1000011  -2000011 # ~e_L-      ~e_R+
    3.43460366E+01      2      1000011  -1000011 # ~e_L-      ~e_L+
    3.06605560E+01      2      2000013  -2000013 # ~mu_R-     ~mu_R+
    2.97915551E-03      2      2000013  -1000013 # ~mu_R-     ~mu_L+
    2.97915551E-03      2      1000013  -2000013 # ~mu_L-     ~mu_R+
    1.60285661E+01      2      1000013  -1000013 # ~mu_L-     ~mu_L+
    4.11036069E+01      2      1000015  -1000015 # ~tau_1-    ~tau_1+
    1.56392552E+00      2      1000015  -2000015 # ~tau_1-    ~tau_2+
    1.56392552E+00      2      2000015  -1000015 # ~tau_2-    ~tau_1+
    1.13627646E+01      2      2000015  -2000015 # ~tau_2-    ~tau_2+
    1.42000099E+03      2      1000012  -1000012 # ~nu_eL     ~nu_eL*
    9.18309702E+00      2      1000014  -1000014 # ~nu_muL    ~nu_muL*
    9.90840058E+00      2      1000016  -1000016 # ~nu_tauL   ~nu_tauL*
    8.97157521E+01      2      1000022   1000022 # chi_10    chi_10
    7.24607387E+01      2      1000022   1000023 # chi_10    chi_20
    4.62550420E+01      2      1000023   1000023 # chi_20    chi_20
    1.04369440E+02      2      1000024  -1000024 # chi_1-    chi_1+
    6.07613093E+01      2           25      23      # h0 Z
    7.89376897E-04      2           35      23      # H0 Z
XS 11 -11 500.0 0.80 0.30 1 # e+ e- XS, Pe-, Pe+, including ISR
---
Omitted
---
XS 11 -11 500.0 -0.80 0.30 1 # e+ e- XS, Pe-, Pe+, including ISR
---
Omitted
---
XS 11 -11 500.0 0.80 -0.30 1 # e+ e- XS, Pe-, Pe+, including ISR
#      Sigma [fb]      NDA      ID1      ID2
---
Omitted
---
DECAY      6      2.43000000E+00 # top
#      BR      NDA      ID1      ID2
    1.00000000E+00      2           5      24 # BR(t -> b W)
Block HiggsBoundsInputHiggsCouplingsFermions
# ScalarNormEffCoupSq PseudoSNormEffCoupSq NP IP1 IP2 IP2
    1.35096488E+00      0.00000000E+00      3 25 5 5 \
    # h0-b-b eff. coupling^2, normalised to SM
    9.29618688E+01      0.00000000E+00      3 35 5 5 \
    # H0-b-b eff. coupling^2, normalised to SM
    0.00000000E+00      9.33128337E+01      3 36 5 5 \

```

B.2. SPHENO OUTPUT FILE FOR THE STC10' BENCHMARK

```

# A0-b-b eff. coupling^2, normalised to SM
#
9.96238836E-01    0.00000000E+00        3 25  6  6 \
# h0-t-t eff. coupling^2, normalised to SM
1.44778036E-02    0.00000000E+00        3 35  6  6 \
# H0-t-t eff. coupling^2, normalised to SM
0.00000000E+00    1.07166395E-02        3 36  6  6 \
# A0-t-t eff. coupling^2, normalised to SM
#
1.35096488E+00    0.00000000E+00        3 25 15 15 \
# h0-tau-tau eff. coupling^2, normalised to SM
9.29618688E+01    0.00000000E+00        3 35 15 15 \
# H0-tau-tau eff. coupling^2, normalised to SM
0.00000000E+00    9.33128337E+01        3 36 15 15 \
# A0-tau-tau eff. coupling^2, normalised to SM
#
Block HiggsBoundsInputHiggsCouplingsBosons
  9.99717182E-01        3 25 24 24 \
    # h0-W-W eff. coupling^2, normalised to SM
---
Omitted
---
Block SPhenoLowEnergy # low energy observables
  1    3.68611438E-04    # BR(b -> s gamma)
  2    1.58751746E-06    # BR(b -> s mu+ mu-)
  3    3.53597554E-05    # BR(b -> s nu nu)
  4    2.17875183E-15    # BR(Bd -> e+ e-)
  5    9.30757701E-11    # BR(Bd -> mu+ mu-)
  6    1.96276244E-08    # BR(Bd -> tau+ tau-)
  7    7.33800924E-14    # BR(Bs -> e+ e-)
  8    3.13485936E-09    # BR(Bs -> mu+ mu-)
  9    6.69449402E-07    # BR(Bs -> tau+ tau-)
 10    9.33338896E-05    # BR(B_u -> tau nu)
 11    9.83656155E-01    # BR(B_u -> tau nu)/BR(B_u -> tau nu)_SM
 12    5.43181549E-01    # |Delta(M_Bd)| [ps^-1]
 13    1.94060298E+01    # |Delta(M_Bs)| [ps^-1]
 14    9.99332777E-01    # RD=[BR(B -> D tau nu)/BR(B -> D e nu)]/ \
[BR(B -> D tau nu)/BR(B -> D e nu)]_SM
 15    9.99946616E-01    # RD*=[BR(B -> D* tau nu)/BR(B -> D* e nu)]/ \
[BR(B -> D* tau nu)/BR(B -> D* e nu)]_SM
 16    2.16178274E-03    # epsilon_K
 17    2.28174833E-15    # Delta(M_K)
 18    2.48894647E-11    # BR(K^0 -> pi^0 nu nu)
 19    8.30973224E-11    # BR(K^+ -> pi^+ nu nu)
 20    1.01919686E-13    # Delta(g-2)_electron/2
 21    4.36027305E-09    # Delta(g-2)_muon/2
 22    4.26006015E-06    # Delta(g-2)_tau/2
 23    0.00000000E+00    # electric dipole moment of the electron

```

APPENDIX B. EXAMPLE FILES

---

```

24    0.00000000E+00    # electric dipole moment of the muon
25    0.00000000E+00    # electric dipole moment of the tau
26    0.00000000E+00    # Br(mu -> e gamma)
27    0.00000000E+00    # Br(tau -> e gamma)
28    0.00000000E+00    # Br(tau -> mu gamma)
29    0.00000000E+00    # Br(mu -> 3 e)
30    0.00000000E+00    # Br(tau -> 3 e)
31    0.00000000E+00    # Br(tau -> 3 mu)
39    1.87611854E-04    # Delta(rho_parameter)
40    0.00000000E+00    # BR(Z -> e mu)
41    0.00000000E+00    # BR(Z -> e tau)
42    0.00000000E+00    # BR(Z -> mu tau)
Block FWCOEF Q= 1.60000000E+02 # Wilson coefficients at scale Q
--
Omitted
--
Block IMFWCOEF Q= 1.60000000E+02 # Im(Wilson coefficients) at scale Q
#    id      order  M      value      comment
    0305 4422   00   0      3.86852739E-07 # C7
    0305 4422   00   2      1.41752296E-05 # C7
    0305 4322   00   2      5.48498928E-06 # C7'
    0305 6421   00   0      3.31364450E-07 # C8
    0305 6421   00   2     -5.91376408E-07 # C8
    0305 6321   00   2      2.39009054E-06 # C8'
03051111 4133   00   2     -4.72237821E-06 # C9 e+e-
03051111 4233   00   2      4.19093520E-08 # C9' e+e-
03051111 4137   00   2      5.06268149E-05 # C10 e+e-
03051111 4237   00   2     -8.23250508E-07 # C10' e+e-
03051313 4133   00   2     -4.72239544E-06 # C9 mu+mu-
03051313 4233   00   2      4.19089410E-08 # C9' mu+mu-
03051313 4137   00   2      5.06267306E-05 # C10 mu+mu-
03051313 4237   00   2     -8.23250730E-07 # C10' mu+mu-
03051212 4137   00   2     -9.97657506E-06 # C11 nu_1 nu_1
03051212 4237   00   2      1.94735469E-07 # C11' nu_1 nu_1
03051414 4137   00   2     -9.97656576E-06 # C11 nu_2 nu_2
03051414 4237   00   2      1.94735469E-07 # C11' nu_2 nu_2
03051616 4137   00   2     -9.93534014E-06 # C11 nu_3 nu_3
03051616 4237   00   2      1.94735630E-07 # C11' nu_3 nu_3
Block MODSEL # Model selection
1    0    # MSSM
3    0    # MSSM particle content
Block FeynHiggs # FeynHiggs observables
1    1.25592997E+02 # massh
2    4.00872496E+02 # massH
3    4.00000000E+02 # massA
4    4.09633520E+02 # massHp
5    2.70193926E-09 # gm2mu
6    8.03850215E+01 # mwmssm

```

```

7      8.03610515E+01 # mwsM
8      4.11609816E-04 # bsgmssM
9      3.80951569E-04 # bsgsm
10     2.31384385E-01 # SW2effMSSM
11     2.31517355E-01 # SW2effSM
12     2.11441313E+01 # DeltaMsMSSM
13     2.08978061E+01 # DeltaMsSM
Block MicrOMEGAs # MicrOMEGAs observables
1      1.15557984E-01 # Omega h^2

```

### B.3 Fittino input file for a pMSSM-10 fit to ILC1 observables

```

#####
### Fittino input file                                     ###
#####

### LE (low energy) observables

### References and comments are given in
#http://arxiv.org/abs/1204.4199

# Name                Value                Experimental uncertainties \
Theory uncertainties  Add. Scanning Unc.

### SM observables

massTop 173.1          GeV +- 1.00 GeV # PDG 2012

alphaem 127.931261 GeV +- 0.014          # SPheno 3.3.9beta default, uncert from \
http://arxiv.org/abs/1010.4180, p.11
alphas 0.1184 GeV +- 0.0007 GeV # PDG 2011
massZ 91.1876 GeV +- 0.0021 GeV # PDG 2011
nofit massBottom 4.18          GeV +- 0.03 GeV # PDG 2012
nofit G_F 1.1663787E-5 +- 0.0000006E-5 # PDG 2011
massTau 1.77682          GeV +- 0.00016 GeV # PDG 2012
nofit massCharm 1.275          GeV +- 0.025 GeV # PDG 2014 \
(SPheno3.3.9beta default is 1.270)

#####
### Parameters                                             ###

```

APPENDIX B. EXAMPLE FILES

---

```

#####

fixParameter alphaem      127.931261
fixParameter G_F          1.1663787E-5
fixParameter alphas       0.1184          GeV
fixParameter massZ        91.1876          GeV
fixParameter massBottom   4.18           GeV
fixParameter massTau      1.77682         GeV
fixParameter massCharm    1.275           GeV
fixParameter SignMu       1
fixParameter massStrange  0.095           GeV
fixParameter massMuon     0.1056583715 GeV

# ILC1
# M0      7.02500000E+03 +- 66.3047
# M12     5.68299988E+02 +- 17.0018
# A0      -1.14265996E+04 +- 72.2945
# Tan     10.0 +- 2.24463
# mu      115.0 +- 1.15
# mA      1000.0 +- 10.0
# top mass 172.0 +- 0.01
#QEWSB= 3.11193091E+03

fitParameter M0           7025.00 GeV +- 70.25          GeV
fitParameter M12          568.30 GeV +- 5.68          GeV
fitParameter A0           -10426.6 GeV +- 104.27         GeV
fitParameter TanBeta      10.00          +- 0.10
fitParameter MOHu         115.0 GeV +- 1.15           GeV          #mu
fitParameter MOHd         1000.0 GeV +- 10.0           GeV          #mA
fixParameter massTop      173.1 GeV          # +- 0.445244 GeV
#fitParameter QEWSB       3112.          GeV +- 100 GeV

#####
### SUSY masses and BR observables      ###
#####

massh0           124.79 GeV +- 0.015 GeV
nofit massA0     1000.00000 GeV +- 100 GeV
nofit massH0     1003.59643 +- 100 GeV
nofit massHplus  1003.592 GeV +- 100 GeV
nofit massSupL   6999.28733 GeV +- 500 GeV
nofit massSupR   7243.81287 GeV +- 500 GeV
nofit massSdownL 6999.71951 GeV +- 500 GeV
nofit massSdownR 6954.63886 GeV +- 500 GeV
nofit massScharmL 6999.23684 GeV +- 500 GeV
nofit massScharmR 7243.74589 GeV +- 500 GeV
nofit massSstrangeL 6999.66950 GeV +- 500 GeV

```

### B.3. FITTINO INPUT FILE FOR A PMSSM-10 FIT TO ILC1 OBSERVABLES

```

nofit massSstrangeR      6954.60772 GeV +- 500 GeV
nofit massSstop1        1926.42097 GeV +- 100 GeV
nofit massSstop2        4906.38296 GeV +- 400 GeV
nofit massSbottom1      4902.28372 GeV +- 400 GeV
nofit massSbottom2      6875.89410 GeV +- 500 GeV
nofit massSelectronL    7159.42615 GeV +- 500 GeV
nofit massSelectronR    6726.73695 GeV +- 500 GeV
nofit massSmuL          7159.28676 GeV +- 500 GeV
nofit massSmuR          6726.44117 GeV +- 500 GeV
nofit massStau1         6642.93428 GeV +- 500 GeV
nofit massStau2         7120.04885 GeV +- 500 GeV
nofit massSnueL         7158.56163 GeV +- 500 GeV
nofit massSnumuL        7158.42237 GeV +- 500 GeV
nofit massSnutau1       7119.22521 GeV +- 500 GeV
nofit massGluino        1522.86581 GeV +- 300 GeV
massNeutralino1         105.875467 GeV +- 0.49 GeV
massNeutralino2         -128.898581 GeV +- 0.58 GeV
nofit massNeutralino3   265.221464 GeV +- 10.0 GeV
nofit massNeutralino4   520.469883 GeV +- 10 GeV
massChargino1           117.184139 GeV +- 0.53 GeV
nofit massChargino2     520.556368 GeV +- 10 GeV

```

#####

# Branching ratios

#####

```

BR ( Neutralino2 -> Neutralino1 Electron Electron~ ) alias 1
BR ( Neutralino2 -> Neutralino1 Muon Muon~         ) alias 2
BR ( Neutralino2 -> Neutralino1 Tau Tau~           ) alias 3
BR ( Neutralino2 -> Neutralino1 Gamma              ) alias 4
BR ( Neutralino2 -> Neutralino1 Down Down~         ) alias 5
BR ( Neutralino2 -> Neutralino1 Up Up~             ) alias 6
BR ( Neutralino2 -> Neutralino1 Strange Strange~   ) alias 7
BR ( Neutralino2 -> Neutralino1 Charm Charm~       ) alias 8
BR ( Neutralino2 -> Neutralino1 Bottom Bottom~     ) alias 9
BR ( Chargino1    -> Neutralino1 Down~ Up          ) alias 21
BR ( Chargino1    -> Neutralino1 Strange~ Charm    ) alias 22
BR ( Chargino1    -> Neutralino1 Electron~ Nue    ) alias 24
BR ( Chargino1    -> Neutralino1 Muon~ Numu       ) alias 25
BR ( Chargino1    -> Neutralino1 Tau~ Nutau       ) alias 26

brsum (br_1 br_2 br_3)          alias 30 #sum of neutralino2 to LSP+ l^+ l^-
brsum (br_5 br_6 br_7 br_8 br_9) alias 31 #sum of neutralino2 to LSP+q qbar
brsum (br_21 br_22)             alias 32 #sum of chargino1 to LSP+q qbarprime
brsum (br_24 br_25 br_26)      alias 33 #sum of chargino1 to LSP+lepton \
    leptonneutrino

```

#H20 uncertainties

## APPENDIX B. EXAMPLE FILES

---

```
BR ( h0 -> Bottom Bottom~ ) 0.582531 +- 0.008155 alias 30 #1.4%
BR ( h0 -> Charm Charm~ ) 0.0278679 +- 0.00066883 alias 31 #2.4%
BR ( h0 -> Tau Tau~ ) 0.0669405 +- 0.001205 alias 32 #1.8%
BR ( h0 -> Gluon Gluon ) 0.0710304 +- 0.0014206 alias 33 #2.0%
BR ( h0 -> Gamma Gamma ) 0.00235383 +- 0.00004708 alias 34 #2.0%
BR ( h0 -> Z Z ) 0.0266113 +- 0.00016500 alias 35 #0.62%
BR ( h0 -> W W ) 0.220746 +- 0.00185427 alias 36 #0.84%
```

```
#####
```

```
### Save amount of DM ###
```

```
#####
```

```
nofitLEObs ( omega ) 0.119 +- 0.0022 alias 111
```

```
#####
```

```
# Cross sections
```

```
#####
```

```
# LR 500
```

```
sigma ( ee -> Chargino1 Chargino1~, 500 GeV,-0.8,0.3 ) alias 301
```

```
sigma ( ee -> Neutralino1 Neutralino2, 500 GeV,-0.8,0.3 ) alias 302
```

```
#sigma ( ee -> Neutralino2 Neutralino3, 500 GeV,-0.8,0.3 ) alias 305
```

```
# LR 250
```

```
sigma ( ee -> Chargino1 Chargino1~, 250 GeV,-0.8,0.3 ) alias 331
```

```
sigma ( ee -> Neutralino1 Neutralino2, 250 GeV,-0.8,0.3 ) alias 332
```

```
#sigma ( ee -> Neutralino2 Neutralino3, 250 GeV,-0.8,0.3 ) alias 335
```

```
# LR 350
```

```
sigma ( ee -> Chargino1 Chargino1~, 350 GeV,-0.8,0.3 ) alias 351
```

```
sigma ( ee -> Neutralino1 Neutralino2, 350 GeV,-0.8,0.3 ) alias 352
```

```
#sigma ( ee -> Neutralino2 Neutralino3, 350 GeV,-0.8,0.3 ) alias 355
```

```
# RL 500
```

```
sigma ( ee -> Chargino1 Chargino1~, 500 GeV,0.8,-0.3 ) alias 401
```

```
sigma ( ee -> Neutralino1 Neutralino2, 500 GeV,0.8,-0.3 ) alias 402
```

```
#sigma ( ee -> Neutralino2 Neutralino3, 500 GeV,0.8,-0.3 ) alias 405
```

```
# RL 250
```

```
sigma ( ee -> Chargino1 Chargino1~, 250 GeV,0.8,-0.3 ) alias 431
```

```
sigma ( ee -> Neutralino1 Neutralino2, 250 GeV,0.8,-0.3 ) alias 432
```

```
#sigma ( ee -> Neutralino2 Neutralino3, 250 GeV,0.8,-0.3 ) alias 435
```

```
# RL 350
```

```
sigma ( ee -> Chargino1 Chargino1~, 350 GeV,0.8,-0.3 ) alias 451
```

### B.3. FITTINO INPUT FILE FOR A PMSSM-10 FIT TO ILC1 OBSERVABLES

```
sigma ( ee -> Neutralino1 Neutralino2, 350 GeV,0.8,-0.3 ) alias 452
#sigma ( ee -> Neutralino2 Neutralino3, 350 GeV,0.8,-0.3 ) alias 455
```

```
#####
# cross section times branching ratio
#####
#500 GeV measurements Tomohiko's numbers from 20.12.2017 scaled to H20:
#LR
xsbr ( sigma_301 br_24 brsum_32) 87.51 fb +- 1.27 fb alias 501 \
# Chargino1 Chargino1~ -> (LSP e nu)(LSP qqbarprime)
xsbr ( sigma_301 br_25 brsum_32) 87.47 fb +- 1.11 fb alias 502 \
# Chargino1 Chargino1~ -> (LSP mu nu)(LSP qqbarprime)
xsbr ( sigma_302 br_1) 10.84 fb +- 0.23 fb alias 511 \
# Neutralino2 LSP -> (LSP e+e-)LSP
xsbr ( sigma_302 br_2) 10.84 fb +- 0.21 fb alias 512 \
# Neutralino2 LSP -> (LSP mu+mu-)LSP
#RL
xsbr ( sigma_401 br_24 brsum_32) 20.10 fb +- 0.56 fb alias 521 \
# Chargino1 Chargino1~ -> (LSP e nu)(LSP qqbarprime)
xsbr ( sigma_401 br_25 brsum_32) 20.09 fb +- 0.48 fb alias 522 \
# Chargino1 Chargino1~ -> (LSP mu nu)(LSP qqbarprime)
xsbr ( sigma_402 br_1) 7.69 fb +- 0.15 fb alias 531 \
# Neutralino2 LSP -> (LSP e+e-)LSP
xsbr ( sigma_402 br_2) 7.69 fb +- 0.14 fb alias 532 \
# Neutralino2 LSP -> (LSP mu+mu-)LSP

#250 GeV H20 int lumi
#LR
xsbr ( sigma_331 br_24 brsum_32) 140.52 fb +- 1.75 fb alias 551 \
# Chargino1 Chargino1~ -> (LSP e nu)(LSP qqbarprime)
xsbr ( sigma_331 br_25 brsum_32) 140.46 fb +- 1.53 fb alias 552 \
# Chargino1 Chargino1~ -> (LSP mu nu)(LSP qqbarprime)
xsbr ( sigma_332 br_1) 19.70 fb +- 0.34 fb alias 561 \
# Neutralino2 LSP -> (LSP e+e-)LSP
xsbr ( sigma_332 br_2) 19.70 fb +- 0.30 fb alias 562 \
# Neutralino2 LSP -> (LSP mu+mu-)LSP
#RL
xsbr ( sigma_431 br_24 brsum_32) 27.48 fb +- 1.22 fb alias 571 \
# Chargino1 Chargino1~ -> (LSP e nu)(LSP qqbarprime)
xsbr ( sigma_431 br_25 brsum_32) 27.47 fb +- 1.06 fb alias 572 \
# Chargino1 Chargino1~ -> (LSP mu nu)(LSP qqbarprime)
xsbr ( sigma_432 br_1) 13.72 fb +- 0.37 fb alias 581 \
# Neutralino2 LSP -> (LSP e+e-)LSP
xsbr ( sigma_432 br_2) 13.72 fb +- 0.36 fb alias 582 \
# Neutralino2 LSP -> (LSP mu+mu-)LSP

#350 GeV H20 int lumi
```

## APPENDIX B. EXAMPLE FILES

---

```

#LR
xsbr ( sigma_351 br_24 brsum_32) 154.64 fb +- 5.80 fb alias 601 \
# Chargino1 Chargino1~ -> (LSP e nu)(LSP qqbarprime)
xsbr ( sigma_351 br_25 brsum_32) 154.58 fb +- 5.08 fb alias 602 \
# Chargino1 Chargino1~ -> (LSP mu nu)(LSP qqbarprime)
xsbr ( sigma_352 br_1) 20.09 fb +- 1.08 fb alias 611 \
# Neutralino2 LSP -> (LSP e+e-)LSP
xsbr ( sigma_352 br_2) 20.09 fb +- 0.97 fb alias 612 \
# Neutralino2 LSP -> (LSP mu+mu-)LSP
#RL
xsbr ( sigma_451 br_24 brsum_32) 33.63 fb +- 4.28 fb alias 621 \
# Chargino1 Chargino1~ -> (LSP e nu)(LSP qqbarprime)
xsbr ( sigma_451 br_25 brsum_32) 33.62 fb +- 3.73 fb alias 622 \
# Chargino1 Chargino1~ -> (LSP mu nu)(LSP qqbarprime)
xsbr ( sigma_452 br_1) 14.12 fb +- 1.17 fb alias 631 \
# Neutralino2 LSP -> (LSP e+e-)LSP
xsbr ( sigma_452 br_2) 14.12 fb +- 1.15 fb alias 632 \
# Neutralino2 LSP -> (LSP mu+mu-)LSP

#####
### Switches ###
#####

fitModel NUHM2

LoopCorrections on
ISR on
UseGivenStartValues on
FitAllDirectly on
CalcPullDist off
CalcIndChisqContr off
BoundsOnX off
ScanX off
SepFitTanbX off
SepFitTanbMu off
SepFitmA off
Calculator SPHENO ./SPheno339beta
HiggsCalculator FEYNHIGGS ./FeynHiggs2104
RelicDensityCalculator MICROMEGAS ./Micromegas
#FlavourCalculator SUPERISO ./slha.x
AfterBurnerDirectory ./afterburner/
#HiggsSignalsPath ./HSwithSLHA
#AstroCalculator ./AstrofitXn

CalculateSPhenoCrossSections on

```

### B.3. FITTINO INPUT FILE FOR A PMSSM-10 FIT TO ILC1 OBSERVABLES

```
UseXsecLimits          off
#GridPath
#Luminosity            20.0   # in fb-1
#RelativeSignalCrossSectionSysUncertainty    0.1
#RelativeBackgroundCrossSectionSysUncertainty 0.1

UseFullCKMMatrix      off
UseMinos              on
UseHesse              on
NumberOfMinimizations 1
ErrDef                1.0
NumberPulls           1
GetContours           off

UseHiggsBounds        off
UseHiggsSignals       off
WriteHiggsCouplings   off

RequireNeut1LSP       on

UseAstroFit           off
AstroCalculator        ./AstrofitXn
UseAFrelic            off
UseAFphoton           off
UseAFsvind            off
UseAFdirect           off

UseMarkovChains       on
MarkovChainReadjustWidth  off
MarkovChainReadjustWidthPeriod 500
MaxMarkovChain        100000

# Uncomment to use adaptive widths in Markov chain
# See ../fittino.in.OnlineMarkovChainOptimisation
UpdateWidths          on
UpdateWidthsScale     2
MarkovInterfaceFilePath /afs/desy.de/group/flc/pool/lehtinen/software/ \
  rundir_fittino/markov/markov.ILC1finH20allilc1noglu.if

MinuitStrategy        2
MachinePrecision      1e-4

Verbose              off

ScanParameters        off
PerformFit            on
```



# Bibliography

- [1] **Particle Data Group** Collaboration, C. Patrignani *et al.*, “Review of Particle Physics,” *Chin. Phys.* **C40** no. 10, (2016) 100001.
- [2] **Particle Data Group** Collaboration, K. A. Olive *et al.*, “Review of Particle Physics,” *Chin. Phys.* **C38** (2014) 090001.
- [3] **ATLAS, CMS** Collaboration, G. Aad *et al.*, “Combined Measurement of the Higgs Boson Mass in  $pp$  Collisions at  $\sqrt{s} = 7$  and 8 TeV with the ATLAS and CMS Experiments,” *Phys. Rev. Lett.* **114** (2015) 191803, [arXiv:1503.07589 \[hep-ex\]](#).
- [4] C. G. Tully, *Elementary particle physics in a nutshell*. Princeton, USA: Univ. Pr., 2011.
- [5] M. Thomson, *Modern particle physics*. Cambridge University Press, New York, 2013. <http://www-spires.fnal.gov/spires/find/books/www?cl=QC793.2.T46::2013>.
- [6] S. L. Glashow, “Partial Symmetries of Weak Interactions,” *Nucl. Phys.* **22** (1961) 579–588.
- [7] A. Salam, “Weak and Electromagnetic Interactions,” *Conf. Proc.* **C680519** (1968) 367–377.
- [8] S. Weinberg, “A Model of Leptons,” *Phys. Rev. Lett.* **19** (1967) 1264–1266.
- [9] H. Fritzsch, M. Gell-Mann, and H. Leutwyler, “Advantages of the Color Octet Gluon Picture,” *Phys. Lett.* **47B** (1973) 365–368.
- [10] F. Englert and R. Brout, “Broken Symmetry and the Mass of Gauge Vector Mesons,” *Phys. Rev. Lett.* **13** (1964) 321–323. [,157(1964)].
- [11] P. W. Higgs, “Broken Symmetries and the Masses of Gauge Bosons,” *Phys. Rev. Lett.* **13** (1964) 508–509. [,160(1964)].
- [12] G. S. Guralnik, C. R. Hagen, and T. W. B. Kibble, “Global Conservation Laws and Massless Particles,” *Phys. Rev. Lett.* **13** (1964) 585–587. [,162(1964)].
- [13] A. Denner, S. Heinemeyer, I. Puljak, D. Rebuszi, and M. Spira, “Standard Model Higgs-Boson Branching Ratios with Uncertainties,” *Eur. Phys. J.* **C71** (2011) 1753, [arXiv:1107.5909 \[hep-ph\]](#).
- [14] C. F. Dürig, *Measuring the Higgs Self-coupling at the International Linear Collider*. PhD thesis, Hamburg University, Hamburg, 2016.

<http://bib-pubdb1.desy.de/search?cc=Publication+Database&of=hd&p=reportnumber:DESY-THESIS-2016-027>.

- [15] **LHC Higgs Cross Section Working Group** Collaboration, D. de Florian *et al.*, “Handbook of LHC Higgs Cross Sections: 4. Deciphering the Nature of the Higgs Sector,” [arXiv:1610.07922](https://arxiv.org/abs/1610.07922) [hep-ph].
- [16] V. C. Rubin, W. K. Ford, Jr., and N. Thonnard, “Extended rotation curves of high-luminosity spiral galaxies. IV. Systematic dynamical properties, Sa through Sc,” *Astrophys. J.* **225** (1978) L107–L111.
- [17] V. C. Rubin, N. Thonnard, and W. K. Ford, Jr., “Rotational properties of 21 SC galaxies with a large range of luminosities and radii, from NGC 4605 /R = 4kpc/ to UGC 2885 /R = 122 kpc/,” *Astrophys. J.* **238** (1980) 471.
- [18] K. Lundmark *Meddelande fran Lunds astronomiska Observatorium* (1930) No. 125, 1.
- [19] F. Zwicky, “Die Rotverschiebung von extragalaktischen Nebeln,” *Helv. Phys. Acta* **6** (1933) 110–127. [Gen. Rel. Grav.41,207(2009)].
- [20] E. Holmberg, “A Study of Double and Multiple Galaxies Together with Inquiries into some General Metagalactic Problems,” *Annals of the Observatory of Lund* **6** (1937) 3.
- [21] M. Milgrom, “A Modification of the Newtonian dynamics as a possible alternative to the hidden mass hypothesis,” *Astrophys. J.* **270** (1983) 365–370.
- [22] D. Clowe, A. Gonzalez, and M. Markevitch, “Weak lensing mass reconstruction of the interacting cluster 1E0657-558: Direct evidence for the existence of dark matter,” *Astrophys. J.* **604** (2004) 596–603, [arXiv:astro-ph/0312273](https://arxiv.org/abs/astro-ph/0312273) [astro-ph].
- [23] M. Markevitch, A. H. Gonzalez, D. Clowe, A. Vikhlinin, L. David, W. Forman, C. Jones, S. Murray, and W. Tucker, “Direct constraints on the dark matter self-interaction cross-section from the merging galaxy cluster 1E0657-56,” *Astrophys. J.* **606** (2004) 819–824, [arXiv:astro-ph/0309303](https://arxiv.org/abs/astro-ph/0309303) [astro-ph].
- [24] P. J. E. Peebles, “Large scale background temperature and mass fluctuations due to scale invariant primeval perturbations,” *Astrophys. J.* **263** (1982) L1–L5.
- [25] J. R. Bond, A. S. Szalay, and M. S. Turner, “Formation of Galaxies in a Gravitino Dominated Universe,” *Phys. Rev. Lett.* **48** (1982) 1636.
- [26] G. R. Blumenthal, H. Pagels, and J. R. Primack, “Galaxy formation by dissipationless particles heavier than neutrinos,” *Nature* **299** (1982) 37–38.
- [27] G. R. Blumenthal, S. M. Faber, J. R. Primack, and M. J. Rees, “Formation of Galaxies and Large Scale Structure with Cold Dark Matter,” *Nature* **311** (1984) 517–525.
- [28] **Planck** Collaboration, P. A. R. Ade *et al.*, “Planck 2015 results. XIII. Cosmological parameters,” [arXiv:1502.01589](https://arxiv.org/abs/1502.01589) [astro-ph.CO].

- [29] J. R. Ellis, T. Falk, K. A. Olive, and M. Srednicki, “Calculations of neutralino-stau coannihilation channels and the cosmologically relevant region of MSSM parameter space,” *Astropart. Phys.* **13** (2000) 181–213, arXiv:hep-ph/9905481 [hep-ph]. [Erratum: *Astropart. Phys.*15,413(2001)].
- [30] S. Dimopoulos, “LHC, SSC and the universe,” *Phys. Lett.* **B246** (1990) 347–352.
- [31] S. P. Martin, “A Supersymmetry primer,” arXiv:hep-ph/9709356 [hep-ph]. [Adv. Ser. Direct. High Energy Phys.18,1(1998)].
- [32] J. P. Miller, E. de Rafael, and B. L. Roberts, “Muon (g-2): Experiment and theory,” *Rept. Prog. Phys.* **70** (2007) 795, arXiv:hep-ph/0703049 [hep-ph].
- [33] **Muon g-2** Collaboration, G. W. Bennett *et al.*, “Final Report of the Muon E821 Anomalous Magnetic Moment Measurement at BNL,” *Phys. Rev.* **D73** (2006) 072003, arXiv:hep-ex/0602035 [hep-ex].
- [34] **Muon g-2** Collaboration, J. Grange *et al.*, “Muon (g-2) Technical Design Report,” arXiv:1501.06858 [physics.ins-det].
- [35] **E34** Collaboration, M. Otani, “Status of the Muon g-2/EDM Experiment at J-PARC (E34),” *JPS Conf. Proc.* **8** (2015) 025008.
- [36] P. Fayet, “U-boson production in e+ e- annihilations, psi and Upsilon decays, and Light Dark Matter,” *Phys. Rev.* **D75** (2007) 115017, arXiv:hep-ph/0702176 [HEP-PH].
- [37] M. Pospelov, “Secluded U(1) below the weak scale,” *Phys. Rev.* **D80** (2009) 095002, arXiv:0811.1030 [hep-ph].
- [38] T. Moroi, “The Muon anomalous magnetic dipole moment in the minimal supersymmetric standard model,” *Phys. Rev.* **D53** (1996) 6565–6575, arXiv:hep-ph/9512396 [hep-ph]. [Erratum: *Phys. Rev.*D56,4424(1997)].
- [39] A. Czarnecki and W. J. Marciano, “The Muon anomalous magnetic moment: A Harbinger for ‘new physics’,” *Phys. Rev.* **D64** (2001) 013014, arXiv:hep-ph/0102122 [hep-ph].
- [40] J. L. Feng and K. T. Matchev, “Supersymmetry and the anomalous magnetic moment of the muon,” *Phys. Rev. Lett.* **86** (2001) 3480–3483, arXiv:hep-ph/0102146 [hep-ph].
- [41] K. J. de Vries *et al.*, “The pMSSM10 after LHC Run 1,” *Eur. Phys. J.* **C75** no. 9, (2015) 422, arXiv:1504.03260 [hep-ph].
- [42] M. B. Green, J. H. Schwarz, and E. Witten, *SUPERSTRING THEORY. VOL. 1: INTRODUCTION*. Cambridge Monographs on Mathematical Physics. 1988. <http://www.cambridge.org/us/academic/subjects/physics/theoretical-physics-and-mathematical-physics/superstring-theory-volume-1>.
- [43] M. B. Green, J. H. Schwarz, and E. Witten, *SUPERSTRING THEORY. VOL. 2: LOOP AMPLITUDES, ANOMALIES AND PHENOMENOLOGY*. 1988. <http://www.cambridge.org/us/academic/subjects/physics/>

theoretical-physics-and-mathematical-physics/  
superstring-theory-volume-2.

- [44] C. Rovelli and L. Smolin, “Loop Space Representation of Quantum General Relativity,” *Nucl. Phys.* **B331** (1990) 80–152.
- [45] A. D. Sakharov, “Violation of CP Invariance, c Asymmetry, and Baryon Asymmetry of the Universe,” *Pisma Zh. Eksp. Teor. Fiz.* **5** (1967) 32–35. [Usp. Fiz. Nauk161,61(1991)].
- [46] H. Georgi and S. L. Glashow, “Unity of All Elementary Particle Forces,” *Phys. Rev. Lett.* **32** (1974) 438–441.
- [47] V. A. Kuzmin, V. A. Rubakov, and M. E. Shaposhnikov, “On the Anomalous Electroweak Baryon Number Nonconservation in the Early Universe,” *Phys. Lett.* **155B** (1985) 36.
- [48] P. Huet and E. Sather, “Electroweak baryogenesis and standard model CP violation,” *Phys. Rev.* **D51** (1995) 379–394, [arXiv:hep-ph/9404302](#) [hep-ph].
- [49] M. Dine, P. Huet, R. L. Singleton, Jr, and L. Susskind, “Creating the baryon asymmetry at the electroweak phase transition,” *Phys. Lett.* **B257** (1991) 351–356.
- [50] A. G. Cohen, D. B. Kaplan, and A. E. Nelson, “Spontaneous baryogenesis at the weak phase transition,” *Phys. Lett.* **B263** (1991) 86–92.
- [51] **Super-Kamiokande** Collaboration, Y. Fukuda *et al.*, “Evidence for oscillation of atmospheric neutrinos,” *Phys. Rev. Lett.* **81** (1998) 1562–1567, [arXiv:hep-ex/9807003](#) [hep-ex].
- [52] **Troitsk** Collaboration, V. N. Aseev *et al.*, “An upper limit on electron antineutrino mass from Troitsk experiment,” *Phys. Rev.* **D84** (2011) 112003, [arXiv:1108.5034](#) [hep-ex].
- [53] P. Minkowski, “ $\mu \rightarrow e\gamma$  at a Rate of One Out of  $10^9$  Muon Decays?,” *Phys. Lett.* **67B** (1977) 421–428.
- [54] P. Yanagida, “Proceedings of the Workshop on Unified Theory and Baryon Number in the Universe, eds. O. Sawada and A. Sugamoto (KEK, Tsukuba, Japan, 1979),”.
- [55] M. Gell-Mann, P. Ramond, and R. Slansky, “Complex Spinors and Unified Theories,” *Conf. Proc.* **C790927** (1979) 315–321, [arXiv:1306.4669](#) [hep-th].
- [56] M. Magg and C. Wetterich, “Neutrino Mass Problem and Gauge Hierarchy,” *Phys. Lett.* **94B** (1980) 61–64.
- [57] G. Lazarides, Q. Shafi, and C. Wetterich, “Proton Lifetime and Fermion Masses in an SO(10) Model,” *Nucl. Phys.* **B181** (1981) 287–300.
- [58] R. N. Mohapatra and G. Senjanovic, “Neutrino Masses and Mixings in Gauge Models with Spontaneous Parity Violation,” *Phys. Rev.* **D23** (1981) 165.
- [59] J. Wess and B. Zumino, “Supergauge Transformations in Four-Dimensions,” *Nucl. Phys.* **B70** (1974) 39–50. [,24(1974)].

- 
- [60] **ZEUS** Collaboration, S. Chekanov *et al.*, “Search for stop production in R-parity-violating supersymmetry at HERA,” *Eur. Phys. J.* **C50** (2007) 269–281, [arXiv:hep-ex/0611018](#) [hep-ex].
- [61] **CDF** Collaboration, T. Aaltonen *et al.*, “Search for R-parity Violating Decays of  $\tau$  sneutrinos to  $e\mu$ ,  $\mu\tau$ , and  $e\tau$  Pairs in  $p\bar{p}$  Collisions at  $\sqrt{s} = 1.96$  TeV,” *Phys. Rev. Lett.* **105** (2010) 191801, [arXiv:1004.3042](#) [hep-ex].
- [62] **ALEPH** Collaboration, D. Buskulic *et al.*, “Search for supersymmetric particles with R-parity violation in  $Z$  decays,” *Phys. Lett.* **B349** (1995) 238–252.
- [63] **CMS** Collaboration, V. Khachatryan *et al.*, “Search for R-parity violating decays of a top squark in proton-proton collisions at  $\sqrt{s} = 8$  TeV,” *Phys. Lett.* **B760** (2016) 178–201, [arXiv:1602.04334](#) [hep-ex].
- [64] B. Vormwald and J. List, “Bilinear  $R$  parity violation at the ILC: neutrino physics at colliders,” *Eur. Phys. J.* **C74** (2014) 2720, [arXiv:1307.4074](#) [hep-ex].
- [65] J. L. Kneur and G. Moultaka, “Inverting the supersymmetric standard model spectrum: From physical to Lagrangian gaugino parameters,” *Phys. Rev.* **D59** (1999) 015005, [arXiv:hep-ph/9807336](#) [hep-ph].
- [66] S. Y. Choi, J. Kalinowski, G. A. Moortgat-Pick, and P. M. Zerwas, “Analysis of the neutralino system in supersymmetric theories,” *Eur. Phys. J.* **C22** (2001) 563–579, [arXiv:hep-ph/0108117](#) [hep-ph]. [Addendum: *Eur. Phys. J.* **C23**,769(2002)].
- [67] D. Pierce and A. Papadopoulos, “Radiative corrections to neutralino and chargino masses in the minimal supersymmetric model,” *Phys. Rev.* **D50** (1994) 565–570, [arXiv:hep-ph/9312248](#) [hep-ph].
- [68] D. Pierce and A. Papadopoulos, “The Complete radiative corrections to the gaugino and Higgsino masses in the minimal supersymmetric model,” *Nucl. Phys.* **B430** (1994) 278–294, [arXiv:hep-ph/9403240](#) [hep-ph].
- [69] D. M. Pierce, J. A. Bagger, K. T. Matchev, and R.-j. Zhang, “Precision corrections in the minimal supersymmetric standard model,” *Nucl. Phys.* **B491** (1997) 3–67, [arXiv:hep-ph/9606211](#) [hep-ph].
- [70] R. Schofbeck and H. Eberl, “Two-loop SUSY QCD corrections to the neutralino masses in the MSSM,” *Phys. Lett.* **B649** (2007) 67–72, [arXiv:hep-ph/0612276](#) [hep-ph].
- [71] R. Schofbeck and H. Eberl, “Two-loop SUSY QCD corrections to the chargino masses in the MSSM,” *Eur. Phys. J.* **C53** (2008) 621–626, [arXiv:0706.0781](#) [hep-ph].
- [72] S. P. Martin and M. T. Vaughn, “Regularization dependence of running couplings in softly broken supersymmetry,” *Phys. Lett.* **B318** (1993) 331–337, [arXiv:hep-ph/9308222](#) [hep-ph].

- [73] S. P. Martin, “Fermion self-energies and pole masses at two-loop order in a general renormalizable theory with massless gauge bosons,” *Phys. Rev.* **D72** (2005) 096008, [arXiv:hep-ph/0509115](#) [hep-ph].
- [74] Y. Yamada, “Two-loop SUSY QCD correction to the gluino pole mass,” *Phys. Lett.* **B623** (2005) 104–110, [arXiv:hep-ph/0506262](#) [hep-ph].
- [75] H. Baer and X. Tata, *Weak scale supersymmetry: From superfields to scattering events*. Cambridge University Press, 2006.  
<http://www.cambridge.org/9780521290319>.
- [76] Y. Yamada, “Radiative corrections to sfermion mass splittings,” *Phys. Rev.* **D54** (1996) 1150–1154, [arXiv:hep-ph/9602279](#) [hep-ph].
- [77] G. Moortgat-Pick *et al.*, “The Role of polarized positrons and electrons in revealing fundamental interactions at the linear collider,” *Phys. Rept.* **460** (2008) 131–243, [arXiv:hep-ph/0507011](#) [hep-ph].
- [78] A. H. Chamseddine, R. L. Arnowitt, and P. Nath, “Locally Supersymmetric Grand Unification,” *Phys. Rev. Lett.* **49** (1982) 970.
- [79] R. Barbieri, S. Ferrara, and C. A. Savoy, “Gauge Models with Spontaneously Broken Local Supersymmetry,” *Phys. Lett.* **119B** (1982) 343.
- [80] L. E. Ibanez, “Locally Supersymmetric SU(5) Grand Unification,” *Phys. Lett.* **118B** (1982) 73–78.
- [81] L. J. Hall, J. D. Lykken, and S. Weinberg, “Supergravity as the Messenger of Supersymmetry Breaking,” *Phys. Rev.* **D27** (1983) 2359–2378.
- [82] N. Ohta, “Grand unified theories based on local supersymmetry,” *Prog. Theor. Phys.* **70** (1983) 542.
- [83] J. R. Ellis, D. V. Nanopoulos, and K. Tamvakis, “Grand Unification in Simple Supergravity,” *Phys. Lett.* **121B** (1983) 123–129.
- [84] L. Alvarez-Gaume, J. Polchinski, and M. B. Wise, “Minimal Low-Energy Supergravity,” *Nucl. Phys.* **B221** (1983) 495.
- [85] L. Randall and R. Sundrum, “Out of this world supersymmetry breaking,” *Nucl. Phys.* **B557** (1999) 79–118, [arXiv:hep-th/9810155](#) [hep-th].
- [86] G. F. Giudice, M. A. Luty, H. Murayama, and R. Rattazzi, “Gaugino mass without singlets,” *JHEP* **12** (1998) 027, [arXiv:hep-ph/9810442](#) [hep-ph].
- [87] K. Choi, K. S. Jeong, and K.-i. Okumura, “Phenomenology of mixed modulus-anomaly mediation in fluxed string compactifications and brane models,” *JHEP* **09** (2005) 039, [arXiv:hep-ph/0504037](#) [hep-ph].
- [88] A. Falkowski, O. Lebedev, and Y. Mambrini, “SUSY phenomenology of KKL<sup>T</sup> flux compactifications,” *JHEP* **11** (2005) 034, [arXiv:hep-ph/0507110](#) [hep-ph].
- [89] H. Baer, V. Barger, H. Serce, and X. Tata, “Natural generalized mirage mediation,” *Phys. Rev.* **D94** no. 11, (2016) 115017, [arXiv:1610.06205](#) [hep-ph].

- 
- [90] K. Choi, A. Falkowski, H. P. Nilles, M. Olechowski, and S. Pokorski, “Stability of flux compactifications and the pattern of supersymmetry breaking,” *JHEP* **11** (2004) 076, [arXiv:hep-th/0411066](#) [hep-th].
- [91] K. Choi, A. Falkowski, H. P. Nilles, and M. Olechowski, “Soft supersymmetry breaking in KKLT flux compactification,” *Nucl. Phys.* **B718** (2005) 113–133, [arXiv:hep-th/0503216](#) [hep-th].
- [92] J. P. Conlon, F. Quevedo, and K. Suruliz, “Large-volume flux compactifications: Moduli spectrum and D3/D7 soft supersymmetry breaking,” *JHEP* **08** (2005) 007, [arXiv:hep-th/0505076](#) [hep-th].
- [93] M. Dine and W. Fischler, “A Phenomenological Model of Particle Physics Based on Supersymmetry,” *Phys. Lett.* **110B** (1982) 227–231.
- [94] C. R. Nappi and B. A. Ovrut, “Supersymmetric Extension of the SU(3) x SU(2) x U(1) Model,” *Phys. Lett.* **113B** (1982) 175–179.
- [95] L. Alvarez-Gaume, M. Claudson, and M. B. Wise, “Low-Energy Supersymmetry,” *Nucl. Phys.* **B207** (1982) 96.
- [96] M. Dine and A. E. Nelson, “Dynamical supersymmetry breaking at low-energies,” *Phys. Rev.* **D48** (1993) 1277–1287, [arXiv:hep-ph/9303230](#) [hep-ph].
- [97] M. Dine, A. E. Nelson, and Y. Shirman, “Low-energy dynamical supersymmetry breaking simplified,” *Phys. Rev.* **D51** (1995) 1362–1370, [arXiv:hep-ph/9408384](#) [hep-ph].
- [98] M. Dine, A. E. Nelson, Y. Nir, and Y. Shirman, “New tools for low-energy dynamical supersymmetry breaking,” *Phys. Rev.* **D53** (1996) 2658–2669, [arXiv:hep-ph/9507378](#) [hep-ph].
- [99] **MSSM Working Group** Collaboration, A. Djouadi *et al.*, “The Minimal supersymmetric standard model: Group summary report,” in *GDR (Groupement De Recherche) - Supersymetrie Montpellier, France, April 15-17, 1998*. 1998. [arXiv:hep-ph/9901246](#) [hep-ph]. [https://inspirehep.net/record/481987/files/arXiv:hep-ph\\_9901246.pdf](https://inspirehep.net/record/481987/files/arXiv:hep-ph_9901246.pdf).
- [100] C. Bartels, *WIMP search and a Cherenkov detector prototype for ILC polarimetry*. PhD thesis, Hamburg University, 2011. <http://www-library.desy.de/cgi-bin/showprep.pl?thesis11-034>.
- [101] **SLD Electroweak Group, DELPHI, ALEPH, SLD, SLD Heavy Flavour Group, OPAL, LEP Electroweak Working Group, L3** Collaboration, S. Schael *et al.*, “Precision electroweak measurements on the  $Z$  resonance,” *Phys. Rept.* **427** (2006) 257–454, [arXiv:hep-ex/0509008](#) [hep-ex].
- [102] T. Falk, K. A. Olive, and M. Srednicki, “Heavy sneutrinos as dark matter,” *Phys. Lett.* **B339** (1994) 248–251, [arXiv:hep-ph/9409270](#) [hep-ph].

- [103] L. J. Hall, T. Moroi, and H. Murayama, “Sneutrino cold dark matter with lepton number violation,” *Phys. Lett.* **B424** (1998) 305–312, [arXiv:hep-ph/9712515 \[hep-ph\]](#).
- [104] T. Han and R. Hempfling, “Messenger sneutrinos as cold dark matter,” *Phys. Lett.* **B415** (1997) 161–169, [arXiv:hep-ph/9708264 \[hep-ph\]](#).
- [105] G. B. Gelmini, P. Gondolo, and E. Roulet, “Neutralino dark matter searches,” *Nucl. Phys.* **B351** (1991) 623–644.
- [106] J. Edsjo and P. Gondolo, “Neutralino relic density including coannihilations,” *Phys. Rev.* **D56** (1997) 1879–1894, [arXiv:hep-ph/9704361 \[hep-ph\]](#).
- [107] G. Gelmini and P. Gondolo, “DM Production Mechanisms,” [arXiv:1009.3690 \[astro-ph.CO\]](#).
- [108] H. Baer, C. Balazs, A. Belyaev, J. K. Mizukoshi, X. Tata, and Y. Wang, “Updated constraints on the minimal supergravity model,” *JHEP* **07** (2002) 050, [arXiv:hep-ph/0205325 \[hep-ph\]](#).
- [109] K. Griest and D. Seckel, “Three exceptions in the calculation of relic abundances,” *Phys. Rev.* **D43** (1991) 3191–3203.
- [110] J. L. Feng, K. T. Matchev, and D. Sanford, “Focus Point Supersymmetry Redux,” *Phys. Rev.* **D85** (2012) 075007, [arXiv:1112.3021 \[hep-ph\]](#).
- [111] K. A. Olive and M. Srednicki, “New Limits on Parameters of the Supersymmetric Standard Model from Cosmology,” *Phys. Lett.* **B230** (1989) 78–82.
- [112] H. Baer, V. Barger, and H. Serce, “SUSY under siege from direct and indirect WIMP detection experiments,” *Phys. Rev.* **D94** no. 11, (2016) 115019, [arXiv:1609.06735 \[hep-ph\]](#).
- [113] T. Bringmann and C. Weniger, “Gamma Ray Signals from Dark Matter: Concepts, Status and Prospects,” *Phys. Dark Univ.* **1** (2012) 194–217, [arXiv:1208.5481 \[hep-ph\]](#).
- [114] P. Gondolo, J. Edsjo, P. Ullio, L. Bergstrom, M. Schelke, and E. A. Baltz, “DarkSUSY: Computing supersymmetric dark matter properties numerically,” *JCAP* **0407** (2004) 008, [arXiv:astro-ph/0406204 \[astro-ph\]](#).
- [115] R. W. Schnee, “Introduction to dark matter experiments,” in *Physics of the large and the small, TASI 09, proceedings of the Theoretical Advanced Study Institute in Elementary Particle Physics, Boulder, Colorado, USA, 1-26 June 2009*, pp. 775–829. 2011. [arXiv:1101.5205 \[astro-ph.CO\]](#).  
<https://inspirehep.net/record/885795/files/arXiv:1101.5205.pdf>.
- [116] M. Kramer, A. Kulesza, R. van der Leeuw, M. Mangano, S. Padhi, T. Plehn, and X. Portell, “Supersymmetry production cross sections in  $pp$  collisions at  $\sqrt{s} = 7$  TeV,” [arXiv:1206.2892 \[hep-ph\]](#).
- [117] B. Fuks, M. Klasen, D. R. Lamprea, and M. Rothering, “Gaugino production in proton-proton collisions at a center-of-mass energy of 8 TeV,” *JHEP* **10** (2012) 081, [arXiv:1207.2159 \[hep-ph\]](#).

- 
- [118] B. Fuks, M. Klasen, D. R. Lamprea, and M. Rothering, “Precision predictions for electroweak superpartner production at hadron colliders with RESUMMINO,” *Eur. Phys. J. C* **73** (2013) 2480, [arXiv:1304.0790 \[hep-ph\]](#).
- [119] CMS Collaboration, A. M. Sirunyan *et al.*, “Combined search for electroweak production of charginos and neutralinos in proton-proton collisions at  $\sqrt{s} = 13$  TeV,” *JHEP* **03** (2018) 160, [arXiv:1801.03957 \[hep-ex\]](#).
- [120] ATLAS Collaboration, “Public supersymmetry results, accessed 29.4.2018,”.
- [121] Private communication with Jenny List (DESY) and Howard Baer (University of Oklahoma).
- [122] CMS Collaboration, C. Botta, “Progress with final states with soft leptons in CMS,”.
- [123] ATLAS Collaboration, M. Aaboud *et al.*, “Search for electroweak production of supersymmetric states in scenarios with compressed mass spectra at  $\sqrt{s} = 13$  TeV with the ATLAS detector,” *Submitted to: Phys. Rev. D* (2017) , [arXiv:1712.08119 \[hep-ex\]](#).
- [124] ATLAS Collaboration, G. Aad *et al.*, “Search for direct production of charginos, neutralinos and sleptons in final states with two leptons and missing transverse momentum in  $pp$  collisions at  $\sqrt{s} = 8$  TeV with the ATLAS detector,” *JHEP* **05** (2014) 071, [arXiv:1403.5294 \[hep-ex\]](#).
- [125] CMS Collaboration Collaboration, “Search for selectrons and smuons at  $\sqrt{s} = 13$  TeV,” Tech. Rep. CMS-PAS-SUS-17-009, CERN, Geneva, 2017. <https://cds.cern.ch/record/2297116>.
- [126] ATLAS Collaboration, M. Aaboud *et al.*, “Search for squarks and gluinos in events with an isolated lepton, jets and missing transverse momentum at  $\sqrt{s} = 13$  TeV with the ATLAS detector,” [arXiv:1708.08232 \[hep-ex\]](#).
- [127] ATLAS Collaboration, M. Aaboud *et al.*, “Search for additional heavy neutral Higgs and gauge bosons in the ditau final state produced in  $36 \text{ fb}^{-1}$  of  $pp$  collisions at  $\sqrt{s} = 13$  TeV with the ATLAS detector,” [arXiv:1709.07242 \[hep-ex\]](#).
- [128] G. Apollinari, O. Brüning, T. Nakamoto, and L. Rossi, “High Luminosity Large Hadron Collider HL-LHC,” *CERN Yellow Report* no. 5, (2015) 1–19, [arXiv:1705.08830 \[physics.acc-ph\]](#).
- [129] B. Schmidt, “The High-Luminosity upgrade of the LHC: Physics and Technology Challenges for the Accelerator and the Experiments,” *J. Phys. Conf. Ser.* **706** no. 2, (2016) 022002.
- [130] LHC Higgs Cross Section Working Group Collaboration, A. David, A. Denner, M. Duehrssen, M. Grazzini, C. Grojean, G. Passarino, M. Schumacher, M. Spira, G. Weiglein, and M. Zanetti, “LHC HXSWG interim recommendations to explore the coupling structure of a Higgs-like particle,” [arXiv:1209.0040 \[hep-ph\]](#).

- [131] **ATLAS** Collaboration, “Prospects for measuring Higgs pair production in the channel  $H(\rightarrow \gamma\gamma)H(\rightarrow b\bar{b})$  using the ATLAS detector at the HL-LHC,”. <http://cds.cern.ch/record/1956733>.
- [132] **ATLAS** Collaboration, “Projections for measurements of Higgs boson cross sections, branching ratios and coupling parameters with the ATLAS detector at a HL-LHC,”. <http://cds.cern.ch/record/1611186>.
- [133] **ATLAS** Collaboration, “Search for the Standard Model Higgs and Z Boson decays to  $J/\psi\gamma$ : HL-LHC projections,”. <http://cds.cern.ch/record/2054550>.
- [134] **ATLAS** Collaboration, “Study of the double Higgs production channel  $H(\rightarrow b\bar{b})H(\rightarrow \gamma\gamma)$  with the ATLAS experiment at the HL-LHC,”. <https://cds.cern.ch/record/2243387>.
- [135] D. Contardo, M. Klute, J. Mans, L. Silvestris, and J. Butler, “Technical Proposal for the Phase-II Upgrade of the CMS Detector,”. <https://cds.cern.ch/record/2020886>.
- [136] “Search for Supersymmetry at the high luminosity LHC with the ATLAS experiment,”. <https://cds.cern.ch/record/1735031>.
- [137] **CMS** Collaboration, “Updates on Projections of Physics Reach with the Upgraded CMS Detector for High Luminosity LHC,”. <https://cds.cern.ch/record/2221747>.
- [138] S. Ask, “A Review of the supersymmetry searches at LEP,” in *38th Rencontres de Moriond on Electroweak Interactions and Unified Theories Les Arcs, France, March 15-22, 2003*. 2003. [arXiv:hep-ex/0305007](https://arxiv.org/abs/hep-ex/0305007) [hep-ex].
- [139] **DELPHI** Collaboration, J. Abdallah *et al.*, “Searches for supersymmetric particles in  $e^+e^-$  collisions up to 208-GeV and interpretation of the results within the MSSM,” *Eur. Phys. J.* **C31** (2003) 421–479, [arXiv:hep-ex/0311019](https://arxiv.org/abs/hep-ex/0311019) [hep-ex].
- [140] **LEP2 SUSY Working Group, ALEPH, DELPHI, L3 and OPAL experiments** Collaboration, “Note LEPSUSYWG/01-03.1,”.
- [141] **LEP2 SUSY Working Group, ALEPH, DELPHI, L3 and OPAL experiments** Collaboration.
- [142] **LEP2 SUSY Working Group, ALEPH, DELPHI, L3 and OPAL experiments** Collaboration, “Note LEPSUSYWG/04-02.1,”.
- [143] T. Behnke, J. E. Brau, B. Foster, J. Fuster, M. Harrison, J. M. Paterson, M. Peskin, M. Stanitzki, N. Walker, and H. Yamamoto, “The International Linear Collider Technical Design Report - Volume 1: Executive Summary,” [arXiv:1306.6327](https://arxiv.org/abs/1306.6327) [physics.acc-ph].
- [144] F. Richard, J. R. Schneider, D. Trines, and A. Wagner, “TESLA, The Superconducting Electron Positron Linear Collider with an Integrated X-ray Laser Laboratory, Technical Design Report Part 1,” [arXiv:hep-ph/0106314](https://arxiv.org/abs/hep-ph/0106314) [hep-ph].

- [145] SLAC, *Zeroth order design report for the Next Linear Collider: vol.1 vol.2*. 1996. <http://www-spires.fnal.gov/spires/find/books/www?cl=QC787.L53Z35::1996>.
- [146] **Linear Collider ACFA Working Group** Collaboration, K. Abe *et al.*, “Particle physics experiments at JLC,” [arXiv:hep-ph/0109166](https://arxiv.org/abs/hep-ph/0109166) [[hep-ph](#)].
- [147] H. Baer, T. Barklow, K. Fujii, Y. Gao, A. Hoang, S. Kanemura, J. List, H. E. Logan, A. Nomerotski, M. Perelstein, *et al.*, “The International Linear Collider Technical Design Report - Volume 2: Physics,” [arXiv:1306.6352](https://arxiv.org/abs/1306.6352) [[hep-ph](#)].
- [148] K. Fujii *et al.*, “The role of positron polarization for the initial 250 GeV stage of the International Linear Collider,” [arXiv:1801.02840](https://arxiv.org/abs/1801.02840) [[hep-ph](#)].
- [149] Private communication, Jacqueline Yan (KEK), 2016.
- [150] “CMS: Simulated Higgs to two jets and two electrons,” <http://cds.cern.ch/record/628469>.
- [151] C. Adolphsen, M. Barone, B. Barish, K. Buesser, P. Burrows, J. Carwardine, J. Clark, H. Mainaud Durand, G. Dugan, E. Elsen, *et al.*, “The International Linear Collider Technical Design Report - Volume 3.II: Accelerator Baseline Design,” [arXiv:1306.6328](https://arxiv.org/abs/1306.6328) [[physics.acc-ph](#)].
- [152] T. Barklow, J. Brau, K. Fujii, J. Gao, J. List, N. Walker, and K. Yokoya, “ILC Operating Scenarios,” [arXiv:1506.07830](https://arxiv.org/abs/1506.07830) [[hep-ex](#)].
- [153] K. Fujii *et al.*, “Physics Case for the 250 GeV Stage of the International Linear Collider,” [arXiv:1710.07621](https://arxiv.org/abs/1710.07621) [[hep-ex](#)].
- [154] D. M. Asner *et al.*, “ILC Higgs White Paper,” in *Proceedings, 2013 Community Summer Study on the Future of U.S. Particle Physics: Snowmass on the Mississippi (CSS2013): Minneapolis, MN, USA, July 29-August 6, 2013*. 2013. [arXiv:1310.0763](https://arxiv.org/abs/1310.0763) [[hep-ph](#)]. <http://inspirehep.net/record/1256491/files/arXiv:1310.0763.pdf>.
- [155] K. Fujii *et al.*, “Physics Case for the International Linear Collider,” [arXiv:1506.05992](https://arxiv.org/abs/1506.05992) [[hep-ex](#)].
- [156] L. Di Luzio, R. Gröber, and M. Spannowsky, “Maxi-sizing the trilinear Higgs self-coupling: how large could it be?,” *Eur. Phys. J.* **C77** no. 11, (2017) 788, [arXiv:1704.02311](https://arxiv.org/abs/1704.02311) [[hep-ph](#)].
- [157] T. Barklow, K. Fujii, S. Jung, R. Karl, J. List, T. Ogawa, M. E. Peskin, and J. Tian, “Improved Formalism for Precision Higgs Coupling Fits,” [arXiv:1708.08912](https://arxiv.org/abs/1708.08912) [[hep-ph](#)].
- [158] M. Baak *et al.*, “Working Group Report: Precision Study of Electroweak Interactions,” in *Proceedings, 2013 Community Summer Study on the Future of U.S. Particle Physics: Snowmass on the Mississippi (CSS2013): Minneapolis, MN, USA, July 29-August 6, 2013*. 2013. [arXiv:1310.6708](https://arxiv.org/abs/1310.6708) [[hep-ph](#)]. <http://www.slac.stanford.edu/econf/C1307292/docs/EnergyFrontier/Electroweak-19.pdf>.

- [159] K. Seidel, F. Simon, M. Tesar, and S. Poss, “Top quark mass measurements at and above threshold at CLIC,” *Eur. Phys. J.* **C73** no. 8, (2013) 2530, [arXiv:1303.3758 \[hep-ex\]](#).
- [160] M. S. Amjad *et al.*, “A precise characterisation of the top quark electro-weak vertices at the ILC,” *Eur. Phys. J.* **C75** no. 10, (2015) 512, [arXiv:1505.06020 \[hep-ex\]](#).
- [161] F. Richard, “Present and future constraints on top EW couplings,” [arXiv:1403.2893 \[hep-ph\]](#).
- [162] A. Juste, S. Mantry, A. Mitov, A. Penin, P. Skands, E. Varnes, M. Vos, and S. Wimpenny, “Determination of the top quark mass circa 2013: methods, subtleties, perspectives,” *Eur. Phys. J.* **C74** (2014) 3119, [arXiv:1310.0799 \[hep-ph\]](#).
- [163] P. Marquard, A. V. Smirnov, V. A. Smirnov, and M. Steinhauser, “Quark Mass Relations to Four-Loop Order in Perturbative QCD,” *Phys. Rev. Lett.* **114** no. 14, (2015) 142002, [arXiv:1502.01030 \[hep-ph\]](#).
- [164] **Top Quark Working Group** Collaboration, K. Agashe *et al.*, “Working Group Report: Top Quark,” in *Proceedings, 2013 Community Summer Study on the Future of U.S. Particle Physics: Snowmass on the Mississippi (CSS2013): Minneapolis, MN, USA, July 29-August 6, 2013*. 2013. [arXiv:1311.2028 \[hep-ph\]](#).
- [165] T. Horiguchi, A. Ishikawa, T. Suehara, K. Fujii, Y. Sumino, Y. Kiyo, and H. Yamamoto, “Study of top quark pair production near threshold at the ILC,” [arXiv:1310.0563 \[hep-ex\]](#).
- [166] E. Devetak, A. Nomerotski, and M. Peskin, “Top quark anomalous couplings at the International Linear Collider,” *Phys. Rev.* **D84** (2011) 034029, [arXiv:1005.1756 \[hep-ex\]](#).
- [167] M. S. Amjad, M. Boronat, T. Frisson, I. Garcia, R. Poschl, E. Ros, F. Richard, J. Rouene, P. R. Femenia, and M. Vos, “A precise determination of top quark electro-weak couplings at the ILC operating at  $\sqrt{s} = 500$  GeV,” [arXiv:1307.8102 \[hep-ex\]](#).
- [168] M. Berggren, “Simplified SUSY at the ILC,” in *Proceedings, 2013 Community Summer Study on the Future of U.S. Particle Physics: Snowmass on the Mississippi (CSS2013): Minneapolis, MN, USA, July 29-August 6, 2013*. 2013. [arXiv:1308.1461 \[hep-ph\]](#).
- [169] M. Berggren, F. Brümmer, J. List, G. Moortgat-Pick, T. Robens, K. Rolbiecki, and H. Sert, “Tackling light higgsinos at the ILC,” *Eur. Phys. J.* **C73** no. 12, (2013) 2660, [arXiv:1307.3566 \[hep-ph\]](#).
- [170] M. Berggren, A. Cakir, D. Krücker, J. List, I. A. Melzer-Pellmann, B. S. Samani, C. Seitz, and S. Wayand, “Non-Simplified SUSY: Stau-Coannihilation at LHC and ILC,” [arXiv:1508.04383 \[hep-ph\]](#).

- [171] P. Bechtle, M. Berggren, J. List, P. Schade, and O. Stempel, “Prospects for the study of the  $\tilde{\tau}$ -system in SPS1a’ at the ILC,” *Phys. Rev.* **D82** (2010) 055016, [arXiv:0908.0876 \[hep-ex\]](#).
- [172] M. Chera, M. Berggren, and J. List, “Evaluation of SGV with particle flow emulation in context of the “point 5,”.
- [173] S. Kanemura, H. Yokoya, and Y.-J. Zheng, “Complementarity in direct searches for additional Higgs bosons at the LHC and the International Linear Collider,” *Nucl. Phys.* **B886** (2014) 524–553, [arXiv:1404.5835 \[hep-ph\]](#).
- [174] M. Habermehl, K. Fujii, J. List, S. Matsumoto, and T. Tanabe, “WIMP Searches at the International Linear Collider,” *PoS ICHEP2016* (2016) 155, [arXiv:1702.05377 \[hep-ex\]](#).
- [175] C. Bartels, M. Berggren, and J. List, “Characterising WIMPs at a future  $e^+e^-$  Linear Collider,” *Eur. Phys. J.* **C72** (2012) 2213, [arXiv:1206.6639 \[hep-ex\]](#).
- [176] S. Heinemeyer, W. Hollik, and G. Weiglein, “Electroweak precision observables in the minimal supersymmetric standard model,” *Phys. Rept.* **425** (2006) 265–368, [arXiv:hep-ph/0412214 \[hep-ph\]](#).
- [177] P. Chen, “An Introduction to Beamstrahlung and Disruption,” *Lect. Notes Phys.* **296** (1988) 495. [,495(1987)].
- [178] A. Grassellino, A. Romanenko, O. Melnychuk, D. Sergatskov, Y. Trenikhina, A. Crawford, A. Rowe, M. Wong, T. Khabiboulline, and F. Barkov, “Nitrogen and argon doping of niobium for superconducting radio frequency cavities: a pathway to highly efficient accelerating structures,” *Supercond. Sci. Technol.* **26** (2013) 102001, [arXiv:1306.0288 \[physics.acc-ph\]](#).
- [179] A. Grassellino *et al.*, “Unprecedented Quality Factors at Accelerating Gradients up to 45 MV/m in Niobium Superconducting Resonators via Low Temperature Nitrogen Infusion,” *Supercond. Sci. Technol.* **30** (2017) 094004, [arXiv:1701.06077 \[physics.acc-ph\]](#).
- [180] S. Catani, Y. L. Dokshitzer, M. Olsson, G. Turnock, and B. R. Webber, “New clustering algorithm for multi - jet cross-sections in  $e^+e^-$  annihilation,” *Phys. Lett.* **B269** (1991) 432–438.
- [181] S. Sasikumar, J. List, and M. Berggren, “Hadron Production in Photon-Photon Processes at the ILC and the BSM signatures with small mass differences,” [https://agenda.linearcollider.org/event/7645/contributions/40126/attachments/32405/49217/Swathi\\_LCWS17.pdf](https://agenda.linearcollider.org/event/7645/contributions/40126/attachments/32405/49217/Swathi_LCWS17.pdf).
- [182] H. Abramowicz *et al.*, “The International Linear Collider Technical Design Report - Volume 4: Detectors,” [arXiv:1306.6329 \[physics.ins-det\]](#).
- [183] A. Vogel, *Beam-Induced Backgrounds in Detectors at the ILC*. PhD thesis, Universität Hamburg, 2008. <https://bib-pubdb1.desy.de/record/84444>.
- [184] A. Vauth, *A Quartz Cherenkov Detector for Polarimetry at the ILC*. PhD thesis, University of Hamburg, Dept. Phys., 2014. <http://www-library.desy.de/cgi-bin/showprep.pl?thesis14-022>.

- [185] S. Boogert *et al.*, “Polarimeters and Energy Spectrometers for the ILC Beam Delivery System,” *JINST* **4** (2009) P10015, arXiv:0904.0122 [physics.ins-det].
- [186] I. Marchesini, *Triple gauge couplings and polarization at the ILC and leakage in a highly granular calorimeter*. PhD thesis, Hamburg University, 2011. <http://www-library.desy.de/cgi-bin/showprep.pl?thesis11-044>.
- [187] R. Karl and J. List, “Polarimetry at the ILC,” in *Proceedings, International Workshop on Future Linear Colliders 2016 (LCWS2016): Morioka, Iwate, Japan, December 05-09, 2016*. 2017. arXiv:1703.00214 [hep-ex]. <http://inspirehep.net/record/1515505/files/arXiv:1703.00214.pdf>.
- [188] **ILD, SiD** Collaboration, J. List, “Beam Polarisation and Triple Gauge Couplings in  $e^+e^- \rightarrow W^+W^-$  at the ILC,” *PoS EPS-HEP2013* (2013) 233.
- [189] K. Kawagoe *et al.*, “Press release: Announcement of the results of the ILC candidate site evaluation in Japan. Accessed 19.11.2017,”. <http://ilc-str.jp/topics/2013/08281826/>.
- [190] **TLEP Design Study Working Group** Collaboration, M. Bicer *et al.*, “First Look at the Physics Case of TLEP,” *JHEP* **01** (2014) 164, arXiv:1308.6176 [hep-ex].
- [191] I. Hinchliffe, A. Kotwal, M. L. Mangano, C. Quigg, and L.-T. Wang, “Luminosity goals for a 100-TeV pp collider,” *Int. J. Mod. Phys. A* **30** no. 23, (2015) 1544002, arXiv:1504.06108 [hep-ph].
- [192] N. Arkani-Hamed, T. Han, M. Mangano, and L.-T. Wang, “Physics opportunities of a 100 TeV proton-proton collider,” *Phys. Rept.* **652** (2016) 1–49, arXiv:1511.06495 [hep-ph].
- [193] Future Circular Collider Study, “Project homepage. Accessed on 19.11.2017,”. <https://fcc.web.cern.ch/Pages/default.aspx>.
- [194] Circular Electron Positron Collider, “Project homepage. Accessed on 19.11.2017,”. <http://cepc.ihep.ac.cn/index.html>.
- [195] J. Tang *et al.*, “Concept for a Future Super Proton-Proton Collider,” arXiv:1507.03224 [physics.acc-ph].
- [196] M. Aicheler, P. Burrows, M. Draper, T. Garvey, P. Lebrun, K. Peach, N. Phinney, H. Schmickler, D. Schulte, and N. Toge, “A Multi-TeV Linear Collider Based on CLIC Technology,”. <https://cds.cern.ch/record/1500095?ln=en>.
- [197] **CLICdp, CLIC** Collaboration, M. J. Boland *et al.*, “Updated baseline for a staged Compact Linear Collider,” arXiv:1608.07537 [physics.acc-ph].
- [198] M. A. Thomson, “Particle Flow Calorimetry and the PandoraPFA Algorithm,” *Nucl. Instrum. Meth. A* **611** (2009) 25–40, arXiv:0907.3577 [physics.ins-det].
- [199] J. S. Marshall and M. A. Thomson, “Pandora Particle Flow Algorithm,” in *Proceedings, International Conference on Calorimetry for the High Energy*

- Frontier (CHEF 2013): Paris, France, April 22-25, 2013*, pp. 305–315. 2013. arXiv:1308.4537 [physics.ins-det].  
<https://inspirehep.net/record/1250003/files/arXiv:1308.4537.pdf>.
- [200] **CALICE** Collaboration, “Construction and performance of a silicon photomultiplier/extruded scintillator tail-catcher and muon-tracker,” *JINST* **7** (2012) P04015, arXiv:1201.1653 [physics.ins-det].
- [201] P. Bechtle, K. Desch, and P. Wienemann, “Fittino, a program for determining MSSM parameters from collider observables using an iterative method,” *Comput. Phys. Commun.* **174** (2006) 47–70, arXiv:hep-ph/0412012 [hep-ph].
- [202] P. Bechtle, K. Desch, M. Uhlenbrock, and P. Wienemann, “Constraining SUSY models with Fittino using measurements before, with and beyond the LHC,” *Eur. Phys. J.* **C66** (2010) 215–259, arXiv:0907.2589 [hep-ph].
- [203] R. Brun and F. Rademakers, “ROOT: An object oriented data analysis framework,” *Nucl. Instrum. Meth.* **A389** (1997) 81–86.
- [204] N. Metropolis, A. W. Rosenbluth, M. N. Rosenbluth, A. H. Teller, and E. Teller, “Equation of state calculations by fast computing machines,” *J. Chem. Phys.* **21** (1953) 1087–1092.
- [205] P. Z. Skands *et al.*, “SUSY Les Houches accord: Interfacing SUSY spectrum calculators, decay packages, and event generators,” *JHEP* **07** (2004) 036, arXiv:hep-ph/0311123 [hep-ph].
- [206] W. Porod, “SPheno, a program for calculating supersymmetric spectra, SUSY particle decays and SUSY particle production at e+ e- colliders,” *Comput. Phys. Commun.* **153** (2003) 275–315, arXiv:hep-ph/0301101 [hep-ph].
- [207] S. Heinemeyer, W. Hollik, and G. Weiglein, “FeynHiggs: A Program for the calculation of the masses of the neutral CP even Higgs bosons in the MSSM,” *Comput. Phys. Commun.* **124** (2000) 76–89, arXiv:hep-ph/9812320 [hep-ph].
- [208] N. Nguyen, D. Horns, and T. Bringmann, “AstroFit: An Interface Program for Exploring Complementarity in Dark Matter Research,” in *Proceedings, 13th ICATPP Conference on Astroparticle, Particle, Space Physics and Detectors for Physics Applications (ICATPP 2011): Como, Italy, October 3-7, 2011*, pp. 1025–1030. 2012. arXiv:1202.1385 [astro-ph.HE].
- [209] A. Arbey and F. Mahmoudi, “SuperIso Relic: A Program for calculating relic density and flavor physics observables in Supersymmetry,” *Comput. Phys. Commun.* **181** (2010) 1277–1292, arXiv:0906.0369 [hep-ph].
- [210] S. Kraml, S. Kulkarni, U. Laa, A. Lessa, W. Magerl, D. Proschofsky-Spindler, and W. Waltenberger, “SModelS: a tool for interpreting simplified-model results from the LHC and its application to supersymmetry,” *Eur. Phys. J.* **C74** (2014) 2868, arXiv:1312.4175 [hep-ph].
- [211] P. Bechtle, O. Brein, S. Heinemeyer, G. Weiglein, and K. E. Williams, “HiggsBounds: Confronting Arbitrary Higgs Sectors with Exclusion Bounds

- from LEP and the Tevatron,” *Comput. Phys. Commun.* **181** (2010) 138–167, arXiv:0811.4169 [hep-ph].
- [212] Sonneveld, J. for the Fittino Collaboration, “Towards a phenomenological MSSM fit with Fittino,” *SUSY2016 conference, Melbourne* (2016) .  
<https://indico.cern.ch/event/443176/contributions/2166576/>.
- [213] W. Porod and F. Staub, “SPheno 3.1: Extensions including flavour, CP-phases and models beyond the MSSM,” *Comput. Phys. Commun.* **183** (2012) 2458–2469, arXiv:1104.1573 [hep-ph].
- [214] F. Staub and W. Porod, “Improved predictions for intermediate and heavy Supersymmetry in the MSSM and beyond,” *Eur. Phys. J.* **C77** no. 5, (2017) 338, arXiv:1703.03267 [hep-ph].
- [215] H. Baer, F. E. Paige, S. D. Protopopescu, and X. Tata, “Simulating Supersymmetry with ISAJET 7.0 / ISASUSY 1.0,” in *Workshop on Physics at Current Accelerators and the Supercollider Argonne, Illinois, June 2-5, 1993*, pp. 0703–720. 1993. arXiv:hep-ph/9305342 [hep-ph]. [http://lss.fnal.gov/cgi-bin/find\\_paper.pl?other/ssc/sscl-preprint-441](http://lss.fnal.gov/cgi-bin/find_paper.pl?other/ssc/sscl-preprint-441).
- [216] O. Buchmueller *et al.*, “Implications of Improved Higgs Mass Calculations for Supersymmetric Models,” *Eur. Phys. J.* **C74** no. 3, (2014) 2809, arXiv:1312.5233 [hep-ph].
- [217] G. Belanger, F. Boudjema, A. Pukhov, and A. Semenov, “MicrOMEGAs: A Program for calculating the relic density in the MSSM,” *Comput. Phys. Commun.* **149** (2002) 103–120, arXiv:hep-ph/0112278 [hep-ph].
- [218] G. Belanger, S. Kraml, and A. Pukhov, “Comparison of SUSY spectrum calculations and impact on the relic density constraints from WMAP,” *Phys. Rev.* **D72** (2005) 015003, arXiv:hep-ph/0502079 [hep-ph].
- [219] M. Drees, J. M. Kim, and K. I. Nagao, “Potentially Large One-loop Corrections to WIMP Annihilation,” *Phys. Rev.* **D81** (2010) 105004, arXiv:0911.3795 [hep-ph].
- [220] B. Herrmann, “Radiative corrections to neutralino annihilation: Recent developments,” *PoS IDM2010* (2011) 123, arXiv:1011.6550 [hep-ph].
- [221] N. Baro, F. Boudjema, G. Chalons, and S. Hao, “Relic density at one-loop with gauge boson pair production,” *Phys. Rev.* **D81** (2010) 015005, arXiv:0910.3293 [hep-ph].
- [222] J. Harz, B. Herrmann, M. Klasen, K. Kovarik, and P. Steppeler, “Precise Prediction of the Dark Matter Relic Density within the MSSM,” *PoS EPS-HEP2015* (2015) 410, arXiv:1510.06295 [hep-ph].
- [223] N. Baro, F. Boudjema, and A. Semenov, “Full one-loop corrections to the relic density in the MSSM: A Few examples,” *Phys. Lett.* **B660** (2008) 550–560, arXiv:0710.1821 [hep-ph].

- [224] J. Harz, B. Herrmann, M. Klasen, K. Kovarik, and P. Steppeler, “Predicting the neutralino relic density in the MSSM more precisely,” *PoS ICHEP2016* (2016) 448, [arXiv:1609.04998 \[hep-ph\]](#).
- [225] F. Feroz and M. P. Hobson, “Multimodal nested sampling: an efficient and robust alternative to MCMC methods for astronomical data analysis,” *Mon. Not. Roy. Astron. Soc.* **384** (2008) 449, [arXiv:0704.3704 \[astro-ph\]](#).
- [226] F. Feroz, M. P. Hobson, and M. Bridges, “MultiNest: an efficient and robust Bayesian inference tool for cosmology and particle physics,” *Mon. Not. Roy. Astron. Soc.* **398** (2009) 1601–1614, [arXiv:0809.3437 \[astro-ph\]](#).
- [227] Y. Akrami, P. Scott, J. Edsjo, J. Conrad, and L. Bergstrom, “A Profile Likelihood Analysis of the Constrained MSSM with Genetic Algorithms,” *JHEP* **04** (2010) 057, [arXiv:0910.3950 \[hep-ph\]](#).
- [228] A. Corona et al., “Minimizing multimodal functions of continuous variables with the ”simulated annealing” algorithm,” *ACM Transactions on Mathematical Software* **13** (1987) 262.
- [229] R. Storn and K. Price, “Differential evolution - a simple and efficient heuristic for global optimization over continuous spaces,” *Journal of Global Optimization* **11** (01, 1997) 341–359.
- [230] M. Bridges, K. Cranmer, F. Feroz, M. Hobson, R. Ruiz de Austri, and R. Trotta, “A Coverage Study of the CMSSM Based on ATLAS Sensitivity Using Fast Neural Networks Techniques,” *JHEP* **03** (2011) 012, [arXiv:1011.4306 \[hep-ph\]](#).
- [231] O. Buchmueller *et al.*, “Supersymmetry in Light of 1/fb of LHC Data,” *Eur. Phys. J.* **C72** (2012) 1878, [arXiv:1110.3568 \[hep-ph\]](#).
- [232] O. Buchmueller *et al.*, “The CMSSM and NUHM1 in Light of 7 TeV LHC,  $B_s \rightarrow \mu^+ \mu^-$  and XENON100 Data,” *Eur. Phys. J.* **C72** (2012) 2243, [arXiv:1207.7315 \[hep-ph\]](#).
- [233] **GAMBIT** Collaboration, P. Athron *et al.*, “GAMBIT: The Global and Modular Beyond-the-Standard-Model Inference Tool,” *Eur. Phys. J.* **C77** no. 11, (2017) 784, [arXiv:1705.07908 \[hep-ph\]](#).
- [234] **GAMBIT** Collaboration, G. D. Martinez, J. McKay, B. Farmer, P. Scott, E. Roebber, A. Putze, and J. Conrad, “Comparison of statistical sampling methods with ScannerBit, the GAMBIT scanning module,” *Eur. Phys. J.* **C77** no. 11, (2017) 761, [arXiv:1705.07959 \[hep-ph\]](#).
- [235] R. Ruiz de Austri, R. Trotta, and L. Roszkowski, “A Markov chain Monte Carlo analysis of the CMSSM,” *JHEP* **05** (2006) 002, [arXiv:hep-ph/0602028 \[hep-ph\]](#).
- [236] M. Cahill-Rowley, J. L. Hewett, A. Ismail, and T. G. Rizzo, “Lessons and prospects from the pMSSM after LHC Run I,” *Phys. Rev.* **D91** no. 5, (2015) 055002, [arXiv:1407.4130 \[hep-ph\]](#).

- [237] H. Baer and J. List, “Post LHC8 SUSY benchmark points for ILC physics,” *Phys. Rev.* **D88** (2013) 055004, [arXiv:1307.0782 \[hep-ph\]](#).
- [238] B. C. Allanach *et al.*, “The Snowmass points and slopes: Benchmarks for SUSY searches,” *Eur. Phys. J.* **C25** (2002) 113–123, [arXiv:hep-ph/0202233 \[hep-ph\]](#).
- [239] G. Belanger, F. Boudjema, A. Pukhov, and A. Semenov, “MicrOMEGAs 2.0: A Program to calculate the relic density of dark matter in a generic model,” *Comput. Phys. Commun.* **176** (2007) 367–382, [arXiv:hep-ph/0607059](#).
- [240] M. Berggren, “SGV 3.0 - a fast detector simulation,” in *International Workshop on Future Linear Colliders (LCWS11) Granada, Spain, September 26-30, 2011*. 2012. [arXiv:1203.0217 \[physics.ins-det\]](#).  
<http://inspirehep.net/record/1091154/files/arXiv:1203.0217.pdf>.
- [241] M. Ball, “Rekonstruktion von Neutralinos mit TESLA,” Diplomarbeit, University of Hamburg, 2003. <http://bib-pubdb1.desy.de/record/295174>.
- [242] N. D’Ascenzo, *Study of the neutralino sector and analysis of the muon response of a highly granular hadron calorimeter at the International Linear Collider*. PhD thesis, Hamburg University, 2009.  
<http://inspirehep.net/record/813195/files/desy-thesis-09-004.pdf>.
- [243] E. Boos, H. U. Martyn, G. A. Moortgat-Pick, M. Sachwitz, A. Sherstnev, and P. M. Zerwas, “Polarization in sfermion decays: Determining tan beta and trilinear couplings,” *Eur. Phys. J.* **C30** (2003) 395–407, [arXiv:hep-ph/0303110](#).
- [244] S. Y. Choi, J. Kalinowski, G. A. Moortgat-Pick, and P. M. Zerwas, “Analysis of the neutralino system in supersymmetric theories: Addendum,” [arXiv:hep-ph/0202039 \[hep-ph\]](#).
- [245] M. M. Nojiri, “Polarization of  $\tau$  lepton from scalar  $\tau$  decay as a probe of neutralino mixing,” *Phys. Rev.* **D51** (1995) 6281–6291, [arXiv:hep-ph/9412374](#).
- [246] S. Y. Choi, A. Djouadi, M. Guchait, J. Kalinowski, H. S. Song, and P. M. Zerwas, “Reconstructing the chargino system at  $e^+e^-$  linear colliders,” *Eur. Phys. J.* **C14** (2000) 535–546, [arXiv:hep-ph/0002033 \[hep-ph\]](#). [,607(2000)].
- [247] **CMS** Collaboration, “Summary results of high mass BSM Higgs searches using CMS run-I data,” <https://cds.cern.ch/record/2142432>.
- [248] **LUX** Collaboration, D. S. Akerib *et al.*, “Results from a search for dark matter in the complete LUX exposure,” *Phys. Rev. Lett.* **118** no. 2, (2017) 021303, [arXiv:1608.07648 \[astro-ph.CO\]](#).
- [249] Mikael Berggren (DESY), Private communication.
- [250] **ATLAS** Collaboration, G. Aad *et al.*, “Summary of the searches for squarks and gluinos using  $\sqrt{s} = 8$  TeV pp collisions with the ATLAS experiment at the LHC,” *JHEP* **10** (2015) 054, [arXiv:1507.05525 \[hep-ex\]](#).

- 
- [251] **CMS** Collaboration, “Search for new physics in the all-hadronic final state with the MT2 variable,” <https://cds.cern.ch/record/2256872?ln=en>.
- [252] H. Baer, M. Brhlik, D. Castano, and X. Tata, “ $b \rightarrow s \gamma$  constraints on the minimal supergravity model with large  $\tan \beta$ ,” *Phys. Rev.* **D58** (1998) 015007, [arXiv:hep-ph/9712305](https://arxiv.org/abs/hep-ph/9712305) [hep-ph].
- [253] **CMS** Collaboration, A. M. Sirunyan *et al.*, “Search for direct production of supersymmetric partners of the top quark in the all-jets final state in proton-proton collisions at  $\sqrt{s} = 13$  TeV,” *JHEP* **10** (2017) 005, [arXiv:1707.03316](https://arxiv.org/abs/1707.03316) [hep-ex].
- [254] L. J. Hall, R. Rattazzi, and U. Sarid, “The Top quark mass in supersymmetric SO(10) unification,” *Phys. Rev.* **D50** (1994) 7048–7065, [arXiv:hep-ph/9306309](https://arxiv.org/abs/hep-ph/9306309) [hep-ph].
- [255] R. Barbieri and G. F. Giudice, “Upper Bounds on Supersymmetric Particle Masses,” *Nucl. Phys.* **B306** (1988) 63–76.
- [256] H. Baer, V. Barger, and M. Savoy, “Upper bounds on sparticle masses from naturalness or how to disprove weak scale supersymmetry,” *Phys. Rev.* **D93** no. 3, (2016) 035016, [arXiv:1509.02929](https://arxiv.org/abs/1509.02929) [hep-ph].
- [257] H. Baer, V. Barger, D. Mickelson, A. Mustafayev, and X. Tata, “Physics at a Higgsino Factory,” *JHEP* **06** (2014) 172, [arXiv:1404.7510](https://arxiv.org/abs/1404.7510) [hep-ph].
- [258] H. Baer, V. Barger, and M. Savoy, “Generalized focus point and mass spectra comparison of highly natural SUGRA GUT models,” *Phys. Rev.* **D93** no. 7, (2016) 075001, [arXiv:1602.06973](https://arxiv.org/abs/1602.06973) [hep-ph].
- [259] H. Baer, V. Barger, M. Savoy, and X. Tata, “Multichannel assault on natural supersymmetry at the high luminosity LHC,” *Phys. Rev.* **D94** no. 3, (2016) 035025, [arXiv:1604.07438](https://arxiv.org/abs/1604.07438) [hep-ph].
- [260] Figure courtesy of Tomohiko Tanabe (University of Tokyo).
- [261] C. Han, A. Kobakhidze, N. Liu, A. Saavedra, L. Wu, and J. M. Yang, “Probing Light Higgsinos in Natural SUSY from Monojet Signals at the LHC,” *JHEP* **02** (2014) 049, [arXiv:1310.4274](https://arxiv.org/abs/1310.4274) [hep-ph].
- [262] **XENON** Collaboration, E. Aprile *et al.*, “Physics reach of the XENON1T dark matter experiment,” *JCAP* **1604** no. 04, (2016) 027, [arXiv:1512.07501](https://arxiv.org/abs/1512.07501) [physics.ins-det].
- [263] L. M. Krauss and J. L. Newstead, “Extracting Particle Physics Information from Direct Detection of Dark Matter with Minimal Assumptions,” [arXiv:1801.08523](https://arxiv.org/abs/1801.08523) [hep-ph].
- [264] Yan, Jacqueline (KEK) and Tanabe, Tomohiko (University of Tokyo).
- [265] P. Mora de Freitas and H. Videau, “Detector simulation with MOKKA / GEANT4: Present and future,” LC-T00L-2003-010.
- [266] F. Gaede, “Marlin and LCCD: Software tools for the ILC,” *Nucl. Instrum. Meth.* **A559** (2006) 177–180.

- [267] F. James and M. Roos, “Minuit: A System for Function Minimization and Analysis of the Parameter Errors and Correlations,” *Comput. Phys. Commun.* **10** (1975) 343–367.
- [268] P. M. Zerwas, J. Kalinowski, A. Freitas, G. A. Blair, S. Y. Choi, H. U. Martyn, G. A. Moortgat-Pick, and W. Porod, “Reconstruction of fundamental SUSY parameters,” [arXiv:hep-ph/0211076](#) [hep-ph]. [Nucl. Phys. Proc. Suppl.117,811(2003)].
- [269] **CMS** Collaboration, A. M. Sirunyan *et al.*, “Search for new physics in events with two soft oppositely charged leptons and missing transverse momentum in proton-proton collisions at  $\sqrt{s} = 13$  TeV,” [arXiv:1801.01846](#) [hep-ex].
- [270] **CMS** Collaboration, A. M. Sirunyan *et al.*, “Search for supersymmetry in multijet events with missing transverse momentum in proton-proton collisions at 13 TeV,” *Phys. Rev.* **D96** no. 3, (2017) 032003, [arXiv:1704.07781](#) [hep-ex].
- [271] **CMS** Collaboration, A. M. Sirunyan *et al.*, “Search for new phenomena with the  $M_{T2}$  variable in the all-hadronic final state produced in proton-proton collisions at  $\sqrt{s} = 13$  TeV,” *Eur. Phys. J.* **C77** no. 10, (2017) 710, [arXiv:1705.04650](#) [hep-ex].
- [272] Mikael Berggren (DESY), Private communication.
- [273] W. Kilian, T. Ohl, and J. Reuter, “WHIZARD: Simulating Multi-Particle Processes at LHC and ILC,” *Eur. Phys. J.* **C71** (2011) 1742, [arXiv:0708.4233](#) [hep-ph].
- [274] S. Y. Choi, M. Guchait, J. Kalinowski, and P. M. Zerwas, “Chargino pair production at e+ e- colliders with polarized beams,” *Phys. Lett.* **B479** (2000) 235–244, [arXiv:hep-ph/0001175](#) [hep-ph]. [,588(2000)].
- [275] Porod, Werner (University of Würzburg), private communication.
- [276] **ILD concept group** Collaboration, S.-L. Lehtinen, H. Baer, M. Berggren, J. List, K. Fujii, J. Yan, and T. Tanabe, “Naturalness and light Higgsinos: why ILC is the right machine for SUSY discovery,” *PoS EPS-HEP2017* (2017) 306, [arXiv:1710.02406](#) [hep-ph].
- [277] K. Desch, J. Kalinowski, G. A. Moortgat-Pick, M. M. Nojiri, and G. Polesello, “SUSY parameter determination in combined analyses at LHC / LC,” *JHEP* **02** (2004) 035, [arXiv:hep-ph/0312069](#) [hep-ph].
- [278] W. Porod, *Phenomenology of stops, sbottoms, staus and  $\tau$ -sneutrino*. PhD thesis, Vienna U., 1998. [arXiv:hep-ph/9804208](#) [hep-ph].





## Acknowledgements

This thesis would not have been written without the contributions of many people. First and foremost I would like to thank my supervisor Jenny List for her inspiring mentorship and dedication throughout the making of this thesis. Secondly, a big thanks goes collectively to the FLC group at DESY for sharing their world-leading expertise in linear collider research. Especially Mikael Berggren has provided essential input on the project throughout. Thank you also to Gudrid Moortgat-Pick for refereeing the written part.

I would like to thank my second supervisor Christian Sander and mentors Karsten Buesser and Thomas Schörner-Sadenius for their support and advice on project time-management. My work would have been impossible without the essential advice on the fitting code from Annika Vauth and Björn Sarrazin, or without the new version of SPheno which Werner Porod created for my project.

I am grateful to Keisuke Fujii, Tomohiko Tanabe and Jacqueline Yan for their contributions to the higgsino project, and for hosting me in Japan for one month. Thank you also to Howard Baer for advice and input on theoretical issues. Thanks go to PIER graduate school and SFB-676 for many opportunities to present my work and improve professional skills.

This thesis would not have been completed without the personal support of many peers and colleagues. Thank you Madalina Chera, Hale Sert, Moritz Habermehl, Swathi Sasikumar, Ambra Provenza, Claude Dürig and Dimitra Tsionou for sharing this time with me.

I am grateful for my friends in Finland and London - thank you for being there for me and for reminding me what is important in life. Thank you to my family for their encouragement and support in pursuing my dreams. Last but not least, I am most indebted to Charlie for his unwavering love and caring in good and in bad times.



## **Eidesstattliche Versicherung**

### **Declaration on oath**

Hiermit erkläre ich an Eides statt, dass ich die vorliegende Dissertationsschrift selbst verfasst und keine anderen als die angegebenen Quellen und Hilfsmittel benutzt habe.

I hereby declare, on oath, that I have written the present dissertation by my own and have not used other than the acknowledged resources and aids.

Hamburg, May 2018

Suvi-Leena Lehtinen